THE ADSORPTION AND DISSOCIATION OF WATER AND HYDROGEN FLUORIDE OVER THE SURFACES OF ALUMINIUM OXIDE POLYMORPHS, A PERIODIC DENSITY FUNCTIONAL THEORY STUDY.

Jonathan D. A. Neville, BSc (Hons).

A thesis submitted to the University of Wales in accordance with the requirements for the degree of Doctor of Philosophy in the Department of Chemistry, University of Wales, Cardiff.

April 2004

UMI Number: U487543

UMI

Dissertation Publishing

ProQuest

Abstract

THE ADSORPTION AND DISSOCIATION OF WATER AND HF OVER THE
SURFACES OF ALUMINIUM OXIDE POLYMORPHS, A PERIODIC DENSITY
FUNCTIONAL THEORY STUDY

Jonathan D. Neville

The polymorphs of aluminium oxide and the low index surfaces are an important class of industrial, commercial and academic interest due to their ability to act as both catalysts in their own right and as supports for other heterogeneous catalysts. The surfaces and the subsequent adsorptions of molecules such as hydrogen fluoride and water can be investigated using a range of computer simulation techniques to supplement the existing experimental literature. This thesis begins with a general introduction to the chemistry of α-, θ- and γ-alumina, with a comprehensive review of previous *ab initio*, atomistic and experimental work.

A combination of atomistic forcefield and density functional theory methods have been used to study surface structure based on periodic models. The forcefield simulations employed the GULP program to consider the stable surfaces of α-alumina, the behaviour of the aluminium terminated {0001} basal plane of α-alumina in isolation, when partially and fully hydroxylated and in the presence of hydrogen fluoride. Molecular adsorption of HF is classified into pure Al-F interaction and/or interaction with both aluminium and the basic oxygen. Stable θ-alumina surfaces and the fully fluorided form of alumina – AlF_3 are also considered.

Quantum mechanical approaches to selecting the most accurate method of calculation for the bulk structure of α-alumina. The aluminium terminated {0001} surface is then fully analysed, followed by the hydroxylated {0001} α-alumina surface, formed by the dissociative chemisorption of water. This is then followed by the energetically favourable chemisorption of hydrogen fluoride onto the clean {0001} α-alumina surface in a 1-2 mode via the Al-F and O-H interactions and the molecular physisorption of water onto the {0001} α-alumina surface. These density functional theory results are completed by the simulations of the stable surfaces of θ-alumina, the investigation into the hydroxylated {101} θ-alumina surface and the β-AlF_3 {100} surface.

Acknowledgments

I would like to acknowledge the following people who have participated in one way or another during the time spent working on this Ph.D., and the writing of this thesis.

Sincere thanks to Dr. David Willock, my supervisor, for all his ideas, direction, and supervision for the last three years and for whom the end could not come sooner.

Prof. Graham Hutchings and Dr. Stuart Taylor for guiding this project from an experimental viewpoint. Mike Jones for doing the experimental work allied to this. Prof. John Casci and Dr. Mike Watson of Synetix for the industrial funding.

I am indebted to most people in the computational chemistry lab during the three years: Robert, Anthony, Karen, Mark N, Chris, Natasha, Rajinder, Farah, Bob, Rudy, Olivier, Ed and Gareth. Also, my good friends past and present in the department: Charlie, George, Tanner, Ben, Smithy, Simon, Will, John, Bitch, Chris, Darragh, Matt, Phil, Dan, Sarah, Jennifer, Graham, Josephine, Pete, Tom, Nick and Baker for many first-rate days/nights out, football and the like.

Also, to my close friends away from work and mostly now away from Cardiff, in no particular order: Lt. Edwards, Vernon, Forrest, Zinny, Trigger, Skip, Jez, Lisa Daniels, Chalky, Angus, Nathan, Reedo, Hayes, King, Buzz, Adam, Archie, Andy and finally Lisa Moore, whom I could always find on the other end of my computer. Indeed, thanks go to everyone with who I have enjoyed many distinguished occasions over the last three years.

Lastly, the biggest thanks of all go to my Mother, Father, Grandmother and Alastair for their support, encouragement and subsidies for which I am eternally obliged.

Contents

Glossary of terms and abbreviations.

ADO	Averaged Dipole Theory.
Al_O	Octahedral aluminium
Al_P	Pentagonal aluminium.
Al_T	Tetragonal aluminium
Al_t	Trigonal aluminium..
B3LYP	Becke (3) – Lee – Yang – Parr basis set.
BFGS	Broyden-Fletcher-Goldfarb-Shanno method of minima searching.
CASTEP	Cambridge Serial Total Energy Package.
CB	Conduction Band.
CBm	Conduction Band minimum.

CBM	Conduction Band Maximum.
CFC	Generic name for a chlorofluorocarbon.
DFP	Davidon-Fletcher-Powell method of minima searching in GULP.
DFT	Density Functional Theory.
DoS	Density of states.
eV	Electronvolt energy unit ($1eV = 96.49$ kJ mol^{-1}).
GAMESS	General Atomic and Molecular Structure System.
γ_s	Surface energy (in J m^{-2}).
GGA	Generalised Gradient Approximation.
GULP	General Utilities Lattice Program.
HCFC-22	Difluorochloromethane.
H-F	Hartree-Fock.
HCl	Hydrogen chloride.
HF	Hydrogen fluoride.
LVB	Lower Valence Band.
LDA	Local Density Approximation.
LITD	Laser Induced Thermal Desorption.
LVBm	Lower Valence Band minimum.
LVBM	Lower Valence Band Maximum.
MP2	Møller-Plesset theory.
PW91	Perdew and Wang gradient corrected correlation energy functional.
θ	Surface coverage (of water or hydroxyl groups).
TPD	Temperature Programmed Desorption.
UVB	Upper Valence Band.
UVBm	Upper Valence Band minimum.
UVBM	Upper Valence Band Maximum.
VASP	Vienna Ab initio Simulation Package.
XRD	X-Ray Diffraction.
XAES	X-ray Auger Electron Spectroscopy.
XANES	X-ray Absorption Near Edge Spectroscopy.
XPS	X-ray Photoelectron Spectroscopy.

Chapter 1

1.1   Properties of alumina structures.

1.1.1   Structure of α-alumina

Industrially, commercially and academically alumina (Al_2O_3) is an important ceramic material with physical properties such as hardness, relative chemical inertness and a high melting temperature, with the aluminium providing Lewis acidity. Environmentally, alumina particles are a major constituent of exhaust from solid rocket motors, for example, a typical shuttle launch will eject approximately 276 000 kg of alumina particles directly into the atmosphere.[1] In addition to the stable phase α-alumina, alumina can exist in a number of metastable polymorphs, predominant amongst these are the catalytically important γ-alumina and θ-alumina. Figure 1.1 illustrates the dehydration sequence of hydrated aluminas to form the polymorphs and ultimately the α-alumina phase. Classification of aluminas is based on the temperature at which the alumina is obtained from the hydroxides.[2]
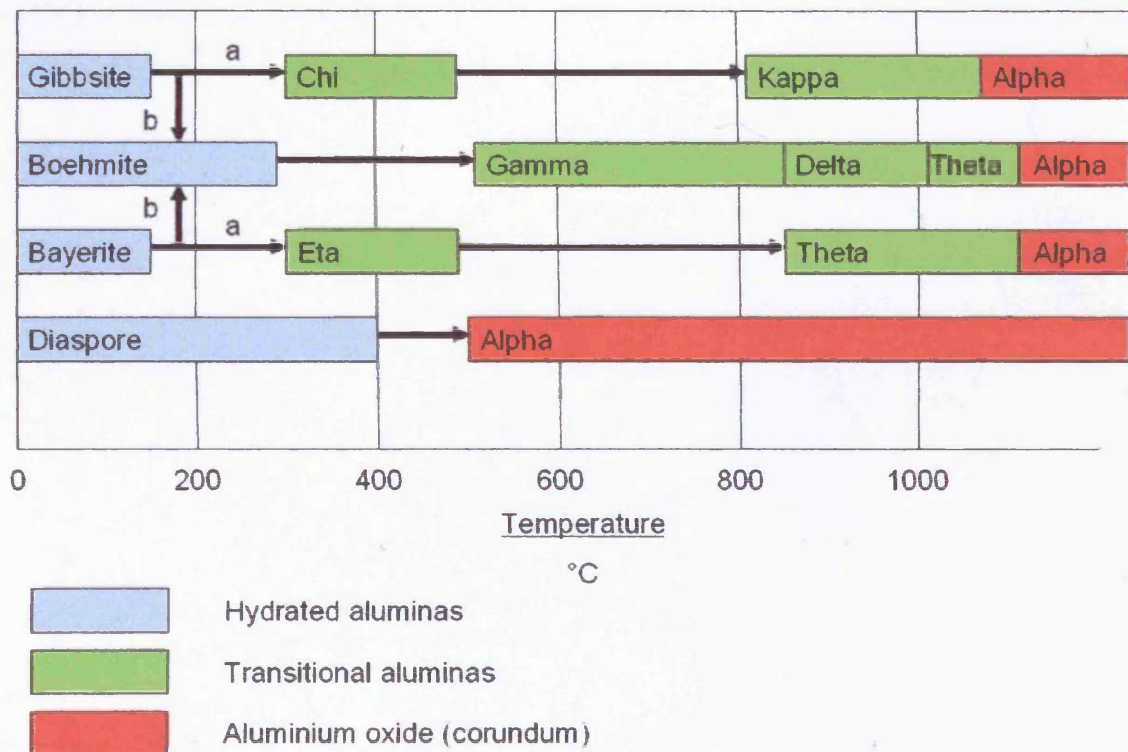
Figure 1.1. Dehydration sequence of hydrated alumina in air. Path b is favoured by moisture, alkalinity and coarse particle size (100 μm), path a is favoured by fine particle size (<10 μm).[3]

Aluminas are divided into two distinct classes based upon either an fcc or hcp arrangement of the oxygen ions: α-alumina has an hcp type packing, conventionally visualised with six rhombohedral unit cells, each with two formula units per primitive cell, of point group D_{3d}^6 symmetry, per hexagonal lattice;[4] γ-alumina being an fcc crystal structure.

In α-alumina, there is only octahedral Al-O_6 cation co-ordination, this phase has been the subject of both experimental and theoretical investigations. For example, the work of Boettger using all-electron, full-potential linear combination of Gaussian type orbitals with local density approximation for exchange-correlation in the GTOFF program calculated high precision total energy results for α-alumina that are consistent to within 0.3% of the zero pressure experimentally determined lattice parameters.[2]

The AlO_6 octahedra in α-alumina are corner sharing in the lattice.[5] From the aluminium atom, this can be visualised as having two triangles, each formed from three oxygen atoms, on either side of the aluminium centre, illustrated in figure 1.2 (a). The other three oxygen atoms form the second triangle lying in a staggered position with respect to the one on the opposite side of the aluminium, shown in figure 1.2 (b). Each oxygen anion in α-alumina is surrounded by four aluminium ions to form an effective sub-unit of Al_4O. When these two structures are combined, a larger hexagonal cell is created: $Al_{12}O_{18}$. alumina can also be visualised as an alternating layering of oxygen and aluminium planes along the [0001] direction, in the sequence $(AlO_3Al) - (AlO_3Al)$.[6]

Experimental crystal structures report lattice parameters for the rhombohedral unit cell of formula $Al_{12}O_{18}$ by Ewald and Hermann,[7] $a = b = 4.7586$ Å and $c = 12.9897$ Å. Further diffraction experiments by Lewis et al have given the lattice parameters as $a = b = 4.7602$ Å and $c = 12.9933$ Å,[8] and text by Wyckoff defines the parameters as $a = b = 5.128$ Å and $c = 13.003$ Å.[9] In the latter structure, the unit cell volume is 85.013 Å^3, with three aluminium-oxygen bonds of 1.857 Å and three bonds of 1.969 Å. In the hexagonal unit cell structure used by Marmier and Finnis in 2002 for theoretical calculations, $a = b = 4.7589$ Å and $c = 12.991$ Å.[4]
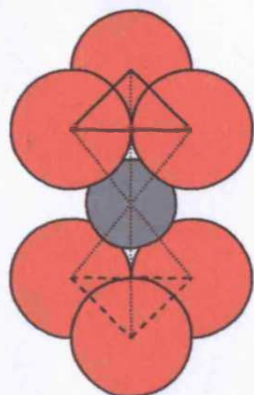
a)   b)
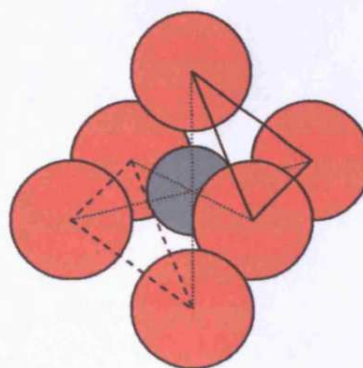
Figure 1.2. (a) An expanded side projection of the co-ordination of six oxygen anions around an aluminium cation in the AlO_6 octahedral unit illustrating the layer arrangement of α-alumina. For clarity, the two distinct triangles in different oxygen layers on opposite sides of the aluminium atom are shown by solid and dashed lines (b) Represents the octahedral nature of the AlO_6 unit as conventionally depicted showing the two axial and four equatorial oxygen atoms. Both diagrams are space filled with bonding superimposed as dotted lines.

1.1.2   Electronic properties of α-alumina.

Figure 1.3 illustrates the band structure of α-alumina phase from the work of Ciraci and Batra using semi empirical calculations based on extended Hückel theory.[3] The lower valence band extends from -36.4 eV to -26.9 eV, consisting mainly of oxygen $2s$ orbitals, whilst the valence band minimum (VBm) and immediately above are formed from the combination of aluminium $3s$ and oxygen $2s$ atomic orbitals. The four bands towards the lower valence band maximum are representative of aluminium $3s$ atomic orbitals. A band gap of about 6 eV occurs between the lower valence band maximum (LVBM) and the upper valence band minimum (UVBm) , before the upper valence band stretching over a range of about 12 eV from -21 eV to -9 eV, in which the atomic orbitals of oxygen $2p$ predominate. In this band, rising from higher to lower energies, the contribution of aluminium $3s$ orbitals declines, giving way to aluminium $3p$ orbitals. At the upper valence band maximum, (VBM), and the immediate region just below to about -12 eV, the bands are relatively flat, reflecting the non-bonding nature of oxygen $2p$ orbitals, a feature common in metal-oxide materials. The shaded area in figure 1.3 denotes the indirect band gap, between the valence band maximum (VBM) and the conduction band minimum (CBm), of 8.7 eV. The CBm is at the centre of the Brillouin

4

Zone, shown by the Greek symbol Γ, this region of the conduction band is assembled from the antibonding aluminium $3s$ and oxygen $2s$ orbitals.

In figure 1.4, the total density of states (a) shows the lower valence band (LVB) at the highest energy of 36 eV to -26.9 eV, the valence band gap from -26.9 eV to ~-20 eV, the start of the upper valence band (UVB) to -8.7 eV, and the conduction band gap from the upper valence band maximum to the conduction band minimum. The sharp peaks at -11 eV in figure 1.4 (a) and (b) is entirely due to oxygen $2p$ since this peak disappears in the partial density of states for oxygen $2s$ (c), and aluminium in (d) and (e). At lower energies, the two peaks at -13 eV and -15 eV along with the indistinct peak at -14.5 eV are due to the hybridisation of aluminium $3p$ and $3s$ interacting with oxygen $2p$ with a slight contribution from oxygen $2s$. The lower valence band is almost entirely representative of oxygen $2s$ with a marginal contribution from aluminium $3p$ and $3s$.
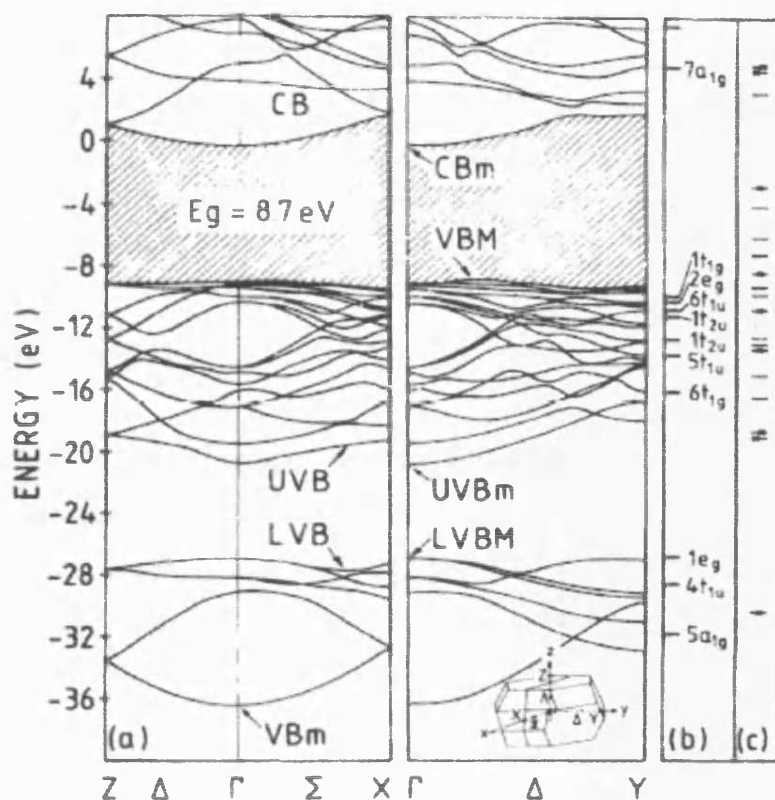
Figure 1.3 (a) Band structure of α-alumina, (b) shows the energy level plot of the AlO$_6$ subunit, and (c) is the energy level plot for Al$_4$O subunit. CB = conduction band, CBm = conduction band minimum, VBM = valence band maximum, UVB = upper valence band, UVBm = upper valence band minimum, LVB = lower valence band, LVBM = lower valence band maximum and VBm = valence band minimum. [3]

5
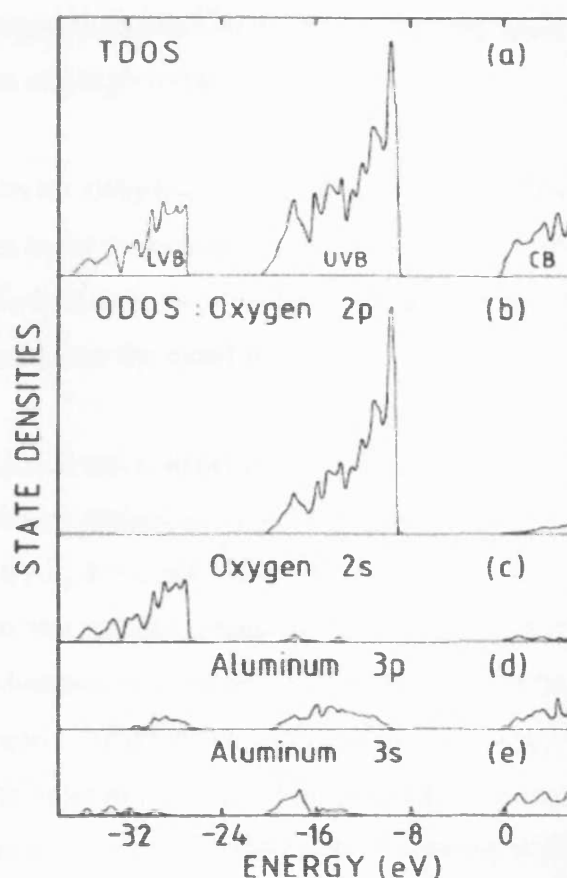
Figure 1.4. Density of states plot for α-alumina. (a) being the total density of states corresponding to the band structure illustrated in figure 1.3 and (b-e) being partial density of states O 2p, O 2s, Al 3p and Al 3s components of the total density of states. [3]

1.1.3 Structure of θ-alumina.

θ-Alumina is the most crystallography ordered of the transition alumina polymorphs and is the penultimate step in the thermal dehydration transformation to α-alumina from boehmite (γ-AlOOH) in the range 1200 to 1300 K [10] or bayerite in the range 875 to 1300 K as shown in figure 1.1. Equation 1.1 shows the typical sequence of dehydration from boehmite:

$$\text{Boehmite} \rightarrow \gamma \rightarrow \delta \rightarrow \theta \rightarrow \alpha \qquad \text{Equation 1.1}$$

θ-alumina is classified as a transition polymorph as it is considered a partially dehydrated aluminium hydroxide rather than the anhydrous α-alumina corundum structure. It is stable at room temperature which leads to industrial applications such as

absorbents, catalyst supports and can be used as a catalysts in its own right due, in part, to the fine particle size and high surface area.

Work by Lippens [11] on the dehydroxylation of highly crystalline boehmite showed that it initially decomposes to the γ-alumina transition form, then to θ-alumina, and finally to α-alumina, this transformation is described as pseudo-morphic as the lattice parameters remained constant throughout the transformation.

Yamaguchi et al [12] carried out a structural determination of θ-alumina which indicates that half of the aluminium cations occupy tetrahedral sites in a crystal analogous to β-Ge_2O_3, where $a = 11.81$ Å, $b = 2.906$ Å, $c = 5.625$ Å and $\beta = 103.8°$, volume $= 93.6$ Å^3. This is in contrast to the nuclear magnetic resonance work by John et al [13] which determined the co-ordination of aluminium to be almost entirely octahedral in samples derived from bayerite (aluminium trihydroxide) and boehmite (aluminium monohydroxide). Both bayerite and boehmite precursors have exclusively octahedrally co-ordinated aluminium, upon transformation to θ-alumina aluminium is found in 50% octahedral and 50% tetrahedral co-ordination. In the work on transitions between η-, γ- and θ-aluminas by Zhou and Snyder.[10] The space group of θ-alumina is defined as C2/m, with $a = 11.854$ Å, $b = 2.904$ Å, $c = 5.622$ Å, volume $= 93.9$ Å^3 and the angle between a and c vector, $\beta = 103.83°$, with an average aluminium-oxygen bond length of 1.75 Å for tetrahedral aluminium, Al_T, and 1.94 Å for octahedral aluminium, Al_O, with an average O-Al-O angle of 110.99° for tetrahedral aluminium, 90.71° for axial/equatorial O-Al_O-O and 173.12° for axial/axial O-Al_O-O bonds.

Density functional theory work has been carried out by Cai and co-workers [14] used the CASTEP (Cambridge Serial Total Energy Package) program with the PW91 generalised gradient approximation to the exchange and correlation energy, ultrasoft pseudopotentials and a kinetic energy cut-off of 380 eV. They were concerned with modelling the dehydration mechanism of the transformation of γ-alumina to θ-alumina. This transformation was found to proceed by the movement of aluminium atoms in γ-alumina to neighbouring interstitial sites to yield a crystal structure closely resembling θ-alumina, in two distinct schemes. The first proposal was that eight aluminium atoms in both octahedral and tetrahedral sites moved to two octahedral sites and six tetrahedral

sites. The second involved fourteen aluminium atoms moving to six octahedral sites and eight tetrahedral sites. The final θ-alumina structures are equivalent and the oxygen lattice is unaltered by the transformation. In the first model, the optimised lattice parameters were $a = 12.20$ Å, $b = 5.727$ Å, $c = 5.529$ Å and $\beta = 103.7°$ with Al_O-O bond length 1.912 Å and Al_T-O bond length 1.738 Å. In the second model the optimised parameters were $a = 12.22$ Å, $b = 5.719$ Å, $c = 5.529$ Å and $\beta = 103.6°$ with Al_O-O bond length 1.911 Å and Al_T-O bond length 1.738 Å.

Further work by Wolverton and Hass [15] used the Vienna *ab initio* simulation package (VASP) incorporating ultrasoft pseudopotentials and using both the local density approximation (LDA) and the generalised gradient approximation (GGA) to calculate the lattice parameters and energies of the stable θ-alumina phase. Compared to the work of Cai [14] that employed a kinetic energy cut-off of 380 eV, Wolverton used a higher cut-off of 495 eV to reach convergence. The results of the two approaches to the exchange correlation using VASP are shown in table 1.1.

This work confirmed the preference for octahedral aluminium co-ordination during the thermal dehydration transformation from boehmite, containing entirely octahedral aluminium, to θ-alumina, in this case containing 50 % tetrahedral and 50 % octahedral aluminium, and further to the exclusively octahedral aluminium co-ordination present in α-alumina. To maintain stoichiometry, octahedral vacancies are preferred, with widely separated vacancies being lower in energy and more stable than near-neighbour vacancies. In terms of accuracy, when taken against an experimental average of both Zhou [10] and Yamaguchi [12], the results of both the LDA and GGA calculations are shown in table 1.1, showing that there is a high degree of accuracy in the VASP calculations with both LDA and GGA exchange correlation functions compared to the experimental average shown. Generally, the LDA calculations underestimate the lattice parameters by approximately 1%, and the GGA calculations overestimate the parameters by ≤ 1%, with the respective volumes being consequentially smaller and larger than the experimentally determined values.

Parameter	Exp. Av. [10] & [12]	VASP (LDA) [15]	% deviation	VASP (GGA) [15]	% deviation
a (Å)	11.8335	11.66	-1.47	11.87	+0.31
b (Å)	2.905	2.881	-0.8	2.929	+0.82
c (Å)	5.6235	5.568	-0.99	5.657	+0.59
Volume (Å³)	93.75	90.7	-3.25	95.4	+1.73

Table 1.1. Percentage comparison of the accuracy of LDA and GGA VASP calculations by Wolverton [15] compared to the experimental results obtained by Zhou [10] and Yamaguchi. [12]

Figure 1.5 shows the unit cell of θ-alumina. The cationic layers of alternating tetrahedral and octahedral co-ordination are a feature of the transition polymorphs in general. The interplanar spacing of the oxygen layers is 2.266 Å. A conclusion drawn from this experimental work suggests that the transition from η- or γ-alumina to θ-alumina is a displacive one brought about by the collapse of the tetrahedrally co-ordinated aluminiums to yield a monoclinic θ-alumina structure with equal octahedral and tetrahedral aluminium cations, and then further loss of Al_T leads to corundum via a reconstructive path.
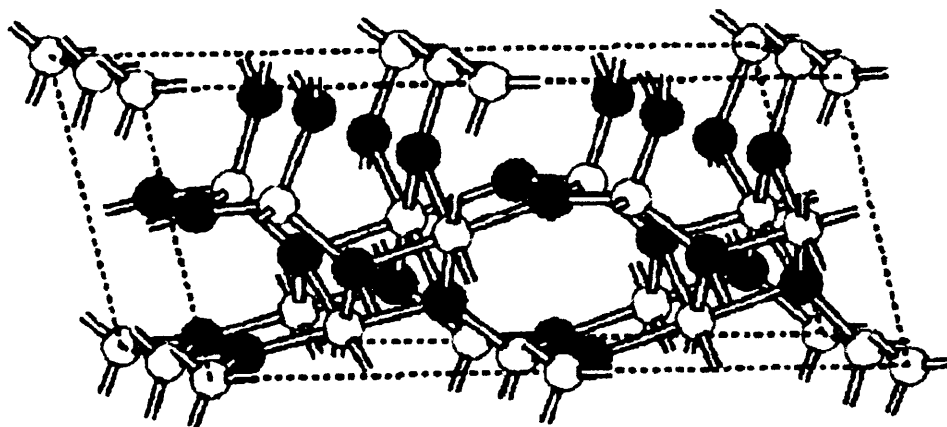
Figure 1.5. θ-alumina unit cell structure, with the formula $Al_{12}O_{18}$. The black spheres indicate oxygen and the white spheres aluminium. The diagonal separation of the oxygen layers is clear when visualised from top left to bottom right. [14]

The work on structure and bonding using ab initio Hartree-Fock methods by Borosy et al [16] shows the differences of bonding between the octahedral and tetrahedral aluminium environments and oxygen. Using the CRYSTAL program, a periodic

Hartree-Fock (H-F) code with an atomic orbital basis set, accurate results for the lattice parameters were obtained and are compared to experimental results in table 1.2.

Parameter	Experimental [12]	Experimental [17]	H-F calculation [16]
a (Å)	11.813	11.795	11.694
b (Å)	2.906	2.91	2.912
c (Å)	5.625	5.6212	5.621
β (deg.)	104.1	103.79	103.9

Table 1.2. Experimental lattice parameters of θ-alumina by Yamaguchi et al [12] and Repelin et al [17] compared to Hartree-Fock calculations by Borosy et al. [16]

For the c vector, the Hartree-Fock calculation differs by less than 1% from the experimental value, whilst the a and b vectors deviate by less than 0.1%. Bond lengths for the different aluminium-oxygen bonds are shown in table 1.3.

Al – O type	Experimental [12]	Experimental [17]	H-F calculation [16]
Al_T-O1 (Å)	1.78	1.815	1.764
Al_T-O2 (Å)	1.73	1.789	1.762
Al_T-O3 (Å)	1.82	1.697	1.776
Al_O-O1 (Å)	1.87	1.838	1.896
Al_O-O2 (Å)	1.86	1.819	1.859
Al_O-O3 (Å)	1.99	1.991	1.946
Al_O-O3^{II} (Å)	1.98	2.097	1.954

Table 1.3. Bond lengths for θ-alumina calculated by Borosy et al [16] compared to experimentally determined values. [12,17]

The average experimental Al_T-O bond length is 1.772 Å, comparing to the theoretically calculated value of 1.767 Å. For Al_O-O bond lengths, the average experimental value is 1.931 Å, whilst the theoretical average value is 1.914 Å, although this must be treated with caution as the octahedrally co-ordinated aluminium contains both axial and equatorial oxygen, with marginally different bond lengths.

The results also indicate the θ-alumina polymorph to be 42 kJ mol^{-1} higher in energy per Al_2O_3 unit than the α-alumina corundum structure when the binding energies of the two phases are considered: -0.848 a.u. (-2226.46 kJ mol^{-1}) for α-alumina and -0.832 a.u. (-2184.45 kJ mol^{-1}) for θ-alumina. This provides a quantitative evaluation that the corundum structure is energetically more stable than the transition θ-alumina polymorph, and explains why the corundum structure is the final stage in the thermal dehydration of boehmite.

1.1.4 Electronic properties of θ-alumina.

The valence band structure calculated by Borosy *et al* for θ-alumina along Brillouin zone symmetry lines is shown in figure 1.6 along with the density of states in figure 1.7. The band analysis gives two distinct valence bands, the upper valence band between 0 and about -8 eV, and the lower valence band between about -22 and -25 eV. The immediate region of the valence band maximum - the uppermost surface of each band - is flat, as in figure 1.3 for α-alumina, representative of the oxygen $2p$ nonbonding electrons, whilst the lower part of each band to the valence band minimum corresponds to oxygen $2s$ electrons. The aluminium contribution to valence band plots is negligible, although the energies would be expected to fall below the lower valence band between -30 and -40 eV, in parallel to the hybridisation of aluminium $3s$ and oxygen $2s$ orbitals outlined for the α-alumina band structure and density of states.
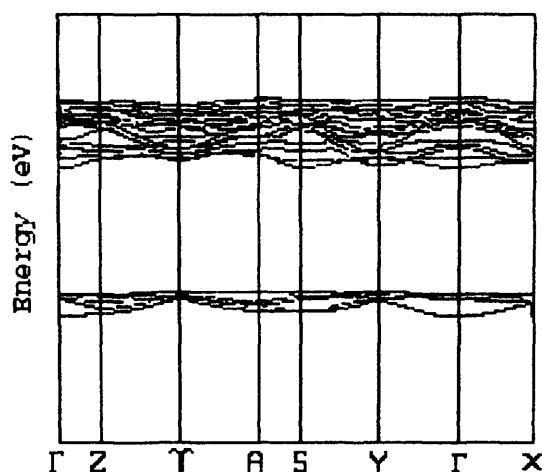
Figure 1.6. Band structure of θ-alumina. The UVB is between 0 and -8 eV and the LVB is between -22 and -25 eV.[16]

11
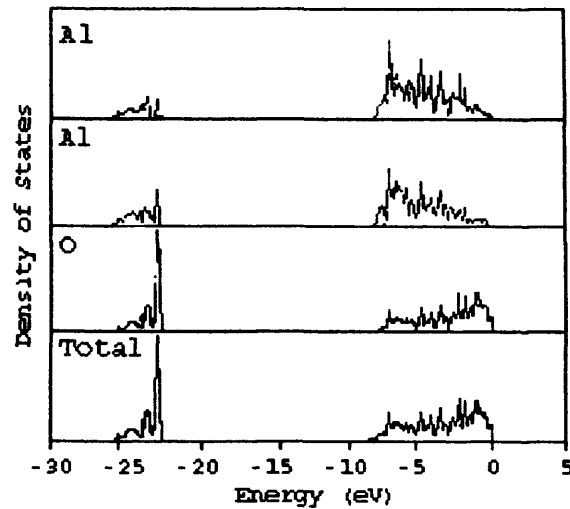
Figure 1.7. Density of states plot corresponding to the band analysis of θ-alumina shown in figure 1.6. The top two plots represent aluminium, the third oxygen and the total density of states is shown in the bottom plot.[16]

1.1.5 Comparison of electronic properties of θ- and α-alumina.

The work by Mo and Ching [18] using first principles orthogonalised linear combination of atomic orbitals with local density approximation (OLCAO-LDA) calculations on both θ- and α-alumina crystals generated the valence and conduction band structures in figure 1.8. A comparison of the band structure and density of states plots for θ- and α-alumina, shows that they both exhibit the same general valence characteristics being grouped in two distinct bands. The lower part of both bands is dominated by the charge transfer from aluminium to oxygen and the non-bonding characteristic of the oxygen 2p states form the upper parts of each band, as shown in figure 1.8 for α-alumina (a) and θ-alumina (b).

12
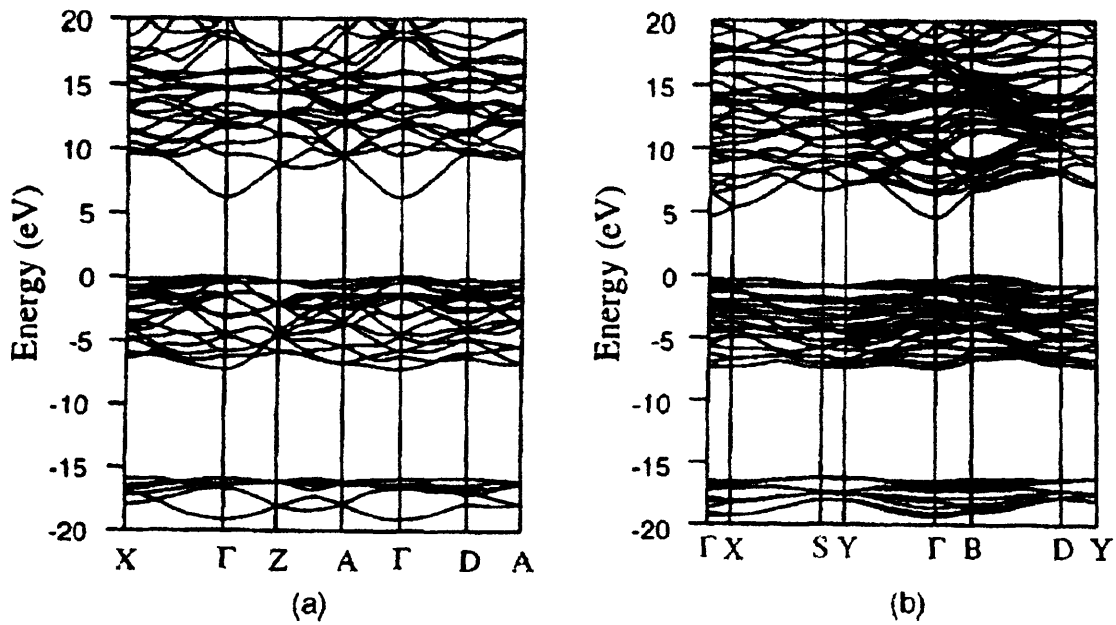
Figure 1.8. (a) α-alumina and (b) θ-alumina band structures.[18]

For α-alumina, the lower valence bandwidth is ~3 eV between ~-16 and ~-19 eV, compared to a bandwidth of 9.5 eV as shown in figure 1.3. The upper bandwidth is 7.27 eV, compared to ~12 eV between -9 eV and -21 eV before. In figure 1.8, this leads to a band gap of 8.7 eV at Γ, the centre of the Brillouin zone, which is also the bottom of the conduction band, which is approximately 5 eV higher in energy than the work by Ciraci *et al.*[3]

For θ-alumina, the upper valence band is in a similar region of 0 to ~-8.0 eV, with the lower bandwidth of equivalent range, but between -16 and -20 eV, equating to approximately 4 eV. However, the top of the upper valence band is centred on B, approximately 1.3 eV less than in the α-alumina band structure. The bottom of the conduction band is centred on Γ, which produces a band gap of 4.64 eV. The band gap between upper and lower band valence bands is 8.86 eV. A discrepancy between this work and that of Borosy *et al* [16] is that a larger unit cell was employed by Mo and Ching. The α-alumina structure has a lower energy than θ-alumina by 1.47 eV per Al_2O_3 formula units, equating to 142 kJ mol⁻¹, as opposed to the quoted value of 42 kJ mol⁻¹ by Borosy *et al*. This range of values allies well with the atomistic potentials work done by Wilson *et al* which gives values for the difference in energy between θ- and α-alumina varying between 27.7 kJ mol⁻¹ using standard Buckingham potentials and 156

kJ mol^{-1} using a 'breathing' polarisable function for the oxygen Buckingham potential.[19] Using the periodic density functional theory program CASTEP and a local density approximation (LDA) for exchange and correlation, the range is reduced to between 55 kJ mol^{-1} and 76 kJ mol^{-1} for the stabilisation of α-alumina to θ-alumina.[14] For the plane-wave pseudopotential CASTEP calculations the cut-off energy is in the range 500-700 eV using between 1 and 14 k-points.

Total density of states calculations for the two alumina polymorphs are shown in figure 1.9. The lower valence band, indicated for both α- and θ-alumina by the downwards arrows at the minimum range -15 to -20 eV is representative of oxygen 2s orbitals, the upper valence band of bonding oxygen 2p in the lower part, nonbonding oxygen 2p orbitals in the upper part, and hybridized aluminium 3s, 3p and 3d orbitals. The other highlighted peaks are for aluminium 3d orbitals at 31 eV in α-alumina and 29 eV in θ-alumina. The partial density of states, shown for aluminium in figure 1.10 and oxygen in figure 1.11, is used to show the individual aluminium and oxygen components of the total density of states as shown in figure 1.9. The dotted lines are the sum of s and d character.
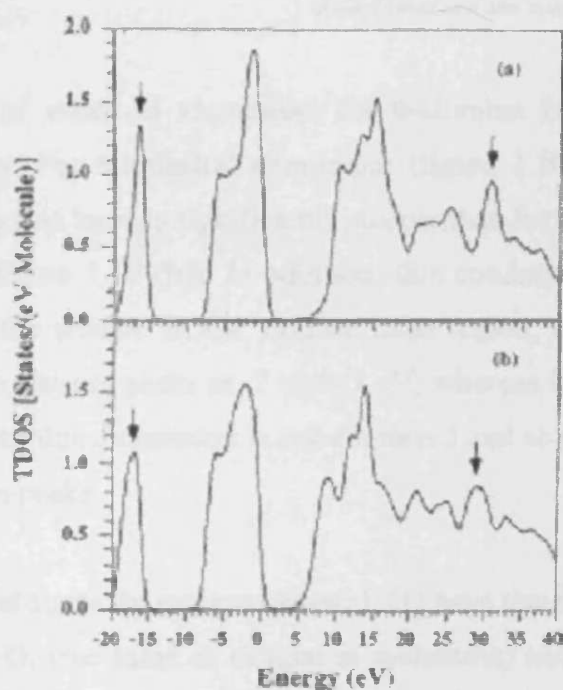
Figure 1.9. Total density of states for (a) α-alumina and (b) θ-alumina. The arrows define the lower valence band oxygen 2s orbitals (left) and the 3d aluminium orbitals (right).[18]
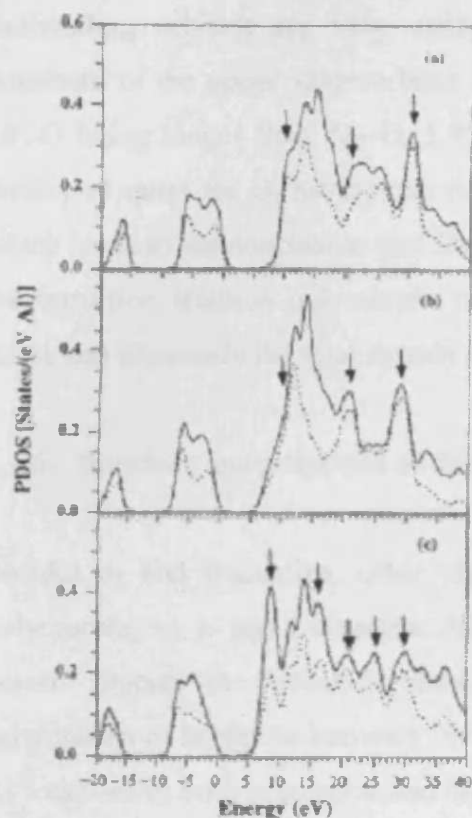
Figure 1.10. Partial density of states for (a) Al_O in α-alumina, (b) Al_O in θ-alumina and (c) Al_T in θ-alumina. The dotted lines are the sum of s and d character.[18]
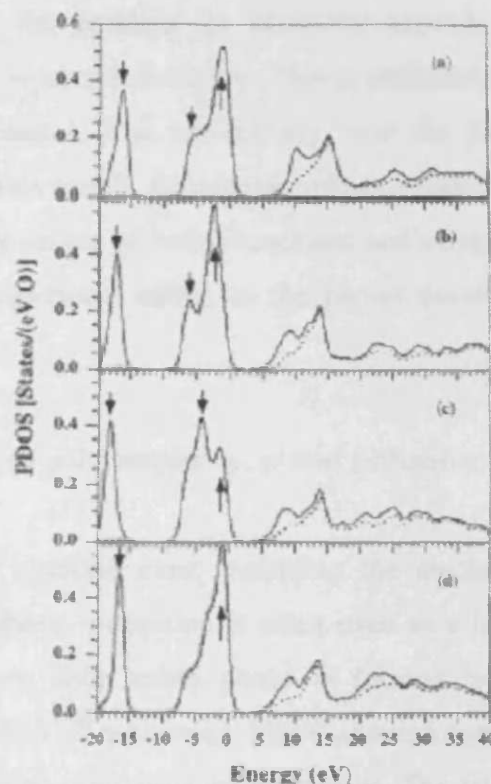
Figure 1.11. Partial density of states of (a) O in α-alumina, (b) fourfold coordinated O_1, and threefold coordinated O_2 (c) and O_3 (d) in θ-alumina. The dotted lines are the sum of s and d character.[18]

The partial density of states of aluminium for θ-alumina has both octahedral and tetrahedral occupancy. For tetrahedral aluminium (figure 1.10 (c)) in θ-alumina, the gradient of the conduction band is significantly steeper than for octahedral aluminium in the same structure (figure 1.10 (b)). In addition, this conduction band contains more peaks, as shown by the arrows. In the valence band region, the s and d components combine to form two distinct peaks at -2 and -7 eV, whereas in tetrahedral aluminium partial density of states this d character is not employed and so the sum of s and d does not result in these two peaks.

The partial densities of states for oxygen (figure 1.11) have three environments, fourfold co-ordinated oxygen O_1 (the same as oxygen in α-alumina) and threefold co-ordinated oxygen atoms O_2 and O_3. The only differences occur in the valence bands. In the upper valence band, for three co-ordinate oxygen, figure 1.11 (c), the bonding $2p$ character has a sharp peak, and the nonbonding $2p$ orbitals are less intense. In figure 1.11 (d), the

15

nonbonding orbitals are very intense and the bonding $2p$ character towards the minimum of the upper valence band orbitals is almost invisible. This is attributable to Al_O-O being longer than Al_T-O, 1.95 Å against 1.77 Å respectively, with the partial density of states for O_2 having two Al_T-O bonds and O_3 containing only one such bond which leads to the conclusion that the local geometry of both aluminium and oxygen in the transition alumina polymorphs have a significant effect on the partial density of states and ultimately the total density of states.

1.1.6 Structure and properties of other alumina polymorphs: η-, γ- and κ-alumina.

Besides α- and θ-alumina, other phases of alumina exist, including the metastable polymorphs η-, γ- and κ-alumina. Amongst these, γ-alumina is often used as a highly porous support for transition metal catalysts, this stable phase is formed by the dehydration of boehmite between 750 and 1025 K.[20] γ-alumina, like θ-alumina contains Al^{3+} cations in both octahedral and tetrahedral co-ordination environments. The relative population is still a matter of debate, XRD experiments indicate a 1:1 ratio while magic angle spinning (MAS) nuclear magnetic resonance (nmr) suggests that 70 ± 2% of Al cations are octahedrally co-ordinated.[21] This indicates that no ordered structure can be obtained using exclusively octahedral aluminium in an fcc arrangement of oxygen anions.

The structure of γ-alumina is often described as a defective spinel polymorph, and denoted as $\square_{2\ 2/3}\ Al_{21\ 1/3}O_{32}$, in which $\square$ is a vacancy. To satisfy stoichiometry there must be $2\frac{2}{3}$ cationic vacancies per cell. At the minimum energy configuration, these vacancies are located at octahedral aluminium sites. Crystallographic data for γ-alumina gives Al-O bond lengths almost identical to those in θ-alumina: Al_T-O being 1.78 Å and Al_O-O being 1.94 Å. The VASP (Vienna *ab-initio* Simulation Program) in the local density approximation with exchange and correlation using a cut-off of 400 eV generated density of states plot is shown in figure 1.12, along with the experimental x-ray photoelectron spectroscopic (XPS) data.[22]
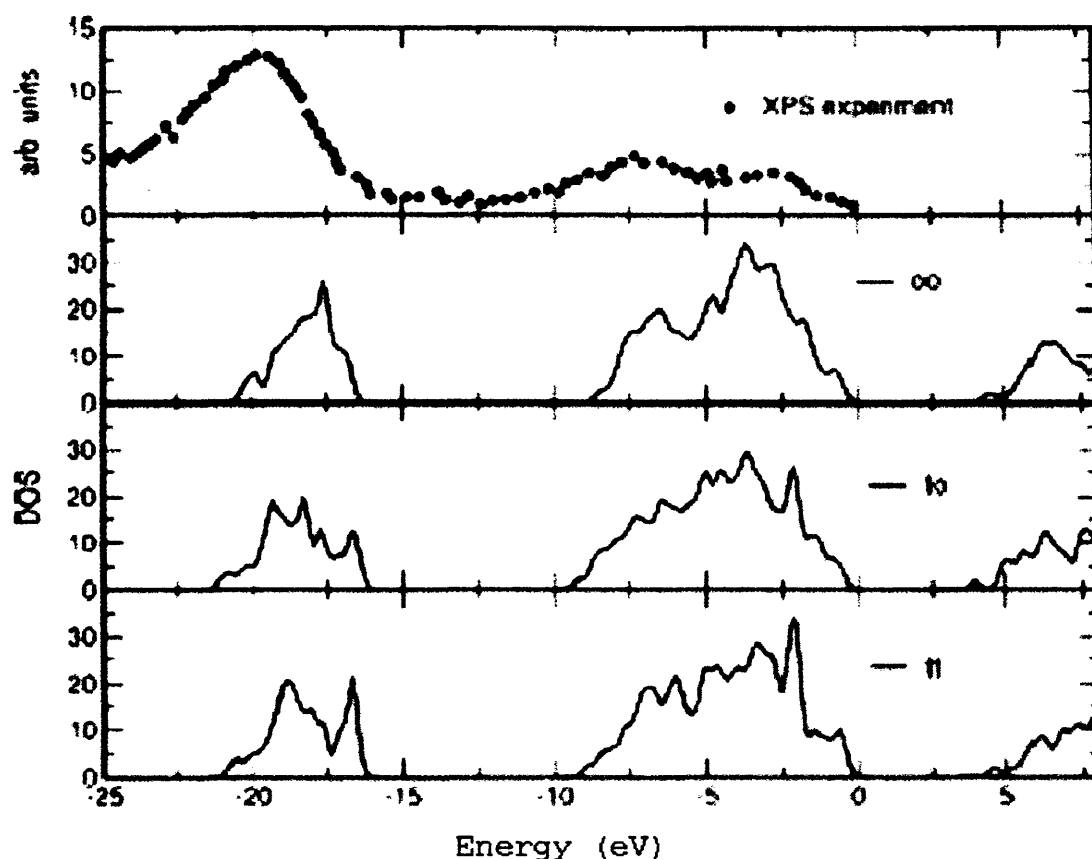
Figure 1.12. Density of states calculated experimentally using XPS and theoretically using VASP for γ-alumina. OO refers to both vacancies being octahedral, OT to one octahedral and one tetrahedral vacancy and TT to both vacancies being tetrahedral in the formula $\square_{2\ 2/3}Al_{21\ 1/3}O_{32}$.[22]

In figure 1.12, the partial density of states has been derived based on: two vacancies occupying both octahedral sites denoted OO; one octahedral and one tetrahedral vacancy, OT; and both tetrahedral vacancies, TT. In all three plots, the upper and lower valence band and the conduction band are unambiguous. Again, the oxygen $2p$ nonbonding orbitals dominate the upper valence band maximum in all three structures, corresponding to the ionic nature of the aluminium – oxygen bond. However, it is the exclusively octahedral vacancy density of states plot with maxima in the upper valence band at -3 and -6.5 eV that replicates the two maxima at -3.16 and -5.47 eV in the XPS data. The resemblance between XPS and calculated density of states is also shown in the lower valence band, with peaks at -20.3 and -17.5 eV respectively.

κ-alumina contains aluminium sites in both octahedral and tetrahedral co-ordination in a unit cell of $Al_{16}O_{24}$, with lattice parameters of a = 4.8351 Å, b = 8.3109 Å and c =

8.9363 Å from the work carried out by Halvarsson.[23] The oxygen planes form a close packed *ABAC* sequence along the *c* axis, interspersed with aluminium in each co-ordination. The total density of states for two structures of κ-alumina calculated by Yourdshahyan *et al* [24] using plane-wave pseudopotential density functional theory calculations at the local density approximation level are shown in figure 1.13 and agrees well with the previous density of states plots for α- and θ-alumina. The solid line with a clear distinction between the upper and lower valence bands illustrates a structure containing only octahedral aluminium cations, and the dashed line indicates only tetrahedral aluminium occupancy, leading to no gap between the upper and lower valence bands, and an unrealistic metallic behaviour in an oxide insulator.
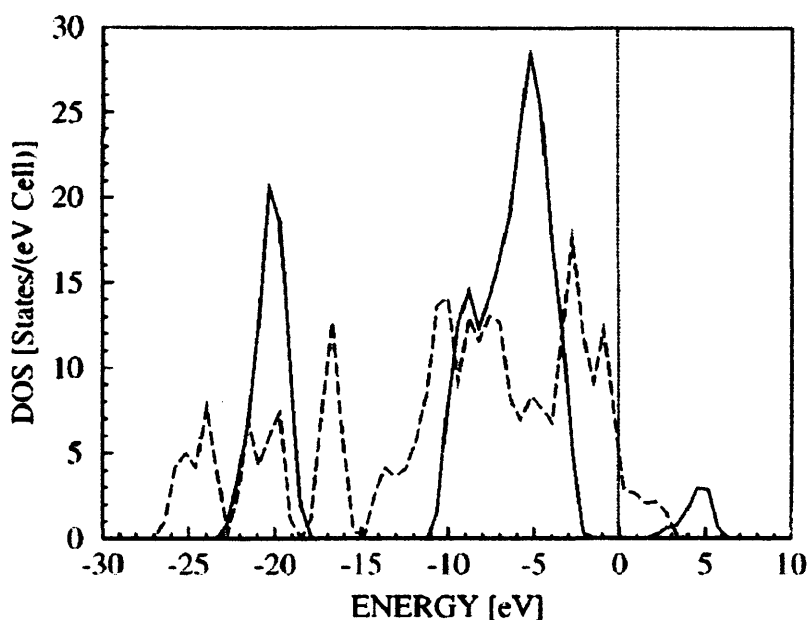
Figure 1.13 Total densities of states for two κ-alumina structures, with the solid line representing entirely octahedral aluminium ions. The dashed line signifying only tetrahedrally coordinated aluminium ions, shows metallic character, having no band gap. [24]

Figure 1.13 shows it is unlikely that κ-alumina contains aluminium solely in tetrahedrally coordinated sites, the partial density of states for a κ-alumina structure containing only octahedral aluminium is shown in figure 1.14, this displays a clear band gap between the upper and lower valence bands, and also between the upper valence band and the conduction band, a typical well-defined plot for an oxide structure, strengthening the evidence for six co-ordinate aluminium in κ-alumina.
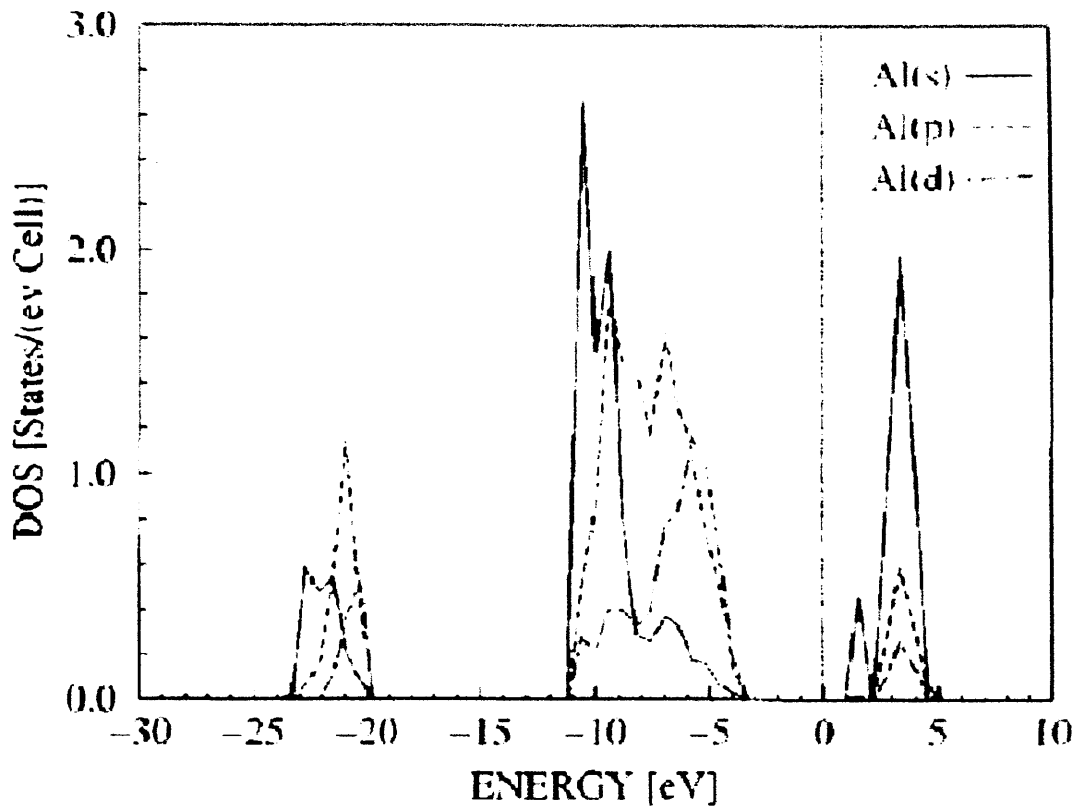
Figure 1.14. Partial density of states for only octahedral aluminium ions in κ-alumina. Solid, dashed and long-dashed lines indicate s, p and d character respectively. [24]

(b)
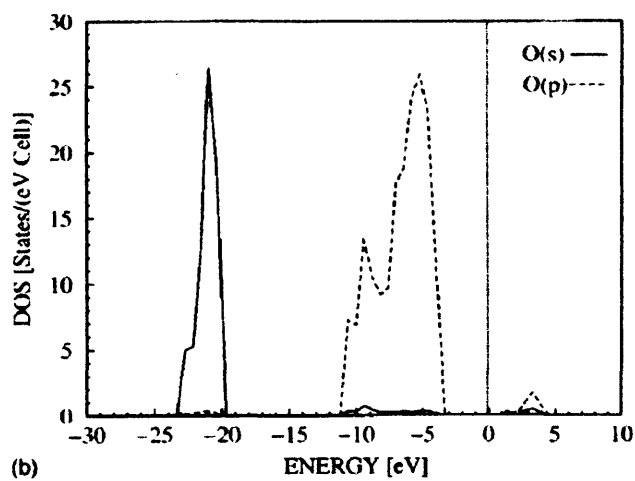
Figure 1.15. Partial density of states for oxygen in κ-alumina. The solid and dashed lines indicate s and p character respectively. [24]

Figure 1.15 shows the partial density of states for the oxygen component of κ-alumina containing only octahedral aluminium, which accounts for all of the charge. The lower valence band is almost entirely 2s in character, whilst the upper valence band is

dominated by the nonbonding $2p$ orbitals – the bonding $2p$ orbitals accounting only for a relatively small sharp peak.

1.2 Atomic and electronic structure of α-alumina surfaces.

1.2.1 {0001} surface structure

The {0001} surface has three possible terminations: oxygen layer; aluminium bi-layer; or aluminium layer. These arrangements are shown in figure 1.16, in which the three different types of aluminium are illustrated. In the bulk structure the first and sixth Al occupy equivalent crystallographic positions from those in the third and fourth layer. These are sandwiched by two oxygen layers.[25]
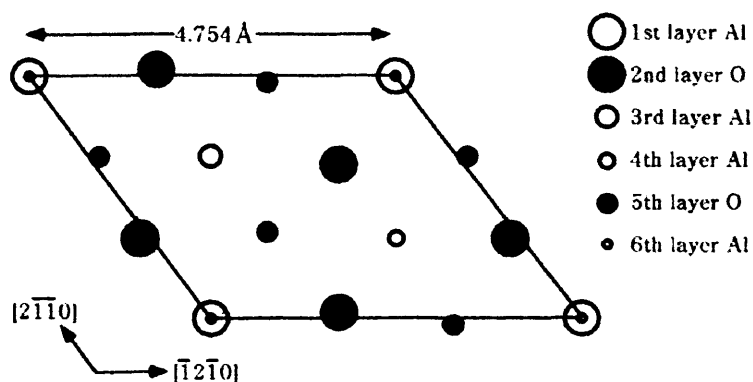
Figure 1.16. Top view of the {0001} α-alumina surface. [25]

The side projection illustrating the aluminium terminated surface and the ordering of the aluminium and oxygen layers is shown in figure 1.17. [26] Each oxygen plane has an aluminium plane above and below at 0.838 Å, this Al-O-Al trilayer is itself stoichiometric with the irreducible formula Al_2O_3. The aluminium atoms occupy two-thirds of all available octahedral sites, alternatively above and below the centres of these sites.
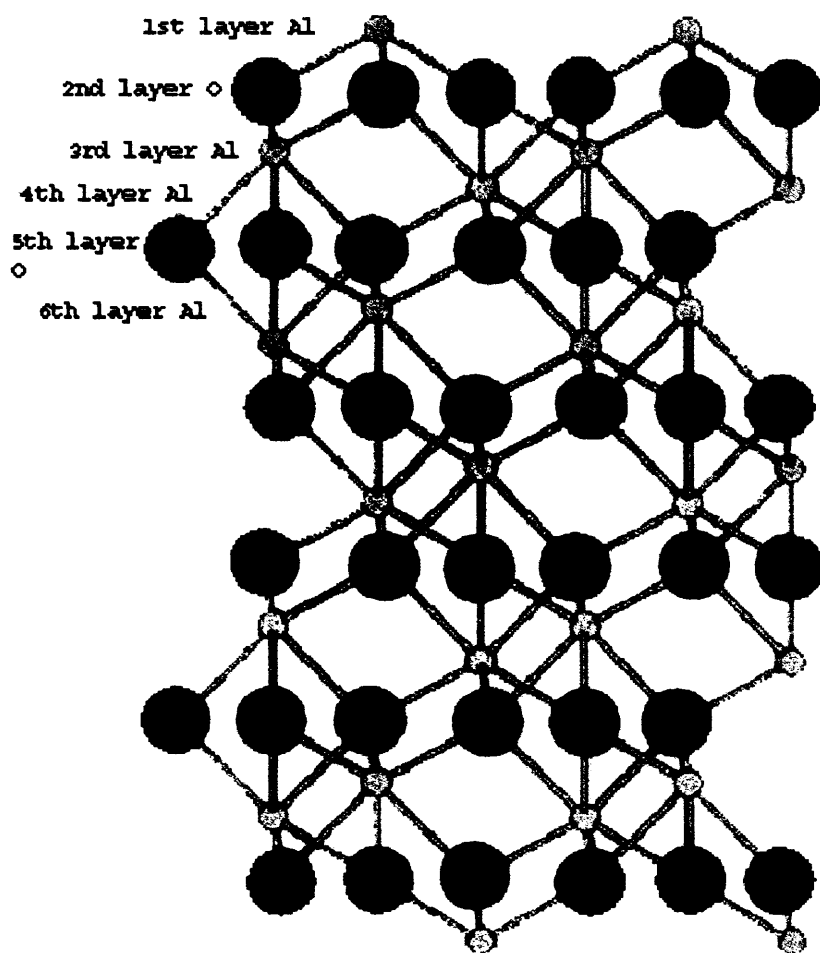
Figure 1.17. Side view of {0001} α-alumina surface terminated at Al1 plane. Aluminium is shown by the small grey circles and oxygen by the large black circles. [26]

1.2.2   Experimental studies of the {0001} α-alumina surface.

X-ray crystallographic data and other surface techniques on the {0001} surface can form a basis from which to evaluate the accuracy of theoretical calculations. Recent x-ray experiments by Guenard *et al* [27] found the Al1-O1, O1-Al2, Al2-Al3 and Al4-O2 relaxations to be -51%, +16%, -29% and +20% respectively.

Regardless of whether theoretical or experimental results are used, the {0001} surface undergoes a nominal restructuring, in which the surface aluminium layer was initially about 1.6 to 1.7 Å above the first oxygen layer, as shown in figure 1.17, relaxes to give a flatter and more compact mixed aluminium and oxygen surface, as illustrated by figure 1.18, where both Lewis acid aluminium and the basic oxygen sites are accessible to adsorbates interacting with the {0001} surface.
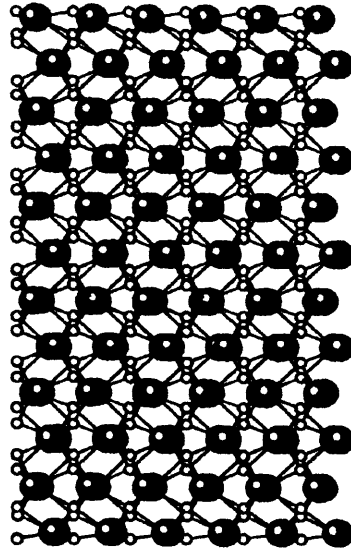
Figure 1.18. Relaxed {0001} surface. Oxygen is shown as filled large circles and aluminium as small unfilled circles indicating the surface containing a mixture of both. [38]

1.2.3 Theoretical studies of the {0001} α-alumina surface.

Most theoretical calculations use a slab method of representing the alumina surface with a variable depth vacuum gap appended above the surface being studied; an illustration of this methodology for the {0001} α-alumina surface is shown in figure 1.19. Percentage interplanar relaxations are calculated using equation 1.2, where D_{final} is the interplanar separation after optimisation, and $D_{initial}$ is the separation before. A negative relaxation indicates a compression of the two planes being analysed, and *vice versa*.

$$Relaxation = \frac{\left(D_{final} - D_{initial} \right)}{D_{initial}} \times 100$$ Equation 1.2

Density functional theory calculations carried out by Manassidis *et al* [28] on the {0001} surface used the local density approximation within the CETEP code found the relaxations of the first four Al1-O1, O1-Al2, Al2-Al3 and Al3-O2 to be -86%, +3%, -54% and +25% respectively. Further density functional theory work by Verdozzi *et al* [29] on cells containing up to 18 layers of oxygen to eliminate any effects of using only a surface a few layers thick found relaxations of -86%, +3%, -42% and +18% for Al1-O1, O1-Al2, Al2-Al3 and Al3-O2 respectively.
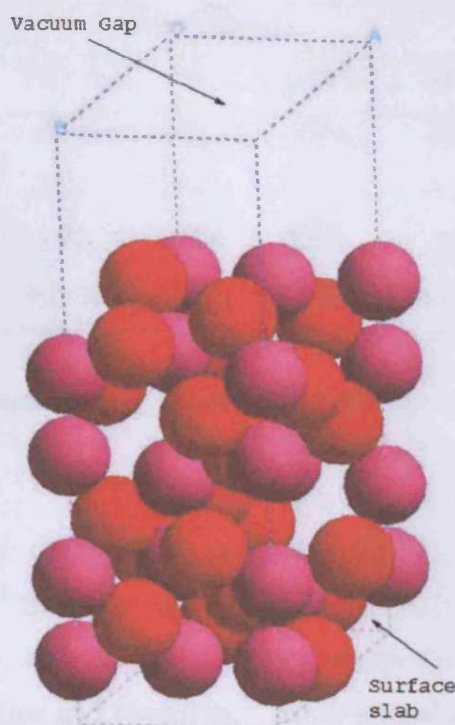
Figure 1.19. Slab and vacuum gap arrangement for crystal surface calculations, showing the periodic boundary conditions as dashed lines.

Empirical shell model calculations within a finite slab model by Catlow *et al* [30] reported these four Al1-O1, O1-Al2, Al2-Al3 and Al3-O2 interlayer relaxations to be -65%, -5%, -32% and +14%, which fit well with results obtained by Mackrodt *et al* [31] using empirical Hartree-Fock calculations on semi-infinite slabs giving relaxations of -59%, +2%, -49% and +26%. Further Hartree-Fock calculations by Puchin *et al* [32] found the top Al-O layer relaxed by 68%.

Calculations of the relaxation of the four top layers in two crystals of nine and fifteen layers employing the B3LYP hybridisation of non-local Fock exchange with the gradient corrected exchange-correlation function along with corresponding Hartree-Fock (H-F) and local density approximation (LDA) calculations by Gomes *et al* [33] are summarised in table 1.4, compared to the experimental XRD data by Guenard *et al*. [25]

23

Layer	Experimental XRD [27]	Nine layers HF	LDA	B3LYP	Fifteen layers HF	LDA	B3LYP
Al1-O1	-51%	-85%	-98%	-85%	-78.8%	-87.7%	-74.1%
O1-Al2	+16%	-2%	-3%	0	-1.6%	-2.8%	0.7%
Al2-Al3	-29%	-35%	-37%	-35%	-30.5%	-27.9%	-25.4%
Al3-O2	+20%	+19%	+20%	+19%	+14.5%	+14.3%	+12.7%

Table 1.4. Relaxation of interlayer spacing of nine and fifteen layer crystal models of the α-alumina {0001} surface. [33]

Density functional theory calculations using a generalised gradient approximation approach by Wang et al [34] finds the interlayer relaxations to be -86%, +6%, -49% and +22% for Al1-O1, O1-Al2, Al2-Al3 and Al3-O2 respectively. This compares well to the values presented by di Felice and Northrup,[35] using a local density approximation and ultrasoft pseudo-potentials who found Al1-O1, O1-Al2, Al2-Al3 and Al3-O2 relaxations of -85%, +3%, -45% and +20%, whilst Batyrev et al [24] calculated the Al1-O1, O1-Al2, Al2-Al3 and Al3-O2 relaxation values to be -77%, +10.6%, -34.3% and +18.5%. These three sets of results have been calculated using a vacuum gap above the aluminium terminated surface, whereas replacing this vacuum gap with a metal surface such as niobium {111} derives information about the behaviour of the interface relaxation of the 7 layers of aluminium terminated α-alumina {0001} when adjacent to ten layers of niobium {111}.[36] The relaxation values for the Al1-O1, O1-Al2, Al2-Al3 and Al3-O2 interlayers are: -69.6%; +10.4%; -34.3% and +18.5% respectively. Two different approaches to the incorporation of basis sets into the density functional theory calculated relaxations by Bankhead [37] use a localised basis set and a plane-wave basis set, the degree of relaxation is shown in table 1.5.

Electrostatic potential molecular dynamics simulations using a polarisable oxygen atom, in which the point core and shell are given a variable proportion in the approximate ratio of 9:1 (core:shell) of the total atomic mass give rise to the Al1-O1, O1-Al2, Al2-Al3 and Al3-O2 relaxation of -58%, +4%, -42% and +24%.[38]

Layer separation	DFT – localised basis set (DSolid)	DFT – plane-wave basis set (VASP)
Al1-O1	-72.5%	-82%
O1-Al2	+2.5%	+4%
Al2-Al3	-35.7%	-41.6%
Al3-O2	+19.3%	+21%
O2-Al4	+2.0%	+6.3%
Al4-Al5	-1.8%	-5.2%

Table 1.5. Comparison of layer relaxation using DSolid and VASP programmes. [37]

The overestimation of the first aluminium-oxygen layer relaxation is a feature of all theoretical calculations, whether carried out by Hartree-Fock, density functional theory, or to a lesser extent, atomistic potentials, where the discrepancy is only 7%. This compares to an average of ~29% for all theoretical results (excluding the potential based molecular dynamics simulation results). However, despite some large deviations in actual values of relaxations, the underlying trend is followed by the majority of the calculated results.

1.2.4 Stabilities of α-alumina {0001} surfaces.

The quantitative stability of oxide materials is commonly quoted as the surface energy, γ_s. This value is calculated by equation 1.3.

$$\gamma_s = \frac{E_{surface} - E_{bulk}}{2A}$$

Equation 1.3

Where $E_{surface}$ is the energy for the slab calculation, as shown in figure 1.19 including the vacuum gap, E_{bulk} is the energy for the stoichiometric equivalent bulk structure and A is the surface area, multiplied by a factor of two as two surfaces are created in a slab calculation, units are J m^{-2}. Equation 1.3 only applies to periodic calculations as long range order is required for all parameters. For a stable surface of an oxide, the expected values are low positive numbers in the approximate range 1 – 5 J m^{-2} (for alumina, the

value is typically 2 – 3 J m^{-2}), any negative value is unphysical, as such a number would mean the surface structure is thermodynamically more stable than the bulk. The surfaces with the lowest energies are the most thermodynamically stable and are usually those with low Miller indices, giving a dense packing arrangement on the surface layer, as shown by figure 1.18.

The surface energy may be calculated for an unrelaxed structure which may be compared to the surface energy for a relaxed structure, giving an indication to the increase in stability upon optimisation/relaxation. Table 1.6 provides a summary of calculated surface energies, it is seen that the surface energy is sensitive to the method, temperature or potential used, however, most results for the relaxed surface fall within the expected range of ~2 to ~3 J m^{-2} and all are less than the unrelaxed surface energy for the same structure which indicates that the {0001} relaxed surface is preferred for purely energetic reasons. Calorimetric experiments give a value of 2.6 J m^{-2}.[39]

Reference	Unrelaxed γ_s J m^{-2}	Relaxed γ_s J m^{-2}
Atomistic simulation. Tasker. [40]	6.53	2.97
Atomistic simulation/electron gas. Mackrodt. [41]	5.95	2.03
Density functional theory. Manassidis and Gillan. [42]	3.77	1.76
Density functional theory + LDA. De Felice and Northrup. [35]		1.98
Localised orbital Hartree-Fock. Mackrodt. [43]	3.20	2.00
Density functional theory + LDA. Manassidis, de Vita and Gillan. [28]	3.77	1.76
Shell model. Marmier and Finnis. [6]		2.951 & 2.454
Shell model molecular dynamics. Baudin and Hermansson. [38]		3.15 (300 K) & 3.06 (700 K)

Table 1.6. Surface energies for unrelaxed and relaxed aluminium terminated {0001} surface with methods of calculation and authors.

1.2.5 Electronic properties of α-alumina {0001} surfaces.

The total density of states plot for the {0001} surface is shown in figure 1.20, with the relaxation calculated by Hartree-Fock and local density approximation, compared against the single point energy, with no relaxation of the atomic co-ordinates. Figure 1.21 shows the partial density of states for the oxygen $2p_z$ orbital. [32]
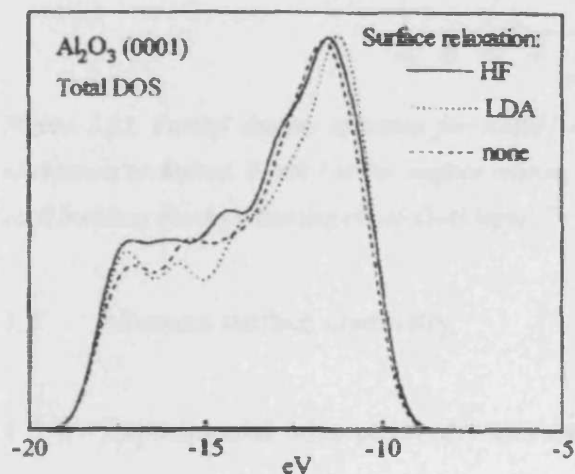
Figure 1.20. Total density of states of {0001} α-alumina surface. [32]
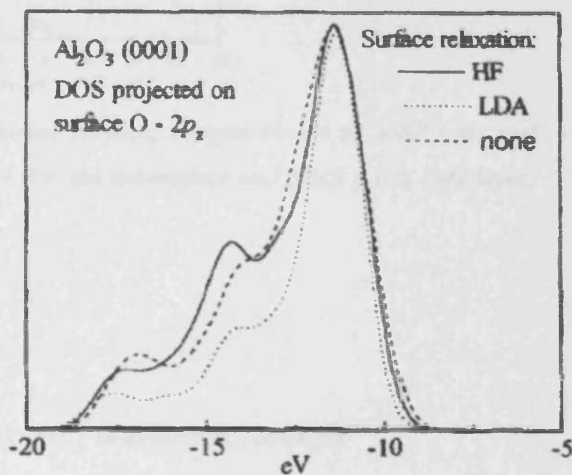
Figure 1.21. Partial density of states plot for surface oxygen $2p_z$ orbitals. [32]

The relaxation effect of the uppermost aluminium layer causes the shoulder at about 14 eV to increase to a pronounced peak of higher intensity, and a concurrent reduction in the extension of the shoulder at ~17 eV to a lesser intensity. It is seen in the literature that there is not a large discrepancy between the density of states plots for the bulk and {0001} surface of α-alumina.

Figure 1.22 shows the partial density of states plots for the {0001} surface, in which the partial density of states for each building block contributing to the crystal surface, each block contains layers of Al-O-Al. For the surface block 1, the lower valence band is 1 eV narrower than the two bulk blocks below, and the upper valence band is 1 eV wider. The valence band averages of the block 1 (surface) and block 2 (subsurface) are shifted upwards and downwards by 1 eV respectively compared to block 3 (bulk) due to nonzero dipole moments. [44]

27
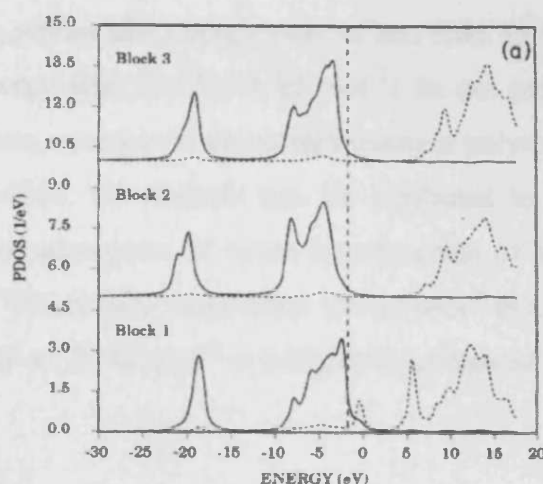
Figure 1.22. Partial density of states for {0001} α-alumina surface, oxygen shown in solid line, and aluminium in dashed. Block 1 is the surface region, block 2 is the subsurface and block 3 is a bulk layer, each building block containing an Al-O-Al layer. [44]

1.3 Alumina surface chemistry

1.3.1 Experimental adsorption of water onto {0001} α-alumina surfaces

When alumina is dehydroxylated at high temperatures under vacuum, water may be adsorbed in different forms, chemisorption via a dissociative mechanism at 150 °C, which is irreversible, or a physisorbed molecular route to give molecular H_2O coordinated to the surface, which at 25 °C is irreversible and at 150 °C is reversible.[45] The general reaction is shown in equation 1.4:

$$H_2O_{vapour} \leftrightarrow H_2O_{coord} + O^{2-} \rightarrow 2OH^-$$ Equation 1.4
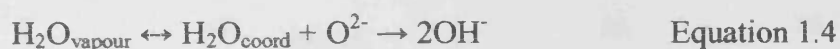
In equation 1.4, the source of O^{2-} ions is the alumina surface itself, shown to be accessible in figure 1.18. Coordinative water merely acts as a precursor to the full dissociation of water at low coverages on the surface. When considering higher coverages, in which the less energetically favourable dissociation sites are saturated, the coordinative mechanism competes with the dissociative mechanism. Microcalorimetric techniques investigated by Della Gatta *et al* [43] found the energy of coordinative adsorption is 18 kcal mol⁻¹ (75 kJ mol⁻¹) at 25 °C; the energies for α-alumina are less than for the transition polymorphs η- and θ-alumina. α-alumina {0001} adsorption sites of between 20 and 40 kcal mol⁻¹ (84 – 167 kJ mol⁻¹) progressively disappear with

28

increasing temperature, whilst low energy sites of less than 15 kcal mol^{-1} (62 kJ mol^{-1}) are preferred. High energy sites (250-292 kJ mol^{-1}) do not preferentially exist on the {0001} α-alumina surface, whereas in the other transition polymorphs these high energy sites are readily accessible, this feature can be attributed to the lack of tetrahedral aluminium. The heats of adsorption of water as a function of uptake on α-alumina are shown in figure 1.23.[46] The results range from 109 kJ mol^{-1} at a low coverage of 1×10^{14} water molecules per cm^2 to 57 kJ mol^{-1} at a higher coverage of 1×10^{15} water molecules per cm^2.
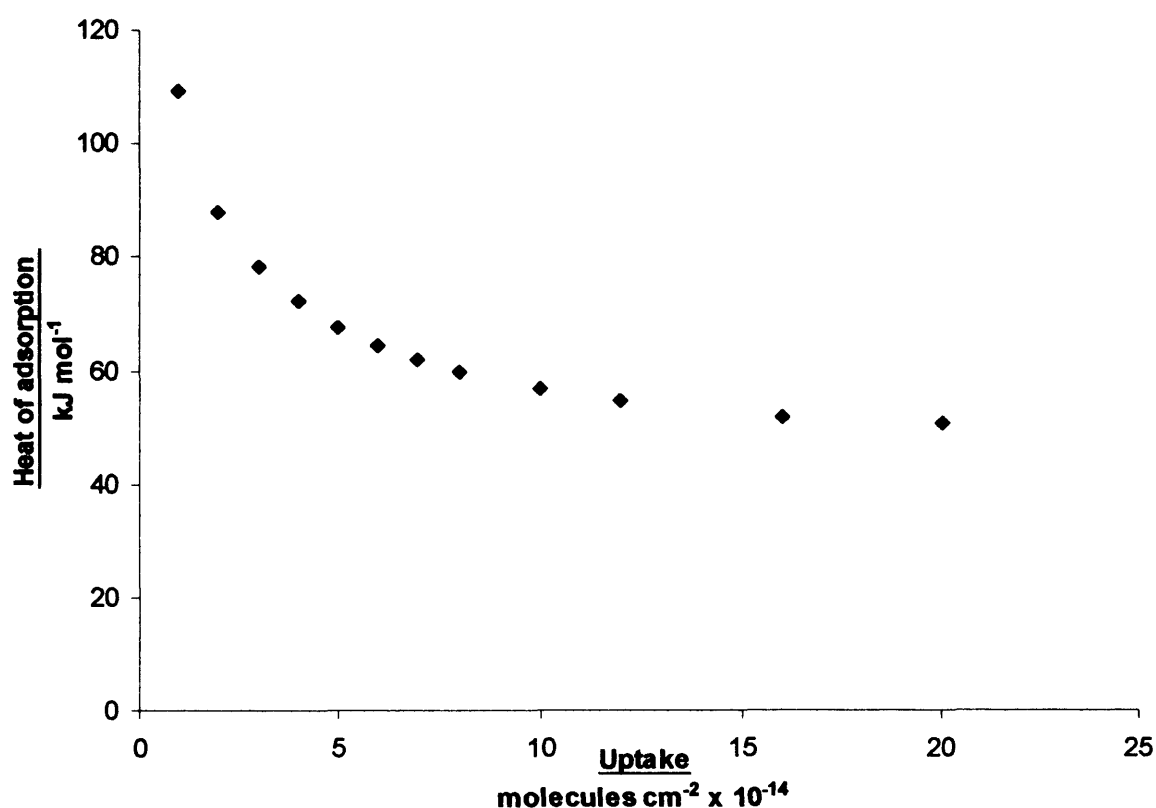
Figure 1.23. Heat of adsorption of water as a function of coverage onto α-alumina.[46]

Temperature programmed desorption (TPD) and laser induced thermal desorption (LITD) studies using isotopically labelled $H_2{}^{18}O$ have been used to separate dissociative adsorption from molecular adsorption. The hydroxylated α-alumina {0001} surface is likely to be formed in the stratospheric region of the atmosphere from approximately 300 tons of alumina exhaust crystals, 100 tons of H_2O and 210 tons of HCl expelled from solid rocket motors used in space shuttle launches.[47] The temperatures in this region are in the range of 200 K in the Polar regions to 270 K at equatorial latitudes.

Equation 1.5 represents the dehydroxylation of water from the α-alumina {0001} surface, where † denotes a surface species:

$$2AlOH^\dagger \rightarrow AlOAl^\dagger + H_2O_{(g)} \qquad \text{Equation 1.5}$$
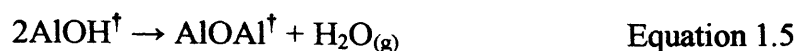
For the desorption of a single water molecule, two surface hydroxyl groups are required, experimentally the surface coverage is twice the value of the LITD signal corresponding to water. Exposure of alumina to $H_2{}^{16}O$ and $H_2{}^{18}O$ at a pressure of 250 mTorr leads to an LITD determined hydroxyl coverage (Θ_{OH}) of 0.32×10^{15} hydroxyl groups per cm^2. Both these isotopic forms of water were found in TPD spectra, which show that a large proportion of $H_2{}^{18}O$ is dissociatively adsorbed onto the alumina {0001} surface. Incorporated into the desorbed water molecules are ^{16}O from the alumina surface and ^{18}O from the adsorbed water. The initial hydroxylation occurring at room temperatures for exposures of 10^0 to 10^{10} Langmuir (1 Langmuir = 10^{-6} Torr s) with pressures varying from 10^{-9} to 13 Torr showed a steep rise in hydroxyl coverage at low H_2O exposures, levelling of at around 0.3×10^9 Langmuir. The conclusion is that hydroxyl coverage on the surface depends on the pressure of the H_2O exposure up to the saturation limit of 0.5×10^{15} OH groups per cm^2 at 10^{10} Langmuirs at 300 K.

The concentration of aluminium cations in the uppermost exposed surface is 0.51×10^{15} atoms cm^{-2}; this suggests an adsorption model where each surface Al^{3+} has two hydroxyl groups produced by adsorption occupying all of the surface aluminium sites. This only equates to 50% of the binding sites, as an alternative scheme suggests the OH group occupies the aluminium site, and the dissociated H from water occupies a binding site created by an oxygen atom in the second surface layer.[48] Such a proposal has twice the number of adsorption sites, so the saturated surface coverage Θ_{OH} should be 1×10^{15} OH groups per cm^2 compared to the measured Θ_{OH} of 0.51×10^{15} OH groups per cm^2.

Further work carried out at 210 K again using LITD determination shows the surface H_2O coverage to range from 0.4×10^{14} molecules per cm^2 at an exposure of 1 L to a saturation coverage of 4.4×10^{14} molecules per cm^2 at an exposure of 2.4×10^6 L, a hydroxyl coverage Θ_{OH} of 8.8×10^{14} molecules cm^{-2}.[49] These are formed again by the binding of OH to an aluminium site and H to a surface oxygen site. For constant

exposure of 2×10^4 L, the desorption spectra area increases at lower exposure temperatures, which means there are more low energy binding sites for adsorption at lower temperatures.

Desorption of these hydroxyl groups takes place through both first and second order kinetics. First order desorption occurs if water is molecularly adsorbed. For exposure at 193 K, OH desorption ranges from ~195 to ~ 600 K, equating to desorption activation energies of ~50 to 160 kJ mol^{-1}, depending on the energies of the binding sites. Compared to exposures at 300 K and desorption activation energies of 95 to 170 kJ mol^{-1}, the exposure at 193 K populates lower energy binding sites. Second order desorption kinetics is representative of the recombinative desorption of the hydroxyls formed by dissociatively adsorbed water. The range of desorption activation energies is ~50 to ~160 kJ mol^{-1}.

The effect is that, in the previously mentioned stratospheric conditions of 200 to 270 K, the alumina particles will be covered by chemisorbed water molecules, leading to hydroxylation of the surface at temperatures of approximately 210 K. These adsorbed species may undergo exchange reactions with further water molecules, or reversibly with HCl molecules to chlorinate the surface, an important reaction when considering the catalytic activity of hydroxylated alumina {0001} surfaces. There is an environmental cost however, since HCl can react with ClONO$_2$ as shown in equation 1.6, producing active chlorine that degrades ozone:

$$ClONO_2 + HCl \rightarrow Cl_2 + H_2O \qquad \text{Equation 1.6}$$
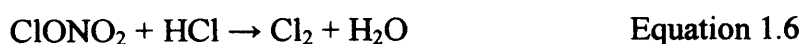
1.3.2 Theoretical adsorption of water yielding hydroxylated α-alumina {0001} surfaces.

As aluminium is in a low co-ordinated site on the surface of alumina {0001}, these are considered strong Lewis acids. Work done by Hass et al [50] using the CPMD v2.5 program on extremely low coverages of 0.57 H$_2$O nm^{-2} indicates dissociation can occur, although molecular binding is energetically stable. This latter type of molecular adsorption occurs via a dative bond of 98 kJ mol^{-1}. The dissociative pathway is

energetically more favourable, by 30 to 40 kJ mol^{-1}, with the OH fragment binding to an aluminium site, and the H fragment to the nearest neighbour surface oxygen.

By modelling the molecularly adsorbed state at a surface-oxygen to water-hydrogen distance of more than 2.7 Å progressing stepwise to the dissociated state at 0.97 Å. Figures 1.24, 1.25, 1.26 and 1.27 illustrate the adsorption coordinates of both 1-2 and 1-4 geometries as both plan and side projections. The {0001} can be visualised of a repeat unit of hexagonal units, consisting of Al_3O_3. In a 1-2 adsorption, hydrogen from water is adsorbed on oxygen in position two adjacent to the position one aluminium, as labelled in figure 1.25. A 1-4 adsorption occurs when the surface oxygen adsorption site is located in position four of this hexagonal unit, as shown in figure 1.26. The 1-2 and 1-4 adsorption pathway energetics are shown in figure 1.28.

Both 1-2 (figures 1.24 and 1.25) and 1-4 (figures 1.25 and 1.26) dissociations are exothermic reactions, being approximately 42 kJ mol^{-1}. The reaction barrier from the molecularly adsorbed water molecule is three times larger for the 1-2 nearest neighbour reaction than for the 1-4 adsorption mode: 27 kJ mol^{-1} versus 9 kJ mol^{-1} respectively. Kinetically this means the 1-4 type reaction will dominate on the clean surface, however, due to the energy released in the molecular adsorption both pathways are thermodynamically favourable implying that a water molecule will progress via either a 1-2 or 1-4 route to the dissociated state rather than remaining physisorbed if suitable aluminium and oxygen sites are available.
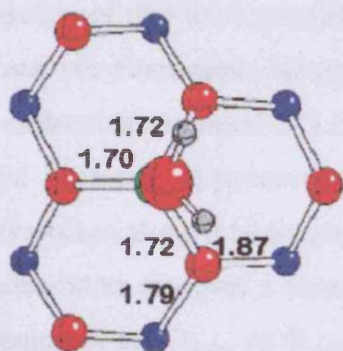
Figure 1.24. Molecular adsorption of H₂O onto a single Lewis acid aluminium site. [50]
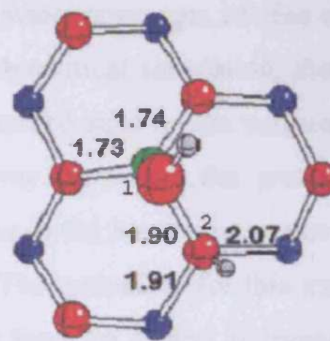
Figure 1.25. 1-2 dissociated water adsorption yielding a hydroxyl group on Lewis acid aluminium site and a proton on neighbouring basic surface oxygen site. $E_a = 27$ kJ mol⁻¹. [50]
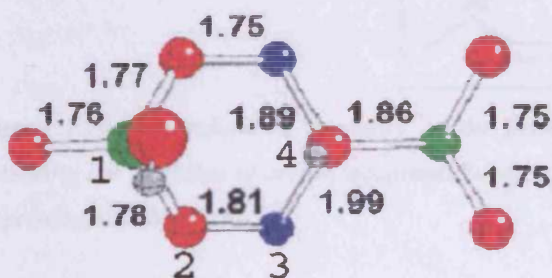
Figure 1.26. Top view of 1-4 dissociated water adsorption with OH on Lewis acid aluminium site and proton on non-neighbouring basic oxygen site. $E_a = 9$ kJ mol⁻¹. [50]
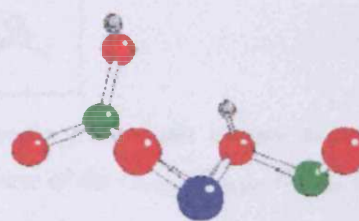
Figure 1.27. Side projection of 1-4 dissociated water adsorption final configuration. $E_a = 9$ kJ mol⁻¹. [50]
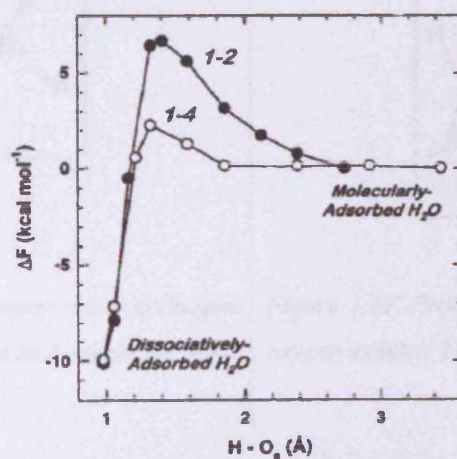
Figure 1.28. Molecular dynamics simulation of free energy at 300 K against H-O interatomic distance for dissociation of a single water molecule in both 1-2 and 1-4 pathways. [50]

A continuation of this work considered intermediate water coverages of nine molecules per cell, one per aluminium adsorption site. In this dynamical simulation, the majority of water molecules remained in a molecularly physisorbed state on the surface. When a dissociated occurred, it proceeded via a 1-4 pathway, in which the proton transfer rapidly take place along a hydrogen bond between the initial host water molecule to the oxygen adsorption site over a timescale of 0.12 ps. The activation for this transition is the shortening of the O_{water} to $O_{surface}$ distance to less than 2.6 Å, and an increase of the $O_{water} - H_{transfer} - O_{surface}$ angle to approximately 180°. This is represented in figure 1.29.
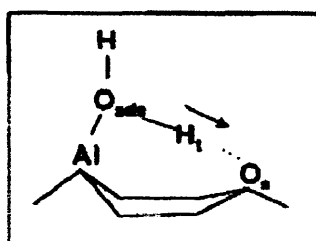
Figure 1.29. The schematic geometry of the proton transfer from water oxygen to surface oxygen following the direction of arrow, accommodating a flattening of the $O_{water}-H_{transfer}-O_{surface}$ bond angle to approximately linear 180°. [50]

It was found that the molecularly physisorbed water also has an important role in the 1-4 adsorption of a further proton from another hydrogen bonded water molecule, as illustrated in figure 1.30, through to the reaction geometry in figure 1.31.
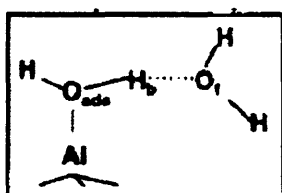
Figure 1.30. Physisorbed water with hydrogen bond to further water molecule as a precursor state to 1-4 adsorption. [50]
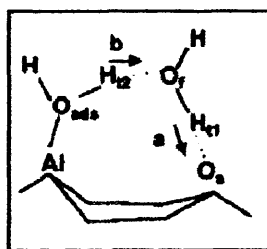
Figure 1.31. Proton transfer from water to surface oxygen to elicit 1-4 adsorption mechanism. [50]

This subsequent adsorption arises due to the simultaneous transfer of two protons, labelled H_{t1} and H_{t2} in figure 1.31. The first stage is the formation of a hydrogen bond from H_{t1} to the surface oxygen (O_s) with a synchronous elongation of the O_f-H_{t1} bond,

and the formation of the second hydrogen bond to H_{t2} from O_f. Consequently, the hydrogen bonds decrease in length and form a concerted reaction mechanism over a timescale of approximately 50 ps. The water molecule created by this reaction repeats this cycle at other physisorbed water sites on the surface. Any water molecules not in direct contact with the surface form intermolecular hydrogen bonds to form water droplets and are withdrawn from the reaction mechanism.

As coverage increases over the surface, binding energies decrease, although not in an entirely linear manner. High binding energy sites are preferentially occupied by the first molecules to adsorb, typically around 200 kJ mol^{-1}. Beyond full occupancy of these sites, all aluminium sites exist with two O_{ads}-H hydroxyl groups at a coverage of approximately 10 OH per nm^{-2}, after this the binding energy decreases as any additional water adsorptions will bind to aluminium sites that are already hydroxylated or surface hydroxyl groups.

At maximum coverage, the water binding energy approaches the heat of vaporisation – 44 kJ mol^{-1} – as the only binding options are through hydrogen bonds to hydroxyl groups or other water molecules. At high coverages, the addition of hydroxyl groups to the surface decreases the strength of aluminium to surface oxygen bonds, possibly leading to the removal of hydrated Al-(OH)$_3$ and Al(OH)$_4^-$ complexes. The result is the replacement of a surface aluminium with three protons. This transition from α-alumina to bulk Al(OH)$_3$ is thermodynamically favoured at room temperature in the presence of excess water, although the kinetic barrier is large with a fully hydroxylated surface.

Calculations on water adsorption on alumina have also been carried out by Wittbrodt et al [51] on clusters extracted from the α-alumina {0001} surface. They used the Gaussian 94 program and a range of basis sets and theory levels. Their results indicated that molecularly adsorbed water undergoes dissociation, starting with an initial state where the surface adsorption aluminium site was 1.7538 Å from the neighbouring oxygen and 1.9208 Å from the physisorbed water oxygen atom. Within the molecularly bound water, the oxygen to hydrogen distance was 0.956 Å, this physisorbed state is shown in figure 1.32.
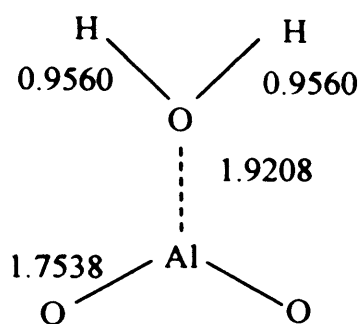
Figure 1.32. Molecularly adsorbed water on a section of an aluminium cluster. All bond lengths are in Angstroms. [51]
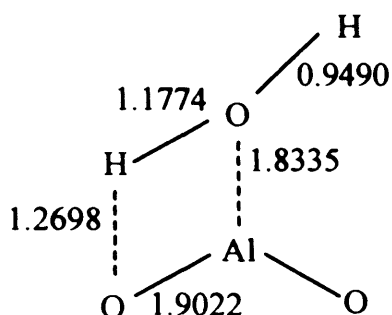
Figure 1.33. Transition state of water forming an $oxygen_{(water)}$ to aluminium bond and $oxygen_{(surface)}$ to hydrogen bond. [51]
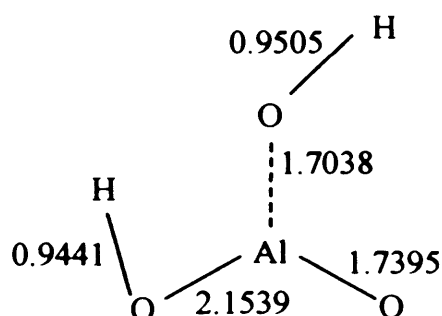
Figure 1.34. 1-2 Dissociatively adsorbed structure, with proton transfer to a surface oxygen species. [51]

The transition state shown in figure 1.33 shows the aluminium to surface oxygen bond length increasing to 1.902 Å and the chemisorbed oxygen initially from water shortened to 1.8335 Å. There was a marginal decrease in the water oxygen to hydrogen distance to 0.9490 Å. The bridging hydrogen distances between water oxygen and the neighbouring surface oxygen were 1.1774 Å and 1.2698 Å respectively. In the final chemisorbed state shown in figure 1.34, the aluminium was 2.1539 Å from the surface oxygen. For comparison a further neighbouring surface oxygen not taking part in the mechanism was 1.7395 Å away, marginally longer than the value of 1.7214 Å in a cluster with no adsorbate or external influences. The aluminium to chemisorbed water oxygen distance was 1.7038 Å, from this atom to hydrogen the distance was 0.9505 Å. Finally the surface oxygen to dissociated water hydrogen was 0.9441 Å. Table 1.7 demonstrates that the dissociative chemisorption is preferred to molecular physisorption by between 62 and 83 kJ mol^{-1}, although the authors acknowledge the limitation of the model

containing only one neighbouring aluminium site compared to two in the three-dimensional lattice.

Theory level	Molecular adsorption kJ mol^{-1}	Transition state kJ mol^{-1}	Dissociative adsorption kJ mol^{-1}
Hartree-Fock/ 6-31+G*	-164.4	-106.2	-248.8
B3LYP/6-311+G*// Hartree-Fock/ 6-31+G*	-163.1	-130.6	-234.9
MP2/6-31+G*// Hartree-Fock/ 6-31+G*	-186.4	-137.4	-248.2

Table 1.7. Energetics for Al_4O_6 - H_2O system.[51]

Using a larger Al_8O_{12} cluster, the dissociation chemisorption pathway is preferred by 25 kJ mol^{-1} to the molecular physisorption mechanism, due mainly to the larger model being more able to accurately represent the lattice constraints of the bulk crystal. Table 1.8 summarises the energetics of the adsorption on the Al_8O_{12} cluster. When the 6-31G* basis set was used, the energies of molecular and dissociative adsorption are approximately equivalent. Hartree-Fock methods calculate values for the barrier height for the transition state to be 8 to 13 kJ mol^{-1} larger than the Al_4O_6 cluster, due to the higher inherent rigidity of the larger lattice. For two water dissociations at an AlO_3 site in Al_4O_6, the aluminium formed a new interaction with a second neighbouring oxygen, to bring about a 210 to 250 kJ mol^{-1} lowering in the energy relative to water dissociation. The complete removal of $Al(OH)_3$ molecule was found to have an energy between 156 and 224 kJ mol^{-1}, depending on the basis sets and theory level used. The addition of a water molecule to the $Al(OH)_3$ molecule lowers the energy by 88 kJ mol^{-1} for all calculations.

| Theory level | Mol. ads. | | Dissociative adsorption | | | |
| | | | 1H$_2$O | 2H$_2$O | 3 H$_2$O | |
	1H$_2$O	En. Barrier	1H$_2$O	2H$_2$O	Al(OH)$_3$	Al(OH)$_3$ H$_2$O
H-F/6-31+G* (3-21G)	-170.5	67.6	-193.9	-413	-155.9	-245.9
H-F/6-31+G*//H-F/6-31+G* (3-21G)	-139.5	72.9	-142	-391	-223.9	-314
B3LYP/6-31+G*// H-F/6-31+G* (3-21G)	-133.2	38.7	-137.2	-346	-198.7	-287.3
B3LYP/6-31+G* (3-21G)	-163.1	34.2	-19.2			
B3LYP/6-31+G*// B3LYP/6-31+G* (3-21G)	-132.3	38.8	-134.5			

Table 1.8. Energetics for 1-2 dissociative mechanism on Al$_8$O$_{12}$ cluster. The barrier is the energy which must be overcome for a molecularly adsorbed state to become dissociatively adsorbed. All values are in kJ mol^{-1}.[51]

When the 1-4 dissociative adsorption was studied on the Al$_8$O$_{12}$ cluster, the aluminium position was not affected as much as in the 1-2 dissociation. Table 1.9 gives the energetics of this mechanism, for both the one and two water approach.

Compared to the 1-2 adsorption on the Al$_8$O$_{12}$ cluster, the energies are higher for both molecular and dissociative adsorption, with the barrier to dissociation 21 to 29 kJ mol^{-1} higher, with the 1-2 dissociation 21 kJ mol^{-1} more exothermic than the 1-4 process.

Across the levels of theory, 1-4 hydroxylation is via the two water process is 88 to 105 kJ mol^{-1} more exothermic than the 1-4 single water approach and 38 to 84 kJ mol^{-1} more exothermic than the 1-2 mechanism.

It seems likely that all of these processes outlined will take place during the hydroxylation of the α-alumina {0001} surface, the mechanism occurring over a timescale of 10^{-12} s after the molecular adsorption onto the surface, possibly as quickly as 5 × 10^{-12} s.

Theory level	One water process			Two water process		
	Mol. Ads.	Trans. St.	Dis. Ads	Mol. Ads.	Trans. St.	Dis. Ads
H-F/6-31+G* (3-21G)	-150.6	-55.4	-139.5	-244.2	-185.5	-233.5
H-F/6-31+G*//H-F /6-31+G* (3-21G)	-133.9	-36.3	-117.2			
B3LYP/6-31+G*// H-F/6-31+G* (3-21G)	-130	-69.5	-114			
B3LYP/6-31+G* (3-21G)	-145.2	-84.3	-130.4			
B3LYP/6-31+G*// B3LYP/6-31+G* (3-21G)	-129.4	-67.4	-111.5			

Table 1.9. The energetics for 1–4 dissociation on the Al_8O_{12} cluster. All values are in kJ mol^{-1}. [51]

Further work by Scott et al [52] on the gas-phase hydration of alumina clusters used the General Atomic and Molecular Electronic Structure System (GAMESS) program incorporating the Hartree-Fock level of theory with 6-311G basis set to aluminium and oxygen. Within these calculations, a d polarisable function to aluminium and a p orbital polarisable function to hydrogen were included. Gaussian 98 optimisation calculations were also performed using the B3LYP exchange and correlation function with an assortment of basis sets. Both these calculation were integrated with results from Hartree-Fock calculations including Møller-Plesset perturbation theory. The hydration process for the small AlO_2^- charged cluster proceeds according to the scheme outlined in equation 1.7, and the subsequent hydration of an $AlO_3H_2^-$ cluster in equation 1.8:

$$AlO_2^- + H_2O \rightarrow AlO_3H_2^-$$ Equation 1.7

$$AlO_3H_2^- + H_2O \rightarrow AlO_4H_4^-$$ Equation 1.8
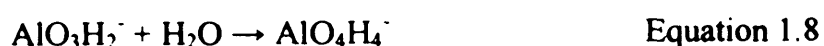
Experimentally, it was found that the initial hydration of the AlO_2^- molecule proceeds at a slower rate than the subsequent hydration of the $AlO_3H_2^-$ ion, when the reactions were monitored using mass spectrometry. The rate constant for the first hydration is 3×10^{-11}

cm^3 molecule^{-1} s^{-1} and exhibits pseudo-first order kinetics, although by varying the water pressure, the rate constant altered by $\pm 30\%$. For averaged-dipole-orientation theory (ADO) the rate constant was 2×10^{-9} cm^3 molecule^{-1} s^{-1}, although by fitting the data for consecutive reactions, the value was found to be 4×10^{-11} cm^3 molecule^{-1} s^{-1} and for the hydration of the $AlO_3H_2^-$ ion, the revised rate constant was four times faster at 4×10^{-10} cm^3 molecule^{-1} s^{-1}. This means the rate determining step is the addition of the first water to the AlO_2^- molecule.

Mass spectroscopic investigation of the hydration of $Al_2O_4H^-$ shows products of monohydrated $Al_2O_4H(H_2O)^-$ and dihydrated $Al_2O_4H(H_2O)_2^-$. The consecutive reactions are shown in equations 1.9 and 1.10.

$$Al_2O_4H^- + H_2O \rightarrow Al_2O_5H_3^- \qquad \qquad \text{Equation 1.9}$$
$$Al_2O_5H_3^- + H_2O \rightarrow Al_2O_6H_5^- \qquad \qquad \text{Equation 1.10}$$

Experimentally, the rate constant was found to be 2×10^{-9} cm^3 molecule^{-1} s^{-1}, equal to the averaged dipole determined value and therefore the fitted value, for the first addition of water. However, the fitted value was calculated to be 8×10^{-10} cm^3 molecule^{-1} s^{-1} for the second addition of water, and is the rate determining step in this series of water additions.

The rate constants for the additions of the second water for hydrations of both $AlO_3H_2^-$ (in equation 1.8) and $Al_2O_5H_3^-$ (in equation 1.10) are both of order 10^{-10} molecule^{-1} s^{-1}. Compared to the work by Wittbrodt et al [49] who found the rate constants for molecular to dissociative adsorption at 300 K to increase from 10^{-2} to 10^{-12} s^{-1}, the gas phase work at 310 K represent the lower limit of hydration of alumina surfaces.

40
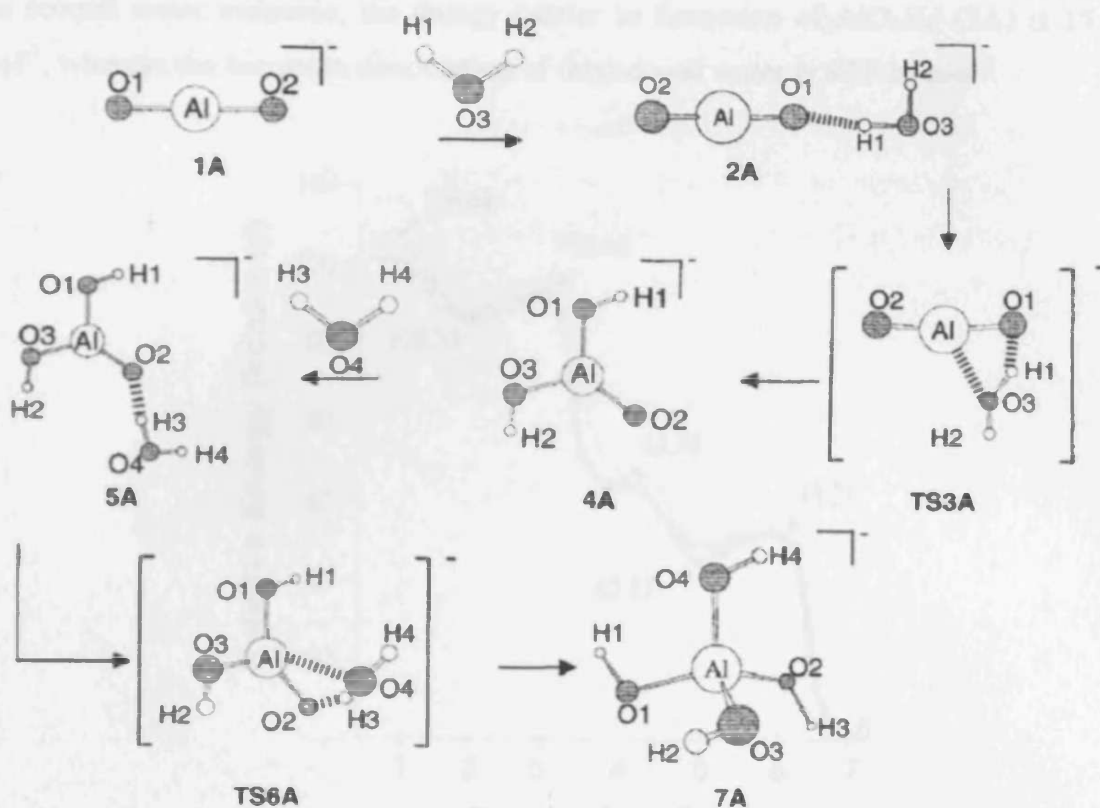
Figure 1.35. Reaction pathway for the hydration of AlO₂⁻ by two water molecules. The structures are based on calculations using the B3LYP/6-311+G(2d,p) level of theory. [52]

The theoretical reaction pathway for equation 1.7 is illustrated in figure 1.35 (specifically for the B3LYP/6-311+G(2d,p) method and basis set) with the energetics for the six types of basis sets incorporated into the calculations. All theoretical calculations on this structure predict a hydrogen bond to form between an oxygen (O1) in AlO_2^- and a hydrogen (H1) in water, followed by a bond between aluminium and O3 in water. As a consequence of this, the water undergoes dissociation by breaking H1-O3 to form $AlO_3H_2^-$. The addition of the second water can be seen to follow broadly the same mechanism, involving simultaneous Al-O bond formation and proton transfer as O4-H3 bond breaks to yield tetrahedral $AlO_4H_4^-$. The energy level diagram for the energetics of addition of two waters to the AlO_2^- molecule is shown in figure 1.36. This shows the transition to the 2A state is thermodynamically favourable, as this state is on average lower than the 1A state, however the energy barrier that needs to be overcome to form $AlO_3H_2^-$ is an average of 16.5 kJ mol⁻¹, whereas the barrier for dissociation is 58.2 kJ mol⁻¹ this means the 2A state isomerises instead of dissociating. On addition of

the second water molecule, the energy barrier to formation of $AlO_4H_4^-$ (7A) is 15 kJ mol^{-1}, whereas the barrier to dissociation of this second water is 87.9 kJ mol^{-1}.
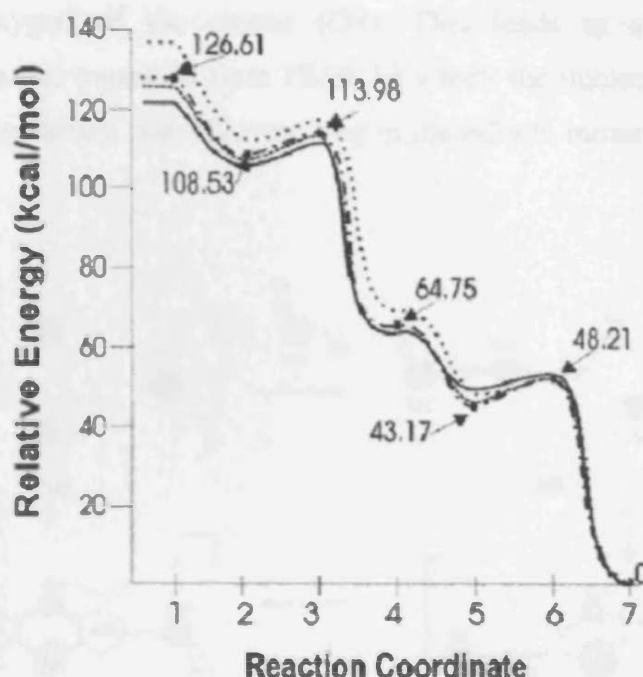
Figure 1.36. Energy level diagram for the reaction $AlO_2^- + 2H_2O \rightarrow AlO_4H_4^-$, with energies shown in kcal mol^{-1}. For completeness, the relative energy values for reaction coordinates 1-7 are: 529.7 kJ mol^{-1}; 454.09 kJ mol^{-1}; 476.9 kJ mol^{-1}; 270.9 kJ mol^{-1}; 180.6 kJ mol^{-1}; 201.8 kJ mol^{-1} and 0 kJ mol^{-1}. [52]

Compared to Wittbodt's [49] values for molecular adsorption on neutral clusters, these values are approximately half, due to the hydroxylation calculations of Wittbrodt using a nucleophilic attack on the aluminium site by the oxygen in water, instead of the initial step being the formation of a hydrogen bond to an oxygen site in alumina. The value of 58.2 kJ mol^{-1} compares well to the experimental range of 57 to 109 kJ mol^{-1} as shown by Hendriksen *et al.* [44]

The product, labelled 7A, is 272 kJ mol^{-1} more stable than the doubly hydrated aluminium structure 4A, and 531.4 kJ mol^{-1} more stable than the initial cluster AlO_2^-, whereas Wittbrodt found two waters adsorbed on the Al_8O_{12} cluster is lower in energy than the initial cluster by 403.8 kJ mol^{-1}

For the $Al_2O_4H^- + 2H_2O \rightarrow Al_2O_6H_5^-$ reaction, only the B3LYP/6-31+G(2d,p) level of theory was used, the reaction mechanism is illustrated in figure 1.37, in general the

42

hydration proceeds as shown in figure 1.35, although the oxygen bridged aluminiums have a rhombohedral structure, distinct from the linear nature of the AlO_2^- cluster. The first addition of water involves the formation of a hydrogen bond between H2 and the unhydroxylated oxygen of the cluster (O4). This leads to structure 2B, which subsequently forms the transition state TS3B, in which the nucleophilic water oxygen (O5) attracts the aluminium site Al2, resulting in the H2-O5 intramoleculer water bond breaking.
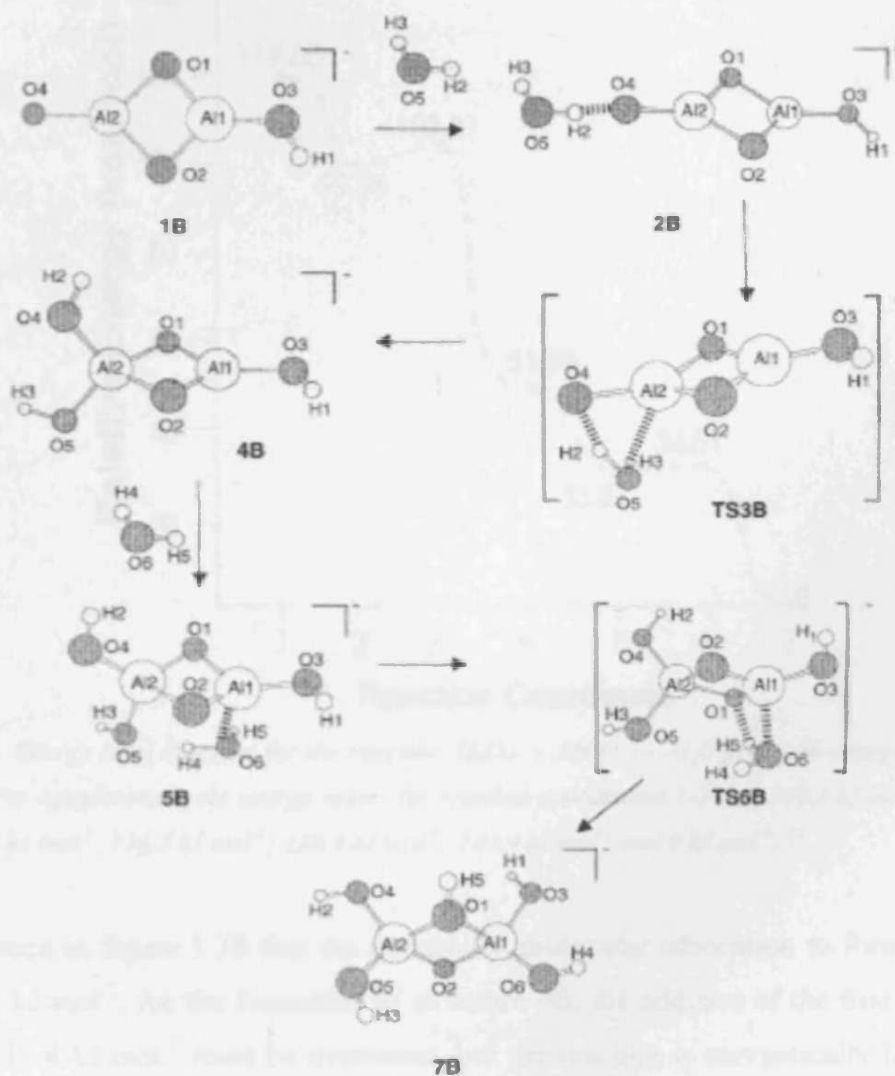
Figure 1.37. Reaction pathway for the hydration of Al_2O_4H with two water molecules. The structures are based on calculations using the B3LYP/6-311+G(2d,p) level of theory. [52]

However, the addition of the second water molecule occurs in an entirely different way to the equivalent mechanism in the AlO_2^- cluster scheme. Referring to figure 1.37 a nucleophilic attack from the oxygen (O6) occurs on the second aluminium centre (Al1)

without any intermediate hydrogen bonded state to form structure 5B, with a hydrogen bond formed between H5 of the water and one of the bridging oxygen sites, (O1). This hydrogen bond results in hydrogen transfer to the bridging oxygen via TS6B. In the final product the Al-O1 bond length has increased by approximately 8%, and the H5-O6 bond of the second water molecule has dissociated. The energy profile for this reaction mechanism is illustrated in figure 1.38.
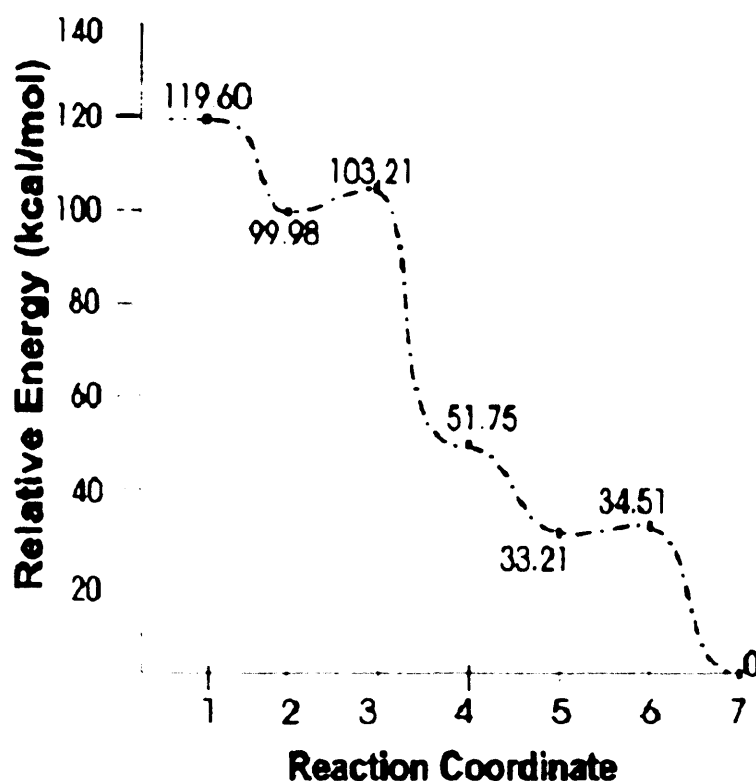
Figure 1.38. Energy level diagram for the reaction $Al_2O_4^-$ + $2H_2O$ → $Al_2O_6H_5^-$, with energies shown in kcal mol^{-1}. For completeness, the energy values for reaction coordinates 1-7 are: 500.4 kJ mol^{-1}; 418.3 kJ mol^{-1}; 431.8 kJ mol^{-1}; 216.5 kJ mol^{-1}; 138.9 kJ mol^{-1}; 144.4 kJ mol^{-1} and 0 kJ mol^{-1}.[52]

It can be seen in figure 1.38 that the energy for molecular adsorption to form structure 2B is 83.7 kJ mol^{-1}, for the formation of structure 4B, the addition of the first water, the barrier of 13.4 kJ mol^{-1} must be overcome, but the reaction is energetically favourable. Structure 4B is stabilised by 283.9 kJ mol^{-1}, with respect to the initial cluster, approximately the same as for AlO_2^-. This relationship is continued when considering the product of the dual addition of water, stabilised to 500.4 kJ mol^{-1} for $Al_2O_6H_5^-$ referenced back to the primary $Al_2O_4H^-$ cluster and two free water molecules. The barrier for this second adsorption is 5.5 kJ mol^{-1}.

1.3.3 Experimental adsorption of water onto γ-alumina surfaces.

In addition to calculating the heats of adsorption of water onto an α-alumina surface, Hendriksen *et al* [46] also investigated the adsorption onto a γ-alumina surface. When the results are compared to α-alumina, it was seen that, for identical uptakes measured as molecules per $cm^{-2} \times 10^{-14}$, the heats of adsorptions are higher for γ-alumina than for the α-alumina phase. Figure 1.39 shows the heat of adsorption as a function of uptake shown for γ-alumina, compared to the data obtained for α-alumina, this shows that at low uptakes volumes the difference between γ- and α-alumina is large, but almost converging at high coverages. For both γ- and α-alumina, the heats of adsorption decrease with increasing water coverage.
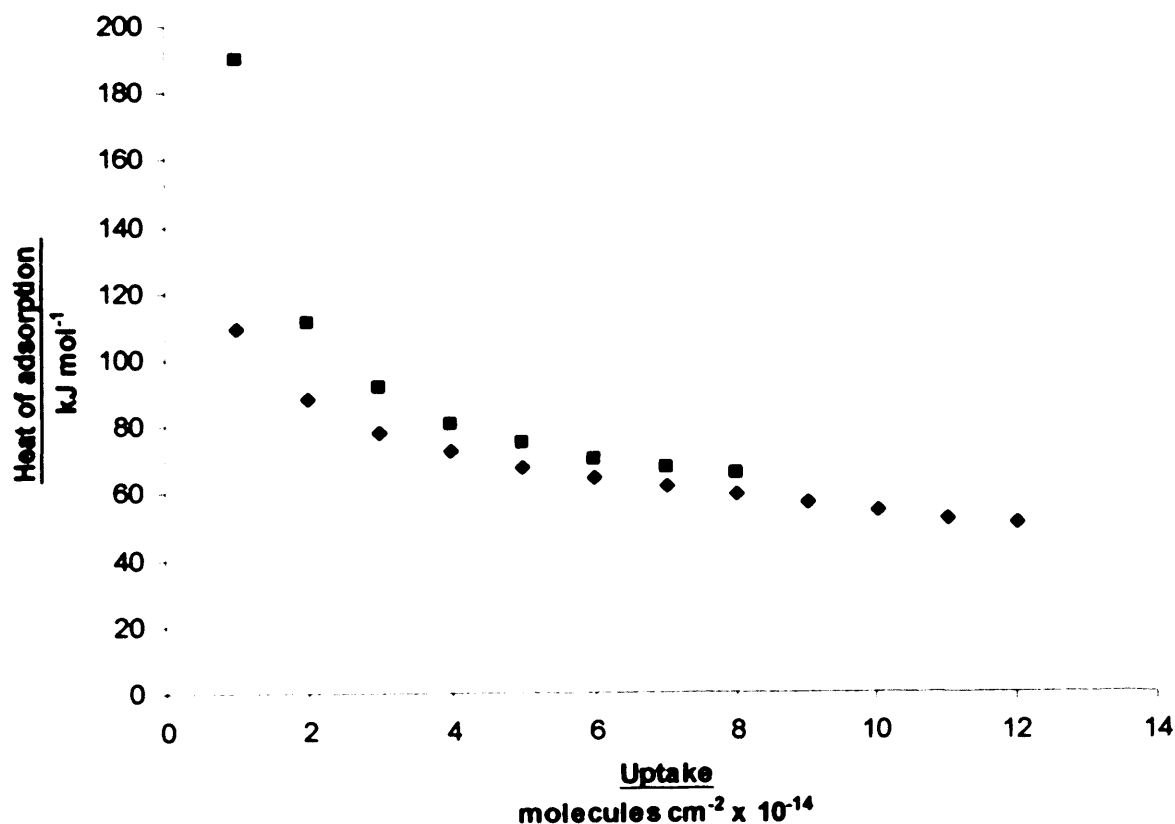
Figure 1.39. Heat of adsorption of water as a function of coverage onto γ-alumina (■) and as a comparison to the heat of adsorption onto α-alumina (♦), as initially shown in figure 1.33. [46]

1.3.4 Theoretical studies of the adsorption of water onto γ-alumina surfaces.

Density functional theory calculations using the Vienna *ab initio* simulation program (VASP) by Digne *et al* [53] in 2002 investigated the $\{11\bar{2}0\}$ and $\{10\bar{1}0\}$ surfaces of γ-alumina for hydroxylation and consequential dehydroxylation of a cell containing eight alumina units. Equation 1.11 describes the equilibrium of the hydroxylation/dehydroxylation process.

$$S_{hkl} + n_{ads}H_2O_{(gas)} \leftrightarrow [S_{hkl}, n_{ads}H_2O]$$
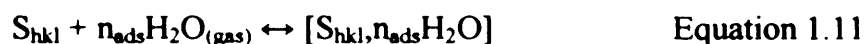
Equation 1.11

Where n_{ads} is the number of adsorbed water molecules and S_{hkl} represents either the $\{11\bar{2}0\}$ or $\{10\bar{1}0\}$ surface. The Gibbs Free energy at temperature T and water pressure p, is calculated by equation 1.12.

$$\Delta_r G_{hkl} = G(S_{hkl} + n_{ads}H_2O) - G(S_{hkl}) - n_{ads}\mu_{H2O}$$

Equation 1.12

Where μ_{H2O} is the chemical potential of water. As this work applied to condensed phases, the variations of internal energy alone were considered and entropic and pV terms were ignored, leading to equation 1.13 and expanded to equation 1.14 at for the reactions at atmospheric pressure.

$$\Delta_r G_{hkl} = n_{ads}\Delta_r g_{hkl}$$

Equation 1.13

$$\Delta_r g_{hkl} = \Delta e_{hkl} + Ts(T) - (h(T) - e(0))$$

Equation 1.14

Where s, h and e are entropy, enthalpy and internal energy of water and Δe_{hkl} is the adsorption energy at 0 K of n_{ads} water molecules onto this surface. The surface energy may be calculated for a hydroxylated surface by:

$$\Gamma_{hkl} = \Gamma_{hkl}^0 + \theta_{hkl} (\Delta_r g_{hkl}/2)$$

Equation 1.15

Where Γ_{hkl}^0 is the surface energy of a fully dehydrated surface and θ_{hkl} is hydroxyl surface coverage as defined by equation 1.16, where A_{hkl} is the area of the surface used in the simulation.

$$\theta_{hkl} = 2n_{ads}/A_{hkl} \qquad\qquad \text{Equation 1.16}$$

Using these equations, the authors determined that for $\theta_{10\bar{1}0} = 0$, no surface coverage of hydroxyl groups, only singular unsaturated surface octahedral aluminium atoms are stable, whereas for $\theta_{11\bar{2}0} = 0$, the stable surface consists of 75% twofold unsaturated octahedral aluminium atoms and 25% singular tetrahedral aluminium atoms. The surface energies are $\Gamma_{10\bar{1}0}^0 = 0.97$ J m^{-2} and $\Gamma_{11\bar{2}0}^0 = 1.545$ J m^{-2}. Figures 1.40 and 1.41 illustrate the calculated differential heats of adsorption as a function of θ, the surface coverage measured in OH groups per nm^{-2}. the differential energy is defined as the difference between the adsorption energies of $n + 1$ water molecules and n water molecules, expressed per water molecule.
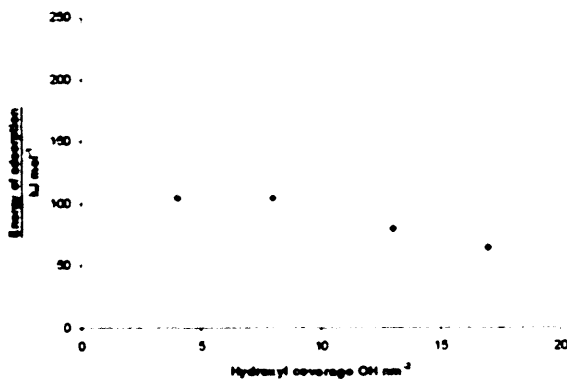
Figure 1.40. Enthalpy of adsorption as a function of θ for the $\{10\ \bar{1}\ 0\}$ γ-alumina surface.[53]
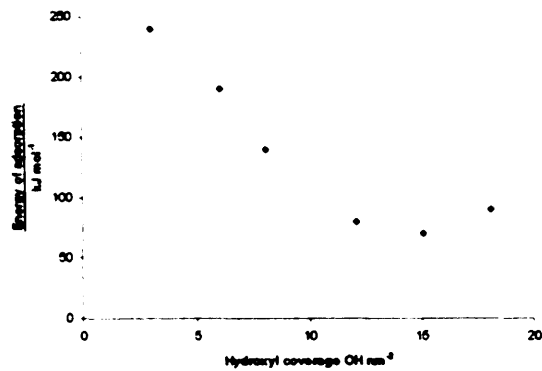
Figure 1.41. Enthalpy of adsorption as a function of θ for the $\{11\bar{2}0\}$ γ-alumina surface.[53]

At a low coverage of 4.3 OH nm^{-2} for the $\{10\bar{1}0\}$ surface, the heat of adsorption, E_{ads}, is 106 kJ mol^{-1} leading to a chemisorbed state, decreasing down to $E_{ads} = 66$ kJ mol^{-1} for a monolayer of adsorbed water molecules, with $\theta_{10\bar{1}0} = 17.1$ OH nm^{-2}. This downward trend is more pronounced on the $\theta_{11\bar{2}0}$ surface, at a low coverage of 3.0 OH nm^{-2}, $E_{ads} = 240$ kJ mol^{-1} as a result of strong Lewis acid three co-ordinate Al$_t$ (trigonal) sites compared to at a monolayer coverage of 17.8 OH nm^{-2}, $E_{ads} = 87$ kJ mol^{-1}. These values compare favourably with the experimental calorimetric work carried out by Hendriksen

et al [44] and summarised graphically in figure 1.39 as the heat of adsorption of water dependant on coverage on α-alumina in which heat of adsorption decreases with increasing coverage. Figures 1.42 and 1.43 illustrate firstly the adsorption site in the relaxed structure, and then the hydroxyl groups present at different coverages for the $\{10\bar{1}0\}$ and $\{11\bar{2}0\}$ surface respectively.

a)   b)
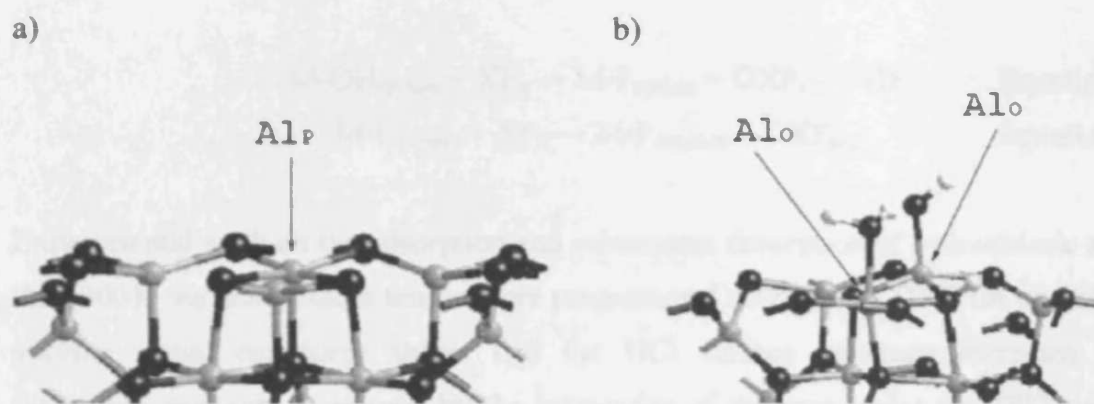
Figure 1.42. The relaxed γ-alumina $\{10\ \bar{1}0\}$ surface (a) illustrating the Al$_P$ five co-ordinate site and subsequent chemisorption of water (b), with adsorptions leading to Al$_O$. This adsorption results gives a surface coverage of $\theta_{10\bar{1}0} = 8.8$ OH nm^{-2}. [53]

a)   b)   c)
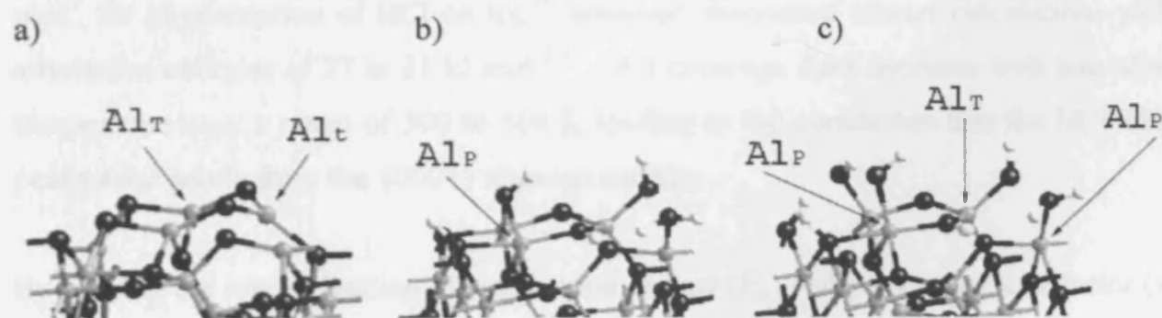
Figure 1.43. The relaxed γ-alumina $\{11\bar{2}0\}$ surface (a) showing the two most significant adsorption sites marked Al$_T$ and Al$_t$ (trigonal). The subsequent chemisorption of water to Al$_P$ is shown in (b), and in (c), chemisorbed water leads to Al$_P$ and Al$_T$ aluminium co-ordinations and a surface coverage of $\theta_{11\bar{2}0} = 8.9$ OH nm^{-2} and 11.8 OH nm^{-2} respectively. [53]

1.3.5 Experimental adsorption of H-X (X=F, Cl) onto the α-alumina {0001} surface.

Metal fluoride and fluorinated metal oxide surfaces are important as heterogeneous catalysts for fluorination of chlorocarbons. Equations 1.17 and 1.18 below describe the fluorination of both clean and hydroxylated oxide surfaces, where M = metal ion, for example aluminium, and typically X = alkali metals such as Cs and K.[54]

$$M\text{-}OH_{surface} + XF_n \rightarrow M\text{-}F_{surface} + OXF_{n\text{-}2} + HF \qquad \text{Equation 1.17}$$

$$M\text{-}O_{surface} + XF_n \rightarrow M\text{-}F_{2surface} + OXF_{n\text{-}2} \qquad \text{Equation 1.18}$$
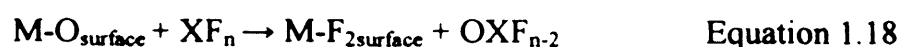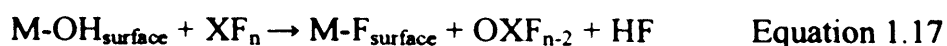
Experimental work on the adsorption and subsequent desorption of hydrochloric acid on the {0001} surface through temperature programmed desorption (TPD) for crystals with varying initial exposures shows that the HCl surface coverage increases versus increasing exposure, measured by the integration of the area under the TPD curves in figure 1.44.[55] There is a single peak centred on approximately 380 K in all the curves, but this does not change position or shape during exposure. A temperature of this magnitude is not reliably attributed to physisorbed or weakly bound HCl on the surface. An estimate for physisorbed E_d is 100.4 kJ mol^{-1} in this case, compared to 16 to 29 kJ mol^{-1} for physisorption of HCl on ice,[56] however, theoretical cluster calculations yield adsorption energies of 27 to 31 kJ mol^{-1}.[57] HCl coverage does decrease with annealing temperature over a range of 300 to 500 K leading to the conclusion that the HCl TPD peaks arise solely from the {0001} alumina surface.

By varying the rate of heating, the activation energy (E_a) and pre-exponential factor (v) for HCl desorption can be calculated, with the assumption that hydrogen and chlorine recombinatively desorb. Figure 1.45 shows the desorption temperature, T_p, measured against the heating rate, β, over a range $\beta = 0.093$ to $\beta = 1.46$ K s^{-1}. The slope of this graph gives E_a of 84 ± 4 kJ mol^{-1} and $v = 3 \times 10^{10\pm1}$ s^{-1} for the lowest energy binding sites for HCl. By calculating first order desorption kinetics from surface sites with different binding energies and the uncertainty in the values above, the range of desorption activation energies range from 79.5 to 150.6 kJ mol^{-1}.
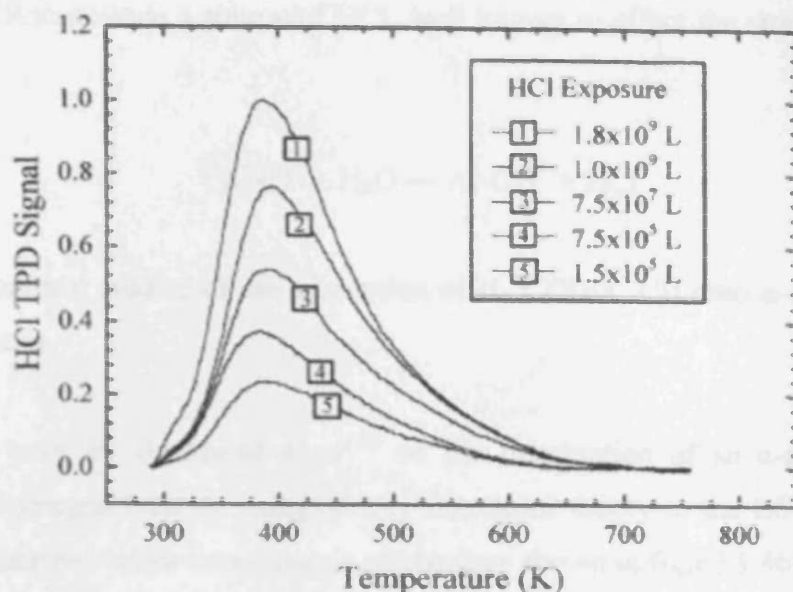
Figure 1.44. HCl temperature programmed desorption spectra after various exposures of HCl to the α-alumina {0001} surface. [55]
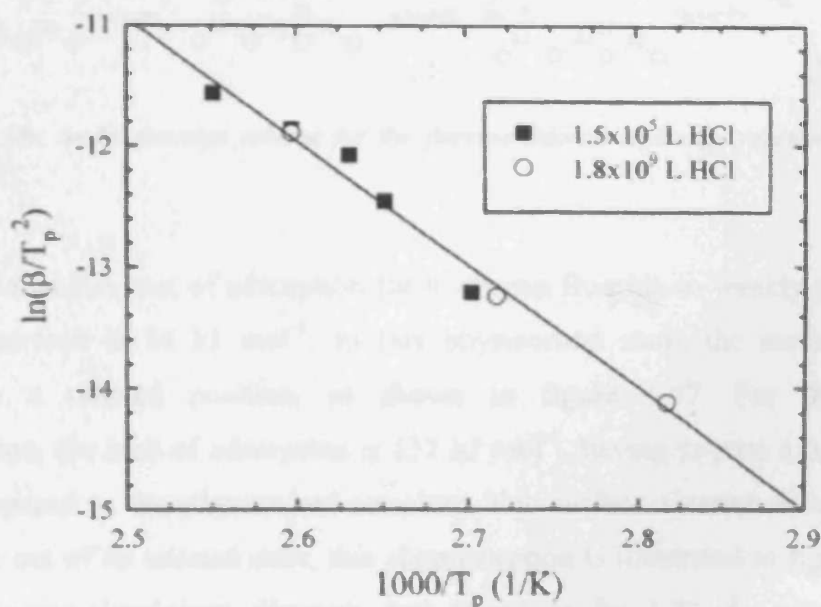
Figure 1.45. The effect of heating rate β measured against peak HCl desorption rate T_p for exposures of HCl at 1.5×10^5 L and 1.8×10^9 L. The slope and intercept $\ln(\beta/T_p^2)$ versus $1/T_p$ give first order kinetics and the parameters $E_a = 20 \pm 1$ kcal mol^{-1} (84 ± 4 kJ mol^{-1}) and $v = 3 \times 10^{10 \pm 1}$ s^{-1} for the lowest energy binding site. [55]

Beyond the scope of industrial catalytic chemistry applications, there is an important environmental impact to consider, HCl adsorbed on α-alumina crystals from rocket motors creates Bronsted and Lewis acid sites participates in H_2O exchange as shown in

equation 1.19 to provide a source of HCl, well known to affect the stratospheric ozone layer.

$$Al\text{-}Cl^* + H_2O \rightarrow Al\text{-}OH^* + HCl \qquad \text{Equation 1.19}$$

1.3.6 Theoretical studies of the adsorption of H-X (X=F, Cl) onto α-alumina {0001} surfaces.

Theoretical work by Bankhead *et al* [58] on the fluorination of an α-alumina {0001} surface by hydrogen fluoride using density functional theory in the DSolid program to model the fluorine – chlorine exchange mechanism shown in figure 1.46.
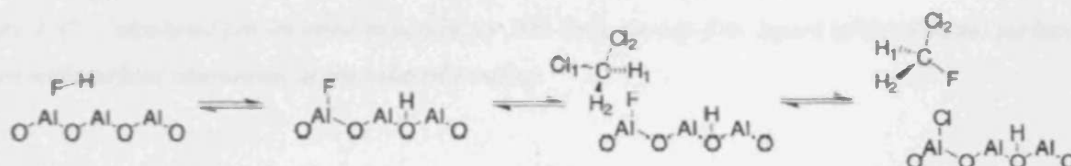
Figure 1.46. The model reaction scheme for the fluorine/chlorine exchange reaction on an alumina surface. [58]

It was seen that the heat of adsorption for hydrogen fluoride to weakly physisorb onto the clean surface is 14 kJ mol^{-1}. In this physisorbed state, the surface aluminium remains in a relaxed position, as shown in figure 1.47. For the subsequent chemisorption, the heat of adsorption is 132 kJ mol^{-1}, having to pass a barrier of 47 kJ mol^{-1}. Compared to the physisorbed structure, this surface aluminium moves towards the fluorine out of its relaxed state, this chemisorption is illustrated in figure 1.48. The ensuing fluorine-aluminium distance was found to be 1.71 Å, compared to the experimental AlF$_3$ bond distance of 1.65 Å.

51
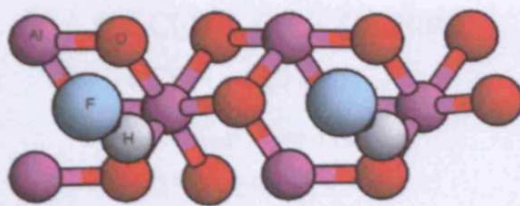
Figure 1.47. Calculated physisorbed structure for HF. Only the top four layers of the alumina surface are shown with surface aluminium in the relaxed position. [58]

a)   b)
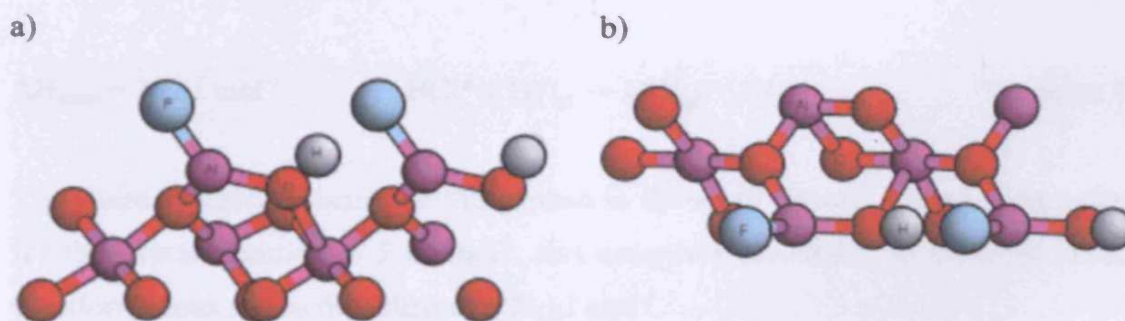
Figure 1.48. (a) Side projection and (b) plan view of the calculated chemisorbed structure for HF on an α-alumina {0001} surface, showing the elevation of the aluminium from a relaxed position to co-ordinate with the incoming fluorine. [58]

The proposed methodology for this exchange is shown in equations 1.20 to 1.26, along with the relevant calculated thermodynamic data, where ΔH_{phys} = heat of physisorption, ΔH_{chem} = heat of chemisorption, ΔH_{exch} = heat of exchange reaction (rate determining step) and ΔH_{desorp} = heat of desorption.
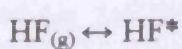
$\Delta H_{phys} = -14 \text{ kJ mol}^{-1}$	$HF_{(g)} \leftrightarrow HF^*$	Equation 1.20
$\Delta H_{phys} = -77 \text{ kJ mol}^{-1}$	$CH_2Cl_{2(g)} \leftrightarrow CH_2Cl_2^*$	Equation 1.21
$\Delta H_{chem} = -118 \text{ kJ mol}^{-1}$	$HF^* \rightarrow O_{surf}\text{-}H + F^*$	Equation 1.22
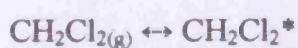
$\Delta H_{exch} = 90 \text{ kJ mol}^{-1}$ $\qquad$ $F^* + CH_2Cl_2^* \rightarrow Cl^* + CH_2ClF^*$ $\qquad$ Equation 1.23

$\Delta H_{desorp} = 89 \text{ kJ mol}^{-1}$ $\qquad$ $CH_2ClF^* \leftrightarrow CH_2ClF_{(g)}$ $\qquad$ Equation 1.24

$\Delta H_{phys} = 30 \text{ kJ mol}^{-1}$ $\qquad$ $Cl^* + O_{surf}\text{-}H \rightarrow HCl^*$ $\qquad$ Equation 1.25

$\Delta H_{desorp} = 124 \text{ kJ mol}^{-1}$ $\qquad$ $HCl^* \leftrightarrow HCl_{(g)} + {}^*$ $\qquad$ Equation 1.26
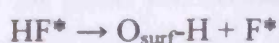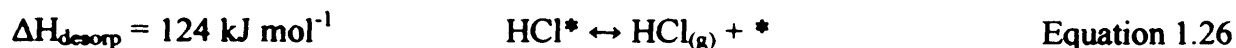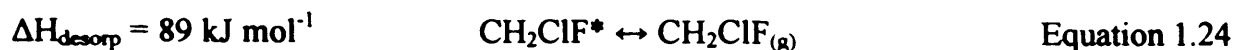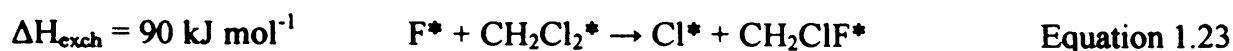
Equation 1.23 shows physisorbed dichloromethane undergoing an exchange reaction on a fluorinated surface to yield a chlorinated surface and chlorofluoromethane, the barrier to which is 233 kJ mol^{-1}, greater than the adsorption energy for dichloromethane, -77 kJ mol^{-1}. As a result, both physisorbed hydrogen fluoride and dichloromethane are in equilibrium, shown by equations 1.20 and 1.21, so the surface reaction is the rate determining step, equation 1.23. The reverse to the exchange reaction would have to pass a barrier of 143 kJ mol^{-1}, and so is unlikely. The energetically favourable route is the desorption of chlorofluoromethane – equation 1.24 – for which the heat of desorption is 89 kJ mol^{-1}. From the penultimate state there is a further exchange between chlorine and fluorine, summarised as:

$\Delta H_{exch} = 35 \text{ kJ mol}^{-1}$ $\qquad$ $HCl^* + HF_{(g)} \rightarrow HCl_{(g)} + HF^*$ $\qquad$ Equation 1.27
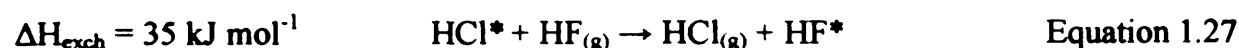
The entire energetic scheme for this process is shown in figure 1.49, the energy change for the overall reaction is 5 kJ mol^{-1}, this compares favourably to the bond enthalpy transformations across the scheme of 21 kJ mol^{-1}.
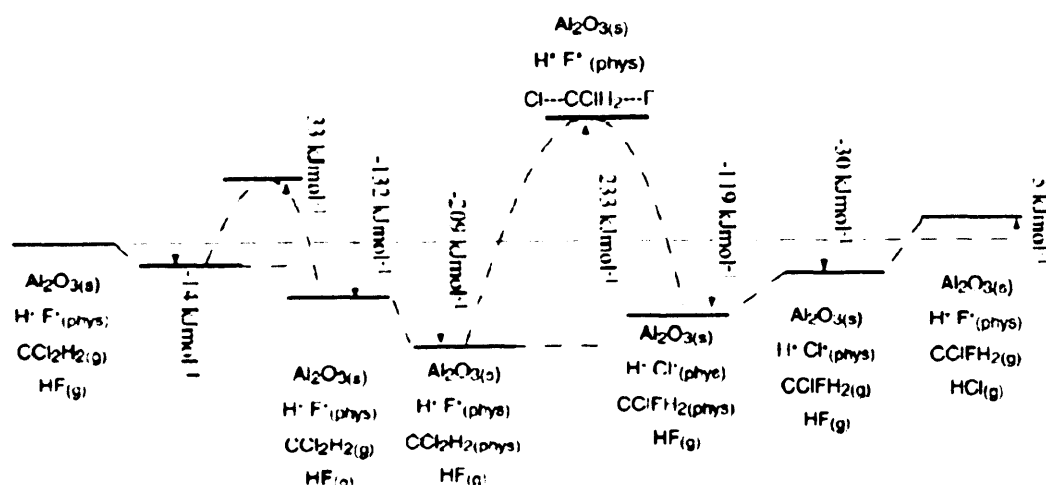
Figure 1.49. The relative energies of the stable intermediates with energy barriers for reactions calculated using the periodic density functional theory program DSolid. [58]

HF adsorption has also been studied using semi empirical calculations by Gale.[59] with slab methodology and adsorbing one hydrogen fluoride molecule onto each {0001} face of the slab to preserve the zero dipole moment. Firstly, HF was adsorbed onto a rigid surface and then the effect of surface relaxation in response to the adsorbate was considered. In the first case, the heat of adsorption was 21 kJ mol^{-1}. This resulted in a hydrogen – fluoride distance of 0.95 Å and a fluorine – aluminium distance of 1.82 Å. In the second case, the relaxation of the surface had an important effect on the heat of adsorption, which was 38.6 kJ mol^{-1}. The geometry of this optimised structure was similar with the hydrogen – fluorine distance 0.95 Å and fluorine – aluminium 1.79 Å. This adsorption also showed there is a displacement of the aluminium site away from the bulk towards the fluorine of the adsorbate molecule by 0.16 Å, with a simultaneous contraction in the hydrogen – fluorine distance. As the hydrogen fluoride molecule dissociates on the surface, such a contraction must not have been the active transition state minimum. An alternative scheme with a tilted hydrogen fluoride with Al – F – H angle of 136° resulted in a stabilisation of 5 kJ mol^{-1} over the original upright adsorption.

A doubling of the coverage to two hydrogen fluoride molecules on each {0001} surface with the maximum available periodic inter-adsorbate distance possible resulted in a lowering of the heat of adsorption to 23.3 kJ mol^{-1} with a fluorine to aluminium distance of 1.8 Å.

Hartree-Fock calculations by Catlow et al [60] with a vertical constraint imposed on the hydrogen-fluoride axis reported a heat of adsorption of 81 kJ mol^{-1}, a considerably higher energy than found above based on density functional theory results. The fluorine-aluminium distance was found to be 1.93 Å in this Hartree-Fock work.

1.3.7   Experimental adsorption of HX (X=F, Cl) onto other alumina surfaces.

The γ-alumina surface acts as a catalyst to support the dismutation of HCFC-22, difluorochloromethane:

$$3CClF_2H \rightarrow 2CF_3H + CCl_3H \qquad \text{Equation 1.28}$$

Work carried out by Chupas *et al* [61] using X-ray diffraction and nuclear magnetic resonance techniques to follow the changes that occurred during reaction 1.28 over the γ-alumina surface showed that at 300°C the reaction did not go to completion and did not result in any major structural changes in the catalyst sample. A further experiment at 400°C yielded a similar product/reactant distribution, however, the γ-alumina catalyst did undergo significant structural changes, with a progressive temperature increase from 300°C to 500°C, a phase transition from γ-alumina to a new phase occurred at approximately 360°C. At the highest temperature, 500°C, the transformation into a different phase was complete. Across the temperature range 300°C to 500°C, the catalyst is active for the dismutation of HCFC-22, with low level fluorination towards the lower temperatures.

Radio traced $^{19}F/^{27}Al$ NMR data showed that at 300°C a fluorination reaction occurred to yield an Al-F octahedral environment, AlF_6. A further resonance was assigned to either $AlF_xO_{6-x}(1 < x < 5)$ or a terminal fluorine atom on the surface. For the experiment at 400°C, an aluminium fluoride phase in the ^{27}Al spectrum was present, with a trace amount of γ-alumina. The ^{19}F spectrum showed a resonance consistent with AlF_3, confirming that dismutation has occurred with γ-alumina sample reconstruction to a fluorinated alumina structure, this having a higher activity for the dismutation reaction than AlF_3. It was suggested that defects were formed on the surface of the newly formed catalyst during fluorination and it is these that are responsible for the higher catalytic activity compared to AlF_3.

Although fluorination occurred at 300°C, no crystal reconstruction was seen. At 360°C, the fluorination of the bulk becomes energetically favoured, and could proceed via the loss of oxygen in the form of CO_2 after complete oxidation of a CFC starting compound, as observed by Deshmukh *et al.*[62] In this case, difluorochloromethane is the reactant, so equation 1.29 was applied to the fluorination of the bulk phase:

$$2HCF_2Cl + Al_2O_3 \rightarrow H_2O + 2AlF_2Cl + CO \qquad \text{Equation 1.29}$$

The chlorine resident on the surface could be removed via a reaction with hydroxyls, to yield HCl, or to further react with difluorochloromethane to produce HCFC-21 and finally chloroform.

Work by Boese *et al* [63] used surface techniques such as XPS (X-ray Photoelectron Spectroscopy), XAES (X-ray Auger Electron Spectroscopy) and XANES (X-ray Absorption Near Edge Spectroscopy) to probe a sample of γ-alumina over the initial stages of fluorination when exposed to HF. For the reaction to proceed, the reactants must have access to the aluminium Lewis acid sites. The fluorination of the crystal is initiated on the surface region, which lead to a coordinatively unsaturated chemisorbed surface fluorine occupying the exposed Lewis acid sites or defects. F Auger analysis found the formula of the sample to be $Al(OH)_{0.7}F_{2.3} \cdot H_2O$. Further catalytically active Lewis acid sites are only formed when the sub-surface region of the crystal is fluorinated, which were strong enough to facilitate F/Cl exchange reactions.

It was thought that substitution of divalent oxygen atoms by monovalent fluorine atoms led to rupturing and subsequent break-up of the oxide lattice to form a disordered oxofluoride/hydroxofluoride phase, sufficient for high catalytic activity. During an F/Cl exchange reaction, the hydroxofluoride phase may transform into AlF_3 and Al_2O_3, so the Lewis acid active centres are $AlO_{x-y}F_y$. Upon fluorination at high temperatures (+300 °C) or prolonged exposure to fluorine the Lewis acidity of the crystal increased.

XPS analysis showed that when γ-alumina was exposed to $CHClF_2$, both fluorine and chlorine were incorporated into the sample, as expressed by Chupas *et al* [59] in the concentrations 5 to 14 atom% for fluorine and < 1 atom% for chlorine. The threshold for catalytic activity was 10 atom% of fluorine, which coincided with the bulk fluorination stage, to yield a catalytically active oxofluoride/hydroxofluoride phase without having to form AlF_3 as a precursor to activity.

1.4   Hydroxylated aluminium oxide surfaces.

1.4.1   Structure of hydroxylated α-alumina surfaces.

Theoretical work by Parker [64] on the relaxation of the hydroxylated α-alumina {0001} surface found the interlayer relaxations occur in approximately the same manner as in the clean surface. Table 1.10 displays the percentage relaxations of this work carried out using the density functional theory code VASP, compared to further results calculated by Bankhead [37] using a localised basis set within both VASP and DSolid for both experimentally determined lattice parameters and equivalent calculations using a purely theoretically established cell. The method of removing the terminating Al1 layer from the surface was used, so the nomenclature for the layers remains the same as for the clean surface, calculated using equation 1.2.

Layer	VASP Parker [64]	VASP Bankhead [58] experimental & (theoretical)	DSolid Bankhead [58] experimental & (theoretical)
O1-Al2	+6 %	+5.9 % (+3.9 %)	+7.5 % (+4.1 %)
Al2-Al3	-39.1 %	-30.2 % (-29.9 %)	-37.7 % (-18.1 %)
Al3-O2	+3.6 %	+10.6 % (+9.1 %)	+15.0 % (+7.9 %)
O2-Al4	-0.6 %	+1 % (+1.9 %)	+0.3 % (+1.2 %)
Al4-Al5		+5.5 % (+8.7 %)	+7.9 % (+5.6 %)

Table 1.10. Comparison of percentage relaxations for a hydroxylated α-alumina {0001} surface calculated by the density functional theory programs VASP and DSolid. For the Bankhead results, the experimental relaxations are calculated using the X-ray determined lattice structure and the theoretical results by purely ab initio methods from an experimental start-point only. [58 64]

The percentage relaxations in table 1.10 mirror the clean surface described in section 1.2.3 for the VASP determined results, although there was a slight decrease for the Al2-Al3 relaxation compared to the clean surface. There was a strong connection between the VASP calculations for both experimentally and theoretically determined cells in the findings of Bankhead. This was not the case for the results entirely produced using DSolid as the purely theoretical relaxations disagreed by a large extent when compared to the experimental lattice calculations which were consistent to both the VASP data for

a hydroxylated surface and the density functional theory sub-surface relaxations shown in section 1.2.3.

The adsorption of water onto Lewis acid aluminium sites and Lewis base oxygen sites has been detailed in section 1.3.1 and 1.3.2 for both experimental and theoretical methods respectively. This adsorption results in the disappearance of both oxygen and aluminium coordinatively unsaturated ions to produce a hydroxylated surface, in which OH^- is bound to aluminium sites, and the remaining H^+ fragment of water forms a hydroxyl at an oxygen site. The surface can be constructed via a cleavage of the crystal and the subsequent saturation of the resultant dangling bonds.

The analysis of completely hydroxylated low index alumina surfaces containing tetrahedrally and octahedrally coordinated aluminium ions by Knözinger and Ratnasamy [65] defined three types of hydroxyl group found on the surface as summarised in table 1.11.

Type of hydroxyl group	Co-ordination of oxygen in hydroxyl group	
Type I	i)	$O - Al_T$
	ii)	$O - Al_O$
Type II	i)	$O - Al_T$ and Al_O
	ii)	$O - Al_O$ and Al_O
Type III	i)	$O - Al_O$, Al_O and Al_O

Table 1.11. Three types of hydroxyl groups on alumina surfaces. Type I is bound to a single hydroxyl group and can be further subdivided according to the co-ordination of the aluminium atom, where Al_T is tetrahedral and Al_O is octahedral. Type II oxygen is bridged across two aluminiums, and type III across three aluminiums. [65]

The infra-red spectroscopic work of Tsyganenko and Mardilovich [66] on hydroxylation of γ-alumina showed that after the saturation of dangling bonds with OH^- and H^+ fragments, two different hydroxyl groups each occurred for single, double and triple exposure of tetrahedral and/or octahedral aluminium as outlined in table 1.12.

Exposure of aluminium	Co-ordination of aluminium (and unique identification)	Co-ordination of oxygen in hydroxyl group
Single	Octahedral. (O_OH)	OH | Al_O
	Tetrahedral. (O_TH)	OH | Al_T
Double	2 × octahedral. ($O_{OO}H$)	OH / \\ Al_O Al_O
	Octahedral and tetrahedral ($O_{TO}H$)	OH / \\ Al_T Al_O
Triple	3 × octahedral. ($O_{OOO}H$)	OH / | \\ Al_O Al_O Al_O
	2 × octahedral and tetrahedral ($O_{TOO}H$)	OH / | \\ Al_O Al_O Al_T

Table 1.12. Co-ordination of both aluminium and oxygen for hydroxylated γ-alumina. Exposure to two aluminium sites yields oxygen bridging across two sites, and exposure to three aluminium sites results in oxygen bridging across three sites. [66]

The γ-alumina structure is constructed of each oxygen atom surrounded by one tetrahedral and three octahedral aluminium ions. For alumina structures that contain both octahedral and tetrahedral aluminium co-ordination, such as the investigated γ-alumina and θ-alumina, one-ninth of aluminium sites should be vacant to fit stoichiometry, giving rise to the effects of defects on the types of hydroxyl groups present on the surface. For γ-alumina and θ-alumina, where both tetrahedral and

octahedral vacancies are allowed, all six types of hydroxyl groups were present in low index surfaces.

1.4.2 Desorption of hydroxyl groups from hydroxylated α-alumina {0001} surfaces.

Tysganenko and Mardilovich [64] have concluded that of the α-alumina {0001} surface the dehydroxylation occurs via a pair of adjacent groups reacting. This consisted of the basic OH⁻ fragment with the highest negative charge combining with the most acidic proton of the highest positive or lowest negative charge to produce the first group to dehydroxylate, an $O_{OO}H$ group. The result of this was a change in the co-ordination of the two surrounding aluminium ions leading to four $O_{PO}H$ groups, (where the O_P is effectively an oxygen bound to an octahedral aluminium with one vacant site) and a surface oxygen. Subsequent desorption lead to the appearance of $O_{PP}H$, $O_{TO}H$ and $O_{TP}H$ groups. The desorption of O_OH proceeded through the interaction of protons from $O_{OOO}H$ groups, which in turn led to the formation of an $O_{POO}H$ group prior to complete dehydroxylation. With the removal of all type I and II groups complete, chains of $O_{OO}H$ condensed to give $O_{PO}H$, then to $O_{PP}H$ groups as the final stage before full dehydroxylation.

Overall, for any phase of fully hydroxylated alumina, partial dehydroxylation causes a burgeoning in the types of hydroxyl groups present, to the extent that the final co-ordination of hydroxyl groups is not related to the initial co-ordinations present. The initial six types were expected to disappear after the removal of approximately 50 – 75% of this original number. As pointed out previously, there was a decrease in the co-ordination number of cationic aluminium ions surrounding the hydroxyl group as dehydration takes place. The effect of this is an increase in the net positive charge of the hydroxyl groups and therefore acidity along with more basic oxygen sites. The O_PH and O_tH (trigonal, formed from O_TH desorption) groups are more stable than their initial counterparts. With type III desorption, the initial groups are less acidic, and therefore more stable than the co-ordinations produced in further stages of dehydroxylation, where the protons preferentially migrated to basic oxygen sites.

1.4.3 Reactions over hydroxylated γ-alumina surfaces

An extension of the density functional theory work by Digne *et al* [53] on hydroxylation of γ-alumina surfaces using the *VASP* code is the chlorination by hydrogen chloride to substitute surface hydroxyl groups:

$$-Al_n(OH)- + HCl_{(gas)} \longleftrightarrow -Al_n(Cl)- + H_2O_{(gas)} \qquad \text{Equation 1.30}$$
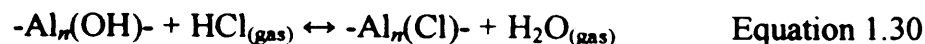
Where n is the co-ordination of the aluminium ion to which the surface hydroxyl group or chlorine species is bound. The majority of these substitution reactions involve an endothermic enthalpy change. Figure 1.42 illustrates the clean (a) and hydroxylated (b) $\{10\bar{1}0\}$ surface, figure 1.43 (b + c) shows the $\{11\bar{2}0\}$ surface with the three hydroxyl group categories: singularly bound, bridged between two aluminium atoms and a surface oxygen basic site bound to three aluminium atoms with a proton attached. It is problematical to contain two- or threefold coordinated chlorine atoms without major structural change as the ideal Al-Cl distance of 2.2 to 2.4 Å is larger than the ideal Al-OH distance of 1.8 to 2.0 Å. In the case of singularly bound hydroxyl groups, on both the $\{10\bar{1}0\}$ (Al$_O$) and $\{11\bar{2}0\}$ (Al$_P$) surfaces, the Al-Cl distance is 2.38 and 2.2 Å respectively, with both processes being almost athermic, +2 and +4 kJ mol^{-1}. For the substitution occurring on the Al$_T$ site the enthalpy change is +19 kJ mol^{-1} and is unfavourable due to the hydrogen bond formed between O-H and Cl being weaker than between O-H and O and not supporting substitution. When this hydrogen bond network is removed, principally at lower coverages, the substitution becomes marginally exothermic, -6 kJ mol^{-1}. The substitution reaction for the chemisorbed water molecule, H$_2$O-Al$_O$ is endothermic leading to the dissociation of the hydrogen chloride molecule. The enthalpy of reaction is +12 kJ mol^{-1} for the $\{10\bar{1}0\}$ surface and +31 kJ mol^{-1} for the $\{11\bar{2}0\}$ surface. Across the series of adsorptions, the singularly bound hydroxyl groups give the most favourable substitution reactions.

1.5   Aluminium fluoride.

1.5.1   Aluminium fluoride surfaces catalytic activity.

Aluminium fluoride, a strong Lewis acid, is prepared by full fluorination of the aluminium oxide by strong fluoriding agents such as hydrogen fluoride. Aluminium fluoride exhibits catalytic activity for halogen exchange reactions and the dismutation of chlorofluoromethanes [67] and hydrochlorofluoromethanes.[68] Numerous phases of AlF_3 exist; it is interesting to note that although α-AlF_3 is highly ordered, the F/Cl exchange reaction is inhibited due to the steric hindrance by the high density of fluorine ions surrounding surface aluminium sites. In contrast, the β-AlF_3 crystal has an open hexagonal structure with the Lewis acid aluminium sites exposed, and so exchange reactions are not impeded.

The $HAlF_4$ (HF-AlF_3) structure consists of an AlF_3 cluster, bound via a hydrogen bond to HF in a cyclic arrangement where Al-F is 199 pm, and H_{HF}-$F_{cluster}$ is 223 pm.[69]. In the latter structure, the weakest bond is the Al-F_{HF}, equations 1.31 and 1.32 describe the fragments occurring where e^- are electrons required to balance the charges:

$$HAlF_4 + e_1^- \rightarrow AlF_3^+ + HF + 2e^- \qquad \text{Equation 1.31}$$
$$HAlF_4 + 2e^- \rightarrow AlF_2^+ + F^- + HF + 2e^- \qquad \text{Equation 1.32}$$
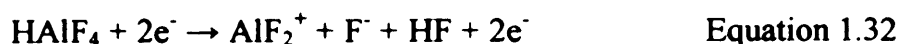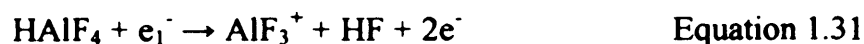
The formation of the bond between HF and the Lewis acid centre may be propagated via electron donation from the fluorine of HF results in a dissociation energy of -67 kJ mol^{-1}, although Scholz *et al* [68] determine the linear hydrogen bond to a fluorine of the cluster to also be a minimum, in this case the dissociation energy is calculated to be -19.4 kJ mol^{-1} using Hartree-Fock calculations for both. The equivalent HCl adsorbates were found to be less stable than the HF adsorbates.

Radiotracer investigation of solid β-AlF_3 and HF co-ordinated onto the active aluminium site was undertaken by Barclay *et al* [70] starting with decomposition of $AlF_3 \cdot 3H_2O$ via $AlF_3 \cdot xH_2O$. The initial fluorination leads to the replacement of some

surface hydroxyl groups, Al-OH, and bridging Al-O-Al groups by Al-F, along with artefacts such as OSF_2, SO_2 and HF from the fluorinating agent SF_4.

Adsorption of $H^{18}F$ at 473 K for one hour produced a ^{18}F labelled surface, indicating exchange and retention of HF by β-AlF_3 occurred. Subsequent exposure to 1-dichloro2-chlorofluoroethane, CCl_2FCClF_2, does not undergo any exchange to incorporate ^{18}F into the adsorbate, although 22% of $H^{18}F$ was lost from the surface during the temperature increase.

Addition of $H^{36}Cl$ to β-AlF_3 yielded a plateau, beyond which progressive additions caused a decrease in the surface count with a proportional increase in vapour count, indicating a change in the surface structure. At room temperature, the addition of HCl to β-AlF_3 calcined at 573 K led to desorption of both H_2O and HCl, although some water is retained in the solid. Low levels of water are a prerequisite for HCl adsorption, leading to a conclusion that there is a co-operative effect between the two adsorbates. Adsorption can be described as HCl hydrogen bonding to water co-ordinated onto the aluminium site [$AlF_3(H_2O)_n$] at room temperature, coordinatively unsaturated aluminium sites resulted at 373 K, as shown in figure 1.50.
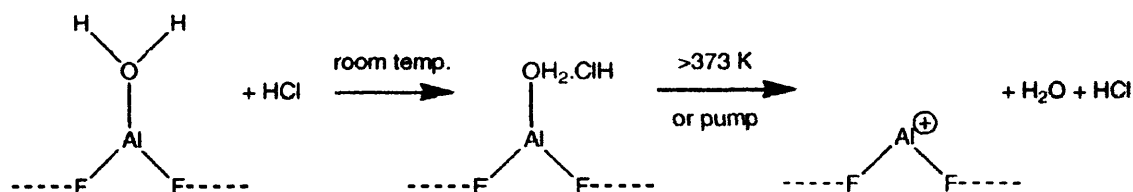
Figure 1.50. Schematic representation of adsorption and subsequent desorption of HCl on an AlF_3 surface. [70]

However, chlorination of the surface hydroxyl groups occurred when $H^{36}Cl$ was exposed to the β-AlF_3 surface, this is illustrated in figure 1.51. Overall, the uptake of HF by β-AlF_3 was found to be greater than the uptake for HCl.
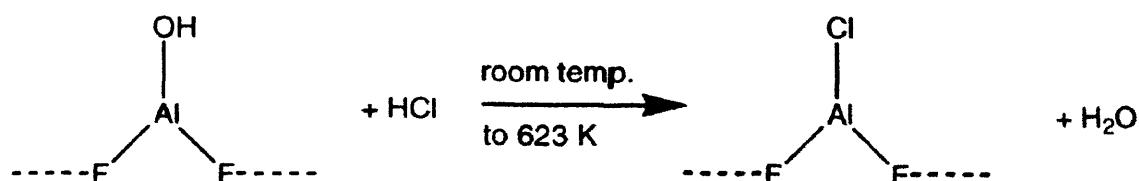
Figure 1.51. Chlorination of hydroxyl sites on an AlF_3 surface beginning at room temperature and rising to 623 K. [70]

1.6 Summary.

Ab initio and atomistic theoretical methods along with complementary experimental techniques have been widely used to investigate the structure, surfaces and reactions involving aluminium oxide. The α-alumina {0001} surface is the most commonly studied structure giving a substantial series of reference material with which to compare results from this work.

The closely packed {0001} α-alumina surface terminates with an aluminium Al1 layer uppermost.[25, 26] This relaxes towards the subsurface oxygen O1 layer by between 50 and 90 % of the original distance depending on the method of calculation or experimental determination.[26-36] The α-alumina structure contains aluminium in only octahedral co-ordination and acts as a Lewis acid when unsaturated on the {0001} surface. The second level basic oxygen is also accessible as an alternative adsorption site, resulting in a mixed oxide surface with the stability measured as the surface energy, γ_s. An ideal value for this is between 1 and 5 J m^{-2} for accurate theoretical calculations.[26, 33, 36-41] The XRD experimental relaxations for the first four interlayer separations are Al1-O1 = -51 %, O1-Al2 = +16 %, Al2-Al3 = -29 % and Al3-O2 = +20 %.[27] It is seen that *ab initio*, semi-empirical and atomistic methods of simulation all overestimate the Al1-O1 relaxation by up to approximately 40 % compared to experimental results.

High quality *ab initio* and semi-empirical work on the methods of water adsorption onto the {0001} α-alumina surface show this to be an energetically favourable process which yields a fully hydroxylated surface with different properties and structures from the aluminium terminated surface.[37, 50 - 52, 64] Energies of adsorption for water range from *ca.* -100 kJ mol^{-1} to *ca.* -180 kJ mol^{-1}, depending on the method of calculation for the initial

molecular adsorption of water. This compares to two experimentally determined values of -75 kJ mol^{-1} [45] and -109 kJ mol^{-1}.[46] Chemisorption of one water molecule occurs from between *ca.* -130 kJ mol^{-1} to *ca.* -250 kJ mol^{-1} depending on the crystal size and method of calculation. A reaction barrier must be overcome from the physisorbed state, with chemisorption being correspondingly higher for further water adsorption in a range between *ca.* -230 kJ mol^{-1} and *ca.* -413 kJ mol^{-1}. Both the dissociative chemisorption and molecular physisorption can occur via either a 1-2 or 1-4 formation. Due to the presence of the hydrogen and oxygen layers, adsorptions of molecules such as HF are not possible onto the inaccessible Lewis acid aluminium sites.

Adsorption of hydrogen fluoride is also a thermodynamically favourable process, ultimately leading to the fully fluorided AlF$_3$ structure. The physisorption of one HF molecule was found to range from -14 kJ mol^{-1} [58] to -81 kJ mol^{-1}.[60] The orientation of the incoming hydrogen fluorine adsorbate affects the energy of adsorption.[59] As with water, a reaction barrier needed to be overcome to yield chemisorbed hydrogen fluoride, the enthalpy of chemisorption was found to be -118 kJ mol^{-1} lower than the enthalpy of physisorption. Depending on the method of adsorption, the aluminium reaction site experienced either a movement away from the surface when fluorine is chemisorbed via a 1-2 co-ordination or remains in the relaxed position when hydrogen fluoride is physisorbed in a 1-2 formation. No adsorptions of hydrogen fluoride using atomistic methods have featured in the published literature to date.

Other phases of alumina are important, primarily θ- and γ-alumina formed from the thermal dehydration of boehmite as the penultimate stage before the corundum phase.[8 -15] Both of these polymorphs contain octahedral and tetrahedral aluminium sites in proportions ranging from an equal distribution to a majority of octahedral co-ordination. This provides scope for surfaces with both octahedral and tetrahedral Lewis acid sites terminating low Miller index surfaces.

[1] W.R. Cofer, G. G. Lala and J.P. Wightman, *Atmos. Environ.*, 21(5), 1187, (1987).
[2] N. N. Greenwood and A. Earnshaw, *Chemistry of the elements*, Pergamon Press, (1984).
[3] W. H. Gitzen, *Alumina as a ceramic material*, The American Ceramic Society Inc, Columbus, Ohio.
[4] J. C. Boettger, *Physical Review B* 55, 750, (1997).
[5] S. Ciraci and I. P. Batra, *Physical Review B* 28, 982, (1983).
[6] A. Marmier and M. W. Finnis, *J. Phys.: Condensed Matter* 14, 7797, (2002).
[7] P. P. Ewald, C. Hermann, *Strukturbericht*, vol. 1, 1913, p240.
[8] J. Lewis, D Schwarzenbach and HD Flack, *Acta Crystallographica A* 38, 733, (1982).

[9] R. W. G. Wyckoff, *Crystal Structures*, 2nd Edition. (Wiley, NY, 1964).

[10] R.-S. Zhou and R. L. Snyder, *Acta. Cryst.* **B47**, 617, (1991).

[11] B. C. Lippens. *Thesis*. Technical University Delft (1961).

[12] G. Yamaguchi, I. Yasui and W. Chiu, *Bull. Chem. Soc. Japan*, **43**, 2487, (1970).

[13] C. S. John, V. C. M. Alma and G. R. Hays, *Appl. Catal.*, **6**, 341-346, (1983).

[14] S.-H. Cai, S. Rashkeev, S. Pantelides and K. Sohlberg, *Physical Review B*, **67** #224104, (2003).

[15] C. Wolverton and K. Hass, *Physical Review B*, **63**, #024102, (2000).

[16] A. P. Borosy, B. Silvi, M. Allavena and P. Nortier, *J. Phys. Chem.*, **98**, 13189, (1994).

[17] Y. Repelin and H. Hudson, *Etudes Structurales d'alumines de transition*, Ecole Centrale, Paris 1989.

[18] S. D. Mo and W. Y. Ching, *Phys. Rev. B*, **57 (24)** 15219, (1998).

[19] M. Wilson, M. Exner, Y.-M. Huang and M. Finnis, *Physical Review B*, **54 (22)**, 15683, (1996).

[20] K. Wefers and C. Misra, Alcoa technical paper No. 19, Alcoa Laboratories, Pittsburg, PA, USA, 1987.

[21] M.-H. Lee, C.-F. Cheng, V. Heine and J. Klinowski, *Chem. Phys. Lett.*, **265**, 673, (1997).

[22] G. Gutierrez, A. Taga and B. Johansson, *Phys. Rev. B*, **65**, #012101, (2001).

[23] M. Halvarsson, V. Langer, S. Vuorinen, *Surf. Coatings. Tech.* **76**, 358, (1995).

[24] Y. Yourdshahyan, U. Engberg, L. Bengtsson, B. Lundqvist and B. Hammer, *Physical Review B*, **55 (14)** 8721, (1997).

[25] T. Suzuki, S. Hishita, K. Oyoshi and R. Souda, *Surf. Sci.*, **437**, 289, (1999).

[26] I. Batyrev, A. Alavi and M. Finnis, *Faraday Discuss.*, **114**, 33, (1999).

[27] P. Guenard, G. Renaud, A. Barbier and M. Gautier-Soyer, *Surf. Rev. Lett.*, **5**, 321, (1998).

[28] I. Manassidis, A. De Vita and M. Gillan, *Surf. Sci. Lett.*, **285**, L517, (1993).

[29] C. Verdozzi, D. Jennings, P. Shultz and M. Sears, *Phys. Rev. Lett.*, **82**, 799, (1999).

[30] C. R. A. Catlow, R. James, W. Mackrodt and R. F. Stewart, *Phys. Rev. B*, **25**, 1006, (1982).

[31] W. Mackrodt, R. Davey, R. Docherty and S. Black, *J. Cryst. Growth*, **80**, 441, (1987).

[32] V. E. Puchin, J. Gale, A. Shluger, E. Kotomin, J. Günster, M. Brause and V. Kempter, *Surf. Sci.*, **370**, 190, (1997).

[33] J. Gomes, I. Moreira, P. Reinhardt, A. Wander, B. Searle, N. Harrison and F. Illas. *Chemical Physics Letters*, **341**, 412, (2001).

[34] X.-G. Wang, A. Chaka and M. Scheffler, *Phys. Rev. Lett.*, **84**, 3650, (2000).

[35] R. di Felice and J. E. Northrup, *Phys. Rev. B*. **60**, 16287, (1999).

[36] I. G. Batirev, A. Alavi, M. Finnis and T. Deutsch, *Phys. Rev. Lett.*, **82**, 1510, (1999).

[37] M. Bankhead, *Ph.D. Thesis*, Liverpool University (2000).

[38] M. Baudin and K. Hermansson, *Surf. Sci.*, **474**, 107, (2001).

[39] J. M. McHale A. Auroux, A. Perrotta and A. Navrotsky, *Science*, **277**, 788, (1997).

[40] P. W. Tasker. 'Advances in Ceramics' in *Structure and Properties of MgO and Al$_2$O$_3$ Ceramics*, **Vol. 10**, p276, (1984).

[41] W. C. Mackrodt, *J. Chem. Soc., Faraday Trans. 2*, **85**, 541, (1989).

[42] I. Manassidis and M. J. Gillan, *J. Amer. Chem. Soc.*, **77**, 335, (1994).

[43] W. C. Mackrodt, *Phil. Trans. R. Soc. London A*. **341**, 301, (1992).

[44] J. Guo, D. F. Ellis and D. J. Lam, *Physical Review B*, **45 (23)** 13647, (1992).

[45] G. Della Gatta, B. Fubini and L. Stradella, *J. Phys. Chem.*, **66**, 72, (1976).

[46] B. A. Hendriksen, D. Pearce and R. Rudham, *J. Catal.*, **24**, 82, (1972).

[47] J. W. Elam, C. E. Nelson, M. Cameron, M. Tolbert and S. George, *J. Phys. Chem. B*, **102** 7008, (1998).

[48] S. Blonski and S. H. Garofalini, *J. Phys. Chem.*, **100**, 2201, (1996).

[49] C. E. Nelson, J. Elam, M. Tolbert and S. George, *Applied Surface Science*. **171**, 21, (2001).

[50] K. C. Hass, W. Schneider, A. Curioni and W. Andreoni, *J. Phys. Chem. B*, **104**, 5527, (2000).

[51] J. M. Wittbrodt, W. Hase and H. Schegel, *J. Phys. Chem. B*, **102** 6539, (1998).

[52] J. R. Scott, G. Groenewold, A. Gianotto, M. Benson and J. Wright, *J. Phys. Chem. A*, **104**, 7079, (2000).

[53] M. Digne, P. Sautet, P. Raybaud, P. Euzen and H. Toulhoat, *J. Catal.*, **211**, 1, (2002).

[54] A. Bendada, D. Boyle, L. McGhee, G. Webb and J. Winfield, *J. Fluor. Chem.*, **71**, 175, (1995).

[55] J. W. Elam, C. Nelson, M. Tolbert and S. George, *Surf. Sci.*, **450**, 64, (2000).

[56] G. -J. Kroes and D. C. Clary, *J. Phys. Chem.*, **96**, 7079, (1992).

[57] M. Lindblad and T. A. Pakkanen, *Surf. Sci.*, **286**, 333, (1993).

[58] M. Bankhead, G. Watson, G. Hutchings, J. Scott and D. Willock, *Appl. Catal. A: Gen.*, **200**, 263, (2000).

[59] J. D. Gale, *Faraday Diss.* **106**, 219, (1997).

[60] C. R. A. Catlow, R. G. Bell and J. D. Gale, *J. Mater. Chem.*, **4**, 781, (1994).

[61] P. Chupas, M. Ciraolo, J. Hanson and C. Grey, *J. Amer. Chem. Soc.*, **123**, 1694, (2001).

[62] S. Deshmukh, V. Kovalchuk, V. Borovkov and J. d'Itri, *J. Phys. Chem. B*, **104**, 1277, (2000).

[63] O. Boese, W. Unger, E. Kenmitz and S. Schroeder, *Phys. Chem. Chem. Phys.*, **4**, 2824, (2002).

[64] S. C. Parker, S. Kerisit, A. Marmier, S. Grigoleit and G. W. Watson, *Faraday Discussions*, **124**, 155, (2003).

[65] H. Knözinger and P. Ratnasamy, *Catal. Rev. Sci. Eng.*, **17**, 31, (1978).

[66] A. Tsyganenko and P. Mardilovich, *J. Chem. Soc., Faraday Trans.*, **92 (23)**, 484, (1996).

[67] A. Hess, E. Kenmitz, A. Lippitz, W. Unger and D.-H. Menz, *J. Catal.*, **148**, 270, (1994).

[68] A. Hess and E. Kemnitz, *J. Catal.*, **149**, 449, (1994).

[69] G. Sholz and R. Stosser, *J. Fluor. Chem.*, **86**, 131, (1997).

[70] C. H. Barclay, H. Bozorgzadeh, E. Kenmitz, M. Nickkho-Amiry, D. Ross, T. Skapin, J. Thomson, G. Webb and J. Winfield, *J. Chem. Soc. Dalton Trans.*, 40, (2002).

Chapter 2

2   Theoretical background.

2.1   Quantum mechanics.

2.1.1   The Schrödinger equation.

Programs based on quantum mechanics attempt to solve the Schrödinger equation to obtain properties such as electron density, via electron wavefunctions which themselves are solutions of the time independent Schrödinger equation:

$$\hat{H}\Psi(\mathbf{r},\mathbf{R}) = E\Psi(\mathbf{r},\mathbf{R})$$ Equation 2.1

Where $\hat{H}$ is the Hamiltonian operator, Ψ (**r**, **R**), is the total wavefunction, E, is the energy of the wavefunction, **r** the electron coordinates and **R** the nuclear coordinates. The Hamiltonian operator is the sum of kinetic and potential energy, $\hat{T}$ and $\hat{V}$ respectively, the total system Hamiltonian is:

$$\hat{H}(\mathbf{r},\mathbf{R}) = \hat{T}_n(\mathbf{R}) + \hat{T}_e(\mathbf{r}) + \hat{V}_{ne}(\mathbf{r},\mathbf{R}) + \hat{V}_{nn}(\mathbf{R}) + \hat{V}_{ee}(\mathbf{r})$$ Equation 2.2

Where $\hat{T}_n(\mathbf{R})$ and $\hat{T}_e(\mathbf{r})$ represent the kinetic energies for the nuclei and electrons respectively, defined by equations 2.3 and 2.4.

$$\hat{T}_n(\mathbf{R}) = \sum_{\alpha} - \frac{1}{2M_\alpha}\nabla^2{}_\alpha(\mathbf{R})$$ Equation 2.3

and

$$\hat{T}_e(\mathbf{r}) = \sum_{i}^{N} - \frac{1}{2}\nabla_i^2$$ Equation 2.4

With M_α the mass of the αth nucleus in the molecule and $\nabla^2{}_\alpha$ the corresponding Laplacian, defined as:

$$\nabla^2_\alpha = \left(\frac{\partial^2}{\partial x^2_\alpha} + \frac{\partial^2}{\partial y^2_\alpha} + \frac{\partial^2}{\partial z^2_\alpha} \right)$$

Equation 2.5

The last three terms in equation 2.2 represent the Coulombic interactions between nuclei: $\hat{V}_{nn}(\mathbf{R})$, electrons: $\hat{V}_{ee}(\mathbf{r})$ and between nuclei and electrons: $\hat{V}_{ne}(\mathbf{r},\mathbf{R})$, defined in equations 2.6, 2.7 and 2.8, where Z_α is the charge on nucleus α:

$$\hat{V}_{nn}(\mathbf{R}) = \sum_\alpha \sum_{\beta > \alpha} \frac{Z_\alpha Z_\beta}{|R_\alpha - R_\beta|}$$

Equation 2.6

$$V_{ee}(\mathbf{r}) = \sum_i^N \sum_{j>i}^N \frac{1}{|r_i - r_j|}$$

Equation 2.7

$$V_{ne}(\mathbf{r}) = \sum_\alpha^N \sum_i^N \frac{1}{|R_\alpha - r_j|}$$

Equation 2.8

However, the Schrödinger equation can only be solved exactly for one electron systems, for all other system, approximations have to be made. The first approximation generally adopted is to decouple the nuclear and electron motion via the Born-Oppenheimer approximation.

2.1.2. The Born-Oppenheimer approximation.

The Born-Oppenheimer approximation assumes that the electronic and nuclear degrees of freedom can be treated separately. This is valid due to the fact that electrons move faster than massive nuclei. The electronic wavefunctions are calculated assuming that the nuclei are stationary, therefore the electronic energy of a system is a function of only the electronic coordinates:

$$\hat{H}\Psi(\mathbf{r};\mathbf{R}) = E\Psi(\mathbf{r};\mathbf{R})$$

Equation 2.9

The semi-colon indicates that Ψ is a function of the electron coordinates at a particular set of nuclear coordinates. The solutions of equation 2.9 map out a series of points on the potential energy surface of the nuclear motion.

2.1.3 Molecular orbital approximation and Hartree-Fock approximation.

The total molecular electronic wavefunction, Ψ, may be written as the product of one-electron molecular orbitals, φ_i:

$$\Psi = \varphi_1\varphi_2\varphi_3.....\varphi_n \qquad \text{Equation 2.10}$$

This is a complex proposition, and often the molecular orbitals (MO's) are described as a linear combination of atomic orbitals (LCAO):

$$\varphi_i = \sum_k c_{ik}\chi_k \qquad \text{Equation 2.11}$$

Where i labels each MO, c_{ik}, are the coefficients of the AO's or in general the basis functions, χ_k, in the MO's, and k is an index whose range depends on the number of AO's used.

The variational principle states that an approximate wavefunction has an energy equal or above the exact energy, where the approximate wavefunction can be calculated by minimising the energy of the system:

$$E_e = \frac{\langle \Psi | \hat{H}_e | \Psi \rangle}{\langle \Psi | \Psi \rangle} \qquad \text{Equation 2.12}$$

As a normalised wavefunction has the property:

$$\langle \Psi | \Psi \rangle = 1 \qquad \text{Equation 2.13}$$

The electronic energy of the approximate wavefunction may be rewritten as:

$$E_e = \langle \Psi | \hat{H}_e | \Psi \rangle \qquad \text{Equation 2.14}$$

The total electron wavefunction is subject to the Pauli exclusion principle, stating that no two electrons may have the same set of quantum numbers in a system, and so is anti-symmetric – in that it must change sign with respect to electron interchange. This is achieved by constructing a wavefunction from Slater determinants:

$$\Psi_{SD} = \frac{1}{\sqrt{N!}} \begin{vmatrix} \varphi_1(1) & \varphi_2(1) & \dots & \varphi_n(1) \\ \varphi_1(2) & \varphi_2(2) & \dots & \varphi_n(2) \\ \vdots & \vdots & \ddots & \vdots \\ \varphi_n(N) & \varphi_n(N) & \dots & \varphi_n(N) \end{vmatrix}$$

Equation 2.15

Where N is the number of electrons and n is the number of spin orbitals. The full form of the wavefunction is calculated by the self consistent field equations, also known as Hartree-Fock equations:

$$\hat{H}^{SCF} \varphi_i = \varepsilon_i \varphi_i$$

Equation 2.16

Where $\hat{H}^{SCF}$ is:

$$\hat{H}^{SCF} = \left\{ H^N + \sum_j J_j - \sum_j{}' K_j \right\}$$

Equation 2.17

Where H^N is the Hamiltonia for all electrons in the system; J_j, the Coulombic inter-electron interaction and K_j, the exchange potential, are calculated from:

$$J_j \varphi_i(1) = \left(\int \varphi_j{}^2(2) \frac{1}{r_{12}} dv_2 \right) \varphi_i(1)$$

Equation 2.18

$$K_j \varphi_i(1) = \left(\int \varphi_j(1) \varphi_i(2) \frac{1}{r_{12}} dv_2 \right) \varphi_j(1)$$

Equation 2.19

The Hamiltonian, $\hat{H}$, contains the molecular wavefunctions, φ_i, the expansion considered in equation 2.11 must be calculated to arrive at c_{ik} values converge to a pre-defined tolerance, i.e. are self consistent. One method is by the introduction of basis sets

related to each atom type within the system, these are either Slater-Type atomic functions – STOs, or Gaussian-Type atomic functions – GTOs. GTOs are primarily used in Hartree-Fock calculations as all integrals can then be evaluated analytically, although behaviour of GTOs near the nucleus does not properly describe the wavefunction character and they fall off too rapidly far from the origin.

2.1.4   Electron correlation.

In the Hamiltonian described above, the only account taken of the interaction of electrons is the electrostatics averaged over the wavefunctions and the exchange energy. The movement of one electron due to another, the correlation, is ignored and is beyond the scope of the Hartree-Fock theory, but is estimated in density functional theory.

2.2   Density functional theory.

Density functional theory (DFT) is a method of obtaining the properties of a system in terms of the charge distribution rather than purely the electronic wavefunction. DFT is an increasingly popular method in computational chemistry, due to the relative efficiency compared to Hartree-Fock methods, particularly for the crystal systems used in this research. In 1964, the work of Hohenberg and Kohn determined that the electronic ground state, E, is uniquely determined by the electron density, $\rho(r)$, in their first theorem – the energy is a functional of the electron density:

$$E = E[\rho(r)]$$ Equation 2.20

The second Hohenberg-Kohn theorem put forward in 1965 provides the energy variational principle behind DFT, stating that for a trial density, ρ_{trial}, the energy functional yields an energy which is equal to or higher than the energy for the exact ground state electron density, $E[\rho]$:[1]

$$E[\rho_{trial}] \geq E[\rho]$$ Equation 2.21

This demonstrates that the electronic energy can be determined without having to include the Schrödinger equation, although it does not offer any means of calculating the density which is required for the Kohn-Sham theorem to be used as a rational computational scheme. To represent the electron density we can use the self consistent field methodology already available for Hartree-Fock calculations. This considers a system of N non-interacting electrons in a Kohn-Sham external potential, $v_s(r)$, rather than the actual nuclear potential, $v(r)$:

$$[-\frac{1}{2}\nabla^2 + v_s(\mathbf{r})]\phi_i = \varepsilon_i\phi_i \qquad \text{Equation 2.22}$$

Where the first term, $-\frac{1}{2}\nabla^2$, is the kinetic energy operator. Equation 2.22 determines the exact density of the interacting system by choosing an external potential which represents all electron-electron interactions. The density can then be calculated as a sum over densities of the occupied orbitals:

$$\rho(\mathbf{r}) = \sum_N |\phi_i|^2 \qquad \text{Equation 2.23}$$

This can then be used to calculate the functional energy $E[\rho(r)]$. The Kohn-Sham potential accounts for the electron – nuclear, $v(r)$, and electron – electron, $V_{Coul}(r)$, interactions, also accounting for the exchange and correlation effect, $v_{XC}(r)$:

$$v_s(\mathbf{r}) = v(\mathbf{r}) + V_{Coul}(\mathbf{r}) + v_{XC}(\mathbf{r}) \qquad \text{Equation 2.24}$$

In terms of the energy, equation 2.24 may be written:

$$E[\rho(\mathbf{r})] = T_s[\rho(\mathbf{r})] + V[\rho(\mathbf{r})] + V_{Coul}[\rho(\mathbf{r})] + E_{XC}[\rho(\mathbf{r})] \qquad \text{Equation 2.25}$$

where $T_s[\rho(\mathbf{r})]$ is the kinetic energy of the electrons, $V[\rho(\mathbf{r})]$ the attraction between the electron density $\rho(r)$ and the external potential $v(r)$, and $V_{Coul}[\rho(\mathbf{r})]$ the Coulomb repulsion within $\rho(r)$. The exchange-correlation energy, $E_{XC}[\rho(\mathbf{r})]$ accounts for the difference between the non-interacting system and the real system of interacting

electrons. Equation 2.25, the Kohn-Sham equation is solved self-consistently, in the same manner as Hartree-Fock calculations.

However, the exact exchange and correlation potential $V_{XC}(r)$ and energy functional $E_{XC}[\rho(r)]$ are not known and are subject to approximations, such as the local density approximation (LDA) and generalised gradient approximation (GGA). The LDA exchange correlation energy is taken from a homogeneous electron gas, and assumes that the density is locally a slowly varying functional:[2]

$$E_x^{LDA}[\rho] = -\frac{3}{4}\left(\frac{3}{\pi}\right)^{\frac{1}{3}}\rho(r)^{\frac{1}{3}}$$

Equation 2.26

In an extension of the LDA, the densities of the α and β spin electrons are calculated separately, and is known as the local spin density approximation, LSDA.

In non-uniform electron gases, the non-local approximation exchange and correlation energies depend not only on the electron density, but also on the gradient:

$$E_{xc}[\rho] \cong E_{xc}^{non-loc}[\rho, \nabla\rho] = E_x^{non-loc}[\rho, \nabla\rho] + E_C^{non-loc}[\rho, \nabla\rho]$$

Equation 2.27

This approach offers a significant improvement in the energy across the entire system. This method is embodied in the Perdew and Wang exchange functional PW91:[3]

$$\Delta\varepsilon_c^{PW91}[\rho] = \rho(H_0(t,r_s,\zeta) + H_1(t,r_s,\zeta))$$

Equation 2.28

Where:

$$H_0(t,r_s,\zeta) = b^{-1}f(\zeta)^3 \ln\left[1 + a\frac{t^2 + At^4}{1 + At^2 + A^2t^4}\right]$$

Equation 2.29

$$H_l(t,\mathbf{r_s},\zeta)=\left(\frac{16}{\pi}\right)^{\frac{l}{3}}(3\pi^2)^{\frac{l}{3}}[C(\rho)-c]f(\zeta)^3 t^2 e^{-\frac{dx^2}{f(\zeta)^2}}$$

Equation 2.30

$$f(\zeta)=\frac{1}{2}\left((1+\zeta)^{\frac{2}{3}}+(1-\zeta)^{\frac{2}{3}}\right)$$

Equation 2.31

$$x=\frac{|\nabla\rho|}{\rho^{\frac{4}{3}}}$$

Equation 2.32

$$t=\left(\frac{192}{\pi^2}\right)^{\frac{l}{6}}\frac{|\nabla\rho|}{2f(\zeta)\rho^{\frac{7}{6}}}$$

Equation 2.33

$$A=a\left[e^{-\frac{b x_c(r_s,\zeta)}{f(\zeta)^3}}-1\right]^{-1}$$

Equation 2.34

$$C(\rho)=\ell_1+\frac{\ell_2+\ell_3 r_s+\ell_4 r_s^2}{1+\ell_5 r_s+\ell_6 r_s^2+\ell_7 r_s^3}$$

Equation 2.35

With the a, b, c and ℓ_{1-7} parameters to be fitted.

2.3 Periodic density Functional Theory.

All the density functional theory calculations presented in this work make use of a periodic representation of the crystal, meaning that, from a relatively small number of atoms, the long range macroscopic properties of the crystal can be calculated. Although the numbers of atoms within surface slabs and adsorbate calculations is often less than two hundred, we still require a considerable computational effort for the calculation. Periodic DFT relies upon Bloch's Theorem.

2.3.1 Bloch's Theorem.

Bloch's theorem [4] states that, for a periodic solid, each electronic wavefunction can be written as the product of a wave-like part, $e^{ik\cdot r}$, and a cell-periodic part, $f_i(\mathbf{r})$:

$$\phi_j(r) = e^{ik\cdot r} f_j(r)$$

Equation 2.36

The cell-periodic part of the wavefunction, f_j ($\mathbf{r}$), can be expanded using a basis set consisting of a discrete set of plane waves, the wavevectors of which are reciprocal lattice vectors of the crystal:

$$f_j(r) = \sum_G c_{j,G} e^{iG\cdot r}$$

Equation 2.37

Where $\mathbf{G}$, the reciprocal lattice vectors, are defined by $\mathbf{G}\cdot a = 2\pi m$, where a is the lattice vector of the crystal, and m is an integer value. This leads to each electronic wavefunction being expressed as the sum of plane waves:

$$\phi_j(r) = \sum_G c_{k+G} e^{i(k+G)\cdot r}$$

Equation 2.38

2.3.2 Brillouin Zones

The wavevectors, k, can be used to construct a three-dimensional reciprocal space grid. At a given G value, the k-vectors can only take on a finite number of values defining the number of states in the band. The set of values are contained within a volume of reciprocal space known as the Brillouin Zone. The first Brillouin zone is defined by the set of points in reciprocal space that can be reached from the origin without crossing any Bragg plane (known as the Wigner-Seitz primitive cell of the reciprocal lattice). The second Brillouin zone is the set of points that can be reached from the first zone by crossing only one Bragg plane, and so on. In an arbitrary oblique two-dimensional array of reciprocal lattice points, connected to k=0 by vectors a*, b* and a* + b*, a region encloses a series of k-points that are closer to k=0 than any of the other two dimensional reciprocal lattice points. Figure 2.1 illustrates this region, defining the first

Brillouin zone. Any point in an outlying region of this k-space is equivalent with one inside the Brillouin zone.
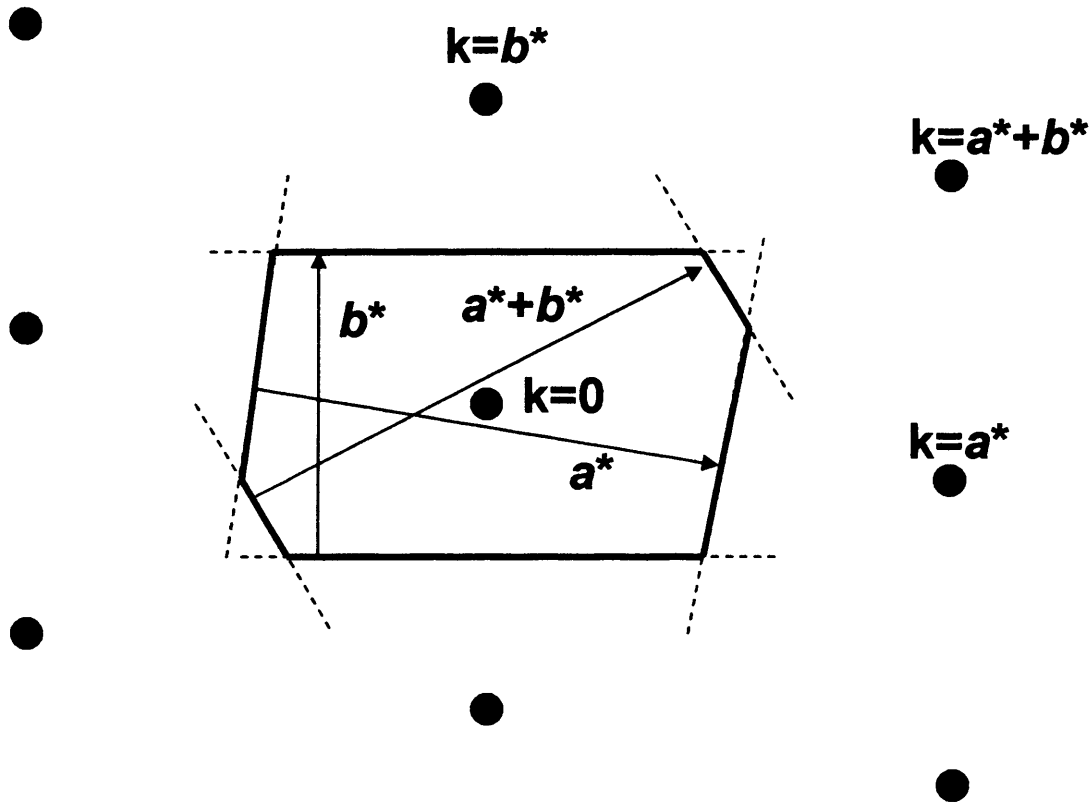
Figure 2.1. The definition of the first Brillouin zone in an arbitrary oblique reciprocal two-dimensional series of lattice points surrounding k=0, where k=a* is connected by a vector a*, k=b* by b* and k=a*+b* by a*+b*.

For the hexagonal space group of α-alumina, the Brillouin zone can be defined by the real space vectors a and b separated by 120°. In the reciprocal space lattice, the corresponding vectors a^* and b^* are perpendicular to a and b, and therefore have an angle of 60°. The first Brillouin zone is the hexagonal cell defined by the geometric construct shown in figure 2.2. This theory can be expanded and constructed for a three-dimensional lattice for a periodic system.

a   b
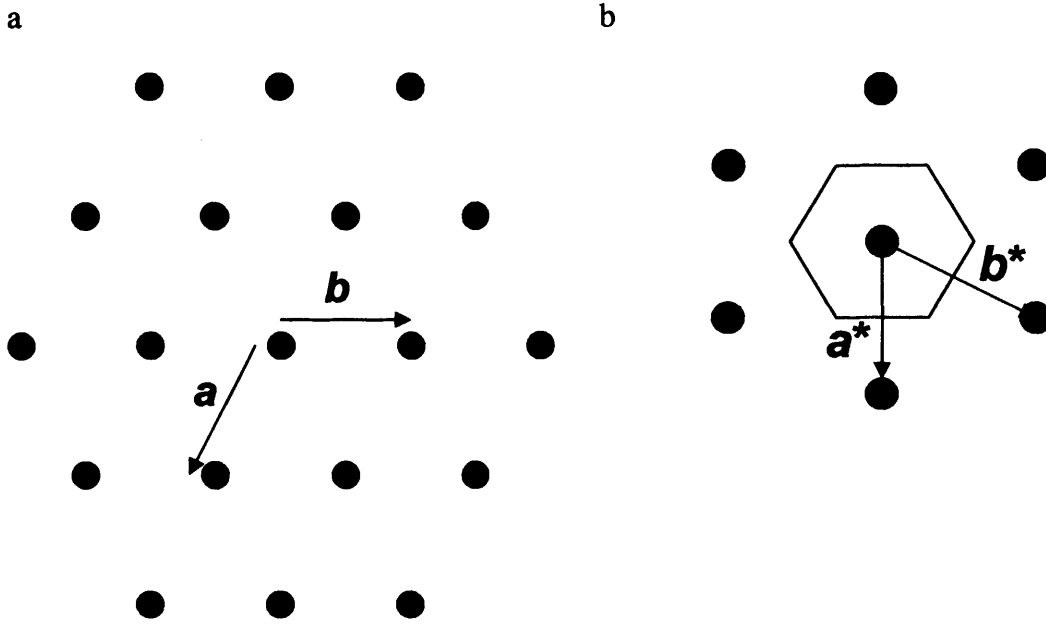
Figure 2.2. The real space two-dimensional hexagonal lattice points (a), with the vectors a and b, and the reciprocal space lattice points (b), showing the vectors a* and b*, and the hexagonal first Brillouin zone.

The Greek letter, Γ, is used to label the origin (where $k = 0$), which is the centre of the Brillouin zone. Directions within the first Brillouin zone are labelled as follows:

$$H = [0, 1, 0]2\pi/ a$$ Equation 2.39

$$P = [\frac{1}{2},\frac{1}{2},\frac{1}{2}]2\pi/ a$$ Equation 2.40

$$N = [\frac{1}{2},\frac{1}{2}, 0]2\pi/ a$$ Equation 2.41

For the band structure analysis, these directions are labelled, along with Γ.

2.3.3   k-point sampling.

The first Brillouin zone can be mapped out by a continuous set of points, called k-points, throughout the region of reciprocal space (k-space). The occupied states at each k-point contribute to the electronic potential of the bulk solid. The number of k-points is near infinite within the Brillouin zone at which the electronic wavefunctions must be calculated. However, since the energy is generally smoothly varying with respect to k we need only to calculate a finite number of electronic wavefunctions, and hence a smaller number of k-points. Hence, only a finite number of k-points are required to

calculate the electronic wavefunctions and therefore determine the total energy of the solid or surface slab.

Approximations to the electronic potential and the contribution to the total energy from filled electronic bands use sets of k-points in the Brillouin zone. Using only a small number of these k-points it is possible to accurately calculate the electronic potential and total energy of insulators such as the alumina systems calculated in this work. For a metal, these properties are more difficult to calculate as a dense set of k-points are needed to accurately define the Fermi surface.

The error in the total energy will be reduced if the number of k-points is increased so that a series of convergence tests should be carried out for any system calculated using a plane wave method by increasing the number of k-points until a workable compromise between accuracy and computational cost is achieved.

2.3.4   Plane-wave basis sets.

The electronic energy at each k-point can be explained by a plane-wave basis set according to Bloch's Theorem, however, a problem arises as an infinite number would be needed to explain an infinite number of k-points. This is overcome by the application of a cut-off energy, which controls the representation of the cell function via a Fourier transform. When more planewaves are used, the representation of the cell density is more accurate.

2.3.5   Pseudopotentials.

Periodic calculations may make use of an approach known as the effective core potential, or pseudopotential, to represent core electrons and reduce the computational cost. [5] [6] [7] Using a plane-wave basis set to encompass core electrons would impair efficiency as well as being inaccurate due to the complex rapid oscillations of electrons close to the massive nuclei, to account for these would need an unfeasibly large kinetic energy cut-off. Pseudopotentials represent these core electrons by effectively removing core electrons and replacing them and the ionic potential by a weak pseudopotential that

acts on pseudo wavefunctions rather than authentic wavefunctions, as illustrated in figure 2.3.
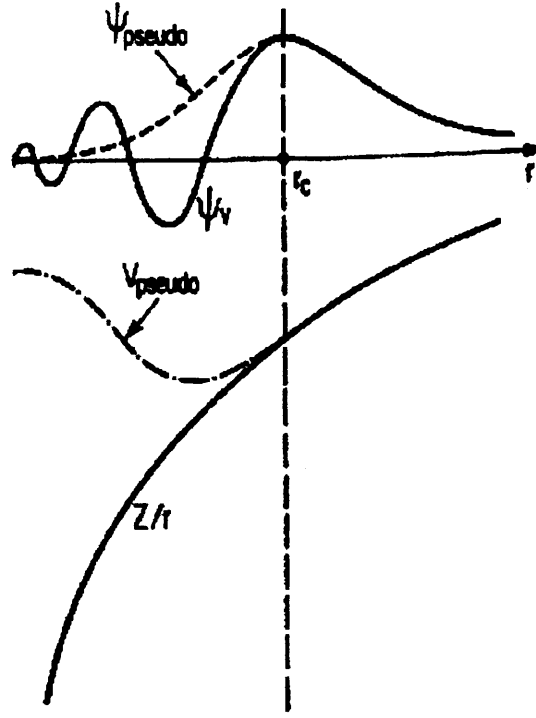
Figure 2.3. Schematic representation of a wavefunction with the all-electron wavefunction shown as a solid line, with and the dashed line representing the wavefunction with the pseudopotential. The radius at which they match is designated r_c. [8]

As figure 2.3 shows, the all-electron wavefunction oscillates rapidly in the core region due to the interaction of electrons with the massive positively charged nuclei. Outside of the core region, the pseudopotential matches exactly the all-electron wavefunction. The pseudopotentials used in this work follow the form:

$$V_{NL} = \sum_{lm} |lm\rangle V_l \langle lm|$$

Equation 2.42

where, $|lm\rangle$, are the spherical harmonics, and V_l, is the pseudopotential for the angular momentum, l. Within this research, the approach of Vanderbilt in modifying the pseudopotential for plane-wave simulations was used, in which a low kinetic energy cut-off is employed with the wavefunction being expanded using a small plane-wave basis set whilst ensuring the phase remains correct for the wavefunction in the core region.

2.3.6 Density of states and band structure.

The density of states, $G(E)$, denotes the number of electron states per energy increment, for a free electron model:

$$G(E) = \frac{V}{2\pi^2} \cdot \left(\frac{2m}{\hbar^2}\right)^{\frac{3}{2}} \cdot E^{\frac{1}{2}} \equiv \frac{\delta N}{\delta E}$$

Equation 2.43

Where N is the number of free electrons, E is the energy, V is the volume of the system and m is the electron mass. Real systems are more complex than the free electron model, as such the density of states requires intensive calculations. The total density of states for the α-alumina bulk structure is shown in figure 1.3a and can be separated into partial density of states to represent the contribution from the aluminium $3p$ and $3s$, and oxygen $2p$ and $2s$ orbital components as in figure 1.3b-e.

The band structure is related to the Brillouin zone determination for a crystal, where the band structure is the plot of the energy variation with wave-vector for the directions in the Brillouin zone; shown in equations 2.39, 2.40 and 2.41. Figures 1.2a and 1.2b show the band structure for two sub-units of the α-alumina bulk crystal. Near Γ, the centre point of the Brillouin zone, the nearly free electron character is seen, but as the k-vector approaches the special points within the Brillouin zone there are stronger electron-nuclear interactions which cause deviations from free-electron behaviour. As can be seen in these two figures, the band gap between the valence band and the conduction band defines the alumina system as an insulator.

Across the Brillouin zone, using the irreducible k-points grid gives the electronic orbital band energies, which fall into the upper and lower valence bands for the oxygen $2p$ and $2s$ orbitals respectively, and conduction band representing mainly the aluminium $3p_{x,y}$ orbitals. Figure 2.4 shows the band structure for the α-alumina {0001} surface taken from the calculations of Ciraci and Batra.[9] There are three clearly defined bands. The concentration of states at a particular band energy results in the density of states for each band; this is shown projected onto the side of the band structure in figure 2.4. For example, the band structure at the upper valence band maximum is known to be tightly

concentrated across a short range having a flat dispersion relation. This leads to a sharp high intensity peak, as is seen in the adjacent density of states. Likewise, the strongly dispersed band at the upper valence band minimum in this example has a related density of states of intermediate intensity peaks. Where there are no electron bands, there are no corresponding density of states peaks, as shown by the minimal peaks at the lower valence band minima.

All of the density of states plots shown in chapter five exhibit the behaviour of an insulator, where the upper and lower valence bands are filled and clearly defined. The conduction band is not calculated as part of the CASTEP density of states, although this is present above the upper valence band. However, this analysis of predicting the band structure from the density of states does not give any indication of where the minima and maxima of the two bands are in the Brillouin zone. The presence of the terminating aluminium atoms in the {0001} α-alumina surface gives an enhancement of the conduction band minima, shown as a darkened area in figure 2.4, due to the contribution of the dominant aluminium character of this surface. This effect cannot be seen with the current CASTEP density of states, although this effect is well known and can be applied to these calculations.
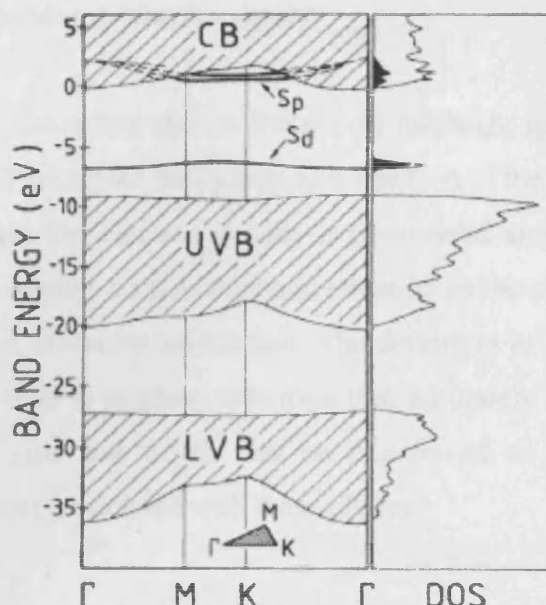
Figure 2.4. The calculated electronic band structure across the Brillouin zone of an α-alumina {0001} surface, showing the upper and lower valence bands with the predominantly aluminium orbital based conduction band. The relationship to the density of states plot is shown attached to the right of the band structure. S_d and S_p refer to surface aluminium states, giving the shaded area in the conduction band.[9]

2.4 Molecular mechanics.

In this section, the theory behind *atomistic* methods of computational chemistry is described. This method seeks to describe the energy of a system based purely on functions of the atomic coordinates.

In general, the *ab initio* and *atomistic* techniques are differentiated by the way individual atoms are dealt with: DFT deals with the electron density and constructing crystal orbitals allowing application to oxide surfaces. GULP (the atomistic code used for molecular mechanics simulations described in detail in chapter three) ignores the individual electron contributions and concentrates on the electrostatic attractions and repulsions between the atomic 'cores' – characterising the positive nuclear positions and the 'shells' – signifying negative valence electrons.

2.4.1 Empirical molecular mechanics theory.

Molecular mechanics, described also as force field methods, ignores electronic motion to calculate the overall energy of the system as a function of the nuclear positions and to generate structural data. No electron density is considered and so no information that relies on the electron density, such as the band structure or the density of electron states, can be generated by an *atomistic* calculation. The definition of molecular mechanics as an empirical method aims to produce potentials that accurately model, for example, the α-alumina bulk structure and which can be transferred to model further alumina polymorphs and surfaces associated with these phases.

Minimisation of the intra and inter molecular forces is achieved with reference to empirical equations giving an energy in terms of bond angles and lengths for intra-molecular contributions along with non-bonding atomic interactions, for example aluminium to aluminium and oxygen to oxygen interactions over long distances. These non-bonded terms are typically described by a Coulomb potential for the electrostatic interactions and Lennard-Jones potentials for the Van der Waals interactions. The Buckingham potential can also be used to represent non-bonding interactions in place of Lennard-Jones.

2.4.2 Bonding potentials.

The potential energy description of a diatomic molecule is the energy as a function of the interatomic separation which is shown schematically in figure 2.5.
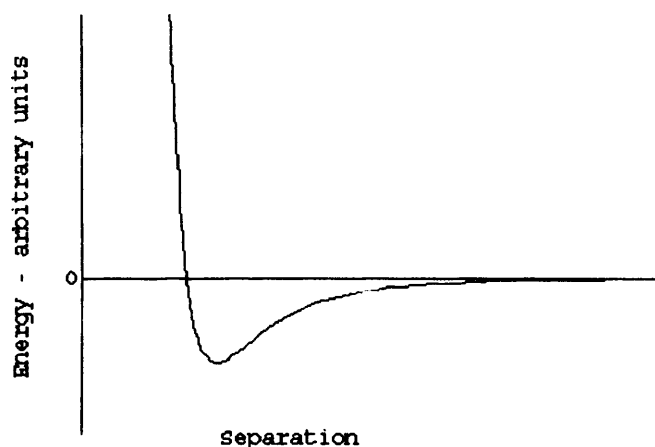
Figure 2.5. The bond energy as a function of interatomic separation for a covalent bond.

The Morse potential is used in this work to model this curve, this has the form:[10]

$$v(l) = D_e\{1 - \exp[-a(l - l_0)]\}^2$$

Equation 2.44

Where the equilibrium bond length is l_0, D_e is the depth of the potential energy minimum, $a = \omega\sqrt{(\mu/2D_e)}$ where μ is the reduced mass and ω is the frequency of the natural vibration of the bond. In the harmonic approximation the frequency is related to the stretching constant of the bond, k, by $\omega = \sqrt{(k/\mu)}$ and near to l_0 the two potentials agree. The Morse potential is useful in catalytic systems due to its ability to represent the energy over a range of bond distances.

A simple harmonic function as defined by Hooke's law provides a suitable potential energy minimum, however at separations other than equilibrium it is not accurate enough to model bond stretching. To improve the curve, cubic and quadratic terms can be incorporated as in equation 2.45. The drawback of using a cubic term is that it passes through a maximum at $l_0 > l$, but provides a more realistic approximation than the quadratic form at values near l_0. This can be overcome by using a quartic term, however this has an impact on the computational efficiency and the number of parameters required by the potential.

$$v(l) = \frac{k}{2}(l - l_0)^2[1 - k'(l - l_0) - k''(l - l_0)^2 - k'''(l - l_0)^3 ...]$$

Equation 2.45

The hybridisation of atomic orbitals at atomic centres leads to directional bonds Therefore, angle bending modes are included in the potentials. Using the harmonic Hooke's law, relating the energy $v(\theta)$ is related to the bond angle θ:[11]

$$v(\theta) = \frac{k}{2}(\theta - \theta_0)^2$$

Equation 2.46

θ_0 is the minimum energy angle. The energy required to effect a distortion in the bond angle is less than for a stretching or a compression of a bond, and so the force constants are proportionally lower. As with bond stretching, the accuracy can be improved by including higher order terms:

$$v(\theta) = \frac{k}{2}(\theta - \theta_0)^2[1 - k'(\theta - \theta_0) - k''(\theta - \theta_0)^2 - k'''(\theta - \theta_0)^3 ...]$$

Equation 2.47

2.4.3 Electrostatic interactions.

The electrostatic interaction is calculated as the sum of interactions between pairs of point charges, using Coulomb's law:

$$V = \sum_{i=1}^{N_A}\sum_{j=1}^{N_B} \frac{q_i q_j}{4\pi\varepsilon_0 r_{ij}}$$

Equation 2.48

Where N_A and N_B are the numbers of point charges in the molecule, q_i and q_j are the charges, ε_o is the permativity of free space and r_{ij} is the separation of these two particles. In periodic systems the convergence of this sum depends on the cut-off method used to include centres. This is usually avoided by the use of the Ewald sum, discussed in section 2.4.5.

2.4.4 Van der Waals interactions

The intra-molecular forcefield terms discussed so far are relevant to bonds in which there is a high degree of covalency. In ionic bonds and for interactions between molecules Van der Waals forces must also be accounted for. For example, to account

for the non-bonding aspect of the largely ionic bonding in alumina crystals, we require interactions of aluminium to oxygen and oxygen to oxygen. For such a situation, the interaction energy is zero at infinite separation, when the interatomic distance is reduced, the energy decreases, passing through a minimum dependant on the atomic species and then increases rapidly as the separation decreases further. This arises due to a balance between the attractive dispersive and repulsive forces, allowing lattice energy to be estimated. As harmonic bond potentials are zero-referenced, so that, at $l = l_0$ the lattice energy is zero and they are not suitable functional forms. However, Buckingham and Lennard-Jones potentials have zero at infinity so the lattice energy can be estimated.

The attractive dispersive term operates over long ranges and can be thought of as the interaction between molecular electron densities as they undergo random fluctuations. This model allows empirical equations to be derived to estimate the order of magnitude of the interaction. Reducing the separation between two polarisable species causes dipolar interactions, leading to the interaction energy, $v(r)$ of a pair of polarisable dipoles interacting through mutual polarisation, the classical mechanical equation:

$$v(r) = -\frac{\alpha^4 \hbar \omega}{2(4\pi\varepsilon_0)^2 r^6}$$

Equation 2.49

and so:

$$v(r) = \frac{C}{r^6}$$

Equation 2.50

Where ω is related to the force constant by $\omega = \sqrt{(k/m)}$ α is the polarisability of the molecule. Equation 2.50 determines that the attractive dispersive term varies as $1/r^6$, and can be expanded as in equation 2.51. All the C co-efficients are negative, giving attractive interactions:

$$v(r) = \frac{C_6}{r^6} + \frac{C_8}{r^8} + \frac{C_{10}}{r^{10}} + \ldots\ldots$$

Equation 2.51

However, if just an attractive dispersive term is included in a non-bonding potential, the energy will not fully represent the system as even a small decrease in the separation

causes a large increase in the energy as the energy goes to $-\infty$ as r approaches zero. The Pauli Exclusion Principle dictates that two electrons may not have the same quantum numbers in a system. This results in a repulsive term which occurs over a short range due to forbidding two electrons of the same spin in the same orbital. This leads to the repulsive part of the Buckingham and Lennard-Jones potentials. These are used in this work to incorporate both attractive dispersive and repulsive terms. The Lennard-Jones form is shown in equation 2.52, containing only two parameters, σ, the separation where energy is zero and the potential well depth ε. Graphically, the Lennard-Jones 12-6 (on account of the powers by which the parameters are raised) is illustrated in figure 2.6 showing the significance of the parameters:[12]

$$v(r) = 4\varepsilon\left[\left(\frac{\sigma}{r}\right)^{12} - \left(\frac{\sigma}{r}\right)^{6}\right]$$

Equation 2.52
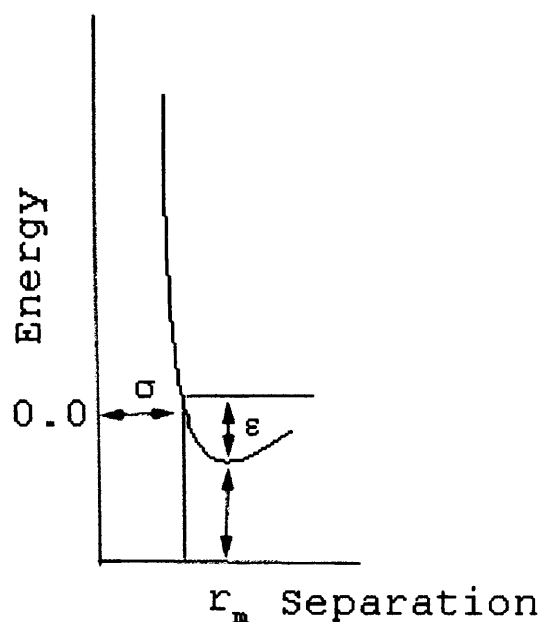
Figure 2.6. Description of the Lennard-Jones potential, showing the potential well depth, ε and the collision parameter were energy is zero, σ.

Figure 2.6 illustrates that the Lennard-Jones potential may also be constructed from parameters based on the separation at which the energy passes through r_m, the energy minimum. The Lennard-Jones potential is then written as:

$$v(r) = \varepsilon\{(r_m / r)^{12} - 2(r_m / r)^6\} \qquad\qquad \text{Equation 2.53}$$

Or alternatively the Lennard-Jones potential may be in the format shown in equation 2.54, where A and C are the parameters input into the GULP program as described in chapter three.

$$v(r) = A/r^{12} - C/r^6 \qquad\qquad \text{Equation 2.54}$$

Where the repulsive part is $A = \varepsilon r_m^{12}$ (or $4\varepsilon\sigma^{12}$) and the dispersive attractive part is $C = 2\varepsilon r_m^6$ (or $4\varepsilon\sigma^6$). More general forms of the Lennard-Jones potential exist, formulated from equation 2.55, amongst the common formats are Lennard-Jones 9 6, where $A = \varepsilon r_m^9$ and $C = 2\varepsilon r_m^6$, where, for example, m = 6 and n = 9:

$$v(r) = \varepsilon\left[\frac{m}{n-m}\left(\frac{r_m}{r}\right)^n - \frac{n}{n-m}\left(\frac{r_m}{r}\right)^m\right] \qquad\qquad \text{Equation 2.55}$$

As the overlap of charge densities as molecules approach is an exponential function, the Lennard-Jones potential uses a higher power for the repulsive term compared to the exponential function in the Buckingham potential:[13]

$$v(r) = \varepsilon\left[\frac{6}{\alpha-6}e^{-\alpha\left(\frac{r}{r_m}-1\right)} - \frac{\alpha}{\alpha-6}\left(\frac{r_m}{r}\right)^6\right] \qquad\qquad \text{Equation 2.56}$$

To allow the use of a Buckingham potential, the three parameters ε, r_m and α must be specified, another drawback of using the Buckingham is that at short ranges the potential becomes strongly attractive. Such a situation may lead to fused nuclei, a particular problem for molecular dynamics simulations, although the molecular mechanics program GULP overcomes this problem by the option to specify r_0, the minimum interaction distance cut-off.

2.4.5. The Ewald summation.

The Ewald summation is a method for summing all long-range electrostatic interactions to an arbitrary accuracy within a periodic system.[14] With the Ewald summation, all of the particles interact with one another in the periodic box and every image box. The position of each periodic image box is related to the central box by a vector, the components of which are an integer multiple of the length of the box. The charge-charge contribution to the potential energy due to all pairs of charges in the central simulation box is:

$$V = \frac{1}{2}\sum_{i=1}^{N}\sum_{j=1}^{N}\sum_{|n|=0}^{\infty}\frac{q_i q_j}{4\pi\varepsilon_o r_{ij}}$$

Equation 2.57

Where i and j represent the atoms within a pair, q denote the charges on atoms i and j V represents the total electrostatic energy which is comprised of atom j in the 'original' box and the images of atom i. The summation in equation 2.57 contains both positive and negative terms which form a series which is infinite. The Ewald summation separates these charges series into two summations: the real space part which includes an opposite charge in the form of a gaussian distribution of equal magnitude to each charge in the real system. This allows the summation to be carried out efficiently. The second sum is simply the reverse gaussian charge set, used to remove the effect of the artificial set of gaussians required in real space. The second sum can be efficiently evaluated in reciprocal space.

In the two Ewald summation series, the initial set of charges are surrounded by a Gaussian distribution, calculated in real space, to which a cancelling Gaussian charge distribution is added, itself calculated in reciprocal space, as in figure 2.7. These two series in the Ewald summation converge more rapidly and is the most 'correct' way to include all the effects of long-range forces into a simulation.[15]
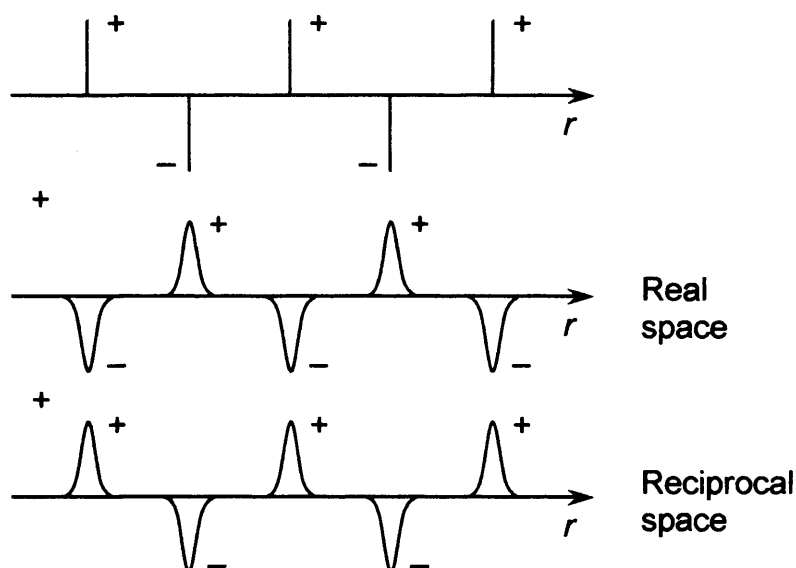
Figure 2.7. The real space Gaussian distribution of the charge around the initial charges, cancelled by the reciprocal Gaussian charge distribution. Together, these give the Ewald summation.[15]

[1] Kohn, W., and Sham, L. J., *Phys. Rev.* **140**, A1133 (1965).

[2] Dirac, P. A. M., Proc. Cambridge Phil. Soc. **26**, 376 (1930).

[3] J. P. Perdew and Y. Wang, *Phys Rev. B.* **1992**, 45, 13244.

[4] Ashcroft, N. W., and Mermin, N. D., Solid State Physics. *Holt, Rinehart and Winston* (1976).

[5] M. L. Cohen and V. Heine, *Solid State Physics,* **24**, 37, (1970).

[6] J. C. Phillips, *Phys. Rev.,* **112**, 685, (1958).

[7] M. T. Yin and M. C. Cohen, *Phys. Rev. B,* **25**, 7403, (1982).

[8] Payne, M. C., Teter, M. P., Allan, D. C., Arias, T. A., and Joannopoulos, J. D., *Rev. Mod. Phys.* **64**, 1045 (1992).

[9] S. Ciraci and I. P. Batra, *Phys. Rev. B,* **28 (2)**, 982, (1983).

[10] Morse, P. M., *Phys. Rev.* **34**, 57 (1929).

[11] Allen, M. P., and Tildesley, D. J., Computer Simulation of Liquids. *Oxford Science Publications* (1990).

[12] Lennard-Jones, J. E., *Proc. R. Soc. London, Ser. A.* **106**, 463 (1924).

[13] Jensen, F., Introduction to Computational Chemistry. *Wiley* (1999).

[14] Ewald, P., *Ann. Phys.* **64**, 253 (1921).

[15] A. R. Leach. *Molecular modelling, principles and applications. 1996.*

Chapter 3

3   Methodology

In this chapter, the principles behind theoretical techniques applied to metal oxide and catalytic computational chemistry are explained. This is followed by the background to the General Utilities Lattice Program (GULP), Cambridge Serial Total Energy Package (CASTEP), Gaussian 98 and Shiftcell codes used within this research. All molecular mechanics simulations were carried out on the Cardiff computational chemistry group's DEC Alpha (EV5s) and Linux machines. Periodic density functional calculations were carried out on *Glyndŵr*, a multiprocessor Silicon Graphics Origin 2000 funded by OCF, *Zebedee*, a single node Silicon Graphics Power Challenge 10000, *Mott*, a jointly owned multiprocessor machine at the Rutherford Appleton laboratories in Oxfordshire and recently, *Helix*, a Beowulf cluster jointly administered and funded by the schools of Chemistry, Biology and Earth Sciences at Cardiff University. File setup and analysis was undertaken using *Beddgelert*, a Silicon Graphics machine running Cerius^2 with built-in interfaces to GULP and CASTEP.

3.1   Introduction to theoretical techniques

Theoretical chemistry can be separated broadly into two categories to find the potential energy surface of a system: quantum mechanics and molecular mechanics. Quantum mechanics is concerned with finding an approximate solution to the Schrödinger equation. This allows calculation of properties such as electron density using, for example, density functional theory. In such a first principles approach, no information other than the Cartesian coordinates of the structure, basis sets and pseudopotentials need to be specified. Molecular mechanics uses parameterised force field functions and the atom co-ordinates to calculate energies and forces for the atoms without attempting to solve the Schrödinger equation. These parameters are obtained from fitting to experimental and/or *ab initio* data at specific minimum energy configurations. Any application of these potentials away from these points can lead to inaccuracies.

Two methods for sampling the potential energy surface are geometric optimisation and molecular dynamics. Geometric optimisations aim to find energetic minima and

transition states. Molecular dynamics applies Newton's laws to calculate the motion of atoms within the system in all directions.

Fundamentally, the choice between the two methods is a compromise on either speed or accuracy. The main benefit of potential based calculations is the speed at which structural information may be obtained. This is at the expense of electronic properties since there is no consideration of electron density within the calculation. *Ab initio* calculations are computationally more expensive, often requiring large parallel computers, due to the calculation of the electronic density at each atomic position. As accurate electronic information results from these methods, they are useful in materials chemistry where chemisorption, physisorption and catalytic processes on surfaces can be studied.

For the calculation of crystals, material structures and surfaces, periodic boundary conditions are used to model the long range order, in this study a 2×2 supercell of the real unit cell was used to allow adsorbates to fit on the surface. Two dimensional models such as METADISE (Minimum Energy Techniques Applied to Dislocation of Interfaces and Surfaces) [1] calculate two regions based on a method developed by Tasker, [2] although this program was not used in this research. The surface region I where the atomic co-ordinates are optimised and region II which is held fixed at bulk structure determined using the same method as the surface simulation. Fully three dimensional programs such as GULP (General Utilities Lattice Program) [3] simulate both the bulk and terminating surface within a periodic box also containing a vacuum gap, representing an infinite array of such crystals.

3.2   Simulating surface catalytic processes.

Solid alumina catalysts can be easily separated from reaction mixtures for reuse, which is problematical for soluble aluminium compound catalysts. Experimentally, Lewis acidity is often generated by the dehydroxylation, via calcination, of surface hydroxyl groups to leave co-ordinatively unsaturated aluminium ions. For α-Al_2O_3, these will be created from octahedral aluminium, whereas in θ-Al_2O_3 both tetrahedral and octahedral unsaturated aluminium sites may be found. Experimentally, the interaction of a single

adsorbate with a surface is difficult to monitor, with many experimental techniques, such as XPS, an average of many adsorbates may dominate the signal.

To effectively simulate catalytic processes, the model system must be as accurate as possible, and an appropriate technique employed to arrive at a suitable description of the catalyst activity. To create a supercell slab large enough to accommodate the addition of adsorbates, the surface and vacuum gap are expanded by an integer value in the a and b direction, then periodic boundary conditions applied to this larger system. Figure 3.1 illustrates this method. The crystal slab contains two equivalent surfaces according to Miller indices, one at the bottom of the unitcell, and the other at the interface of the slab structure and the vacuum gap. Figure 3.2 illustrates the basic principle behind this for the {0001} α-Al_2O_3 surface. As stated in section 1.2.4, the stable surfaces for metal oxides are likely to be of low Miller index and atomically dense, which result in a compact even surface with few, if any, defects. Simulations of catalytic reactions can determine alternative well defined surfaces that are likely to be catalytically active, for example, in the aluminium oxide surfaces investigated in this research, the presence of Lewis acid aluminium sites is known to be significant for adsorption of molecules such as chlorofluorocarbons.
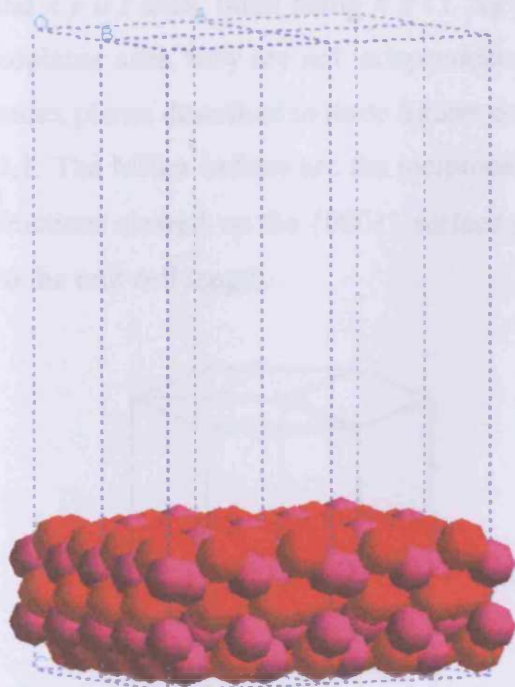
Figure 3.1. 2×2 cell with internal periodic boundary conditions remaining, these are removed to create a supercell with the external boundaries as the periodic repeat unit.
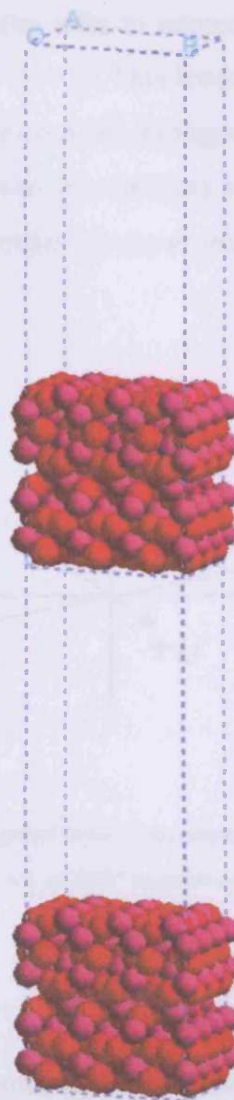
Figure 3.2. Representation of periodicity in the c direction in the α-Al₂O₃ {0001} surface. Both surfaces are identical and can interact with an adsorbate in the vacuum gap.

3.3 Hexagonal systems surface description.

The α-Al$_2$O$_3$ crystal is a hexagonal system constructed of three 60° rhombohedra as shown in figure 3.3. The vertical prism edge of each rhombus forms the z axis, normal to this are the x and y directions making an angle of 120° with each other. There are three distinct possibilities for the x and y directions, all of which are equally significant. Therefore hexagonal unit cells incorporate four axes, x, y and u at 120° to each other, normal to the vertical z axis. Each index symbol contains four figures corresponding to

the $x\ y\ u\ z$ axes, these being $h\ k\ i\ l$. As the first three refer to intercepts on three fixed coplanar axes, they are not independent and $h + k + i = 0$. This leads to the low Miller index planes described in three figures describing the α-Al_2O_3 hexagonal system in table 3.1. The Miller indices are the reciprocals of the intercept numbers in parentheses with fractions cleared, so the $\{0001\}$ surface plane intercepts $x\ y\ u\ z$ at (∞,∞,∞, 1) in respect to the unit cell length.
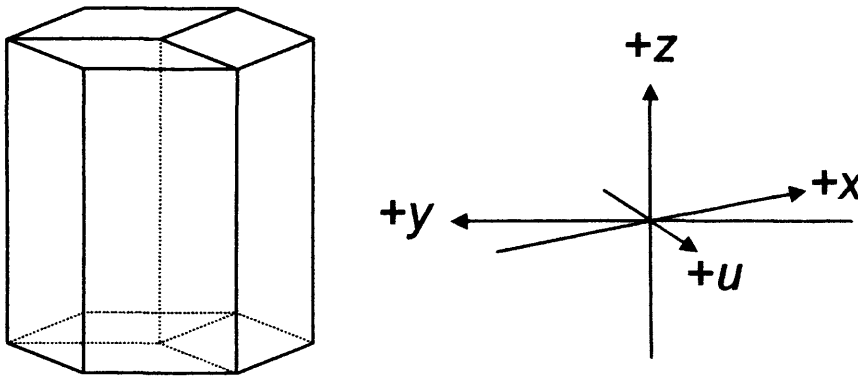
Figure 3.3. The three rhombohedra structural units of a hexagonal crystal accompanied by the hexagonal system Miller-Bravais crystallographic axes. $+x$, $+y$ and $+u$ are at $120°$ to each other and normal to the vertical z axis.

Three figure Miller index (xyz)	Four figure Miller-Bravais index for hexagonal crystals ($xyuz$)
001	0001
011	$01\bar{1}1$
010	$01\bar{1}0$
100	$10\bar{1}0$
101	$10\bar{1}1$
110	$11\bar{2}0$
111	$11\bar{2}1$

Table 3.1. The three-figure Miller indices for low index surfaces and the corresponding Miller-Bravais four figure indices for hexagonal space group crystals.

3.4 Metal oxide surfaces.

Tasker [4] defined metal oxide surfaces as falling into three categories: type I, type II and type III, depending on where the dipole moment falls in relation to the surface. A condition for calculating the surface energy is that there no dipole perpendicular to the surface in the repeat unit, as such a dipole leads to a divergent surface energy.[5] Figure 3.4 illustrates the principle behind a type I surface, in this case a magnesium oxide MgO {100} surface, in which a dipole exists both horizontally between the magnesium and oxygen atoms in a layer along the surface, but also between layers, where magnesium and oxygen alternate. For this slab, the dipoles cancel each other out, resulting in no net dipole either across or perpendicular to the surface. Type I metal oxides in general conform to M_xO_x.

Type II surfaces are also stable, but generally exist for metal oxides following the formula M_xO_y, (where $x \neq y$) such as alumina, where the bulk structure and surfaces are more complex than for type I. For the basal plane of α-alumina, {0001}, the stable surface configuration is constructed of four aluminium atoms with six oxygen atoms to retain stoichiometry, three of these slabs construct the {0001} surface, shown in figure 3.5, with dipoles superimposed upon the atoms. Both of the type I and II surfaces exist with no net dipole perpendicular to the surface. As such, the α-alumina {0001} surface is electrostatically stable.

Stoichiometry of a surface slab is no guarantee of a metal oxide surface being stable, this is typified by type III surfaces, which possess a dipole replicated across the surface slab geometry. Type III surfaces are not stable in this form, but may be stabilised by either a chemical reconstruction within the slab, or the adsorption of a chemical onto the surface to negate the dipole. Figure 3.6 illustrates the type III magnesium oxide {111} surface, showing that the same crystal can have both stable and unstable surfaces, as the {100} surface of MgO is a type I surface.
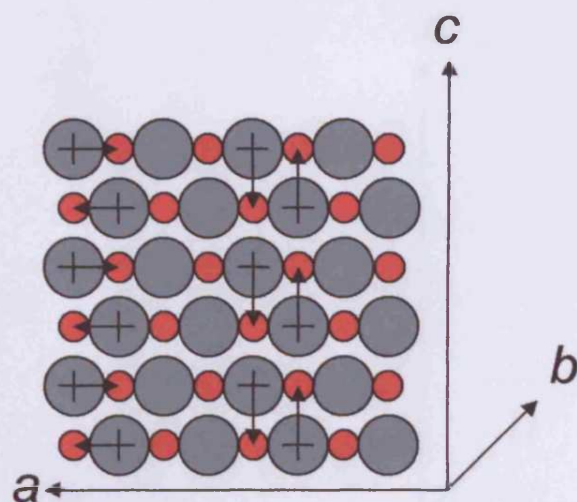
Figure 3.4. A periodic representation of the MgO {100} surface, where the grey filled circles represent magnesium and the red filled circles signify oxygen. The black arrows superimposed on the atoms signify dipoles.
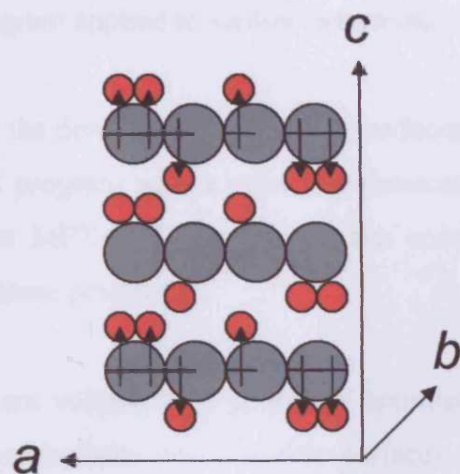
Figure 3.5. The {0001} surface of α-alumina, where the grey circles represent aluminium and the oxygen are red circles. The dipoles are superimposed upon both of the surface slabs to illustrate zero net dipole perpendicular to the surface.
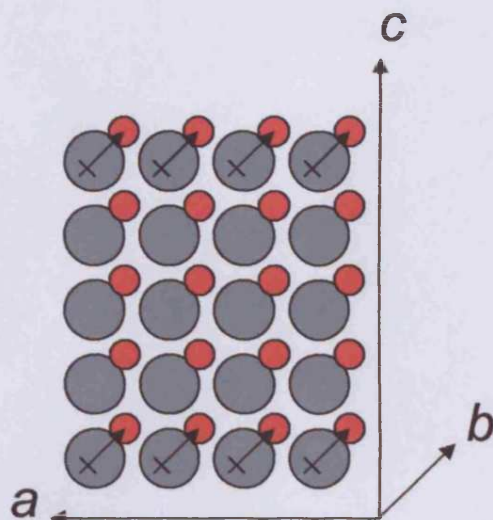
Figure 3.6. Illustration of the type III magnesium oxide {111} surface, with magnesium represented by grey circles and oxygen by red. The dipole is inclined from the surface, but over the stoichiometric slab cannot be cancelled out and therefore the surface is unstable.

3.5   The Shiftcell program applied to surface determination.

Shiftcell was written for the determination of stable surfaces from a bulk optimisation using the DELTAPOCS program with a prior two dimensional surface optimisation being carried out in the METADISE program,[1] the coordinates being seamlessly transferred between the three programs.

The outputs from constant volume bulk geometry optimisations in both GULP and CASTEP results in crystals from which stable surfaces may be established. The Shiftcell program analyses the Cartesian coordinates of the bulk optimisation based on the Miller index planes, to define all surfaces of type I or II, along with the distance from the cell origin to cut the Miller index surface. The procedure for creating a stable surface in Shiftcell relies on the dipole moment perpendicular to the surface falling below the threshold tolerance specified in the program, nominally as close to zero as possible.

Table 3.2 shows part of the format of a Shiftcell output file, for the {0001} surface of the bulk cell optimisation of α-alumina using GULP. The Miller index is detailed with

the repeat distance (rptdsi), in this case the c vector. Out of this crystal repeat distance, the *Shift* tag represents the percentages that should be taken to create a surface. For example, the *Shift* 0.8242 also must be taken with the 0.1576 shift to make two equivalent surfaces out of the total repeat distance. This first step is diagrammatically shown in figure 3.7, where the repeat distance is shown as the full length of the c vector, 12.681 Å from the GULP calculation. The blue segment at 82.42 % and 15.76 % of the repeat distance c shows the two resultant surfaces constructed from this method in the plane ab.

From this information, the Cerius^2 interface is used to construct the surface from the bulk structure and add a vacuum gap to the surface, figure 3.8 illustrates the principle of how a vacuum gap is incorporated onto a surface for a constant volume optimisation.

```
(  0,  0,  1) ->        0.000000000000000   -0.000000000000000
1.000000000000000
rptdsi = 12.680999999999999
Shift =  -0.009048585127356 (+/-  0.026930003627474)
Dipole =  -0.00000224399999
Shift =   0.157616414281208 (+/-  0.026924998777699)
Dipole =  -0.00000224400000
Shift =   0.324286427450517 (+/-  0.026925008161817)
Dipole =  -0.00000224399999
Shift =   0.490951420747575 (+/-  0.026929999881713)
Dipole =  -0.00000224399998
Shift =   0.657616442236417 (+/-  0.026924998738270)
Dipole =  -0.00000224399999
Shift =   0.824286389677470 (+/-  0.026924998777699)
Dipole =  -0.00000224399999
```

Table 3.2. An example of the α-Al_2O_3 {0001} Shiftcell output, detailing the Miller index, the repeat distance, and the shift as a percentage of the repeat distance to find stable surfaces with no net dipole.
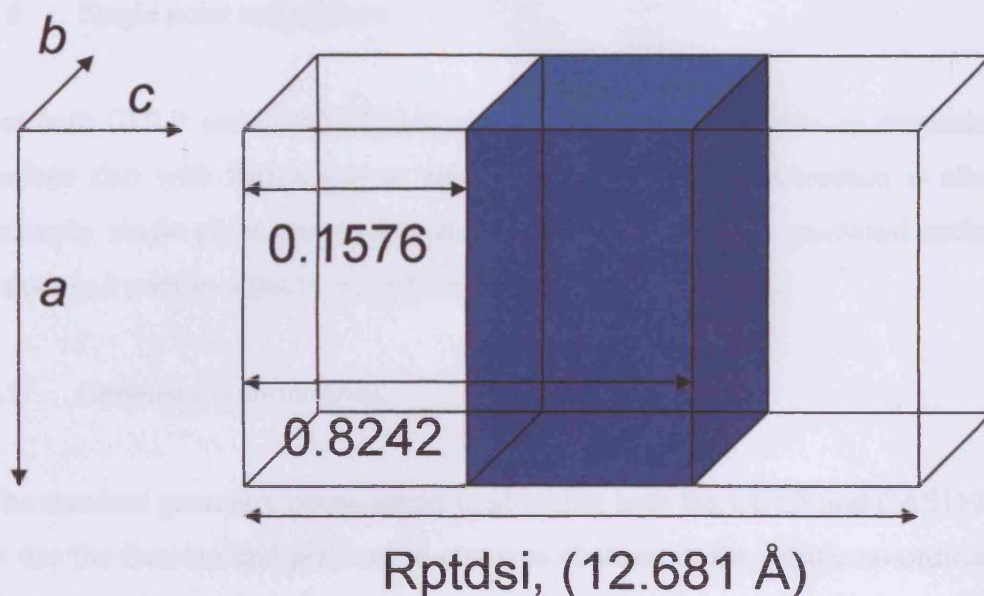
Figure 3.7. The Shiftcell process applied to the α-alumina crystal. The blue subsection is the required surface slab {0001}, with two equivalent surfaces in the ab plane at cuts 15.76 % and 82.42 % of the total repeat distance (rptdsi) from the origin. The atoms within the two blank subdivisions will be discarded.
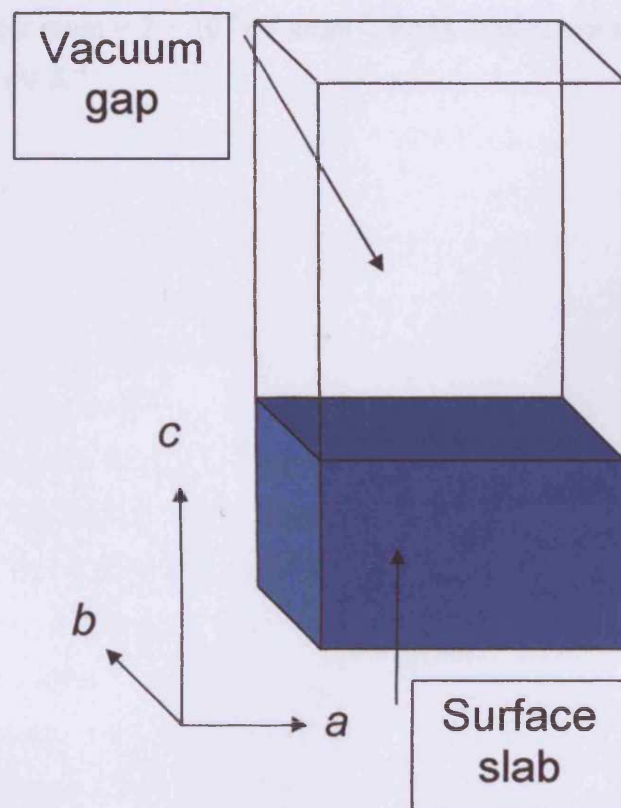
Figure 3.8. The visualisation of a vacuum gap added to the surface to create a crystal for a constant volume optimisation. The cell is periodic in the three dimensions a, b and c.

3.6   Single point calculations.

For both GULP and CASTEP, a single point calculation is used to determine a static surface slab with frozen atomic co-odinates, where no optimisation is allowed. For example, single point calculations are carried out to find the unrelaxed surface energy values (γ_s) prior to a geometry optimisation.

3.7   Geometry optimisations.

The standard geometry optimisation used within both the GULP and CASTEP codes is to use the Hessian and gradient to compute changes in the atomic co-ordinates within the lattice which reduce the gradient. This is achieved by a quasi-Newton method using the Broyden-Fletcher-Goldfarb-Shanno (BFGS) method for Hessian matrix update. Alternatively GULP includes the Davidon-Fletcher-Powell update mechanism, chosen as the default in the calculations presented in this work. The tolerance for the gradient normalisation convergence is 0.1 eV Å^{-1}. The CASTEP convergence criteria were set at: energy change per atom = 2×10^{-5} eV atom^{-1}, RMS displacement = 1×10^{-3} Å and RMS force = 5×10^{-2} eV Å^{-1}.

3.8   General Utilities Lattice Program.

3.8.1   Background to the General Utilities Lattice Program.

The General Utilities Lattice Program (GULP) is an atomistic potential based program for the simulation of three dimensional periodic structures. GULP uses symmetry constraints for energy minimisation of solids using first and second derivatives and can be used for crystals, inorganic and organic systems.[6] In addition GULP has the facility to fit potentials for a known structure. To overcome the difficulty of calculating all interactions between all species to infinity, GULP divides the individual components of the total lattice energy into short and long range interatomic potentials.

The long range Coulomb potentials are the major term for the lattice energy in oxide materials such as alumina, for the periodic crystals used within this research, the Ewald summation [7] can be used to evaluate this accurately for systems containing fewer than 10 000 ions. Section 2.4.5 describes the Ewald summation in detail.

The short range interactions consist of a wide range of interatomic potentials, within this research the main terms used were Buckingham, Lennard-Jones, Harmonic, Morse, Three-body harmonic and the spring term between the core and shell of oxygen. The formulae are listed in table 3.3. A polarisable oxygen atom is used in these simulations, where the nucleus and electrons are treated separately. A shell model is used to split the charge between the nucleus, which contains all of the mass of the atom and the massless shell.[8] The shell representation of the outer electrons is attached to the nucleus – the core – via a harmonic spring. In this way, the oxygen ion may be polarised by the displacement of the shell charge from an equilibrium position centred on the nucleus, as is illustrated in figure 3.9. The shell model relies on only two parameters: the spring constant k and the shell charge, since the shell charge and core charge must sum to the ionic charge. Parameters are generally non-transferable between ionic environments, so separate parameters are required for bulk oxygen and hydroxyl oxygen in the hydroxylated alumina systems considered in this work.

Zero field
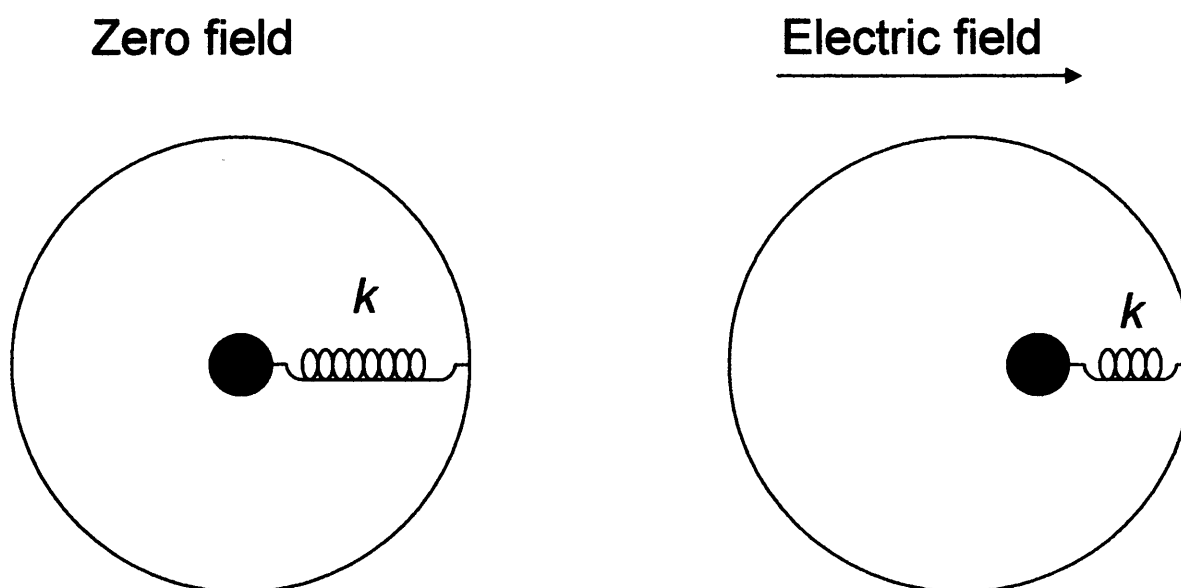
Electric field

Figure 3.9. Illustration of the polarisable ionic massless shell used to represent oxygen at equilibrium and the displacement of the shell under the influence of an external electric field. The nucleus is connected to the electron shell by a harmonic spring of spring constant k.

Potential name	Formula	Units
Buckingham	$A \exp(-r/\rho) - C\, r^{-6}$	A in eV, ρ in Å, C in eV $Å^6$
Lennard-Jones	$A\, r^{-m} - B\, r^{-n}$	A in eV $Å^{-m}$ B in eV $Å^{-n}$
[Combination rules]	$[\varepsilon_{ij}.(c_1(\sigma_{ij}/r_{ij})^{m}-c_2(\sigma_{ij}/r_{ij})^{n})]$	[ε in eV, σ in Å]
	$c_1 = \left(\left(\dfrac{n}{(m-n)}\right) \times \left(\dfrac{m}{n}\right)\right) \times \left(\dfrac{m}{m-n}\right)$	m and n are integers.
	$c_2 = \left(\left(\dfrac{m}{m-n}\right) \times \left(\dfrac{m}{n}\right)\right) \times \left(\dfrac{n}{m-n}\right)$	
Morse	$D(\{1 - \exp[-a(r-r_0)^2]\}^2 - 1)$	D in eV, a in $Å^{-2}$, r_0 in Å
Three-body harmonic	$\frac{1}{2} k_3 (\theta - \theta_0)^2$	k_2 in eV rad^{-2}, θ_0 in degrees
General	$A \exp(-r/\rho)r^{-m} - C\, r^{-n}$	A in eV $Å^{-m}$, ρ in Å, C in eV $Å^n$
Spring (core-shell)	$\frac{1}{2} k_2\, r^2$	k_2 in eV $Å^{-2}$

Table 3.3. The names, functional forms and input parameters required for interatomic potentials with GULP used in this research.

The majority of calculations using GULP presented in chapter four are constant volume energy minimisations, where the convergence is to a stationary point at which the gradients with respect to ion positions are zero or close to zero as defined by the optimisation tolerance. At such a stationary point, the second derivative – the hessian matrix – must also have converged to a positive definite form with real eigenvalues. The minimisation technique used is Newton-Raphson, where the hessian forms the basis of the minimisation search direction:

$$x = -H^{-1}g$$

Equation 3.1

Where H is the hessian matrix and g is the gradient vector and is updated by either the Broyden-Fletcher-Goldfarb-Shanno (BFGS) algorithm or the Davidson-Fletcher-Powell method used in the simulations presented in chapter four.

The Buckingham potential consists of a repulsive exponential and an attractive dispersive term between pairs of species as shown in chapter two. The short range cut-off is controlled by the dispersive term, $-C/r^6$, as the exponential repulsion term dependence on distance decays rapidly. It is possible to accelerate the convergence of the dispersive term with distance by separating this term into reciprocal and real space parts using a similar approach to the Ewald sum used for charges. The calculation of both the real and reciprocal space for the dispersive term is computationally negligible.

Although Lennard-Jones potentials may already exist in the literature, interaction parameters for adsorbate/surface are rare. In this work, these interaction parameters were calculated using combination rules from single atomic parameters. In table 3.3, ε_{ij} is the minimum energy of interaction, r_{ij} is the interatomic distance and σ_{ij} is the interatomic distance at which the energy is zero. As defined in chapter two, for a 9 6 Lennard-Jones potential, $m = 9$ and $n = 6$, in a 12 6 Lennard-Jones potential, $m = 12$ and $n = 6$. The data available is presented in ε_{ij} and σ_{ij} format, where the combination rules are shown in equations 3.2 and 3.3. Figure 3.10 shows a schematic plot of the Lennard-Jones interaction.

$$\varepsilon_{ij} = \frac{2 \cdot \left(\varepsilon_i \cdot \varepsilon_j\right)^{1/2} \cdot \left(\sigma_i^3 \cdot \sigma_j^3\right)}{\left(\sigma_i^6 + \sigma_j^6\right)}$$

Equation 3.2

$$\sigma_{ij} = \left(\frac{\sigma_i^6 + \sigma_j^6}{2}\right)^{1/6}$$

Equation 3.3
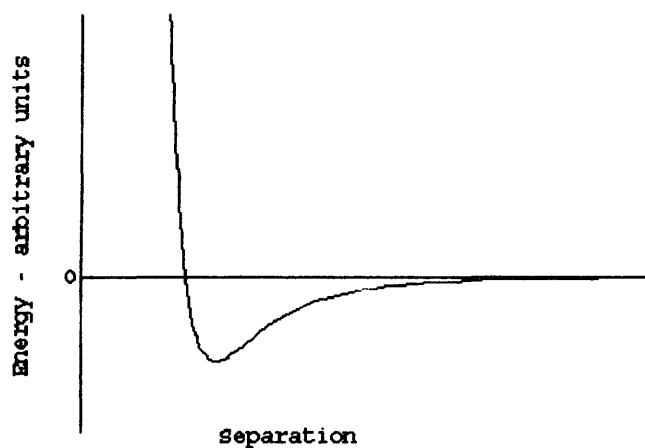
Figure 3.10. The Lennard-Jones potential for a typical intermolecular interaction.

3.8.2 Setting up and running a GULP simulation.

When considering the input file, the first line should contain the keywords which control and specify the type of the calculation to be performed. Table 3.4 summarises the names and defines the keywords used within the results presented in chapter four.

Keyword	Definition
compare	within the output, a table is produced containing initial and final geometries
conp	perform a constant pressure calculation, varying both atomic positions and cell parameters
conv	perform a constant volume calculation, fixing the cell parameters but optimising atomic coordinates
dfp	use the Davidson-Fletcher-Powell method of updating the hessian within the minimisation procedure
distance	output interatomic distances
fit	perform a fitting run on the coordinates defined
optimise	minimise the energy with respect to the geometry, using the defined update method
property	output the bulk lattice properties after optimisation
relax	within a fitting run, use relaxed fitting
simultaneous	within a fitting run, perform a simultaneous optimisation
single	perform a single point energy calculation

Table 3.4. Summary of keywords and definition for GULP. [9]

GULP allows multiple potentials to act between the same species over different length regimes. It is also possible to have different potentials acting at the same distance, although individual naming of species in different environments as shown in table 3.5 avoids unintended duplication which would overestimate the interactions present. For example, a potential named *O shel Al core* will act on every oxygen and aluminium, and so this potential, which may encompass either bulk oxygen, surface hydroxyl group oxygen or water oxygen, is separated as shown in table 3.5. Similarly, in the θ-Al_2O_3 phase with both tetrahedral and octahedral aluminium, both environments may be named to avoid any confusion. The charges presented in table 3.5 are derived from existing literature for the aluminium oxide structure whereas a Mulliken [10] population analysis of the geometry optimisation of the CASTEP determined fully hydroxylated {0001} α-alumina surface was used to find the charge for the O2 and H1 atom types. A geometry optimisation using the B3LYP [11] density functional Hamiltonian in the

109

Gaussian 98 [12] program was used to find the charges for the hydrogen fluoride molecule. The charge for fluorine in aluminium fluoride is set at -1 to counteract the +3 charge for aluminium for AlF_3 stoichiometry.

Atom name	Description of atomic environment	Charge
Al	Aluminium, further suffix 4 for Al_{tet} and 6 for Al_{oct}	+ 3.000 [13]
O1	Bulk oxygen in alumina.	$O1_{core}$ + 1.000 [13]
		$O1_{shell}$ - 3.000 [13]
O2	Oxygen in hydroxyl group	$O2_{core}$ + 0.900
		$O2_{shell}$ - 2.300
H1	Hydrogen in hydroxyl group	+ 0.400 [14]
F5	Fluorine in hydrogen fluoride	- 0.465
H5	Hydrogen in hydrogen fluoride	+ 0.465
F1	Fluorine in aluminium fluoride	- 1.000

Table 3.5. Species' names for interatomic potentials.

Once the tasks for GULP to perform in a calculation have been specified, the data for the calculation must be given. This consists of the input geometries, output file options, potentials and species. The potentials parameters used in the simulations presented in chapter four are shown in tables 3.6, 3.7, 3.8 and 3.9.

The input geometries consist of the cell parameters and the atomic names and coordinates, in Cartesian format, although fractional coordinates may also be used. Each individual atom charges must be specified, for a polarisable atom such as oxygen, this includes the partitioning of the formal charge between the core and shell. For the input of potentials, the type must be specified according to the names in table 3.5, followed by the interacting atomic species and the parameters of the potential.

Atom 1	Atom 2	A eV	ρ Å	C eV Å^6	min Å	max Å
Al[13]	$O1_{shell}$	1474.4	0.3006	0.0	0.0	12.0
$O1_{shell}$[14]	$O1_{shell}$	22764.3	0.149	27.88	0.0	12.0
$O1_{shell}$[14]	$O2_{shell}$	22764.3	0.149	27.88	0.0	12.0
$O2_{shell}$[14]	$O2_{shell}$	22764.3	0.149	27.88	0.0	12.0
Al[15]	$O2_{shell}$	1032.08	0.3006	0.0	0.0	12.0
$O1_{shell}$[16]	H1	7614.58003	0.19913	0.0	0.0	12.0
$O2_{shell}$[9]	H1	589.25412	0.19913	0.0	0.0	12.0
F5[17]	F5	153044.1	0.24108	0.0	0.0	12.0
H5	H5	2649.6	3.74	27.36	0.0	12.0
Al	F1	1359.041	0.2725	0.0	0.0	12.0

Table 3.6. Buckingham potentials $V(r) = A \exp(-r/\rho) - C r^6$ for the species defined in table 3.5. Min and max refer to the range over which these potentials act.

Atom 1	Atom 2	ε_{ij} eV	S_{ij} Å	min Å	max Å
Al	H5	0.309975	2.670565	0.0	12.0
O1	H5	0.083302	3.149798	0.0	12.0
Al	F5	0.437257	3.106515	0.0	12.0
O1	F5	0.117507	3.388064	0.0	12.0

Table 3.7. 9 6 Lennard-Jones potentials $V(r) = \varepsilon.(c_1(s_{ij}/r_{ij})^9 - c_2(s_{ij}/r_{ij})^6)$ for the species in table 3.5.

Atom 1	Atom 2	ε_{ij} eV	S_{ij} Å	min Å	max Å
H5	F5	13150.8	45.64	0.0	12.0

Table 3.8. 12 6 Lennard-Jones potential $V(r) = \varepsilon.(c_1(s_{ij}/r_{ij})^{12} - c_2(s_{ij}/r_{ij})^6)$ for the species in table 3.5.

Intermolecular Morse potentials		$V(r) = D(\{1 - \exp[-a(r - r_0)^2]\}^2 - 1)$				
Atom 1	Atom 2	$\underline{D}$	$\underline{a}$	$\underline{r_0}$	min	max
		eV	Å^{-2}	Å	Å	Å
H1 [18]	O2	7.0525	3.17490	0.9485	0.3	1.2
H5	F5	543.746	2.66499	0.93	0.0	1.1

General potential 2 1		$V(r) = A \exp(-r/\rho)r^{-m} - C r^{-n}$				
Atom 1	Atom 2	$\underline{A}$	ρ	$\underline{C}$	min	max
		eV Å^{-m}	Å	eV Å^n	Å	Å
H1 [19]	H1	23042.17	0.135868	0.0197	0.0	12.0

Three-body harmonic potentials			$V(r) = \frac{1}{2} k_3 (\theta - \theta_0)^2$				
Atom 1	Atom 2	Atom 3	$\underline{k_2}$	$\underline{\theta_0}$	$\underline{max}_{1-2}$	$\underline{max}_{1-3}$	$\underline{max}_{2-3}$
			eV rad^{-2}	degrees	Å	Å	Å
Al4	O1	O1	2.09724	109.47	2.0	2.0	3.0
Al6 [14]	O1	O1	2.09724	90	2.0	2.0	3.0

Spring potentials	$V(r) = \frac{1}{2} k_2 r^2$
Atom	$\underline{k_2}$
	eV rad^{-2}
O1 [20]	60.78
O2 [6]	74.92

Table 3.9. Further potentials required to simulate alumina, hydroxylated alumina surfaces, hydrogen fluoride and water for the species defined in table 3.5.

3.8.3 Potential fitting within GULP.

As GULP is a potential based code, it relies on the input of interatomic potential parameters to function and perform production calculations of lattice energies. The parameters used in the alumina series of calculations were taken from the literature, however, no potential parameters could be found for AlF_3 or hydrogen fluoride. Within the GULP code there is a facility for constructing these parameters based either on fitting to data from reference *ab initio* calculations, or by reproducing experimental data, such as x-ray diffraction determined structural information.

In the case of the F⁻ potential the parameters were fitted simultaneously to β-, κ- and θ-AlF₃ x-ray diffraction determined crystal structures.[21] This ensures the potentials will be fitted to a range of F⁻ environments. The quality of fit is assessed using the 'sum of squares' output quantity in GULP, a measure of how good the fit is. For complicated systems such as AlF₃ is it unrealistic to expect the sum of squares value to be zero. The sum of squares F is defined as:

$$F = \sum w.(f_{calc} - f_{obs})^2 \qquad \text{Equation 3.4}$$

Where f_{calc} and f_{obs} are the calculated and observed quantities and w is a weighting factor, which depends upon factors such as the relative magnitudes of data, and the expected error in the data. As this input data is a crystal structure, the reliability is high and so this affects the weighting factor.

The sum of squares value is minimised in a fitting run by altering potential parameters, achieved via a rapid Newton-Raphson functional minimisation technique of the numerical first derivatives. This supersedes the gradient minimisation approach for accuracy as it is based on second derivatives optimisation.

During the fitting, the dispersive C term for the Buckingham potential was held fixed and the A and ρ terms fitted first, as it was found that the C term has a tendency to go to zero or to be overestimated by orders of magnitude.

The procedure for fitting uses standard Cartesian co-ordinates for the atomic positions of β-, κ- and θ-AlF₃. The keyword to effect fitting is *fit*, the keyword *conp* is also specified to give relaxed fitting with both atomic coordinate and cell parameter degrees of freedom.

With reference to table 3.3, the format of the Buckingham potential input for an aluminium fluoride interaction is:

Buck

Al core F core <A> <ρ> <C> <min> <max>

Where symbols in <> brackets indicate where the values of the corresponding potential parameters should be inserted. To allow for fitting, flags are added at the end of the potential definition line with the convention: 1 to allow fitting, 0 to remain fixed. For example, to hold C constant whilst fitting A and ρ, the input is:

Buck

Al core F core A ρ C min max 1 1 0

The full parameters that were fitted for aluminium fluoride are detailed in table 3.6. The accuracy of any fitted potentials must be evaluated against known structures, in this case the ideal method is to compare the GULP lattice geometries against high precision calculations using the CASTEP code and experimental data to determine whether the GULP aluminium fluoride potentials can be carried forward into production calculations.

The Morse potential was fitted in the way described above for a single hydrogen fluoride molecule, to yield the potentials in tables 3.6 and 3.9 respectively. These potentials are used for the simulation of hydrogen fluorine onto the α-alumina {0001} surface.

3.9   Cambridge Serial Total Energy Package.

3.9.1   Background to the Cambridge Serial Total Energy Package.

The Cambridge Serial Total Energy Package, CASTEP, [22] [23] is a parallelised first principles density functional theory computer code incorporating plane waves and pseudopotentials with the ability to simulate the chemistry and physics of condensed matter, including catalysts, proteins, minerals and liquid metals. Development of CASTEP began about two decades ago led by the research group of Mike Payne at Cambridge University as part of the United Kingdom Car-Parrinello (UKCP) consortium.[24] The UKCP encompasses the plane-wave pseudopotential density functional theory method pioneered in the 1980's by Roberto Car and Michele Parrinello,[25] which fundamentally contains two approximations. The first approximation

is the exchange and correlation energy of the electrons with the system, via the Local density approximation (LDA) or extended to include density gradients, in the Perdew and Wang generalised gradient approximation (GGA).[26]

The second approximation is the pseudopotential representation of core electrons within the system, meaning that only the valence electrons are treated explicitly. The interaction between valence electrons and the ionic core is described by a pseudopotential, and is different for every type of atom in a system. CASTEP makes use of various pseudopotential approximations; primarily the most cost effective in terms of computational resources is Vanderbilt's [27] [28] ultrasoft pseudopotential which conserves the integration of charge within both the pseudo region to match an all-electron solution.

As a first principles density functional theory code, CASTEP is based on the full application of quantum mechanics in order to solve the Kohn-Sham equations, described in section 2.2, to find the energy of given system in terms of the electron density. In density functional theory approaches, the calculation of electron-electron interaction is based on the implementation of two key principles. The first is that the total energy of a system of electrons and nuclei is a unique functional of the electron density, which effectively means that the density defines the potential acting on the electrons. The second principle is that the variational minimum of the energy with respect to electron density is exactly equivalent to the ground state energy.

CASTEP iteratively solves the total energy; from this it is possible to predict stabilities, adsorption energies, phonon frequencies, reaction barriers and structures. Within the periodic *ab initio* plane wave pseudopotential results presented in chapter five, CASTEP version 4.2 was utilised, a code written specifically for parallelised multiprocessor UNIX based computers, amongst the features of this version are:

- Calculation of total energies, with forces and the unit cell stresses on every atom.
- Geometry optimisations with or without internal and external constraints.

- Ultrasoft and norm-conserving pseudopotential library across the entire periodic table.

- Adjustable parameters selection including basis sets via planewave cut-off, FFT grid, k-points, convergence criteria.

- Density of states and band structure calculation.

3.9.2 Setting up and running a CASTEP calculation.

Via the Cerius^2 interface, seven files are produced for a geometry optimisation, whereas for a single point energy calculation, the *.optim* file is excluded. Table 3.10 defines these seven files written, in addition to the *.run* file, the local initialisation file defining the input directory and location of CASTEP.

For a constant pressure calculation, used to relax the lattice parameters and atomic coordinates, the *optimisation* calculation type is selected in the interface. No further manipulation of the input files is needed for a constant pressure simulation other than the *.run* file. A constant volume calculation, as used extensively in this research, does not allow for the optimisation of lattice parameters, only the energy minimisation of the atomic coordinates, the modifications to the seven input files are three-fold:

i.   In *.optim*, the first line of integer values for the lattice parameters a, b, c, α, β and γ are replaced by six zeros to ensure no optimisation of the cell constraints.

ii.   In *.param*, the line indicating lattice optimisation is changed to zero.

iii. In *.rundat*, the BFGS cell optimisation value is set to zero, whilst retaining the BFGS atomic optimisation value of three.

116

File appendage	Input information.
.optim	Specified for BFGS geometry optimisations, contains the constraints and initial Hessian.
.param	Contains parameters for memory assignment during the calculation, the FFT grid and the number of plane-waves.
.rundat	Contains options and variables for the control of CASTEP calculations.
.geom	Contains the geometry of the structure: atomic coordinates, cell parameters and k-point information of the system.
.ewdata	Contains data for the Ewald summation and is identical regardless of the calculation to be carried out.
.symm	Contains symmetry information of the structure defined in the .geom file, when used for a high symmetry crystal the calculation is more efficient.
.recpot	Contains reciprocal space library data for the pseudopotentials being used within the calculation.

Table 3.10: Names and details of input files for CASTEP version 4.2.

The FFT grid, k-points, pseudopotential, exchange and correlation function, kinetic energy cut-off and convergence criteria (shown in section 3.7) are defined in Cerius[2].

After the code execution has completed the output file (*.cst*) contains information about the convergence of the minimisation to the specified thresholds and the Cartesian coordinated produced can be visually analysed using Cerius[2], from this detailed electronic properties such as the band structure, density of states and electron population may be investigated.

[1] G.W. Watson, E. T. Kelsey, N. H. de Leeuw, D. J. Harris and S. C. Parker, *J. Chem. Soc., Faraday Trans.*, **92(3)**, 433, (1996).
[2] P. W. Tasker, *Philos. Mag. A*, **39**, 119, (1979).
[3] J. D. Gale, General Utilities Lattice Program (GULP). Royal Institution of Great Britain/Imperial College London, (1992-1996).
[4] P. W. Tasker, *J. Phys. Chem.*, **12**, 4977, (1979).
[5] F. Bertaut, *The electrostatic term of the surface energy, CR Acad Sci.*, **246**, 3447, (1958).
[6] J. Gale. *J. Chem. Soc., Faraday Trans.*, **93(4)**, 629, (1997).
[7] P. Ewald, *Ann. Phys.*, **64**, 253, (1921).

[8] B. G. Dick and A. W. Overhauser, *Phys.Rev.*, **112**, 90, (1958).

[9] J. Gale, *GULP version 1.2.* http://www.ch.ic.ac.uk/gale/Research/gulp.html.

[10] R. S. Mulliken, *J. Chem. Phys.*, **23 (10)**, 1833, (1955).

[11] A. D. Becke, *J. Chem. Phys.*, **98**, 5648, (1993).

[12] Gaussian 98. M. Frisch, G. Trucks, H. Schlegel, G, Scuseria, M. Robb, J. Cheeseman, V. Zakrzewski, J. Montgomery, R. Stratmann, J. Burant, S. Dapprich, J. Millam, A. Daniels, K. Kudin, M. Strain, O. Farkas, J. Tomasi, V. Barone, M. Cossi, R. Cammi, B. Mennucci, C. Pomelli, C. Adamo, S. Clifford, J. Ochterski, G. Petersson, P. Ayala, Q. Cui, K. Morokuma, D. Malick, A. Rabuck, K. Raghavachari, J. Foresman, J. Cioslowski, J. Ortiz, B. Stefanov, G. Liu, A. Liashenko, P. Piskorz, I. Komaromi, R. Gompertz, R. Martin, D. Fox, T. Keith, A. Al-Laham, C. Peng, A. Nanayakkara, C. Gonzalez, M. Challacombe, P. Gill, B. Johnson, W. Chen, M. Wong, J. Andres, M. Head-Gordon, E. Replogle and J. Pople, Gaussian Inc., Pittsburgh PA 1998.

[13] G. V. Lewis and C. R. A. Catlow, *J. Phys. Chem. Solid State Physics.*, **18**, 1149, (1985).

[14] M. J. Sanders, M. J. Leslie and C. R. A. Catlow, *J. Chem. Soc. Chem. Com*, 1271 (1984).

[15] Private communication.

[16] M. Sierka and J. Sauer, *Faraday Discuss.*, **106**, (1997).

[17] R. G. Della Valle and D. Gazzillo, *Phys. Rev. B*, **59 (21)**, 13699, (1999).

[18] M. A. Nygren, D. H. Gay, C. R. A. Catlow, *Surface Science*, **380**, 113, (1997).

[19] M. Gastreich and C. M. Marian, *J. Mol. Struc./Theochem*, **506**, 107, (2000).

[20] Private communication.

[21] J. A. A. Ketelaar, *Nature*, **128**, 303, (1931).

[22] M. Payne, M. Teter, D. Allan, T. Arias and J. Joannopoulos, *Reviews of Modern Physics*, **64 (4)**, 1992.

[23] M. Segall, P. Lindan, M. Probert, C. Pickard, P. Hasnip, S. Clark and M. Payne. *J. Phys.: Condensed Matter.* **14**, 2717, (2002).

[24] See http://www.cse.clrc.ac.uk/cmg/NETWORKS/UKCP/index.shtml.

[25] R. Car and M. Parrinello, *Phys. Rev. Lett.*, **55**, 2471, (1985).

[26] Perdew, J. P., and Wang, Y., *Phys. Rev. B.* **45**, 13244 (1992).

[27] D. Vanderbilt, *Physical Review B*, **41**, 7892, (1990).

[28] C. Lee, D. Vanderbilt, K Laasonen, R. Car and M. Parrinello. *Physical Review B*, **47**, 4863, (1993).

Chapter 4

4   Periodic potential simulations.

In this chapter, the results obtained using the GULP code are presented. The theory behind molecular mechanic simulations is detailed in chapter two, and the format of GULP calculations input files is described in chapter three. Both α-alumina and θ-alumina structures have been investigated using these methods. Because of the efficiency of potential based simulations a comprehensive range of lattice structures, surface energies, hydroxylated surfaces and adsorption modes were studied to provide a complementary series of results which can be compared to the notionally more accurate quantum mechanical results obtained from CASTEP, shown in chapter five.

Firstly the bulk and surface calculations of α-alumina will be discussed, followed by the equivalent series of simulations for θ-alumina. In addition, the fine tuning of the interatomic potentials defined in chapter three allowed adsorptions of hydrogen fluoride to be considered onto the {0001} α-alumina surface. The aluminium fluoride structures and surfaces will be described as aluminium fluoride is the fully fluorided form of α-alumina.

4.1   α-Alumina structure determination.

The GULP methodology of calculating the bulk and surface properties begins using the α-alumina bulk crystal determined by x-ray crystallography.[1] The initial constant pressure optimisation allowing the atomic and cell co-ordinates to minimise resulted in the cell parameters shown in table 4.1. There is a small expansion in the a and b directions, with a contraction in the c direction. These values represent the bulk crystal of α-alumina within 2.5 % of the original, comparable to the DFT results shown in chapter five for the CASTEP constant pressure calculation. The potentials used for these simulations are discussed in chapter three.

Parameter	Original	Minimised	Percentage difference
a / Å	4.7590	4.8178	+1.23 %
b / Å	4.7590	4.8178	+1.23 %
c / Å	12.991	12.681	-2.39 %
Volume / Å^3	254.803	254.903	+3.9 ×10^{-4} %

Table 4.1. Cell parameters for the constant pressure calculation of α-alumina using GULP.

4.2 Surfaces of α-alumina.

Following a constant volume simulation with the lattice parameters calculated by the constant pressure minimisation, Shiftcell was used to find the stable surfaces of the fully relaxed α-alumina crystal using the method outlined in chapter three. As a result of this, the {0001}, {01$\bar{1}$1} and {11$\bar{2}$1} surfaces were found to contain no inherent dipole across the stoichiometric surface slab and were possible to terminate with aluminium ions. Table 4.2 details the surface energy analysis for these three surfaces. As expected, all of the relaxed values fall within the ideal range of 1-5 J m^{-2}, although the {11$\bar{2}$1} value is slightly outside this upper limit, all the surfaces show a reduction in surface energy upon minimisation. A stabilisation of the {0001} shows that the minimised surface is not significantly altered from the input structure, although is slightly thermodynamically more stable. A supercell of 4×4 expanded in the a and b directions of the unit cell was used for the {0001} slab calculations, with a 20 Å vacuum gap. For the {01$\bar{1}$1} surface, a supercell of 1×3 was used for the simulations, the {11$\bar{2}$1} surface calculations were carried out using a 2×3 supercell.

The {0001} surface is terminated by aluminium as described in chapter one, the atoms in this surface layer experience a relaxation towards the surface oxygen layer immediately beneath. Table 4.3 lists these interlayer relaxations upon minimisation using the Davidon-Fletcher-Powell (DFP) method of updating the hessian. The method used to determine these relaxations is defined in equation 1.2.

Surface	a Å	b Å	Unrelaxed γ_s J m^{-2}	Relaxed γ_s J m^{-2}	Percentage change of γ_s on relaxation
{0001}	19.2712	19.2712	8.03	2.23	-72.2 %
{01$\bar{1}$1}	4.8178	13.5654	8.19	3.77	-54 %
{11$\bar{2}$1}	8.3447	13.5654	17.16	2.99	-82.6

Table 4.2. Unrelaxed and relaxed surface energies for the three Miller-Bravais surfaces of α-alumina crystals. The unrelaxed values are calculated from a single point energy of the surface slab, with the relaxed surface energy calculated from the geometry optimised structure, both at constant volume. The Davidon-Fletcher-Powell method of updating the hessian was used in these calculations.

Layer	Relaxation %
Al1-O1	-86.9
O1-Al2	+8.0
Al2-Al3	-30.9
Al3-O2	+14.3

Table 4.3. Percentage relaxations for the first four layer separations of the {0001} α-alumina surface. A negative value indicates that the layer separations reduced upon minimisation, whilst a positive value indicates an increase in the separation according to the definition in equation 1.2.

These values compare well to the theoretical investigations described in detail in section 1.2.3 as the magnitude of the Al1-O1 relaxations is widely reported to be greater than ca. 58 % for atomistic and ab initio calculations. However, as acknowledged in the literature discussed in chapter one, many theoretical methods overestimate this initial relaxation by a considerable degree. Experimental grazing angle X-ray crystallographic work shown in section 1.2.2 gave this first Al1-O1 layer relaxation to be -51 %.[2] A compression of the next layer occurs, followed by an expansion between the Al2 and Al3 layers, the analysis completed with a compression of the Al3-O2 layer, all in broad agreement with existing data.

The optimised surface is shown in figure 4.1 as a side projection illustrating the aluminium and oxygen mixed character of this plane, and as a plan view in figure 4.2. In figure 4.2, the hexagonal ring structure of the basal plane of α-alumina is clearly

seen, by isolating the Al1 and O1 terminating layers, and the two subsurface Al2 and Al3 layers both of which are bound to the O1 sites. Each Al_3O_3 subunit contains one Al1 terminating aluminium site, bound to two surface terminating O1 basic oxygen sites. One of these oxygen sites is bound to an Al2 level aluminium atom, sited directly in the layer underneath the Al1 and O1 mixed surface. The other of these two oxygen atoms is bound to an Al3 aluminium situated in the marginally deeper layer. Bridging these Al2 and Al3 sites is the third surface oxygen O1 atom to complete the Al_3O_3 ring unit. All of the aluminium atoms contain another bond to an O1 atom positioned in the adjacent unit. Figure 4.3 illustrates the isolated Al_3O_3 unit shown as a plan view with the bonds to other atoms within the four top layers, Al1, O1, Al2 and Al3. Table 4.4 shows the averaged bond lengths across the supercell for both the unrelaxed and geometrically optimised surface. A side projection of this is shown in figure 4.4. This illustrates the translation needed to move from, for example, an Al1 site to another Al1 site, a displacement of one subunit to find an equivalent atom.
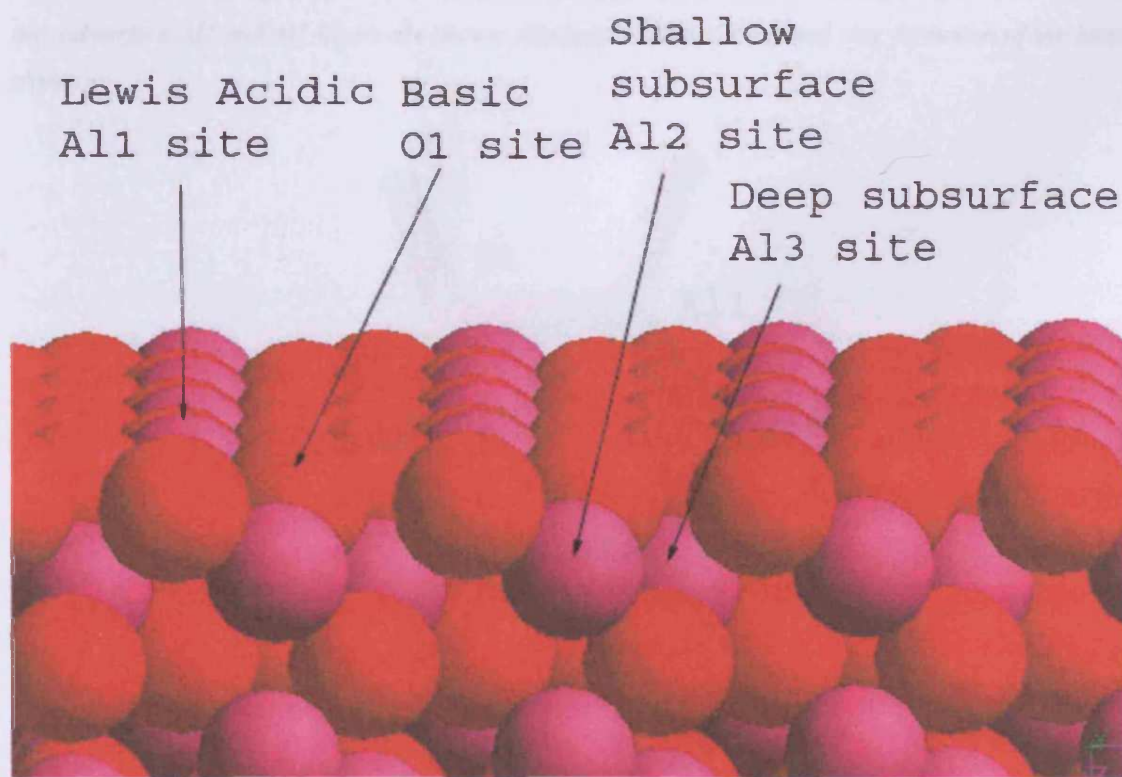
Figure 4.1. Side projection of the {0001} α-alumina surface the terminating aluminium and oxygen mixed surface, and the arrangement of the subsurface structure leading towards the bulk repeating unit.
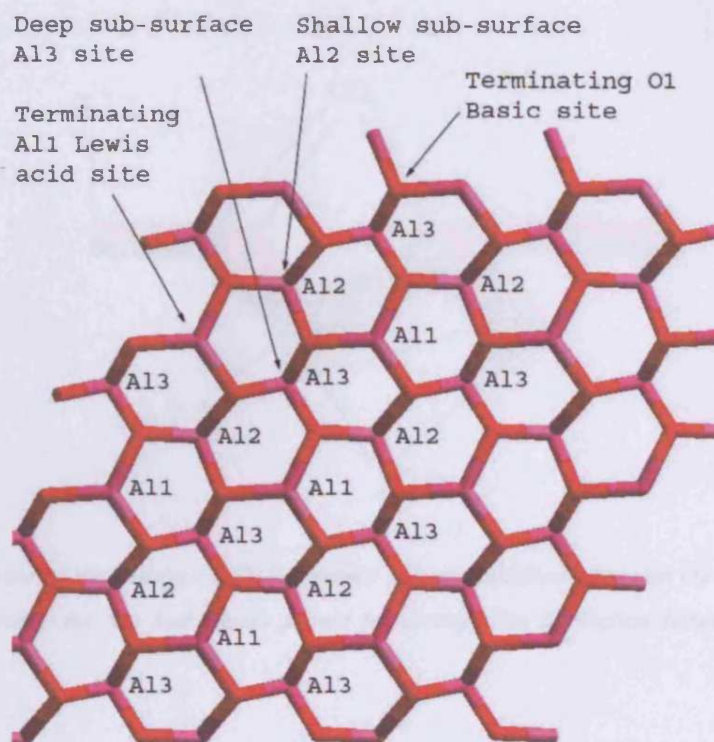
Figure 4.2. Plan view of the {0001} α-alumina surface, for clarity only the terminating Al1, O1 and the two subsurface Al2 and Al3 layers are shown, demonstrating the hexagonal ring formation of the basal plane.
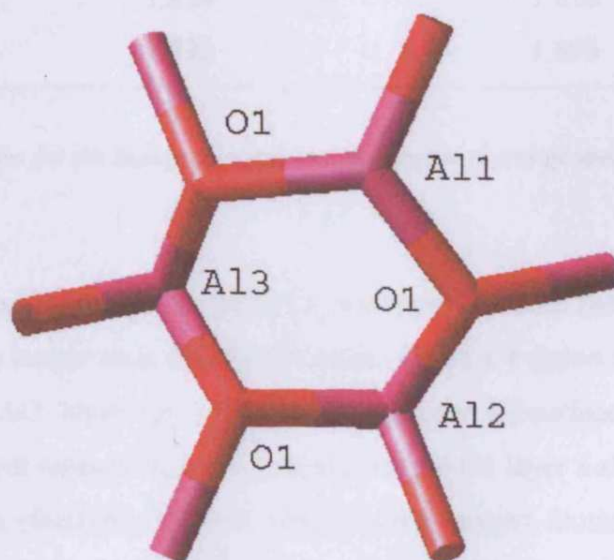
Figure 4.3. Plan view of an isolated Al₃O₃ ring, showing the a surface Al1 site, bound to two surface O1 sites, with a further bond to another O1 atom forming part of a different Al₃O₃ unit, with the shallow subsurface Al2 octahedral aluminium and the deep subsurface Al3 aluminium, both bridged by a surface O1. Table 4.4 details these bond lengths for the unrelaxed and relaxed surface.
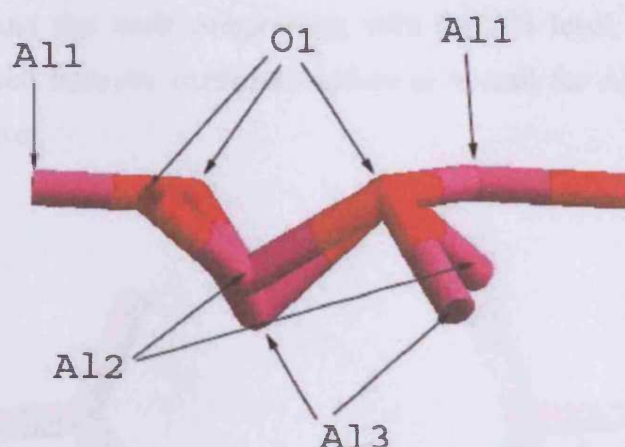
Figure 4.4. Side view of the isolated Al₃O₃ hexagonal subunit visualised down an O1-O1 axis with bonds to other atoms within the top four layers shown for clarity. The distinction between Al2 and Al3 is evident.

Bond	Ring in unrelaxed structure Å	Ring in relaxed structure Å
Al1-O1	1.743	1.741
Al2-O1	1.818	1.818
Al3-O1	1.893	1.893

Table 4.4. Bond lengths for the hexagonal rings in both unrelaxed and geometrically optimised {0001} surface slabs..

From the bond lengths detailed in table 4.4, it is seen that both the Al2-O1 and Al3-O1 bond distances are longer than the Al1-O1 bond, figure 4.4 shows that this is due to the deep subsurface Al3 layer lying below the shallow subsurface Al2 layer. As the aluminium Al1 layer relaxes back towards the surface O1 layer a shortening of the Al1-O1 bond length is observed, the two neighbouring oxygen atoms are forced apart to accommodate this, as shown by table 4.5 and illustrated in figure 4.5. The optimisation results in these oxygens neighbouring Al1 moving from 2.992 Å to 3.01 Å, a *ca.* 0.02 Å increase. As the layer relaxations for the subsurface layers are less significant than the Al1-O1 value, the interatomic distances show less distortion. The interatomic distance for the two oxygen atoms neighbouring Al2 are different by *ca.* 0.01 Å, with the value for the oxygen atoms neighbouring Al3 separating by < 0.01 Å As can be predicted by

the Al1 moving towards O1 upon optimisation with the Al2 layer moving away by a lesser percentage and this itself compressing with the Al3 level, all the interatomic distances are lowered from the unrelaxed surface as overall the Al1 layer is closer to Al3 after optimisation.

a)   b)
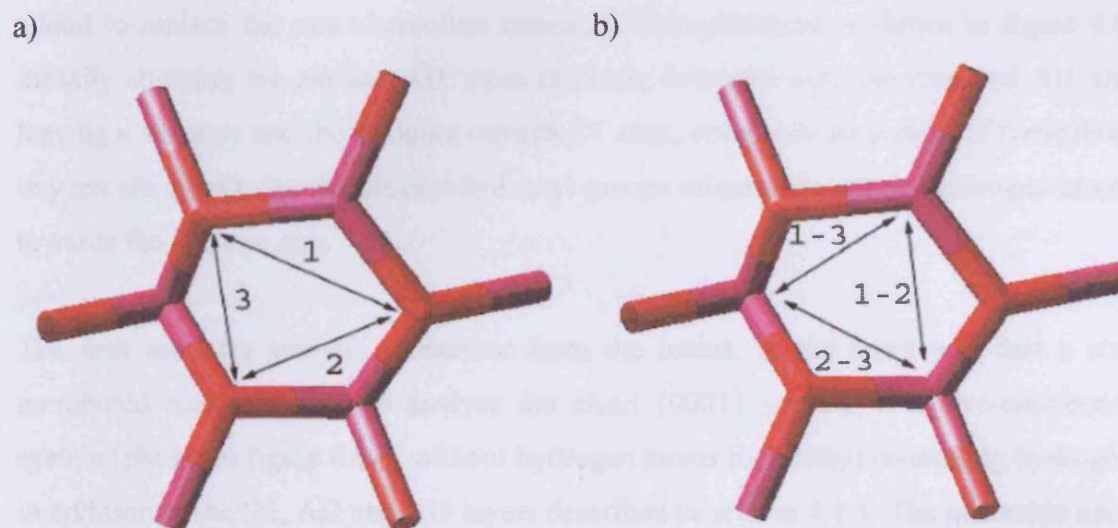
Figure 4.5. (a) The interatomic separation between the three O1 layer oxygen atoms in the ring unit, where 1 indicates the separation between the oxygen atoms neighbouring Al1, 2 defining the distance between the two O1 sites flanking Al2 and 3 for the pair of oxygen atoms bound to Al3. (b) Shows the interatomic aluminium distances, where for example 1-3 defines the distance between Al1 and Al3. The orientation is exactly the same as in figure 4.3. Table 4.5 summarises these interatomic distances.

	Unrelaxed structure	Relaxed structure
	Å	Å
Aluminium to aluminium		
1-2 (Al1-Al2)	2.901	2.892
1-3 (Al1-Al3)	3.057	3.044
2-3 (Al2-Al3)	2.736	2.735
Oxygen to oxygen		
1 (O1-Al1-O1)	2.992	3.010
2 (O1-Al2-O1)	2.722	2.733
3 (O1-Al3-O1)	2.422	2.416

Table 4.5. Comparsion of the average aluminium to aluminium and oxygen to oxygen interatomic distances in the unrelaxed and relaxed hexagonal ring system.

4.3   Full hydroxylation of {0001} α-alumina surface.

The fully hydroxylated {0001} plane was generated by removing the Al1 layer in the 4×4 supercell slab, a removal of sixteen aluminium atoms from each surface in the slab. In each of the effective three co-ordinate defects remaining, three hydrogen atoms were added to replace the one aluminium removed. This procedure is shown in figure 4.6, initially showing the surface Al1 atom in place, followed with the removed Al1 site leaving a vacancy and the bridging oxygen O1 sites, and a side projection of these three oxygen sites; with the constructed hydroxyl groups orientated with the hydrogen atoms towards the vacuum gap.

The unit used for analysis is excised from the lattice, in the same way that a six-membered ring was used to analyse the clean {0001} surface, a twelve-membered system (shown in figure 4.6 b, without hydrogen atoms for clarity) containing hydrogen in addition to the O1, Al2 and Al3 layers described in section 4.1.1. The potentials used for the addition of hydrogen to the surface are given in chapter three, where H1 and O2 represent hydroxyl hydrogen and oxygen respectively. To allow for the computation of the hydroxylated α-Al_2O_3 {0001} surface, the potentials used for O1 (lattice oxygen) and O2 (hydroxyl oxygen) are distinguished as discussed in section 3.8.2.

a)   b)   c)
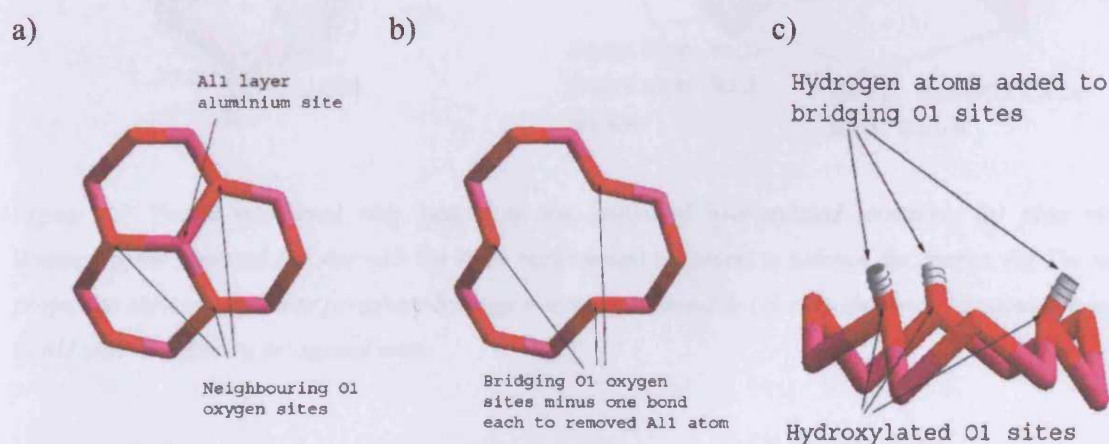
Figure 4.6. Illustration of the hydroxylation process: (a) three six-membered rings centred on an Al1 atom, (b) twelve-membered system without Al1 atom and (c) the side projection of the isolated cluster with hydroxylated O1 oxygen sites with no net charge difference following the replacement of aluminium with three hydrogen atoms. In (c), as the three other O1 sites were also bound to a removed Al1 site, these will be hydroxylated in addition to the three illustrated, but have H atoms omitted for clarity.

127

Figure 4.7 illustrates the fully hydroxylated structure viewed as both plan and side projections of the minimised structure. This shows the orientation of hydrogen atoms in relation to the surface, relaxed compared to the starting point the hydroxyl H atoms have towards the surface due to the electrostatic attraction of the negative charge of the O1 layer. Each hydroxylated O1 site bridges one aluminium site in the Al2 layer and one in the Al3 layer, the average O1-Al2 bond length is 1.768 Å; a reduction of 0.05 Å from the relaxed clean {0001} surface, whereas the O1-Al3 bond length is now 1.916 Å; an increase of 0.023 Å compared to the same clean surface. This demonstrates that the hydroxylation of the {0001} surface causes a slight disruption within the subsurface structure. Figure 4.8 illustrates the plan view of the fully hydroxylated {0001} α-alumina surface showing the mixed hydrogen and oxygen surface, with a minor contribution from the aluminium Al2 subsurface layer.

a)   b)
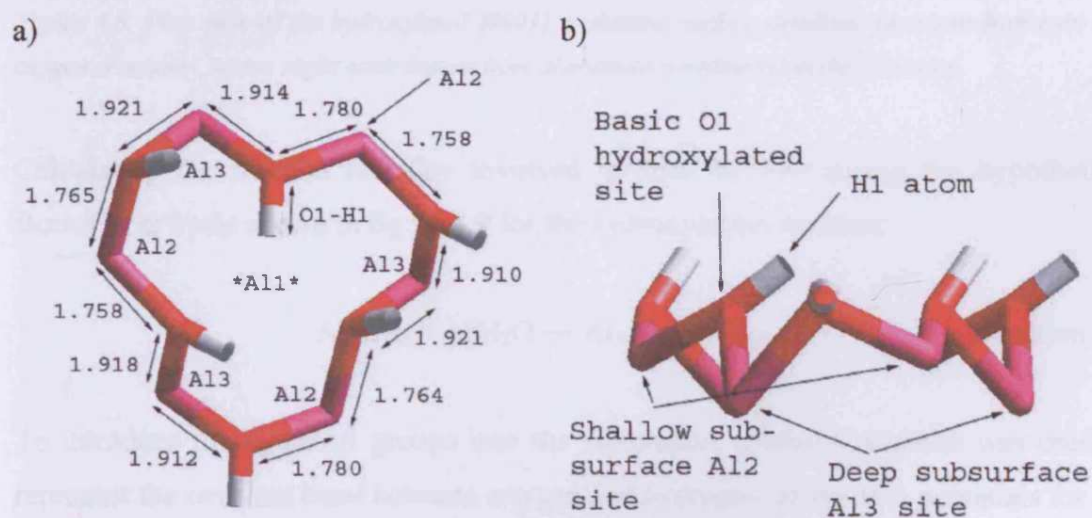
Figure 4.7 Twelve-membered ring system in the optimised hydroxylated structure, (a) plan view illustrating the removed Al1 site with the three replacement H1 atoms to balance the charge. (b) The side projection showing the three periphery hydrogen atoms are bound to O1 sites that were previously bound to Al1 sites in adjacent hexagonal units.
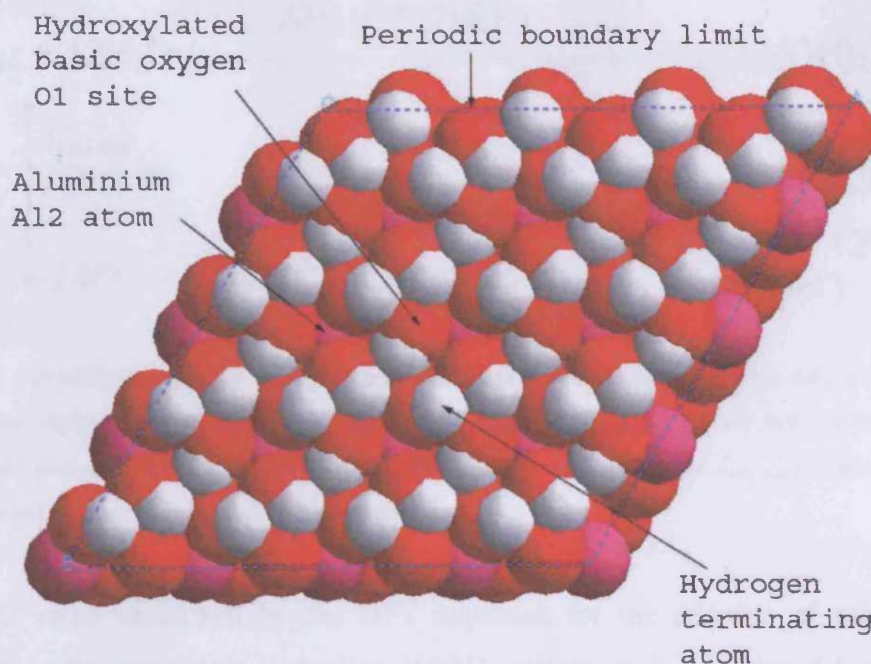
Figure 4.8. Plan view of the hydroxylated {0001} α-alumina surface detailing the major hydrogen and oxygen character, with a slight contribution from aluminium coordinated in the Al2 layer.

Calculating the reaction enthalpy involved is done by introducing the hypothetical Born-Haber cycle shown in figure 4.9 for the hydroxylation reaction:

$$Al_{16}O_{24} + 12H_2O \rightarrow Al_{16}O_{12}(OH)_{24} \qquad \text{Equation 4.1}$$
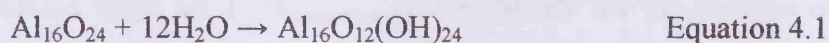
To introduce the hydroxyl groups into the simulation, a Morse potential was used to represent the covalent bond between oxygen and hydrogen, along with potentials for the inclusion of hydrogen in the hydroxyl group in the simulation cycle. At equilibrium in the gas phase, an OH⁻ group would be expected to be at its optimum bond distance and so a correctional energy must be used to compensate for these additional potentials introduced in the hydration process. The reaction shown in equation 4.4 cannot be estimated based explicitly on potentials in the same way for the DFT CASTEP calculations for the full hydroxylation in chapter five. What can be done is to compare the value of the enthalpy of reaction from one particular DFT calculation with these forcefield lattice energy calculations to arrive at an estimate for the energy of reaction for equation 4.1.

$$\Delta H_r \text{ (CASTEP)}$$

$$Al_{16}O_{24} + 12H_2O \xrightarrow{\hspace{5cm}} Al_{16}O_{12}(OH)_{24}$$

$$\uparrow E_{oxide} \text{(GULP)} \qquad\qquad 12(O^{2-} + H_2O \rightarrow 2OH^-) \qquad \uparrow E_{hydroxide} \text{(GULP)}$$

$$16Al^{3+} + 24O^{2-} + 12H_2O \xrightarrow[\;12 \times E_{correction}\;]{\hspace{3cm}} \begin{array}{l} 16Al^{3+} + 12O^{2-} \\ + 24(OH^-) \end{array}$$
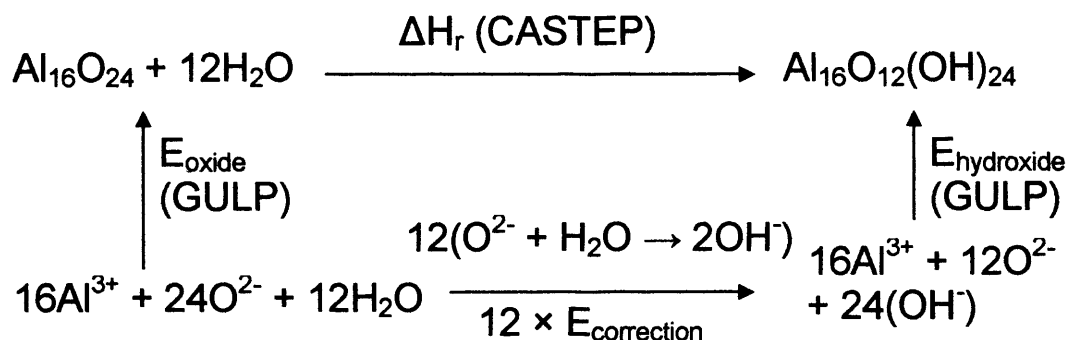
Figure 4.9. Born-Haber cycle for the hydroxylation of an alumina surface, where ΔH_r is the energy of hydroxylation defined using CASTEP in chapter five. E_{oxide} and $E_{hydroxide}$ are the lattice energies for the clean surface and fully hydroxylated α-alumina {0001} surfaces respectively. $E_{correction}$ is the correctional energy applied for the $O^{2-} + H_2O \rightarrow 2OH^-$ reaction.

Using the value calculated by the DFT approach for the addition of twelve water molecules to the equivalent α-alumina {0001} surface as in equation 4.1 of $\Delta H_r = -12.274$ eV, the Born-Haber cycle can be used to define the $E_{correction}$ value:

$$E_{correction} = E_{oxide} + \Delta H_r - E_{hydroxide} \qquad\qquad \text{Equation 4.2}$$

Where $E_{oxide} = -1259.9361$ eV and $E_{hydroxide} = -1408.5958$ eV from CASTEP calculations. The calculated value for $12 \times E_{correction}$ is 136.386 eV for the reaction of twelve water molecules onto the {0001} α-alumina surface. Therefore the $E_{correction}$ value for a single water molecule is:

$$E_{correction} = 11.366 \text{ eV} \qquad O^{2-} + H_2O \rightarrow 2(OH)^- \qquad \text{Equation 4.3}$$

This compares to the value calculated by Nygren, Gay and Catlow [3] in 1997 using the atomistic MARVIN code [4] of 4.365 eV and a further value of -9.74 eV calculated by Catlow in 1977 using a thermodynamic method.[5] Once this value had been established, it is possible to vary the concentration of hydroxyl groups on the surface and therefore, by definition, the number of reacting water molecules required to achieve the reaction. With the value of $E_{correction}$ now known the Born-Haber cycle in figure 4.9 can be used to calculate the energies of reaction directly for any surface coverage of hydroxyls without recourse to DFT simulations for each structure.

4.4 Progressive hydroxylation of the {0001} α-alumina surface.

4.4.1 {0001} surface.

For the simulations and results discussed in this section, a different α-alumina {0001} surface unit cell originating from previous unpublished METADISE two-dimensional simulations was used.[6] To overcome a smaller vacuum gap used in the original calculations, the c-parameter was increased to 30 Å – a vacuum gap of 10 Å above a slab of 20 Å deep with the lattice parameters shown in table 4.6.

To obtain the relaxed clean surface prior to hydroxylation, the hexagonal alumina unit cell was doubled in the b direction to give $a = b = 9.6358$ Å. This expansion gave a unitcell of $Al_{72}O_{108}$, terminated with four aluminium atoms on each surface in the Al1 layer. This stoichiometry was used due to the convergence of the surface energy with an increasing slab thickness, as shown in table 4.8; this follows the work of Bankhead et al shown in table 4.7.[6] As can be seen from table 4.8, surface energy convergence is reached in the slab containing nine oxygen layers; this is a slab of $Al_{72}O_{96}$, where the thickness counters any interface interference across the slab. Between the slabs containing nine and twelve oxygen layers there are comparable percentage relaxations for the first four layers of the {0001} surface. The thicker slab took 311 s to optimise, compared against the nine layered slab of 169 s, with the longer calculation offering no improvement in precision for surface energy and relaxation values. Figure 4.10 shows the optimised nine layered slab, showing the relaxed positions of the four aluminium Al1 layer atoms towards the O2 oxygen layer.

Lattice parameter	Magnitude
a [Å]	9.6358
b [Å]	4.8179
c [Å]	30.0000
Volume [Å^3]	1206.14

Table 4.6. Lattice parameters for the optimised aluminium terminated α-alumina {0001} slab used in previous METADISE calculations.[6]

The percentage relaxations detailed in table 4.8 compare favourably with the results obtained using the periodic density functional theory method embodied in the CASTEP code, shown in chapter five in table 5.8. The top layer Al1-O1 relaxation is -86.53 % in this work against -85.12 % for the CASTEP calculation in chapter five and -86.9 % for the {0001} α-alumina slab shown in section 4.2, providing a better approximation than the literature molecular mechanics determined value of -58 % in section 1.2.3.[7] An overestimation occurs in the second relaxation for O1-Al2 of +14.75 %, where the majority of density functional theory methods find this value to be less than 5 %. The next two relaxations for Al2-Al3 and Al3-O2 measure well against the experimental work and the majority of density functional theory, Hartree-Fock and atomistic potentials simulations. All calculations in this section were optimised using the BFGS method of minima searching.

Thickness of slab/oxygen layers	Percentage Al1-O1 relaxation	Surface energy $J\,m^{-2}$
3	-85.14	1.75
6	-84.95	1.84
12	-73.74	2.09

Table 4.7. Effect of increasing the slab thickness on the degree of layer relaxation and surface energy.[6]

Thickness of slab/oxygen layers	Unrelaxed surf. energy $J\,m^{-2}$	Relaxed surf. energy $J\,m^{-2}$	Layer	Percentage relaxation
3	6.544	2.262	Al1-O1	-96.6%
			O1-Al2	+18.9%
			Al2-Al3	-48.09%
			Al3-O2	+35.18%
6	6.604	2.409	Al1-O1	-86.05%
			O1-Al2	+15.44%
			Al2-Al3	-36.71%
			Al3-O2	+24.74
9	6.662	2.410	Al1-O1	-86.49%
			O1-Al2	+14.78%
			Al2-Al3	-35.6%
			Al3-O2	+23.99%
12	6.719	2.410	Al1-O1	-86.53%
			O1-Al2	+14.75%
			Al2-Al3	-35.57%
			Al3-O2	+23.97%

Table 4.8. Effect of increasing the slab thickness on the unrelaxed and relaxed surface energies along with the degree of layer relaxation for the first four layers; Al1, O1, Al2, Al3 and O2 for the geometrically optimised slab.
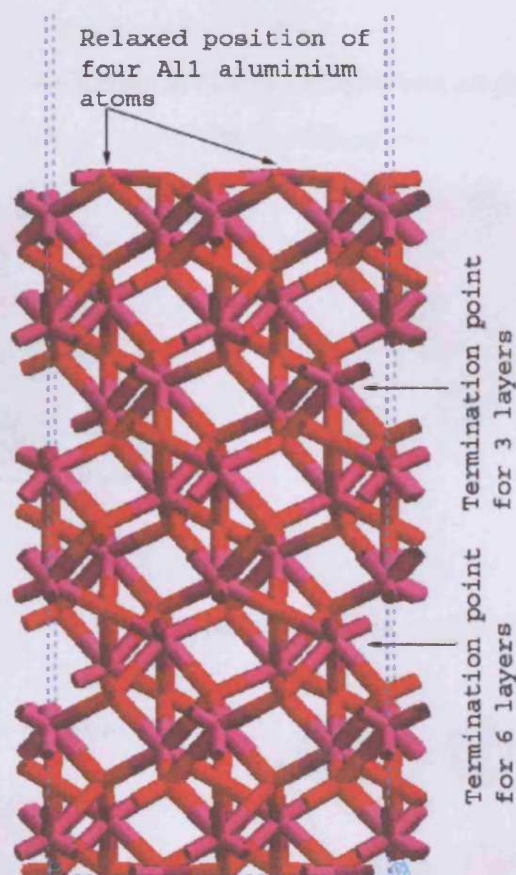
Figure 4.10. Minimised nine oxygen layer α-alumina {0001} slab, showing the relaxed positions of the four aluminium terminating Al1 layer atoms on each surface. From this structure, the repeat unit for the three and six oxygen layer slabs can be seen.

Using the same procedure for hydroxylation of the α-alumina {0001} surface as outlined in section 4.3, the two Al1 layers on the two slab interfaces were removed; a total of eight across the unit cell. This left a fully oxygen (O2 layer) terminated slab. Figures 4.11a and 4.11b illustrate the steps in moving from an $Al_{72}O_{108}$ slab to an non-stoichiometric $Al_{64}O_{108}$ slab. With this oxygen terminated surface slab, twelve oxygen atoms (six on each surface) in the unit cell were removed to attain stoichiometry of $Al_{64}O_{96}$. This resulted in six oxygen atoms left on each surface, and the configuration of these removals and subsequent hydroxylation gave a range of slabs being simulated to reduce errors and obtain an average value for the lattice energy, $E_{hydroxide}$.

a)

$Al_{72}O_{108}$ $\rightarrow$ Removal of four Al1 aluminium atoms on   b) $Al_{64}O_{108}$

both surfaces $\rightarrow$

Al1 layer
terminating
aluminium

O1 oxygen
subsurface layer

Al2 layer
subsurface
aluminium

O1 oxygen
terminating layer

$\downarrow$

Removal of six oxygen atoms on both surfaces

d)

c) $\downarrow$ $Al_{64}O_{96}$

Al2 layer aluminium atom, exposed for
an incoming adsorbate

Oxygen O1 layer atoms
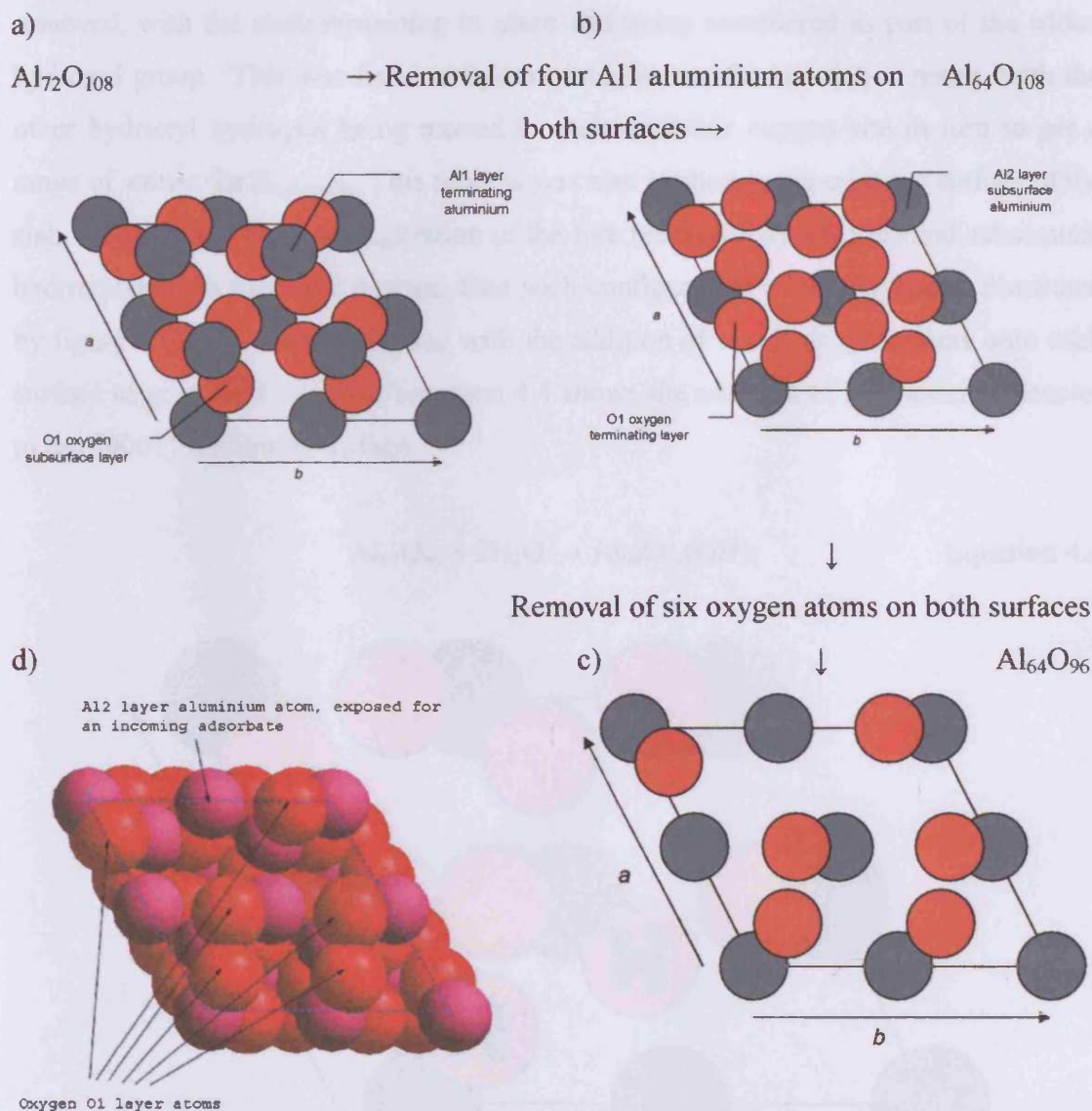
Figure 4.11. Schematic illustration of the process of constructing the oxygen surface for hydroxylation by the removal of eight aluminium atoms in Al1 (a) to leave an non-stoichiometric slab (b) and one possible conformation the resultant slab may take (c). (d) Shows the appearance of this slab as a plan view.

4.4.2   Addition of hydroxyl groups.

The formation of a hydroxylated surface can now be thought of as the addition of water to the exposed surfaces in figure 4.11c. For example, the adsorption of two water molecules to the {0001} α-alumina slab by the addition of one molecule to each surface, results in the hydroxylation of one surface oxygen site in figure 4.11c, and the addition of a hydroxyl OH⁻ to a Lewis acid aluminium site. Instead of removing all six surface oxygen atoms in the method illustrated by figure 4.11a-c, five oxygen atoms were

135

removed, with the sixth remaining in place and being considered as part of the added hydroxyl group. This was fixed as hydroxylated across the simulation series, with the other hydroxyl hydrogen being moved to each available oxygen site in turn to get a range of values for $E_{hydroxide}$. This process was also applied to the opposite surface of the slab, retaining the same configuration of the five removed oxygen sites and subsequent hydroxylation as the other surface. One such configuration of the surface is illustrated by figure 4.12; this slab is $Al_{64}O_{98}$, with the addition of two hydrogen atoms onto each surface to give $Al_{64}O_{94}(OH)_4$. Equation 4.4 shows the addition of two water molecules to the {0001} α-alumina surface.
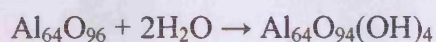
$$Al_{64}O_{96} + 2H_2O \rightarrow Al_{64}O_{94}(OH)_4 \qquad \text{Equation 4.4}$$
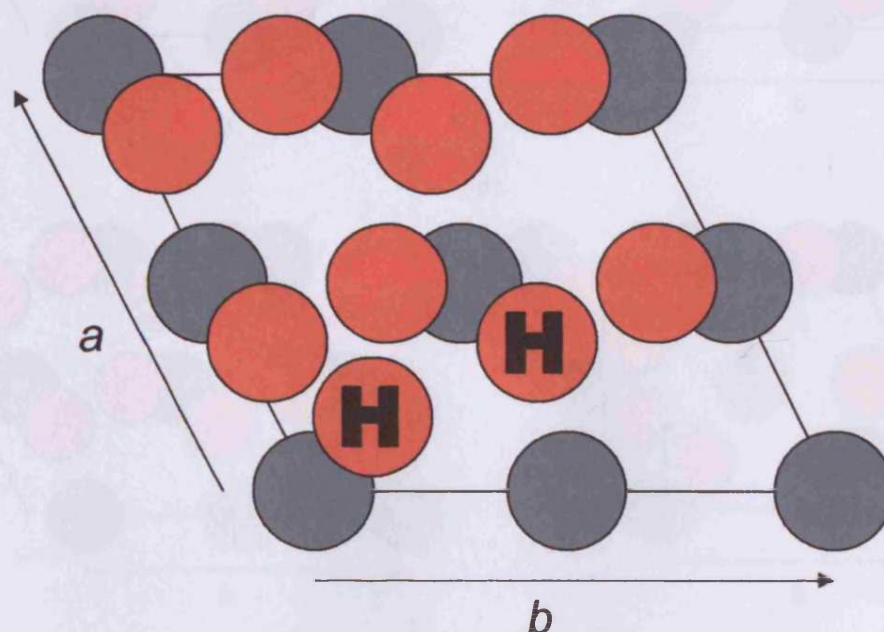
Figure 4.12. Plan view of one possible full-size top surface structure with seven surface oxygen atoms. Two of these oxygen atoms are hydroxylated by placing a hydrogen atom 1 Å directly above into the vacuum gap, as illustrated by **H**. *Oxygen is coloured red and aluminium atoms from the Al2 layer coloured grey.*

For the addition of four water molecules to the system, shown by equation 4.5, figures 4.13a-d schematically illustrate four oxygen terminating structures prepared for the addition of four hydrogen atoms to this surface of the slab and four to the opposite surface on the same oxygen sites. Four hydroxyl groups exist on each surface, yielding 50% coverage. The hydroxylated slab is constructed by removing four oxygen atoms on

136

each surface. A hydrogen atom was placed 1 Å above four of the oxygen atoms remaining. Moving the hydrogen atoms to alternate oxygen sites ensures that an average value for the $E_{hydroxide}$ may be obtained.

$$Al_{64}O_{96} + 4H_2O \rightarrow Al_{64}O_{92}(OH)_8 \qquad \text{Equation 4.5}$$

a)

b)

c)

d)
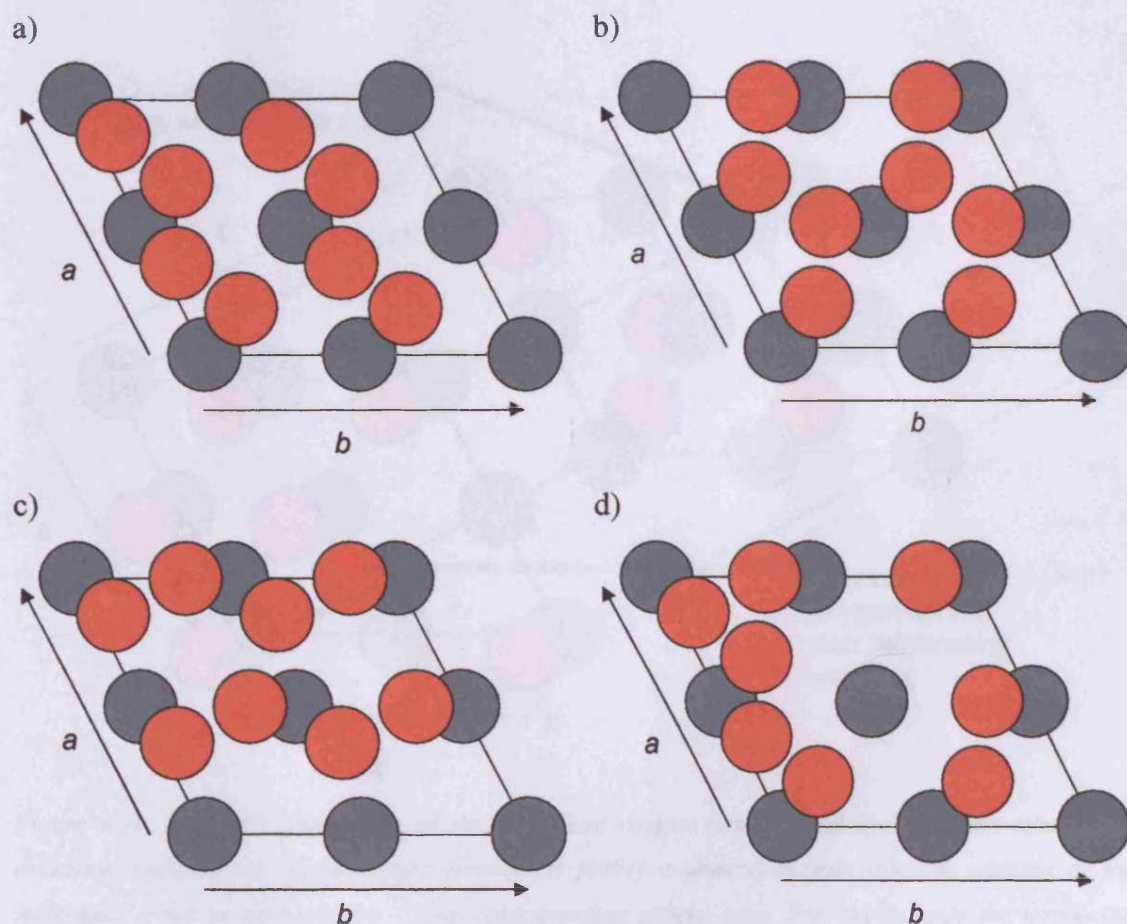
Figure 4.13a-d. Four possible structures for the oxygen terminating surface, four of which are hydroxylated, giving eight in all in the unit cell. Two of these oxygen atoms can be considered to be from adsorbed water, and remain hydroxylated with two other oxygen sites possessing a hydrogen atom each in sequence. The resultant hydrogen atoms are omitted for clarity.

A symmetry element was imposed on the unit cell for the construction of the starting geometries for all calculations described within this section to ensure that the two surfaces of the slab are geometrically equivalent. This was achieved by removing oxygen atoms in equivalent positions, hydroxylating equivalent oxygen sites and moving hydrogen atoms in sequence to equivalent oxygen sites. This is shown by figure

137

4.14, in which only the two surface terminations essential for understanding are shown at the vacuum gap interfaces. For example, in an arbitrary configuration for the construction of two hydroxyl groups on each surface, five equivalent oxygen atoms are removed on both surfaces, leading to the addition of hydrogen to the two equivalent oxygen sites shown, followed by a similar method for the third and fourth hydrogens. It is apparent from figure 4.14 which oxygen sites are equivalent.
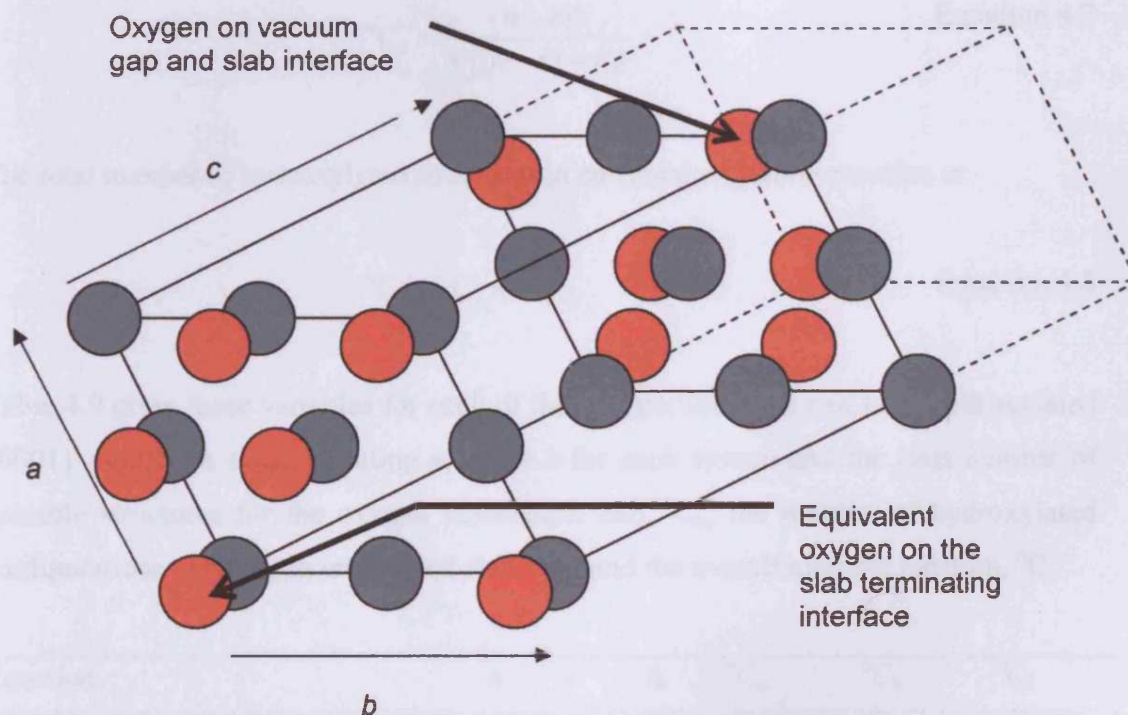
Figure 4.14. Schematic illustration of the equivalent oxygen removal and hydroxylation sites for an arbitrary configuration of the oxygen terminated {0001} α-alumina surface prior to addition of four hydrogens – two to each surface – onto corresponding oxygen sites. For clarity, only the terminating oxygen and subsurface aluminium layers are shown on both interfaces.

The number of possible oxygen terminated structures is given by ^nC_o, defined by equation 4.6, in which n is the number of available oxygen sites per surface prior to removal, this is 12 for all simulations, as given by figure 4.11b. The second variable is r, the number of oxygen sites to be removed to obtain the oxygen terminated surface to be hydroxylated:

$$^nC_o = \frac{n!}{r!(n-r)!}$$

Equation 4.6

From this, the total number of hydroxyl group arrangements per oxygen terminated slab can be calculated, ^nC_h, defined by equation y, in which h is the number of hydroxyl groups to be added per surface to gain a stoichiometric slab:

$$^nC_h = \frac{(n-r)!}{h!((n-r)-h)!}$$

Equation 4.7

The total number of hydroxylated structures in each hydroxylation reaction is:

$$^nC_t = {}^nC_o \times {}^nC_h$$

Equation 4.8

Table 4.9 gives these variables for each of the five partially and one fully hydroxylated {0001} α-alumina slabs, detailing n, r and h for each system and the total number of possible structures for the oxygen terminated slab, ^nC_o, the number of hydroxylated configurations per oxygen terminated slab, ^nC_h, and the overall total per reaction, ^nC_t.

Reaction	n	r	h	^nC_o	^nC_h	^nC_t
$Al_{64}O_{96} + 2H_2O \rightarrow Al_{64}O_{94}(OH)_4$	12	5	2	792	21	16 632
$Al_{64}O_{96} + 4H_2O \rightarrow Al_{64}O_{92}(OH)_8$	12	4	4	495	70	34 650
$Al_{64}O_{96} + 6H_2O \rightarrow Al_{64}O_{90}(OH)_{12}$	12	3	6	220	84	18 480
$Al_{64}O_{96} + 8H_2O \rightarrow Al_{64}O_{88}(OH)_{16}$	12	2	8	66	45	2790
$Al_{64}O_{96} + 10H_2O \rightarrow Al_{64}O_{86}(OH)_{20}$	12	1	10	12	11	132
$Al_{64}O_{96} + 12H_2O \rightarrow Al_{64}O_{84}(OH)_{24}$	12	0	12	1	1	1

Table 4.9. Values for n, r and h giving ^nC_o ^nC_h and ^nC_t according to equations x, y and z, where ^nC_t is the total number of structures possible for each hydroxylation reaction.

For the six reactions carried out, one oxygen terminated surface out of the number of configurations possible, ^nC_o was chosen. Using this slab, every combination for the hydroxyl group arrangement was modelled, yielding the total number of structures calculated in this work as ^nC_h for the partially hydroxylated slabs, whereas for the

hydroxylated slab with ten hydroxyl groups per surface ($Al_{64}O_{86}(OH)_{20}$), every permutation was simulated.

4.4.3 Energetics of the progressive hydroxylation.

Using the Born-Haber cycle in figure 4.9, a modified scheme was constructed to represent the progressive hydroxylation of the $Al_{64}O_{96}$ {0001} slab, this is shown in figure 4.15. With the $E_{correction}$ value of 11.366 eV per water molecule found by equation 4.3 for the addition of twelve water molecules to a {0001} α-alumina slab, this can be multiplied by n to represent the construction of any number of hydroxyl groups formed on the surfaces, and therefore the energy of hydroxylation may be calculated by using the $E_{hydroxide}$ lattice energy for each structure referred against the lattice energy of the oxide surface, E_{oxide}. The lattice energies, E_{oxide} and $E_{hydroxide}$ are extracted directly from the GULP output file.

$$\Delta H_H = \frac{-E_{oxide} + nE_{correction} + E_{hydroxide}}{n}$$ Equation 4.9

$$Al_{64}O_{96\,(s)} + 12H_2O_{\,(g)} \xrightarrow{\quad n\Delta H_H \quad} Al_{64}O_{96-n}(OH)_{2n\,(s)}$$

$$\uparrow E_{oxide} \qquad\qquad\qquad\qquad \uparrow E_{hydroxide}$$

$$64Al^{3+}_{\,(g)} + 96O^{2-}_{\,(g)} + nH_2O_{\,(g)} \xrightarrow{\quad nE_{correction} \quad} 64Al^{3+}_{\,(g)} + 96O^{2-}_{\,(g)} + 2n(OH^-)_{\,(g)}$$
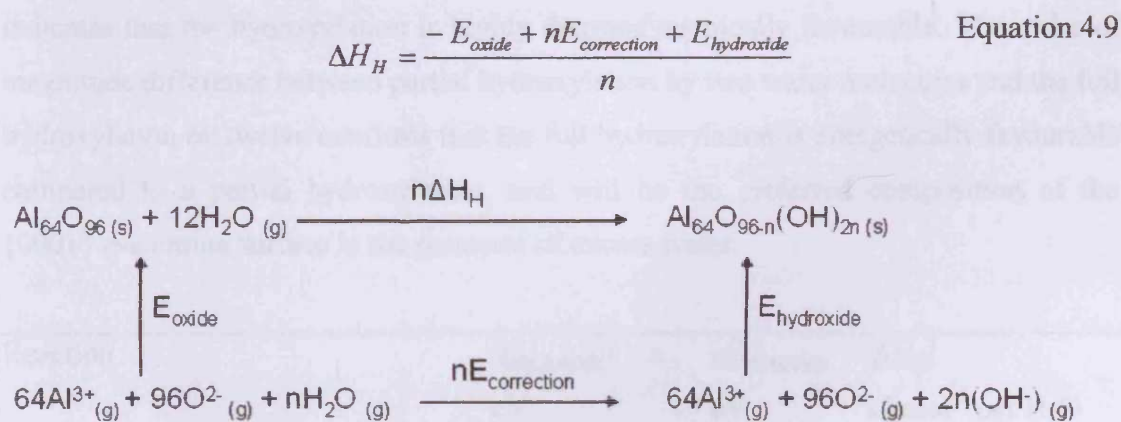
Figure 4.15. Modified Born-Haber cycle for the formation of the oxide and water reactants from the constituent atoms, represented by E_{oxide} lattice energy, and the relationship to the formation from this of the hydroxylated product, with energy change ΔH_H. Alternatively, the hydroxide may be formed from the constituent atoms as shown by $E_{hydroxide}$.

4.4.4 Results of the progressive hydroxylation of the {0001} α-alumina surface.

Table 4.10 shows the reactions considered in these simulations, the range of $E_{hydroxide}$ lattice energy values and the calculated energy of hydroxylation range for each reaction.

The E_{oxide} lattice energy value for the $Al_{64}O_{96}$ is -5080.113 eV. Equation 4.9 is used to calculate the energy of hydroxylation value.

Amongst the surface configurations possible for each hydroxylated slab, there was found to be a wide distribution of the ΔH_H values as shown in figure 4.16. For example, the addition of two water molecules to the slab results in energy of hydroxylation values between 554 kJ mol^{-1} and 706 kJ mol^{-1} per water molecule across the range of simulated slabs. These values exceed the range of *ca.* -210 kJ mol^{-1} to *ca.* -450 kJ mol^{-1} found for the low coverage of hydroxyl groups on the {0001} α-alumina surface, where one-third of the available sites are hydroxylated.[6] Generally, it is seen from the hydroxylation energies in table 4.10 that an increase in the number of water molecules added to the system yields a decrease in the energy of hydroxylation, to the extent that addition of twelve water molecules to create a fully hydroxylated surface containing twenty four hydroxyl groups split equally between the two surfaces has an energy of -222 kJ mol^{-1} per water molecule. A negative value as shown for all configurations investigated indicates that the hydroxylation is highly thermodynamically favourable. The order of magnitude difference between partial hydroxylation by two water molecules and the full hydroxylation by twelve confirms that the full hydroxylation is energetically favourable compared to a partial hydroxylation, and will be the preferred composition of the {0001} α-alumina surface in the presence of excess water.

Reaction	$|E_{hydroxide}|$ eV	n	$nE_{correction}$ eV	$|\Delta H_H|$ kJ mol^{-1} per H_2O
$Al_{64}O_{96} + 2H_2O \rightarrow Al_{64}O_{94}(OH)_4$	-5089.78	2	22.732	670
$Al_{64}O_{96} + 4H_2O \rightarrow Al_{64}O_{92}(OH)_8$	-5126.95	4	45.464	187
$Al_{64}O_{96} + 6H_2O \rightarrow Al_{64}O_{90}(OH)_{12}$	-5150.11	6	68.196	-20
$Al_{64}O_{96} + 8H_2O \rightarrow Al_{64}O_{88}(OH)_{16}$	-5180.79	8	90.928	-106
$Al_{64}O_{96} + 10H_2O \rightarrow Al_{64}O_{86}(OH)_{20}$	-5212.31	10	113.66	-176
$Al_{64}O_{96} + 12H_2O \rightarrow Al_{64}O_{84}(OH)_{24}$	-5244.1	12	136.392	-222

Table 4.10. ΔH_H, the energy of hydroxylation per water molecule, for the progressive hydroxylation of the α-alumina {0001} surface, showing the six reactions; the average $E_{hydroxide}$ lattice energies and n, which is the multiplication for the $E_{correction}$ value of 11.366 eV.

As there can be only one structure for the fully hydroxylated surface, the proximity of this value to the immediate precursor state of twenty hydroxyl groups qualifies the precision of the method used. This energy of hydroxylation of the ten water reaction is within 50 kJ mol^{-1} of the final fully hydroxylated slab energy, again emulating the results found for previous work on this system, which are summarised in table 4.11. Compared to the CASTEP determined value for the fully hydroxylated surface, as -99 kJ mol^{-1} described in chapter five, this value of -222 kJ mol^{-1} is more negative, although a thicker slab was used in these GULP calculations.

$E_{correction}$ per H_2O	-7.943 eV	
Hydroxylation coverage	Number of water molecules	Range of ΔH_H kJ mol^{-1}
One-third	1	ca. -210 to ca. -450
Two-thirds	2	ca. -600 to ca. -700
Full	3	ca. -1000

Table 4.11. Distribution of ΔH_H for the addition of one, two and three water molecules to an α-alumina {0001} surface leading to full hydroxylation in the work of Bankhead et al. The value of $E_{correction}$ per water dissociation is also shown.[6]

Figure 4.16 illustrates the distribution of the calculated hydroxylation energies for the complete series of water additions to the surface. It is immediately obvious that the largest deviation in ΔH_H values occurs for the two water process, this is due to the relatively defective nature of the {0001} surface as shown in figure 4.11d, where there is the possibility of aggregation of oxygen sites to leave edges and accessible unsaturated Lewis acid aluminium sites from the sub-surface layer as illustrated schematically in figure 4.13d. Hydroxylation at the lower coverages, especially the addition of one water molecule to each surface, does not classify the defective nature of the slab, which is oxygen terminated and unstable. With the introduction of more hydroxyl groups, the stabilising effect of these reduces the oxygen terminating character, which is thermodynamically favourable. The large number of unfavourable oxygen terminated regions account for the wide range of energy values in the low hydroxyl coverage slabs in figure 4.16 and the large difference in calculated

hydroxylated energy for low and high coverages. For higher coverages of hydroxyl groups, there is less variation in the range of energies of reaction.

Figure 4.17 shows the average values for each of the six surface coverages modelled; with the range of energies of hydroxylation for each series adding a further two water molecules to the surface. It is apparent that this deviation from the average ΔH_H value reduces with increasing coverage across the series of calculations. Table 4.12 shows the change in the average ΔH_H value per water molecule with every addition of one further molecule per surface.
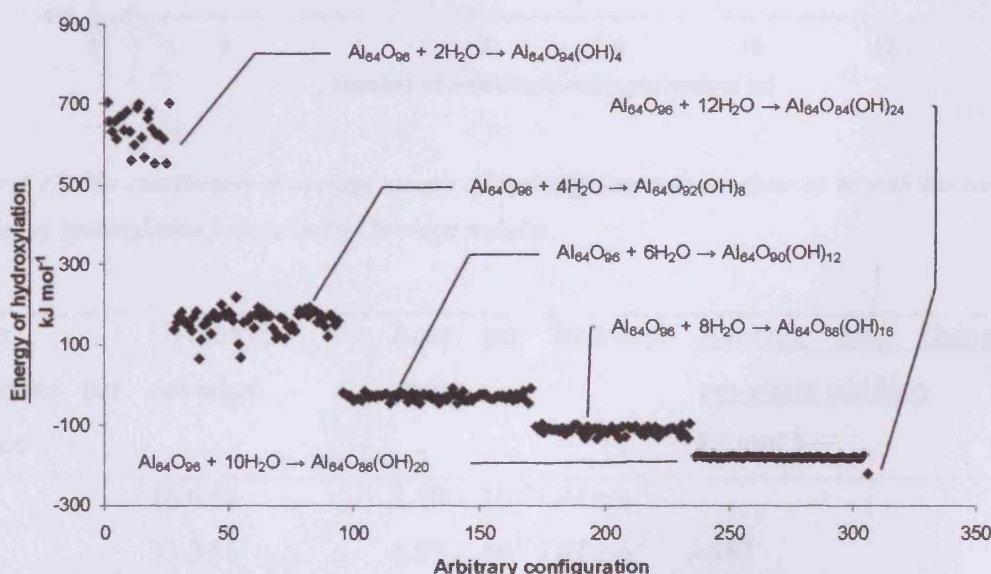
Figure 4.16. Distribution plot of ΔH_H per water molecule for the unique arbitrary configurations calculated for the six water addition reactions.

Table 4.12 shows that the largest rise in the average ΔH_H value is the addition of the second water molecule to each {0001} surface with one existing hydroxyl group. The change is less pronounced as the hydroxyl group coverage increases towards full hydroxylation of twelve groups per surface, where the change is 45 kJ mol^{-1} less than the average value found for ten hydroxyl groups per surface: 83.3 % hydroxyl coverage.

143
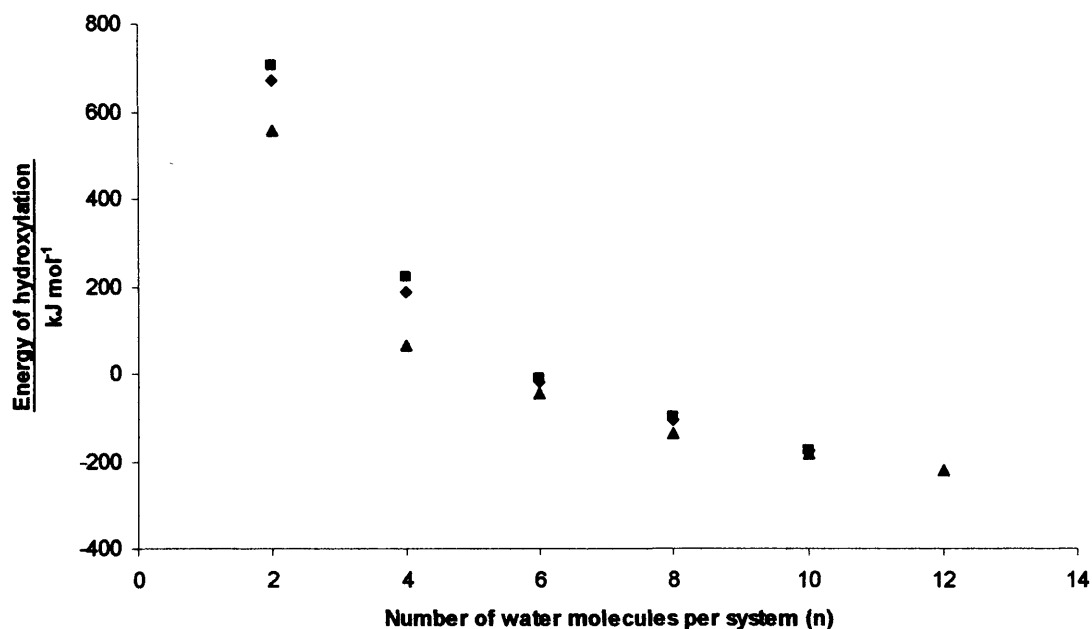
Figure 4.17. The distribution of average energy of hydroxylation values, show as ♦, with the range of energies of hydroxylation for each series between ■ and ▲.

Water molecules per surface	Hydroxyl coverage	Area per hydroxyl group	Average ΔH_H change per water addition kJ mol^{-1}
1	16.6 %	$2.48 \times 10^{14} \, OH \, cm^{-2}$	
2	33.3 %	$4.97 \times 10^{14} \, OH \, cm^{-2}$	-483
3	50 %	$7.45 \times 10^{14} \, OH \, cm^{-2}$	-207
4	66.6 %	$9.93 \times 10^{14} \, OH \, cm^{-2}$	-86
5	83.3 %	$1.24 \times 10^{15} \, OH \, cm^{-2}$	-70
6	100 %	$1.49 \times 10^{15} \, OH \, cm^{-2}$	-45

Table 4.12. Change in average energy of hydroxylation with the addition of one further water molecule to each surface leading to full hydroxylation with six molecules per surface.

Examples of the optimised surface slabs for the partial hydroxylation calculations are shown in figure 4.18a-f, with one minimised structure given for each addition of water in the reaction series, starting with two hydroxyl groups on each surface progressively up to the fully hydroxylated slab. The illustration of the slab containing two hydroxyl groups on each surface in figure 4.18a portrays the predominantly oxygen character of

this defect slab, a situation that is unstable where the presence of two hydroxyls is insufficient to stabilise the slab. In 4.18a, as described in section 4.4.2, it is clear to see the seven oxygen atoms remaining after the removal of five oxygen sites. Two of the remaining seven are hydroxylated by the addition of a hydrogen atom to simulate the addition of one water molecule per surface. With the addition of further water molecules, the oxygen termination effect is lessened; therefore stabilisation of the slab is reached along the series up to full hydroxylation. Figure 4.18b is a picture of one of the alternate surfaces that result from the four oxygen terminated slabs in figure 4.13a-d and following equation 4.5. Figure 4.18e clearly shows the removed oxygen site in the bottom right corner of the slab to construct a stoichiometric slab. Figure 4.18c illustrates the presence of a step defect in the surface, created by the removal of three oxygen sites in the bottom right corner of the slab, although it is noticeable from the six slabs that vacant sites decrease along the series, with figure 4.18f, the fully hydroxylated slab, containing no vacancies in the unit cell. At the higher coverages, the proximity of the hydroxyl groups allows the formation of local hydrogen bonding like interactions. This may also be a stabilising factor at high hydroxyl coverages, which is only present in a few of the configurations at low coverages.

4.4.5 Surfaces energies for hydroxylated {0001} α-alumina surfaces.

Using a modification of the approach for finding the surface energy of a pure metal oxide surface as defined in chapter one, the surface energy, γ_s, may be calculated by:

$$\gamma_s = \left[\frac{E_{hydroxide} - (E_{bulk} + n\Delta H_H)}{2A} \right] \times 16.0219 \qquad \text{Equation 4.10}$$

This is justified by the use of the total energy of hydroxylation factor, in eV, for the reactions shown in table 4.10 to account for the energy of forming $E_{hydroxide}$ from a pure bulk α-alumina structure, E_{bulk} and thereby incorporates the chemical reaction energy into the equation.[3] The units must remain consistent across the equation, (eV). The 16.0219 value converts eV Å^{-2} to J m^{-2}. The calculated surface energy values are shown in table 4.11. It is seen that the most defective surfaces produce small positive values for γ_s. This method of calculating the surface energy for CASTEP determined data

produced the fully hydroxylated surface energy as 1.00 J m^{-2}, compared to -1.07 J m^{-2} with GULP.

a) $Al_{64}O_{94}(OH)_4$.
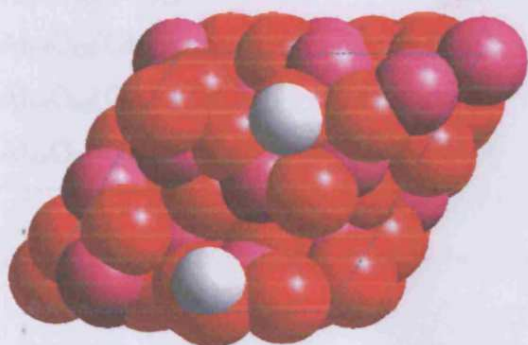
b) $Al_{64}O_{92}(OH)_8$
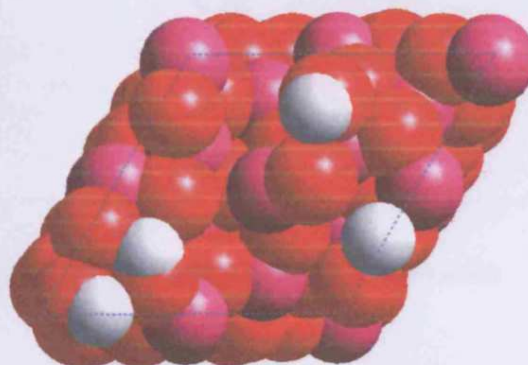
c) $Al_{64}O_{90}(OH)_{12}$
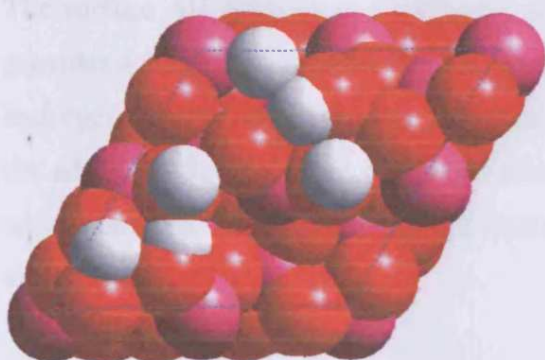
d) $Al_{64}O_{88}(OH)_{16}$
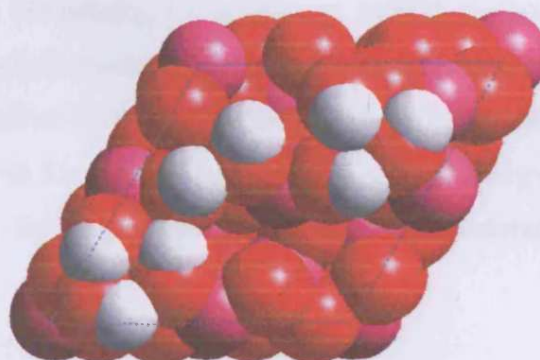
e) $Al_{64}O_{86}(OH)_{20}$
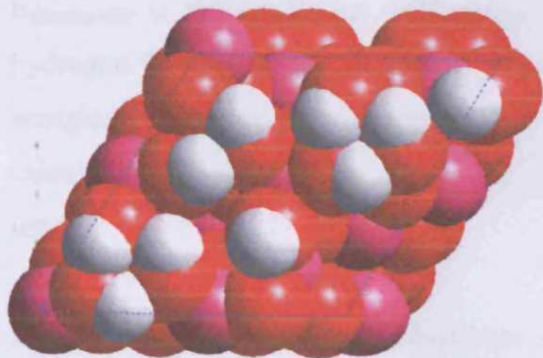
f) $Al_{64}O_{84}(OH)_{24}$
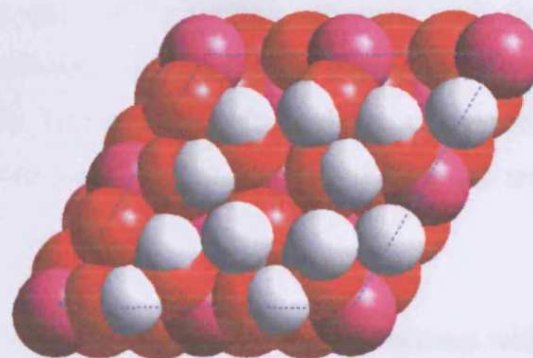
Figure 4.18. Minimised structures for one slab of each partial hydroxylation, a) shows one surface with two hydroxyls revealing the mainly oxygen character of this slab, b) shows four hydroxyls, c) shows six hydroxyls, d) shows eight hydroxyls, e) gives ten hydroxyls and f) shows twelve hydroxyls in the fully hydroxylated slab.

146

Hydroxylated slab	Total ΔH_H eV	Surface energy γ_s J m^{-2}
$Al_{64}O_{94}(OH)_4$	13.89	0.15
$Al_{64}O_{92}(OH)_8$	7.75	0.12
$Al_{64}O_{90}(OH)_{12}$	-1.24	0.32
$Al_{64}O_{88}(OH)_{16}$	-8.78	-0.56
$Al_{64}O_{86}(OH)_{20}$	-18.24	-0.82
$Al_{64}O_{84}(OH)_{24}$	-27.48	-1.07

Table 4.11. Surface energies for the series of partially and fully hydroxylated {0001} α-alumina slabs.

4.5   Adsorption of hydrogen fluoride.

The surface Al1 aluminium Lewis acid site terminating the α-alumina {0001} surface provides a surface adsorption site for nucelophilic molecular groups. To examine this, a hydrogen fluoride molecule was positioned directly above the surface aluminium with the adsorbate fluorine atom orientated towards the Al1 site and then the system energy was minimised. The enthalpy of adsorption for these simulation models is calculated via:

$$\Delta H_{adsorption} = E_{alumina+HF} - (E_{alumina} + E_{HF}) \qquad \text{Equation 4.11}$$

$E_{alumina+HF}$ is the calculated total energy for the {0001} surface optimised with the hydrogen fluoride molecule present in the unit cell, and $E_{alumina}$ and E_{HF} are the total energies for the individual components. The lattice parameters and the method of calculation remain constant across the reaction and constant volume calculations are used.

Initially, the hydrogen fluoride molecule was coordinated away from direct contact with the surface in the centre of the vacuum gap to give a reference energy without molecular-surface interactions.

The molecular adsorption of hydrogen fluoride onto an α-alumina surface may take place via one of three modes:

i.   A single aluminium to fluorine interaction.

ii. A single oxygen to hydrogen interaction.

iii. Two interactions: one between aluminium and fluorine and a second between oxygen and hydrogen.

A review of the literature for the adsorption of small diatomic species such as hydrogen fluoride and triatomic molecules such as water finds the third method of molecular adsorption (and chemisorption) may be subdivided into two further categories:[8] [9] [10]

i.   1-4 type adsorption, where the aluminium site with an adsorbed fluorine atom is denoted 1 with the oxygen at position 4 in the hexagonal ring system shown in figure 4.3 is the adsorption site for the hydrogen.

ii. 1-2 type adsorption. The hydrogen adsorbs onto the oxygen atom in position 2 in the hexagonal ring system.

An 1-4 type configuration of a molecularly adsorbed hydrogen fluoride is shown in figure 4.19, with the numbered atoms defined for the hexagonal ring system.
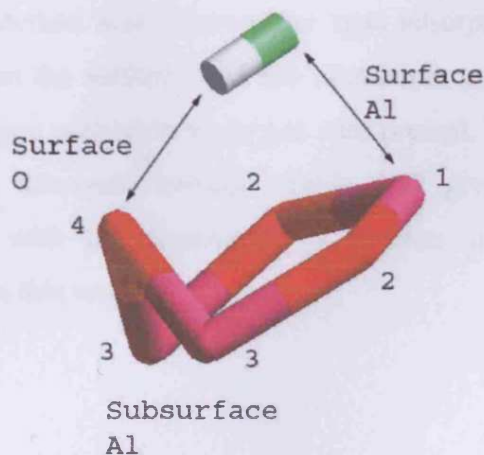
Figure 4.19. Nomenclature for adsorption of hydrogen fluoride onto the {0001} α-alumina surface, only the hexagonal ring system is shown for clarity. Here a 1-4 type adsorption is shown, as the hydrogen is bound to the oxygen at the position marked 4. For a 1-2 type adsorption, the hydrogen (shown in white) will interact with either of the oxygen sites marked 2.

The degree of overlap of the van der Waals radii is important in these simulations as an indication of the strength of local bonding interactions. So a series of calculations with various initial interatomic distances for F to Al1 was carried out. This distance was set between 5 and 0.5 Å to generate a range of stable adsorbed configurations and to show whether the initial distance has any influence over the mode of adsorption and/or the adsorption energy. To begin with, a model was constructed with the hydrogen fluoride molecule over 5 Å away from the surface to exclude any interaction of the surface and HF and ensure that the potentials used do not give unrealistic values for the system energy. This was repeated with alternative HF co-ordinates in the vacuum gap to ensure any errors were reduced. The values for the energy of adsorption calculated by equation 1 for this non-interacting case was between 0 and 3 kJ mol^{-1}, with the HF molecule remaining in the vacuum gap and not interacting with either of the slab's surfaces.

4.5.1 Adsorption of a single hydrogen fluoride molecule.

The starting orientation of the HF molecule in relation to the surface was also varied. Two starting orientations were considered: firstly, the HF molecule was set perpendicular to the surface, with the intention of promoting only the aluminium fluorine interaction whilst keeping the hydrogen as far from the oxygen sites as possible. The second method was a horizontal type adsorption mode, where the HF molecule is lying flat on the surface, with the aluminium and fluorine interaction and the interaction of hydrogen with surface oxygen sites present. The perpendicular manner of adsorption will be discussed initially. Table 4.12 gives the results found for adsorptions occurring with the aluminium to fluorine interaction dominating the adsorption interaction in this way.

Energy of adsorption	Final aluminium-fluorine distance
kJ mol^{-1}	Å
-50.6	2.140
-51.1	2.143
-51.2	2.147
-51.3	2.345
-52.5	2.362

Table 4.12. Energies of adsorption for the addition of hydrogen fluoride to an aluminium site, occurring through the aluminium and fluorine interaction.

As can be seen from the data in Table 4.12, the relaxed aluminium to fluorine distances range from 2.140 Å to 2.362 Å, with the energy of adsorption between approximately - 50 kJ mol^{-1} and -53 kJ mol^{-1}. There is no correlation between the final aluminium-fluorine distance and the energy of adsorption, and these are therefore independent of each other. For this series of calculations, it is evident that the aluminium atom is elevated away from the relaxed position in the minimised surface configuration, discussed earlier in this chapter, towards the incoming fluorine atom of the HF molecule. Figure 4.20 illustrates the three ring structures surrounding the adsorption site Al1 for the calculations with an adsorption energy of -52.5 kJ mol^{-1}, but does not show the HF molecule.

The data from figure 4.20 is compared with the clean surface in table 4.13, giving a direct indication of the effect of an adsorbate molecule introduced onto the Al1 adsorption site. Three ring system attached to the central Al1 atom, give an impression of the presence of HF beyond the immediate surface adsorption site.
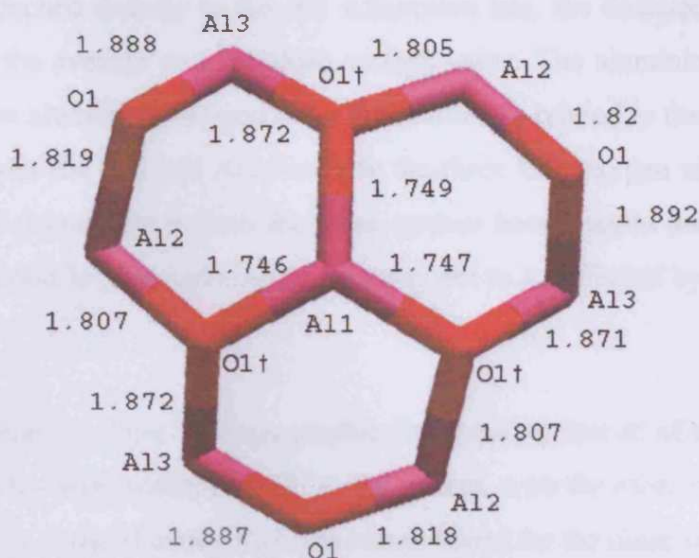
Figure 4.20. The optimised three-ring system surrounding the central adsorption site Al1, for the single interaction mode between aluminium and fluorine. HF is omitted for clarity. All distances in Angstroms.

Bond	Clean surface	Surface with HF adsorbate
	Å	Å
Al1-O1†	1.741	1.747
Al2-O1	1.818	1.812
Al2-O1†		1.806
Al3-O1	1.893	1.880
Al3-O1†		1.872

Table 4.13. Comparison between the average values of the three bond lengths, Al1-O1, Al2-O1 and Al3-O1 in the clean surface and when there is an adsorbed HF molecule interacting via a single Al1-F interaction.

Table 4.13 shows there is no significant deviation from the original values found for this surface earlier in this chapter when the isolated hexagonal system was considered. The Al1-O1† bonds increase marginally due to the elevation of the Al1 towards F, this is accompanied by the other two bond lengths existing in this ring system being shortened, on average. However, a closer analysis of figure 4.20 will give a discrepancy between the average bond lengths displayed in Table 4.13 and the actual bond lengths in the minimised structure. It is seen that for the Al2-O1† and Al3-O1† bonds, where the O1†

oxygen site is attached directly to the Al1 adsorption site, the distance is significantly lower than both the average and the clean surface value. The aluminium promotion is lessened when the aluminium-oxygen bond is not directly related to the adsorption site. Table 4.13 includes the Al2 and Al3 bonds to the three O1† oxygen sites immediately neighbouring Al1; compared to both the clean surface bond lengths and the other Al2-O1 and Al3-O1 bond lengths sufficiently far away not to be affected by the presence of HF.

Figure 4.21 summarises these findings graphically, showing that all of the O1† bonds to Al2 and Al3 shorten with addition of HF to the system, with the other Al2-O1 and Al3-O1 bonds deviating insignificantly from the values found for the clean surface.
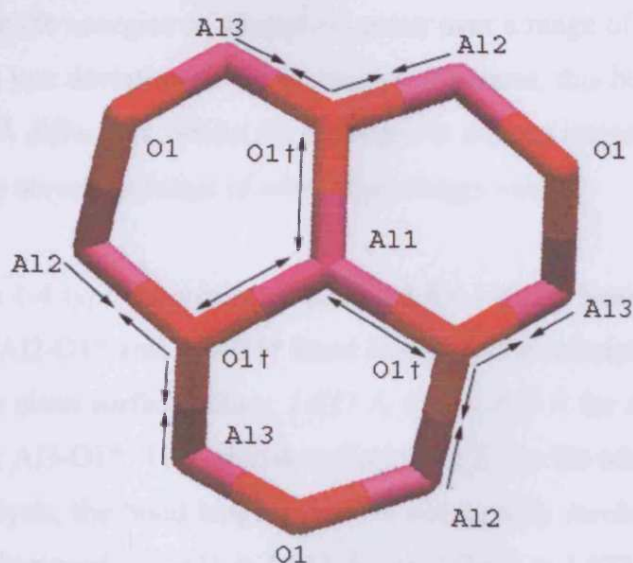
Figure 4.21. Qualitative description of the alteration in bond lengths from the clean surface structure. Al1 is the adsorption site, O1† is bound directly to this but in the end-on adsorption mode does not directly interact with HF. The arrows indicate that bond lengths increase (↔) or decrease (→←).

The planar adsorption of HF offers more initial configurations, with the choice of hydrogen towards the oxygen sites in either position 2 or 4 in figure 4.19. It is found across the series of simulations that the 1-4 mode is more energetically favourable; as to adsorb in this configuration does not sterically hinder HF interaction with the surface. Table 4.14 details the results of the planar adsorption of HF 1-4 configurations.

Energy of adsorption	Aluminium-fluorine distance	Oxygen-hydrogen distance
kJ mol^{-1}	Å	Å
-64.5	2.492	2.166
-64.7	2.393	2.065
-66.2	2.459	2.11
-66.9	2.431	2.146
-74.8	2.453	2.106
-74.9	2.442	2.062
-77.3	2.474	2.147

Table 4.14. Energies of adsorption for the 1-4 type adsorption, with the relevant interatomic distances.

Table 4.14 shows the energies of adsorption occur over a range of approximately 13 kJ mol^{-1}. There is a low deviation in the interaction distances, this being from 2.393 Å to 2.492 Å, *ca.* 0.1 Å difference, whilst the hydrogen to oxygen interactions show a similar close relationship across the range of adsorption energy values.

The effect of the 1-4 type adsorption is analysed for a single hexagonal ring system in figure 4.22. The Al2-O1* and Al3-O1* bond lengths to the adsorption site oxygen atom increase from the clean surface values, 1.827 Å from 1.818 Å for Al2-O1* and 1.907 Å from 1.893 Å for Al3-O1*. The asterisk indicates the O1 is the adsorption site. As with the previous analysis, the bond lengths that are not directly involved in the adsorption mechanism are shortened, Al2-O1 is 1.811 Å and Al3-O1 is 1.877 Å. The plan view of this configuration in figure 4.23 illustrates the lengthening and shortening of the bond lengths from their values in the aluminium terminated surface with no adsorbate interactions.
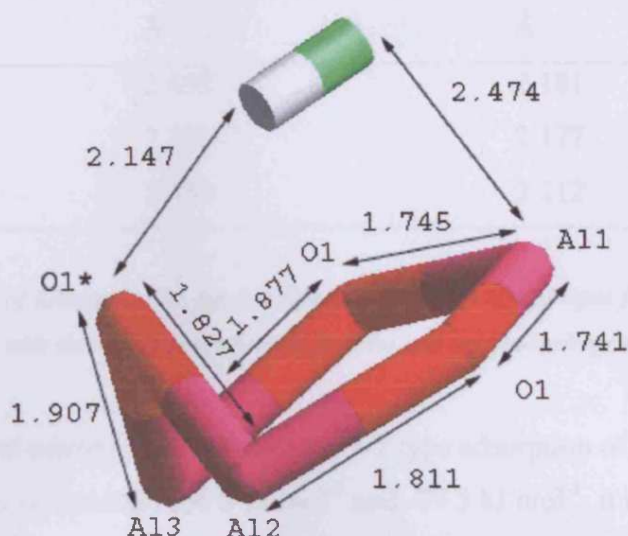
Figure 4.22. Interatomic distances for the 1-4 type with adsorption energy of -77.3 kJ mol⁻¹. All distances in Angstroms.
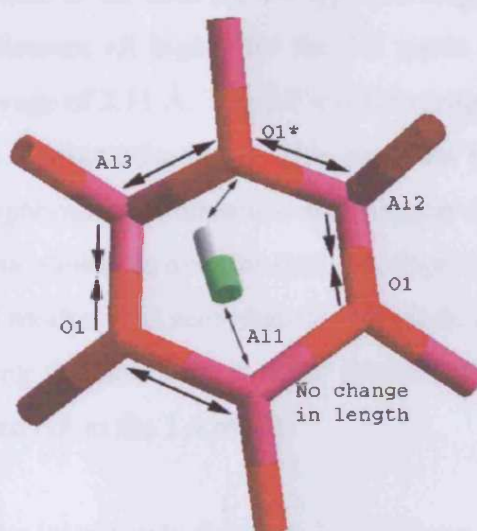
Figure 4.23. Plan view of the 1-4 type adsorption with adsorption energy of -77.3 kJ mol⁻¹. The arrows indicate that the bond length increases (↔) or decreases (→←) compared to the clean surface O1* indicates the adsorption site for H, whilst A11 is the adsorption site for F.

The alternative mode of adsorption for an HF molecule physisorbed onto the surface with interactions between both aluminium-fluorine and oxygen-hydrogen is in a 1-2 configuration; with the hydrogen adsorbing onto an oxygen site neighbouring the A11 adsorption site. Table 4.15 details the energies of adsorption and corresponding interatomic distances.

154

Energy of adsorption	Aluminium-fluorine	Oxygen-hydrogen
kJ mol⁻¹	Å	Å
-60.7	2.455	2.181
-54.1	2.366	2.177
-59.4	2.454	2.212

Table 4.15. Energies of adsorption for the 1-2 type physisorption of hydrogen fluoride onto the {0001} surface of α-alumina, with the resultant aluminium-fluorine and oxygen-hydrogen distances.

When the energy of adsorption values for the 1-2 type adsorption of HF are compared to the 1-4 type values of between -64.5 kJ mol⁻¹ and -77.3 kJ mol⁻¹, it is seen that all of the 1-4 adsorption structures have more favourable adsorption energies than the 1-2 mode. The most favourable value for 1-2 adsorption is approximately -61 kJ mol⁻¹ whilst for the 1-4 mode this is -77.3 kJ mol⁻¹. Table 4.15 gives the aluminium-fluorine distance at around the same magnitude as for both the 1-4 type and single Al-F physisorption, with the oxygen-hydrogen distance all higher for the 1-2 mode – an average of 2.19 Å – against the 1-4 type average of 2.11 Å. The 1-2 mode hydrogen-fluorine bond is slightly longer in line with the weaker adsorption. This confirms the geometric constraint of adsorbing HF onto neighbouring aluminium and oxygen sites, although this is only noticeable for interatomic distances and not energies. Figures 4.23a and 4.23b illustrate both of the 1-2 and 1-4 modes. It is seen that the 1-2 mode of adsorption forms a four-membered ring, meaning the structure is more strained than the six-membered ring formed with the adsorbed HF in the 1-4 mode.

Figure 4.25 illustrates the interatomic distances in the hexagonal ring systems in the 1-2 type adsorption with an adsorption energy of -60.7 kJ mol⁻¹. Table 4.16 compares the Al1-O1, Al2-O1 and Al3-O1 bond lengths for the 1-2 type adsorption against the equivalent distances found for the isolated hexagonal ring arrangement for the clean surface with no adsorbate.

a

b
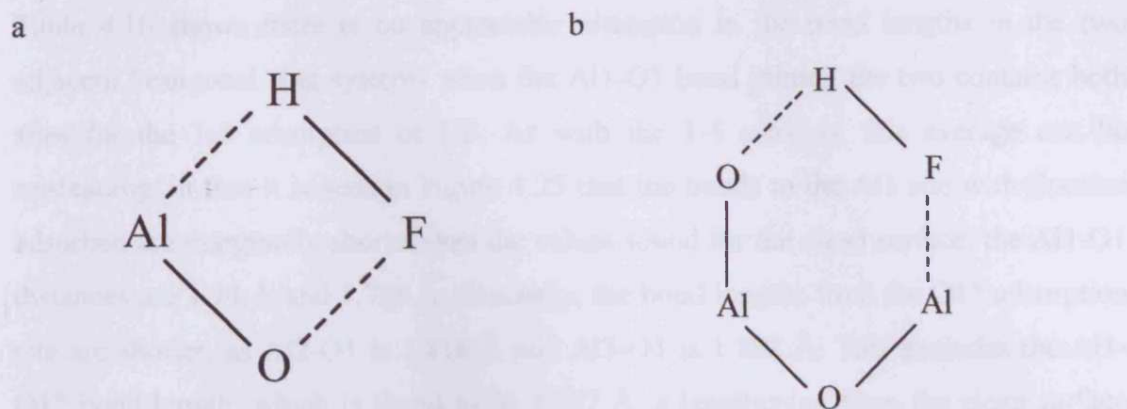
Figure 4.24. Schematic forms of the 1-2 mode of adsorption (a) and the 1-4 mode (b) for HF physisorbed onto the {0001} α-alumina surface.
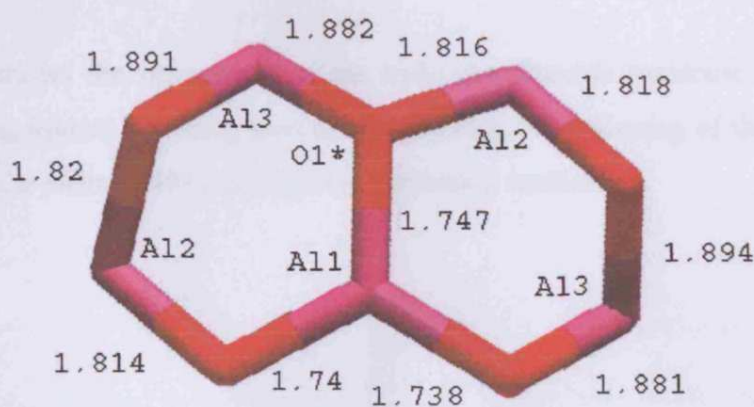
Figure 4.25. Bond lengths found for the two immediate hexagonal ring systems involved in a 1-2 type adsorption. O1* defines the hydrogen adsorption site, with fluorine adsorbing onto the Al1 site. HF is omitted for clarity. All lengths are in Angstroms.

Bond	Clean surface	1-2 HF adsorption distance average
	Å	Å
Al1-O1	1.741	1.742
Al1-O1*		1.747
Al2-O1	1.818	1.817
Al2-O1*		1.816
Al3-O1	1.893	1.887
Al3-O1*		1.882

Table 4.16. {0001} α-alumina surface bond lengths for the 1-2 adsorption of HF compared to the clean isolated ring system.

156

Table 4.16 shows there is no appreciable alteration in the bond lengths in the two adjacent hexagonal ring systems when the Al1-O1 bond joining the two contains both sites for the 1-2 adsorption of HF. As with the 1-4 analysis, this average can be misleading, in that it is seen in Figure 4.25 that the bonds to the Al1 site with fluorine adsorbed are marginally shorter than the values found for the clean surface; the Al1-O1 distances are 1.74 Å and 1.738 Å. Similarly, the bond lengths from the O1* adsorption site are shorter, as Al2-O1 is 1.816 Å and Al3-O1 is 1.882 Å. This excludes the Al1-O1* bond length, which is found to be 1.747 Å, a lengthening from the clean surface value of 1.742 Å, similar to the effect observed for the Al1-O1 bond lengths of the single interaction of fluorine onto the Al1 site shown in figure 4.20.

Figure 4.26 shows the orientation of the hydrogen fluoride molecule relative to the hexagonal ring system, showing also the lengthening or shortening of the surface bond lengths from the clean {0001} aluminium terminated surface.
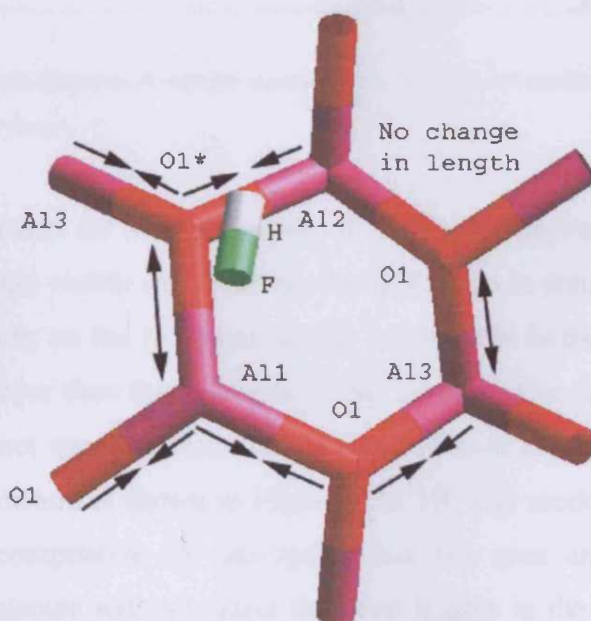
Figure 4.26. Surface structure of the 1-2 adsorption of HF onto Al1 and O1 sites, showing the orientation of the adsorbate molecule and the effect this has on the associated bond lengths in the {0001} surface hexagonal ring system. ↔ Signifies bond lengthening and →← indicates bond shortening. The energy of adsorption is -60.7 kJ mol^{-1}.*

4.5.2 Adsorption of additional HF.

Using the surface supercells constructed for this work, it is possible to adsorb more than one HF molecule simultaneously. An example of this with both 1-2 and 1-4 types of adsorptions is summarised in Table 4.17. The physisorption energy of -129.9 kJ mol^{-1} for two well separated HF molecules fit into the format discussed above: that the 1-4 aluminium-fluorine distance is marginally longer than in the 1-2 mode; due to the necessary movement of HF towards the O1 adsorption site at position four in the hexagonal ring to facilitate the 1-4 mode. The oxygen-hydrogen distance in the 1-4 type is again shorter than found for the 1-2 adsorption, as the averages for tables 3 and 4 indicate.

Adsorption mode	Aluminium-fluorine Å	Oxygen-hydrogen Å
1-2	2.390	2.248
1-4	2.444	2.089

Table 4.17. Interatomic distances found for simultaneous 1-2 and 1-4 modes of adsorption for HF on the {0001} α-alumina surface.

Figure 4.27 illustrates the side projection of the double physisorption of HF onto the {0001} surface, this visibly demonstrates the difference in distances found for the two adsorption methods; as the hydrogen in the 1-2 form is further from the terminating alumina surface layer than the hydrogen in the 1-4 type. The distance between the two HF molecules is not apparent from the side projection in Figure 4.27, the plan view of the minimised structure is shown in Figure 4.28. HF was modelled on these particular sites to ensure competition for adsorption was not seen and the influence of an additional HF molecule will not affect the bond lengths in the hexagonal ring system. Figure 4.28 illustrates the distance between the two adsorbates, with a possible alternate adsorption site showing the definitions of the 1-2 and 1-4 type adsorptions on the surface when the atoms are depicted as spheres.
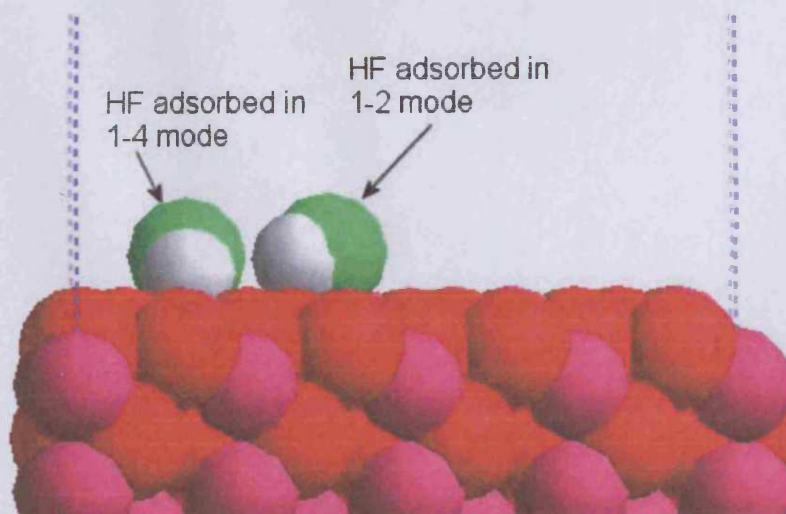
Figure 4.27. Side projection of HF adsorbed in both the 1-2 and 1-4 modes on the same slab of {0001} α-alumina. The energy of adsorption for this reaction is -129.9 kJ mol⁻¹.
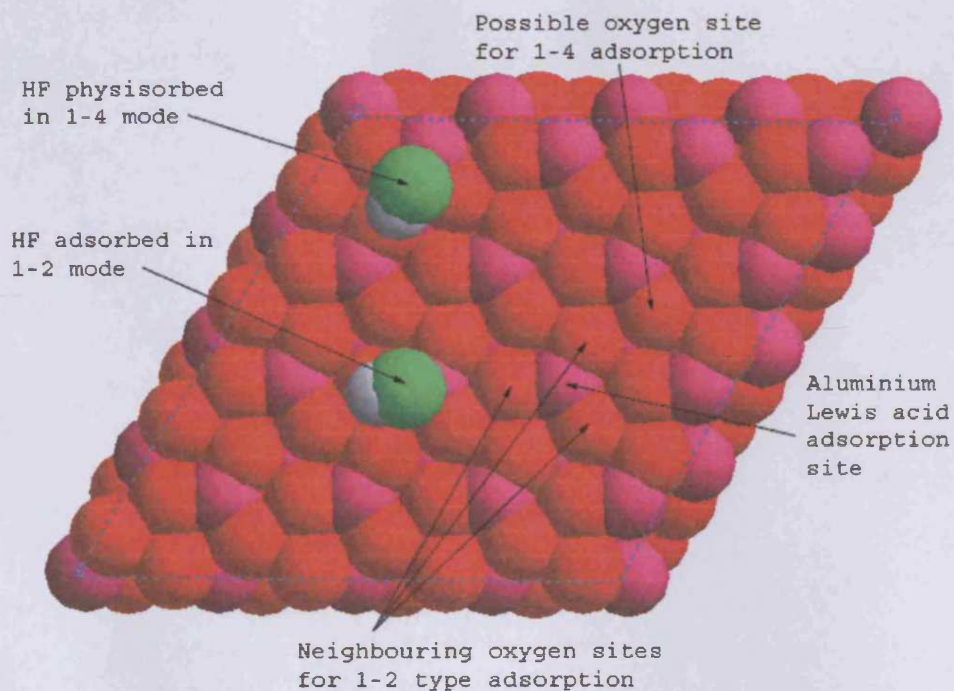
Figure 4.28. Illustration of the separation between the two physisorbed HF molecules on the {0001} α-alumina surface. Also shown is a generic aluminium Lewis acid adsorption site, surrounded by the three oxygen neighbours that would be involved in a 1-2 type adsorption, along with a possible oxygen site for a 1-4 type adsorption.

Neither figures 4.26 or 4.27 offers descriptions of the hexagonal ring system used throughout this chapter to describe the local α-alumina surface environment and bond lengths. Figure 4.29 shows part of the surface slab with the two HF molecules

physisorbed, this reinforces the distance between the HF adsorbates, far enough apart to not interfere with the other hexagonal ring structure, along with the bond distances. This is linked to the earlier observations that for the calculations with a single adsorption site, the surface atoms more than 2-3 bonds away from the adsorption site are unaffected by the presence of HF. This follows the trends outlined above for the bond distances neighbouring the adsorption sites Al1 and O1*, that these distances are increased if one of the atoms is involved directly in the adsorption of HF in the 1-4 mode. This compares with the 1-2 mode, in which the Al1-O1 bonds shorten, whilst the Al1-O1* bond lengthens along the coordination of the HF molecule.
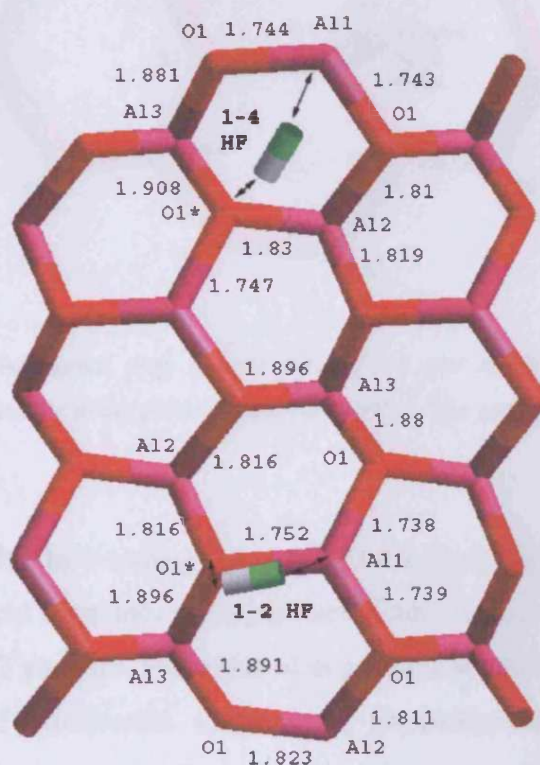
Figure 4.29. Annotated {0001} α-alumina surface shown with the network of interlinking hexagonal ring systems for the 1-2 and 1-4 physisorptions of two HF molecules. All distances in Angstroms. The Al-F and O-H distances are shown in table 4.19.

Using a model where the two HF molecules are physisorbed on neighbouring Al1 sites gives the energy of adsorption to be -117.8 kJ mol^{-1}. In contrast to the double adsorption with both 1-2 and 1-4 types observed, this double HF physisorption occurs with one 1-4 mode on the same site and a single aluminium-fluorine interaction in place of the previous 1-2 type. Figure 4.30 illustrates the proximity of these HF molecules and the

160

atom names for this minimised structure. Table 4.18 gives the bond lengths for the optimised structure combined with the average bond lengths found for the {0001} surface with both 1-2 and 1-4 type adsorptions shown in figure 4.29.
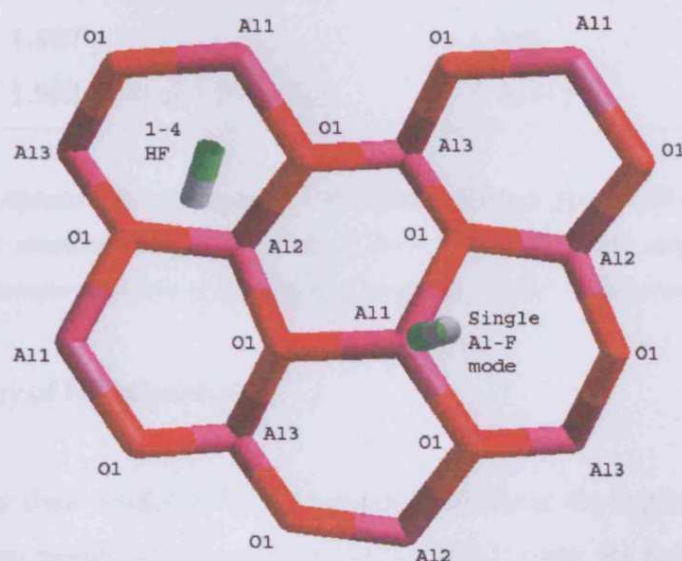
Figure 4.30. Optimised hexagonal ring systems for the 1-4 and single Al-F interaction for the adsorption of two HF molecules to the {0001} α-alumina surface. The energy of adsorption is -117.8 kJ mol⁻¹.

This analysis shows that by bringing the two HF molecules closer together to adsorb on adjacent Al1 Lewis acid sites does not significantly alter the bond lengths in the top four layers of Al1, O1, Al2 and Al3. From this, it is possible to predict that for full coverage of HF on the {0001} α-alumina surface, the physisorptions will not cause much alteration of the slab structure, other than the elevation of the Al1 adsorption site towards the fluorine molecule. In a full coverage model there will be twelve HF molecules, a coverage of one HF molecule per 26.8 Å², compared to the double HF coverage of one HF molecule per 160.8 Å² and the single HF coverage of one HF molecule per 321.6 Å².

Bond	1-2/1-4 2×HF adsorption	1-4/Al-F 2×HF adsorption
Al1-O1	1.741	1.743
Al1-O1*	1.747 (1-4) & 1.752 (1-2)	1.745 (1-4)
Al2-O1	1.816	1.817
Al2-O1*	1.83 (1-4) & 1.816 (1-2)	1.831 (1-4)
Al3-O1	1.887	1.888
Al3-O1*	1.908 (1-4) & 1.896 (1-2)	1.902 (1-4)

Table 4.18. Bond distances for the double HF adsorption shown in figure 4.29 where the 1-4 and 1-2 adsorptions occur simultaneously given by the 1-2/1-4 2×HF adsorption column and the 1-4/Al-F simultaneous physisorptions shown in figure 4.30 given in the 1-4/Al-F 2×HF adsorption column.

4.5.3 Summary of HF adsorptions.

Returning to the three modes of HF adsorption outlined at the beginning of section 4.5, it is seen that two modes are simulated using the GULP code: the single Al-F interaction and the double Al-F and O-H interaction in either a 1-2 or 1-4 formats. The O-H single interaction was not considered in this series of simulations. These calculations give a valuable insight into the behaviour of the aluminium Lewis acid site when an adsorbate molecule is placed sufficiently close to give physisorption. The energies of adsorption indicate that the single Al-F interaction occurs over a range of -51 to -53 kJ mol^{-1}, the 1-2 mode over a range of -54 to -61 kJ mol^{-1} and the 1-4 mode from -65 to -77 kJ mol^{-1}, giving the most favoured as 1-4, then 1-2 and finally Al-F. The average values for the three modes are summarised in table 4.19.

Adsorption mode	Average energy of adsorption kJ mol^{-1}
Al-F	-51.3
1-2	-58.1
1-4	-69.9

Table 4.19. The average values for the three adsorption modes found for the physisorption of HF onto the {0001} α-alumina surface.

4.6   θ-alumina.

Lewis acid sites present on α-alumina surfaces are octahedral, whereas in θ-alumina aluminium is in octahedral and tetrahedral co-ordinated sites and therefore surfaces may contain these two distinct environments. Periodic potential models for θ-alumina have been used to provide information on surfaces and surface energies.

The potentials used for these simulations are shown in chapter three, and are the same as for α-Al_2O_3 except for: the aluminium-oxygen Buckingham potential was separated to represent octahedral and tetrahedral aluminium, and a three body term for each aluminium environment.

The {001}, {010}, {011}, {101}, {110} and {111} θ-alumina surfaces were constructed from the CASTEP output of the ultrasoft pseudopotential and precise basis set calculations, presented in chapter five. Table 4.20 shows the surface energy (γ_s) values for the low Miller index GULP surface optimisations using the Newton-Raphson optimisation method with the Davidon-Fletcher-Powell method of updating the hessian on the CASTEP relaxed bulk structure analysed by Shiftcell to provide stable surfaces. No zero dipole surfaces were found for the {100} surface of θ-alumina. These results show that the CASTEP surface energies are reduced before optimisation in GULP to an approximation to the ideal values of between 1 and 5 J m^{-2} and are further reduced by GULP minimisations.

Across the series the surface energy values follow the trend of decreasing upon optimisation, a result mirrored in both the standard method and the DFT results shown in chapter five. Figures 4.30 to 4.35 show the minimised surfaces found by the calculations summarised in table 4.20, all of which exhibit both aluminium and oxygen character in the slab terminating layer.

Surface	Stoichio-metry	Unit cell			Unrelaxed	Relaxed	Change of γ_s
		$\underline{a}$	$\underline{b}$		γ_s	γ_s	upon
		Å	Å		$J\,m^{-2}$	$J\,m^{-2}$	minimisation
{001}	$Al_{72}O_{108}$	18.1678	8.5889		6.45	0.38	-94 %
{011}	$Al_{36}O_{54}$	6.2428	11.7686		4.91	-6.64	-242 %
{010}	$Al_{56}O_{84}$	11.7050	11.0951		6.99	0.44	-94 %
{101}	$Al_{48}O_{72}$	14.1966	8.5889		6.85	0.59	-91 %
{110}	$Al_{32}O_{48}$	11.0951	12.1118		4.80	1.42	-70 %
{111}	$Al_{64}O_{96}$	12.4855	12.1118		0.87	-0.40	-146 %

Table 4.20. Comparison of unrelaxed surface energy values calculated for single point and minimised surfaces constructed from the ultrasoft pseudopotential and precise basis set CASTEP determined bulk optimised structure, both series evaluated using the GULP code. The Davidon-Fletcher-Powell method of updating the hessian was used to calculate these values.
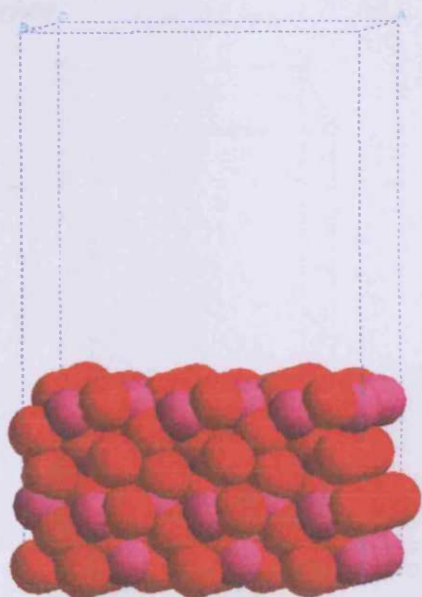
Figure 4.31. Minimised θ-Al_2O_3 {001} surface
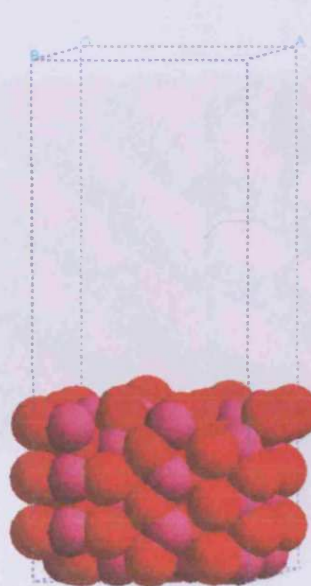
Figure 4.32. Minimised θ-Al_2O_3 {010} surface
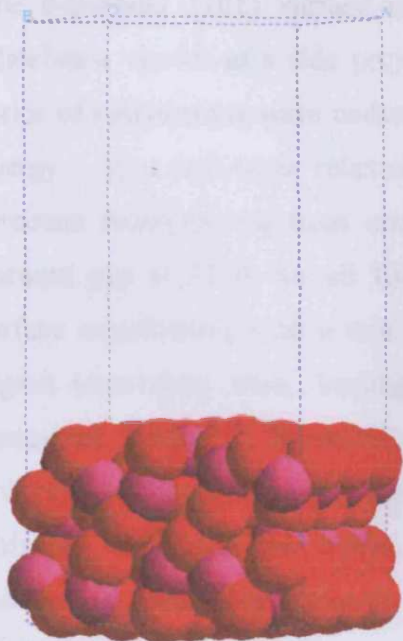
Figure 4.33. Minimised θ-Al₂O₃ {101} surface
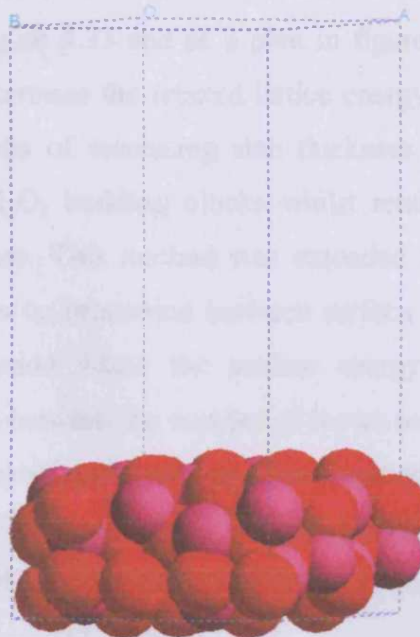
Figure 4.34. Minimised θ-Al₂O₃ {110} surface
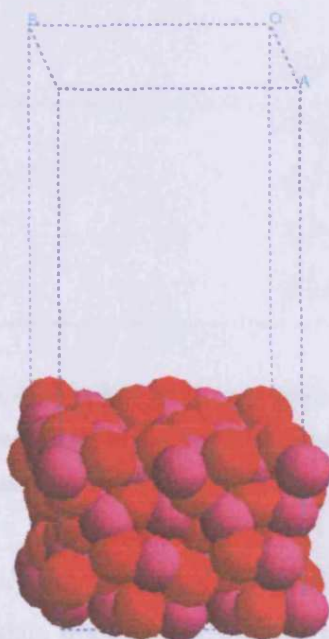
Figure 4.35. Minimised θ-Al₂O₃ {111} surface
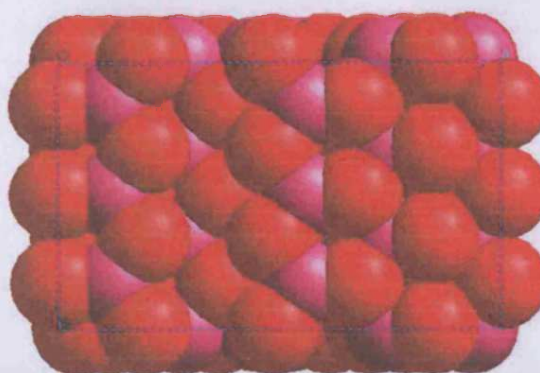
Figure 4.36. Plan view of the θ-Al₂O₃ {101} surface, mainly oxygen in character, with accessible tetrahedral aluminium sites.

The θ-alumina {101} surface exists with tetrahedral aluminium sites accessible to adsorbates, shown as a side projection in figure 4.33 and as a plan in figure 4.36. A series of calculations were undertaken to determine the relaxed lattice energy, surface energy – γ_s – and layer relaxations for slabs of increasing slab thickness in the c direction incorporating from one to five Al_2O_3 building blocks whilst retaining the vacuum gap at 20 Å for all five simulations. This method was extended to {110} surface calculations, with a thin slab there is no separation between surface and bulk region aluminium sites, leading to a situation where the surface energy will be inaccurate. Table 4.21 shows the relationship between the number of repeat units in the unit cell and the surface energy for both unrelaxed and geometrically optimised crystals. This data shows that four repeat units are sufficient to give a surface slab that ensures that the two surfaces are separate from the bulk region in the crystal, this giving a small positive value for the surface energy.

Number of repeat units	Unrelaxed surface γ_s $J\,m^{-2}$	Relaxed surface γ_s $J\,m^{-2}$
1	-4.41	-0.89
2	-4.27	-1.15
3	-3.71	-0.44
4	-3.14	0.18

Table 4.21. Influence of sequentially adding further repeat units of $Al_{24}O_{36}$ to the unit cell to increase the distance between the two {110} surfaces has on the surface energy for both unrelaxed and optimised crystals.

The {110} surface of θ-alumina contains purely tetrahedral aluminium sites terminating the slab, upon optimisation these were found to relax into the bulk, as was found for α-alumina {0001} surfaces, although significantly these tetrahedral sites are replaced as the terminating layer by the first oxygen layer as can be seen from figure 4.34, although these Lewis acid aluminium sites are still accessible to incoming adsorbates.

These two surfaces also display a positive surface energy value, both offering a significant reduction in γ_s compared to the unrelaxed structure.

4.7 Aluminium fluoride.

As described in section 1.5, the full fluorination of alumina by hydrogen fluoride yields aluminium fluoride, AlF_3. Molecular mechanical simulations were carried out to obtain the bulk and surface structures of three phases of aluminium fluoride: β-, κ- and θ-AlF_3, to compare against DFT results for the equivalent calculations using the CASTEP code and presented in chapter five. The potentials used for these simulations were fitted by the method outlined in section 3.8.3, and defined in table 3.6.

4.7.1 Constant pressure geometry optimisation of AlF_3 phases.

Table 4.22 shows the experimentally determined lattice parameters of β-, κ- and θ-AlF_3,[11] with the subsequent constant pressure optimisation, allowing both unit cell and atomic optimisation. For these three phases $\alpha = \beta = \gamma = 90°$. All calculations are undertaken using the DFP method of minima searching.

Phase		a	b	c	Volume
		Å	Å	Å	Å³
β-AlF_3	Experimental [11]	6.931	12.002	7.134	593.448
	conp optimisation	7.119	12.331	7.229	634.583
κ-AlF_3	Experimental [11]	11.396	11.396	3.562	462.576
	conp optimisation	11.654	11.654	3.615	490.975
θ-AlF_3	Experimental [11]	10.146	10.146	7.125	733.354
	conp optimisation	10.355	10.355	7.262	778.775

Table 4.22. The experimental and constant pressure unit cell parameters for β-, κ- and θ-AlF_3.

As table 4.22 shows, the potentials used for these three phases give results which increase the a, b and c unit cell parameters by under 2.8%, and under 6.4% for the volume. The percentage increase for the a and b parameters is approximately double the increase found using the well established potentials for the α-alumina constant pressure optimisation; in these AlF_3 minimisations the c parameter increases in accordance with the a and b values.

4.7.2 Surfaces of aluminium fluoride phases.

Using the same method as with α-alumina, a constant volume optimisation was carried out on the atomic coordinates derived from the constant pressure simulation yielding the parameters in table 4.22. A Shiftcell analysis and stable surface determination was carried out on the constant volume coordinates, finding the surfaces shown in table 4.23. Constant volume optimisations obtained the relaxed surface slab resulting in the surface energy, γ_s, with single point calculations giving the unrelaxed surface energy, detailed in table 4.23. No stable surface slabs were found for the κ-AlF$_3$ phase, due to a dipole existing across the surface for all slabs generated.

Surface	Unrelaxed γ_s $J\ m^{-2}$	Relaxed γ_s $J\ m^{-2}$	Percentage reduction of γ_s
β-AlF$_3$			
{100}	3.44	2.09	-39.4
θ-AlF$_3$			
{010}	1.08	0.31	-70.8
{011}	4.30	1.09	-74.5
{100}	5.42	2.25	-58.5
{101}	4.31	1.17	-72.9
{111}	4.69	1.49	-68.2

Table 4.23. Unrelaxed and relaxed surface energies for the stable surfaces found for the β- and θ-AlF$_3$ phases.

Table 4.23 shows the γ_s values decrease upon minimisation, reflecting the results found for the α-alumina {0001}, {01$\bar{1}$1} and {11$\bar{2}$1} surfaces, with the relaxed surfaces being more stable than the unrelaxed surfaces for all of the slabs calculated by the percentages indicated. As with α-alumina, the catalytic activity of aluminium fluoride surfaces will depend upon the availability of accessible Lewis acid aluminium adsorption sites. Figures 4.38a and 4.38b show the unrelaxed and geometry optimised β-AlF3 {100} surface respectively.

a   b
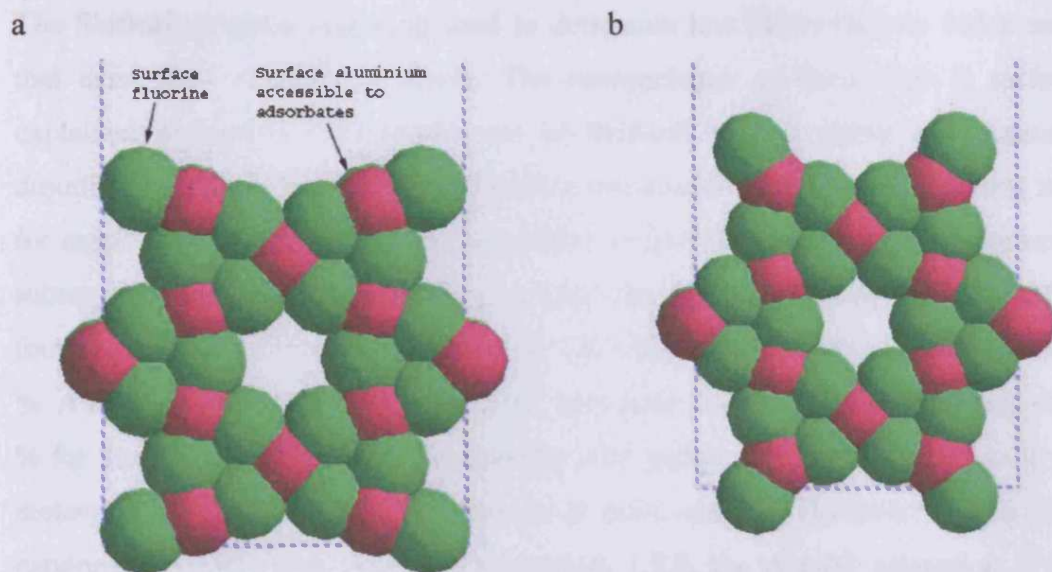
Figure 4.38. GULP determined β-AlF₃ {100} unrelaxed (a) and geometry optimised (b) surfaces, showing the accessible Lewis acid aluminium sites in the unrelaxed slab, disappearing in the optimised crystal.

In the minimised structure shown in figure 4.38b, the terminating fluorine and aluminium atoms move away from the second layer (itself a combination of both atoms), the exact opposite situation found for the {0001} surface of α-alumina. As the surface energy for the elevation of the terminating layer in the relaxed slab is approximately 60% of the surface energy for the higher energy and therefore thermodynamically unstable unrelaxed slab, this layer elevation is influential in the stabilisation of the β-AlF₃ {100} surface.

4.8   Summary of forcefield simulations.

The results described in this chapter began with the bulk structure geometry optimisation of the α-alumina crystal, a constant pressure simulation using the GULP code and the potentials defined in chapter three give the lattice parameters as $a = b = 4.8178$ Å and $c = 12.681$ Å, compared to the experimental lattice parameters of $a = b = 4.759$ Å and $c = 12.991$ Å. These result in a cell volume of 254.903 Å³, in very close agreement with the experimental volume of 254.803 Å, demonstrating that the potentials used for the alumina system give reasonable results compared to previous experimental and theoretical results as shown in section 1.1.1.

169

The Shiftcell program was then used to determine low Miller-Bravais index surfaces that exist with no inherent dipole. The nomenclature of these type II surfaces is explained in section 3.4 and the use of Shiftcell to find stable configurations is described in section 3.5. The {0001} surface was found to satisfy the conditions laid out for metal oxide surfaces, with the aluminium termination following the literature. The subsequent layer relaxations for this surface slab, calculated using equation 1.2, were found to be: Al1-O1 = -86.9 %, O1-Al2 = + 8.0 %, Al2-Al3 = -30.9 %, Al3-O2 = +14.3 %. A negative value indicates that the two layers are closer together. The figure of -86.9 % for the top-most Al layer is comparable with previous theoretical simulations using molecular mechanics methods, and also to ab $initio$ methods. However, compared to the experimental XRD data described in section 1.2.2, the Al1-O1 relaxation is larger, mirroring the situation found for all previous computational results. The surface energy, γ_s, is calculated by equation 1.3 and is 2.23 J m^{-2} for the relaxed {0001} surface, compared to literature values of 2.03 and 2.97 J m^{-2} shown in table 1.6. This analysis gives an indication of the stability of a metal oxide surface, and should, for a thermodynamically stable surface, be in the region of 1-5 J m^{-2}.

The next series of simulations was the full hydroxylation of the {0001} α-alumina slab, this process was initiated by the removal of the terminating aluminium atoms on both surfaces. For each Al1 removal, the three oxygen sites remaining were hydroxylated by the addition of one hydrogen atom each 1 Å towards the vacuum gap. Equation 4.1 details the reaction occurring in this hydroxylation involving twelve water molecules, the energy for this process can be defined using a Born-Haber cycle as in figure 4.9, with the reference hydroxylation energy, ΔH_r, calculated by CASTEP. This method gives an $E_{correction}$ value of 11.366 eV, which compares to previous literature values of 4.365 eV [3] and -9.74 eV.[5] The $E_{correction}$ value is important to the next stage of simulations on a partially hydroxylated {0001} α-alumina slab, involving the modelling of a series of reactions beginning with two water molecules added to the system giving two hydroxyl groups on each surface up to a full coverage of twelve hydroxyl groups per surface. The hydroxylation energies of these slabs is found by the use of a further modified Born-Haber cycle, shown in figure 4.15, where the lattice energies for the hydroxylated slab may be used directly, without explicitly considering the water molecule. This approach is required due to the presence of more potentials for the

hydroxylated surface than the clean surface, none of which can be isolated and individually quantified.

The hydroxylation energies are shown in table 4.10 for the six reactions modelled. The average energies range from 670 kJ mol^{-1} per water molecule for the addition of two waters progressively down to -222 kJ mol^{-1} per water molecule for the addition of twelve waters. The distribution of hydroxylation energies is shown in figure 4.16, showing a stepwise profile leading to full hydroxylation. The high coverage calculations show a negative energy of reaction, suggesting that hydroxylation will be thermodynamically favourable. In addition, the higher coverages are found to be more favourable than the lower per adsorbed water molecule. This suggests that surface hydroxyl interactions actually favour high adsorption densities, at least up to the point of complete hydroxylation. Another consideration is that the low coverage sites use defective surface structures to retain stoichiometry; this may contribute to the thermodynamic favouring of high coverages.

The experimental results shown in figure 1.23 give the energies of adsorption as higher at low coverages of water decreasing with further uptake of water molecules.[12] Desorption of water from fully hydroxylated α-alumina surfaces was shown to exist from approximately 50 to 160 kJ mol^{-1} in LITD/TPD experimental work, agreeing with the results presented in this chapter.[13]

The addition of hydrogen fluoride to the {0001} α-alumina surface found three distinct types of adsorption: the Al-F physisorption with no interaction between hydrogen and oxygen in a range of adsorption energies between -50.6 and -52.5 kJ mol^{-1}. The second type exists between aluminium-fluoride and oxygen-hydrogen in a 1-4 type as defined in figure 4.19, giving adsorption energies of between -64.5 and -77.3 kJ mol^{-1}. The third type is the 1-2 type, where the oxygen site responsible for hydrogen adsorption neighbours the aluminium-fluorine site and finds energies of adsorption of between -54.1 and -60.7 kJ mol^{-1}. Adsorption of two hydrogen fluoride molecules to the surface finds the presence of more than one type of adsorption, giving a total adsorption energy of -129.9 kJ mol^{-1} and -117.8 kJ mol^{-1}. Extrapolating this data to find the full coverage

of HF onto the sixteen available aluminium adsorption sites gives an approximate value of -62 kJ mol^{-1} per HF.

These results can be compared to experimental work carried out on γ-alumina surfaces, in which Jones [14] found hydrogen fluoride adsorption equalling -48 kJ mol^{-1}, representing the interaction of HF onto pre-fluorinated alumina surfaces. The range of values for the Al-F interaction between -50.6 kJ mol^{-1} to -52.5 kJ mol^{-1} is consistent with these experimental TPD findings.

To conclude this chapter, simulations on the θ-alumina surfaces were undertaken to offer a comparison when both tetrahedral and octahedral aluminium sites are present. The {001}, {010}, {101} and {110} surfaces offer suitable surface energy values in the range expected for stable metal oxide surfaces: 0.38, 0.44, 0.59 and 1.42 J m^{-2} respectively. No adsorptions of HF onto any θ-alumina surfaces reached convergence when the same potentials as with the readily converged α-alumina adsorptions were used.

Finally, the simulations of three phases of aluminium fluoride, AlF$_3$, were investigated using fitted potentials derived from experimental structures of β-, κ- and θ-AlF$_3$. The method of fitting is described in 3.8.3, and the lattice parameters using the single Buckingham aluminium-fluorine potential are shown in table 4.22, where all three phases offer lattice parameters and cell volumes close to the original experimental values. Subsequent Shiftcell determined surface slabs found no stable surfaces for the κ-AlF$_3$ phase, whereas the single surface found for β-AlF$_3$ and the five surfaces for θ-AlF$_3$ gave surface energies which are in the expected range for metal oxides (1-5 J m^{-2}) and compare favourably to the calcium fluoride CaF$_2$ surface energies found by de Leeuw et al [15] using density functional theory of 0.39 J m^{-2} and Bennewitz et al using atomistic methods giving a value of 0.52 J m^{-2}.[16] No adsorptions were carried out on the aluminium fluoride surfaces using hydrogen fluoride.

[1] Cerius^2 database. Version 4.2. Accelrys Inc. San Diego.
[2] P. Guenard, G. Renaud, A. Barbier and M. Gautier-Soyer, *Surf. Rev. Lett.*, **5**, 321, (1998).
[3] M. A. Nygren, D. H. Gay and C. R. A. Catlow, *Surf. Sci.* **380**, 113 (1997).
[4] D. H. Gay and A. L. Rohl, *J. Chem. Soc., Faraday Trans.*, **91**, 925, (1995).
[5] C. R. A. Catlow, *J. Phys. Chem.*, **38**, 1131, (1977).
[6] M. Bankhead, G. W. Watson, G. J. Hutchings, J. Scott and D. J. Willock, *unpublished*.

[7] M. Baudin and K. Hermansson, *Surf. Sci.*, **474**, 107-113, (2001).

[8] K. C. Hass, W. Schneider, A. Curioni and W. Andreoni, *J. Phys. Chem. B*, **104**, 5527, (2000).

[9] J. M. Wittbrodt, W. Hase and H. Schegel, *J. Phys. Chem. B*, **102** 6539, (1998).

[10] J. R. Scott, G. Groenewold, A. Gianotto, M. Benson and J. Wright, *J. Phys. Chem. A*, **104**, 7079, (2000).

[11] J. A. A. Ketelaar, *Nature*, **128**, 303, (1931).

[12] B. A. Hendriksen, D. Pearce and R. Rudham, *J. Catal.*, **24**, 82, (1972).

[13] J. W. Elam, C. E. Nelson, M. Cameron, M. Tolbert and S. George, *J. Phys. Chem. B*, **102** 7008, (1998).

[14] M. Jones, *Ph. D. Thesis*, Cardiff University, 2004.

[15] N. H. de Leeuw, J. A. Purton, S. C. Parker, G. W. Watson and G. Kresse, *Surface Science*, **452**, 9, (2000).

[16] R. Bennewitz, M. Reichling and E. Matthias, *Surface Science*, **387**, 69, (1997).

Chapter 5

5 Periodic Density Functional Theory results.

In this section, the results for periodic density functional theory calculations using CASTEP are detailed. The background to density functional theory is described in chapter two and the methodology of setting up and analysing CASTEP calculations is explained in chapter three. Initially, the surface structures for cleaving α-alumina with its purely octahedral aluminium sites is presented, followed by chemisorbed and physisorbed water and hydrogen fluoride. Analogous structural calculations with θ-alumina are presented, this containing both octahedral and tetrahedral aluminium.

As was discussed in chapter one, aluminium oxide exposed to hydrogen fluoride will eventually become a wholly aluminium fluoride structure. Further periodic density functional theory calculations using CASTEP were performed on aluminium fluoride structures and their stable surfaces. In addition, this first principles approach provides a reference from which to assess the accuracy of the fitted potentials using the GULP code.

5.1 α-Alumina bulk structure determination.

5.1.1 Selecting the most accurate method of calculation.

From the Cerius[2] interface crystallographic database, the experimentally determined α-alumina bulk unit cell has the formula $Al_{12}O_{18}$, the unit cell parameters for this structure are shown in table 5.1.

With the CASTEP code and other planewave based quantum chemistry packages, the first consideration is to determine the k-point sampling grid at which convergence is reached. This reciprocal space grid was sampled using $1\times1\times1$ grid to $6\times6\times6$ Monkhurst Pack sampling grids. Figure 5.1 shows a series of constant volume minimisation calculations at expansion factors ranging from 94 % to 102 % of the experimental unit cell parameters in table 5.1, incorporating the $1\times1\times1$ grid to the $6\times6\times6$ grid.

Unit cell parameters		Cell angles		Cell volume
Å		°		Å^3
a	4.795	α	90	254.7774
b	4.795	β	90	
c	12.991	γ	120	

Table 5.1. Cerius^2 crystal database unit cell parameters for α-alumina determined by x-ray crystallography experiments.

In terms of the Monkhurst-Pack grid, convergence is reached at a 2×2×2 reciprocal space grid, as this has almost precisely the same energy as the 3×3×3, 4×4×4, 5×5×5 and 6×6×6 k-point sampling grids, whereas the 1×1×1 k-point sampling grid has a significantly higher total energy. For computational efficiency, it was considered sufficient to model subsequent crystal systems using a 2×2×2 k-point sampling grid.

In terms of the experimental cell expansion factors of between 94 % and 102 %, figure 5.1 shows that, for the converged 2×2×2 to 6×6×6 k-point grids, the energy minima is at 99 % of the experimental unit cell volume. In essence, this means that CASTEP has a tendency to marginally underestimate the unit cell parameters of this particular metal oxide system, so a constant pressure calculation will find a contraction of the a, b and c parameters by approximately 1 % to an energetic minimum.

CASTEP has a range of pseudopotentials to represent electrons within the core region of an atom to allow for efficient computation, specifically for aluminium and oxygen the Cerius^2 library pseudopotentials are the '00', '02' and the ultrasoft pseudopotentials. The '00' and '02' pseudopotentials are norm-conserving, requiring higher cut-offs for planewaves than the ultrasoft or 'bgga' pseudopotentials. The 'bgga' pseudopotential is a parameterisation of the ultrasoft potential derived from work on silicates.[1] Combined with these are basis sets to control the planewave kinetic energy cut-off, shown in table 5.2.

Basis set	Planewave kinetic energy cut-off (eV)			
	00	02	usp	bgga
Coarse	330	620	260	240
Medium	450	780	300	280
Fine	500	900	340	300
Precise	560	1000	380	340

Table 5.2. Kinetic energy cut-offs and subsequent total energies for the basis set and pseudopotential combinations.

Percentage of experimentally determined cell parameters a, b and c.
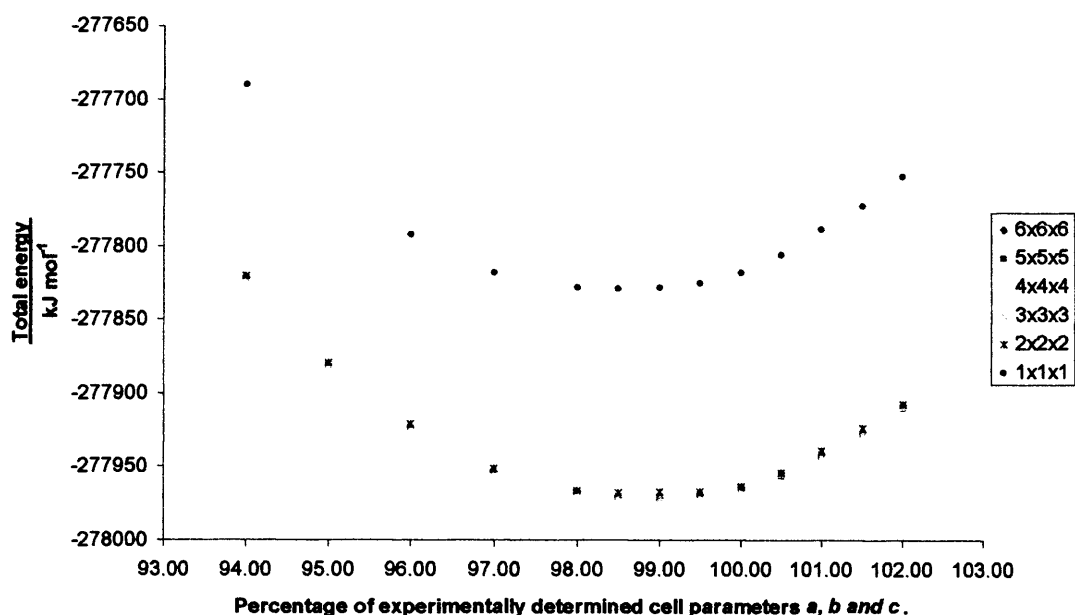
Figure 5.1. Calculated total energy of constant volume relaxations of a single unit cell of α-alumina using k-point sampling grids from 1×1×1 to 6×6×6. The expansion factors are 94 % to 102 % of the experimentally determined cell parameters of α-alumina. The ultrasoft pseudopotential and a kinetic energy cut-off of 240 eV were used for these simulations.

Once the k-point convergence criteria had been established at a 2×2×2 grid, the combinations of these pseudopotentials with each basis set were used in constant pressure calculations. When defining the basis set, a high kinetic energy cut-off is more accurate as this gives a large number of planewaves. However, there is a trade off with computational expense. Table 5.3 shows the '00' pseudopotential unit cell parameters when calculated with the four standard basis sets cutoffs in a constant pressure simulation allowing unit cell parameters and atomic coordinates to simultaneously

177

optimise. Table 5.4 shows the same data for the '02' pseudopotential, table 5.5 for the 'usp' (ultrasoft) pseudopotential and table 5.6 for the 'bgga' pseudopotential.

Basis set	a and b Å	% of exp.	c Å	% of exp.	Volume Å^3	% of exp.
Coarse	4.664	98.00	12.749	98.13	240.135	94.25
Medium	4.534	95.26	12.406	95.50	220.827	86.67
Fine	4.493	94.41	12.273	94.47	214.564	84.22
Precise	4.475	94.03	12.250	94.29	212.444	83.38
Experimental	4.795	4.795	12.991		254.7774	

Table 5.3. Unit cell parameters calculated for the '00' pseudopotential with each basis set, showing the a, b and c parameters and cell volume with the percentage differences compared to the reference experimental structures.

Basis set	a and b Å	% of exp.	c Å	% of exp.	Volume Å^3	% of exp.
Coarse	4.839	101.69	13.190	101.53	267.535	105.01
Medium	4.839	101.67	13.132	101.09	266.264	104.51
Fine	4.845	101.80	13.032	100.31	264.902	103.97
Precise	4.844	101.78	13.100	100.84	266.181	104.48
Experimental	4.795	4.795	12.991		254.7774	

Table 5.4. Unit cell parameters calculated for the '02' pseudopotential with each basis set, showing the a, b and c parameters and cell volume with the percentage differences compared to the reference experimental structures.

In table 5.3, it can be seen that the '00' pseudopotential consistently underestimates the value of the a, b and c unit cell parameters by no more than 6 %, but this is compounded when considering the cell volume, for which the underestimation ranges from -5.75 % to -16.62 %. This implies that the '00' pseudopotential is not accurate enough to model the α-alumina bulk structure and keep the cell volume to within ±1 % of the experimental cell volume.

Basis set	a and b Å	% of exp.	c Å	% of exp.	Volume Å³	% of exp.
Coarse	4.750	99.82	12.995	100.03	253.962	99.68
Medium	4.732	99.43	12.978	99.90	251.656	98.77
Fine	4.718	99.13	12.955	99.73	248.713	98.01
Precise	4.692	98.59	12.979	99.91	247.416	97.11
Experimental	4.795	4.795	12.991		254.7774	

Table 5.5. Unit cell parameters calculated for the ultrasoft pseudopotential with each basis set, showing the a, b and c parameters and cell volume with the percentage differences compared to the reference experimental structures.

Basis set	a and b Å	% of exp.	c Å	% of exp.	Volume Å³	% of exp.
Coarse	4.824	101.36	13.206	101.66	266.116	104.45
Medium	4.836	101.62	13.065	100.57	264.615	103.86
Fine	4.840	101.7	13.077	100.66	265.299	104.13
Precise	4.848	101.88	13.034	100.33	265.331	104.14
Experimental	4.795	4.795	12.991		254.7774	

Table 5.6. Unit cell parameters calculated for the 'bgga' pseudopotential with each basis set, showing the a, b and c parameters and cell volume with the percentage differences compared to the reference experimental structures.

The '02' pseudopotential, shown in table 5.4, is significantly more accurate for the a, b and c parameters than the '00' pseudopotential, with this method of representing the core electrons with each of the four basis sets, however, instead of underestimating these parameters, the '02' pseudopotential overestimates these parameters by no more than approximately +2 %. This has the effect of increasing the cell volume by +3.97 % to +5.01 %, a significant increase in accuracy over the '00' pseudopotential combined with any of the four basis sets. When compared to the kinetic energy cut-offs employed in the calculations using the '00' pseudopotential, it is seen that for each basis set, the cut-offs are significantly higher, this has important consequences for the accuracy of any metal oxide calculation, as when more planewaves are incorporated under a higher

threshold a more reliable representation of the system is obtained. Table 5.2 gives the planewave cut-offs as a function of the combination of pseudopotential and basis set, due to different pseudopotentials using varying cut-offs to include a larger number of planewaves.

When considering the ultrasoft pseudopotential against the '00' and '02' results, this method of expressing the core electrons offers a substantial improvement in accuracy over both these methods, as the parameters do not alter by any more than -1.41 %, this means that the cell volume falls in the range -0.32 % to -2.89 % of the experimental value. The coarse basis set is closest to these parameters, whilst the precise basis set is at the top end of the range. However, the energy converges in this range, with the precise basis set resulting in the lowest energy. The ultrasoft pseudopotential also has the advantage that the kinetic energy cut-offs can be smaller than for the other pseudopotentials.

The 'bgga' pseudopotential gave unit cell parameters in the range +0.33 % to +1.88 % of the experimental parameters, with the effect that the cell volume falls within a range +3.86 % to +4.45 % of the experimental volume, just outside the accuracy achieved using the ultrasoft pseudopotential.

From the evidence outlined, the most appropriate pseudopotential to use to model the α-alumina crystal would be either the ultrasoft or 'bgga' pseudopotential, as both give closer agreement with experimental unit cell parameters than either the '00' and '02' pseudopotentials. To decide which combination of pseudopotential and basis set to choose, the results were plotted as the total energy referenced against the lowest energy obtained from any calculation against cell volume.

As can be seen from figure 5.2, the 'bgga' pseudopotential fell someway away from the experimental cell volume, and so was neglected from any further consideration for the α-alumina bulk crystal; this left the coarse and precise basis sets within the ultrasoft pseudopotential as possible candidates for further investigation of α-alumina surfaces. The coarse basis set is the nearest to the experimental cell volume, but has the less accurate kinetic energy cut-off and a higher total energy than the precise basis set. From

the data shown in section 1.1.1, where the experimental unit cell parameters were: a and b = 4.7586 Å,[2] 4.7602 Å[3] and 5.128 Å;[4] with c = 12.9897 Å,[2] 12.9933 Å[3] and 13.003 Å.[4] These compare to previously theoretically determined values of a and b = 4.758 Å and c = 12.991 Å.[5] The parameters calculated for the ultrasoft pseudopotential and precise basis set combination compare favourably to both these experimental and theoretical values. The calculated a and b values are underestimated by 0.0674 Å compared to the experimental value and 0.012 Å to the theoretically determined value. The c parameter is closer to the experimental value, being smaller by 0.0125. Although the precise basis set is further away from the experimental unit cell parameters and volume, it has the advantage of a lower calculated total energy since the higher cut-off allows more planewaves representing the best basis set used. It is for these reasons that the combination of an ultrasoft pseudopotential and a precise basis set function was chosen for all subsequent calculations.
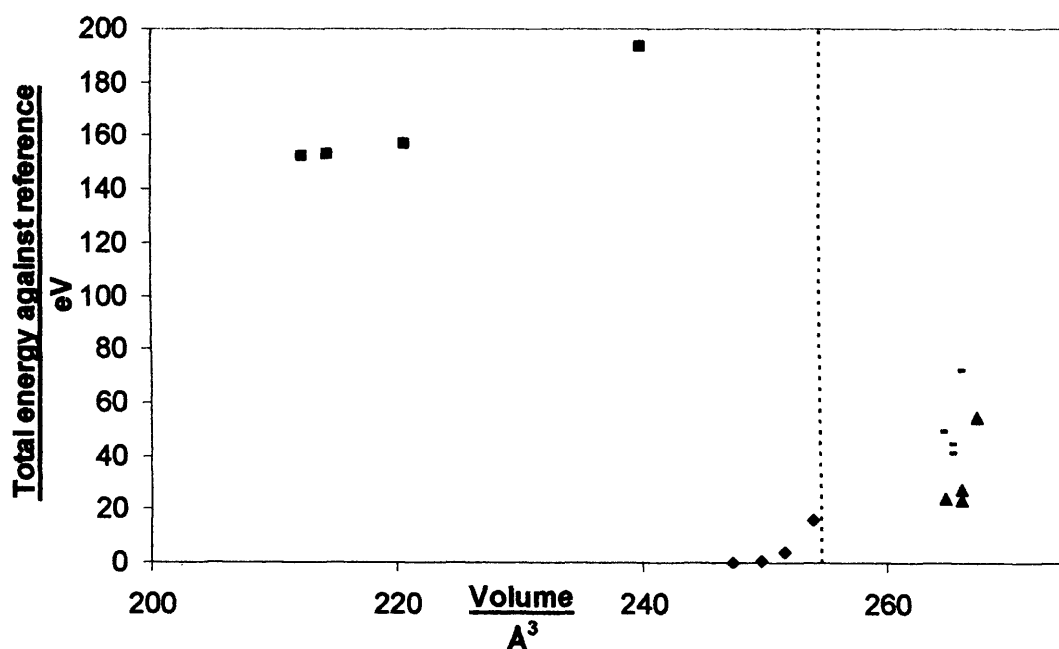
Figure 5.2. Total energy referenced against the ultrasoft pseudopotential with precise basis set – the lowest energy – plotted against the constant pressure calculated cell volume. The vertical dashed line indicates the experimental cell volume. In all cases the calculated energy falls as the basis set is changed from coarse to precise. ■ indicates the '00' pseudopotential, ▲ the '02' pseudopotential, – the 'bgga' pseudopotential and ♦ the 'usp' pseudopotential.

5.1.2 Electronic structure of the α-alumina crystal.

The density of states plot for the bulk α-alumina crystal is shown in figure 5.3, this may be compared to the density of states plot calculated using extended Hückel Theory by Ciraci and Batra [6] in figure 1.4a. The lower valence band (LVB) stretching from -36.4 eV to -26.9 eV, and the upper valence band (UVB) from -21 eV to -9 eV, with a resultant band gap of marginally less than 6 eV.
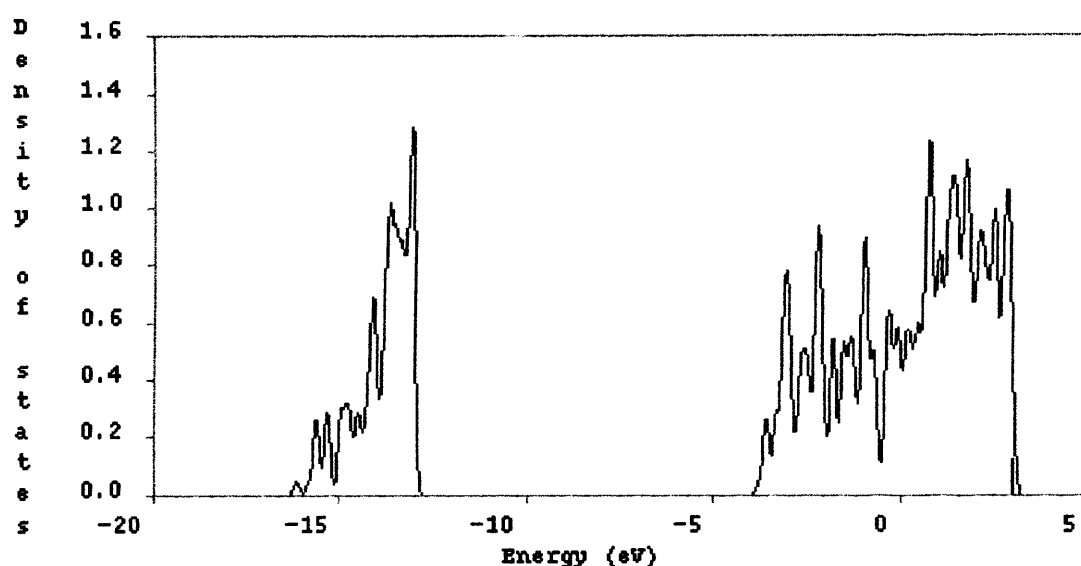
Figure 5.3. Total density of states calculated by CASTEP using the ultrasoft pseudopotential and precise basis set combination for the α-alumina bulk crystal. LVBm = -16.14 eV, LVBM = -13.06 eV, UVBm = -3.75 eV and UVBM = 3.04 eV.

Figure 5.3 shows the lower valence band over a range of *ca.* 3 eV between approximately -16 eV and -13 eV. The upper valence band is between -3.75 eV and 3.04 eV. This data does not correlate well to the total density of states calculated by Ciraci *et al* shown in figure 1.4a, with the band gap similar at *ca.* 6 eV compared to 8.5 eV here. Comparable results were obtained by Mo and Ching [7] using a local density approximation approach as illustrated in figure 1.9, where the lower valence band gap is from -19 eV to -16 eV and the upper valence band is from -7 eV and 0 eV. The band gap in figure 1.9 is larger than the band gap illustrated in figure 5.3. There is no absolute uniformity between the density of states shown in figures 1.3a and 1.8, and the density of states shown in figure 5.3. This work is in good agreement with the previous DFT-LDA results.

The band structure composition may be estimated from the total density of states in figure 5.3, with the bands at the lower valence band minimum likely to be uneven across the Brillouin zone due to the presence of many low intensity bands at less than *ca.* -15 eV. The steep intense band at the LVBM will give rise to a correspondingly flat band structure as in figure 1.3. Using the same reasoning, the band structure at the UVBm will be uneven due to the presence of the low intensity peak at *ca.* -3.75 eV, whilst the UVBM band structure will again be flat due to the intense peak at the maxima of 3.04 eV.

5.2   Surfaces of α-alumina.

Following a constant pressure bulk optimisation using the ultrasoft pseudopotential with a precise basis set and a reciprocal space k-point grid of 2×2×2 the theoretical cell geometry was obtained. From this structure, the stable surfaces were determined using the Shiftcell code as described in chapter three.

Within the Shiftcell scheme, the stoichiometric surfaces that possess no net dipole across a stoichiometric slab were found to be the $\{0001\}$, $\{10\bar{1}1\}$, $\{01\bar{1}0\}$, $\{10\bar{1}0\}$ and $\{11\bar{2}0\}$ surfaces. Beginning with the basal plane, $\{0001\}$, of which many experimental and computational studies have been undertaken as described in chapter one, geometric optimisations were undertaken to determine the behaviour of the surface when modelled using the CASTEP code.

5.2.1. $\{0001\}$ α-alumina surface.

The *c* parameter is perpendicular to the $\{0001\}$ surface and so the *a* and *b* vectors were the same as for the bulk crystal unit cell. A review of the literature in chapter one showed that the clean $\{0001\}$ surface is terminated by aluminium atoms. With every geometric minimisation using both *ab initio* and molecular mechanics methods, this aluminium Al1 atom relaxes back towards the oxygen O1 layer, which itself moves marginally upwards towards the topmost aluminium. Section 1.2.3 describes many of the previous theoretical investigations into the properties of the $\{0001\}$ α-alumina surface.

The surface energy, γ_s, is calculated using equation 5.1, for an aluminium oxide surface the value should be positive and between one and five J m^{-2}, much higher than this indicates a surface that would be thermodynamically difficult to attain.

$$\gamma_s = \frac{E_{surface} - E_{bulk}}{2A}$$

Equation 5.1

In equation 5.1 E_{bulk} is the total energy of the geometrically optimised bulk crystal, $E_{surface}$ is the total energy of the slab constructed from the bulk crystal, containing an equivalent number of atoms and retaining stoichiometry, and calculated using the same pseudopotential, basis set, kinetic energy cut-off and k-point grid sampling. A is the surface area, as each simulation slab contains two equivalent surfaces; the factor of 2 is included. For the {0001} basal plane, the ultrasoft pseudopotential combined with the coarse, medium and fine basis sets yielded the unrelaxed and relaxed results as shown in table 5.7.

	Unrelaxed	Relaxed
	γ_s	γ_s
Basis set	J m^{-2}	J m^{-2}
Coarse	3.60	1.434
medium	3.75	1.412
fine	3.71	1.436
precise	3.78	1.530

Table 5.7. Surface energies, γ_s, for the {0001} surface calculated using the ultrasoft pseudopotential and the coarse, medium, fine and precise basis sets. The unrelaxed surface energy values are calculated from the single point energy of the input structure, the relaxed surface energies are calculated following geometric optimisation.

The ultrasoft pseudopotential with the four basis sets for the α-alumina {0001} surface provide relaxed surface energies within the expected range, these being between 1.412 J m^{-2} for the medium basis set and 1.53 J m^{-2} for the precise basis set. These values compare well to the published literature, as summarised in table 1.6, in which the relaxed surface energy has a range of 1.76 J m^{-2} to 3.15 J m^{-2}, depending on simulation

technique. In general, the previous density functional theory methods are at the low end of the range, being 1.76 J m^{-2} and 1.98 J m^{-2}. The Hartree-Fock method of calculation resulted in a value of 2.00 J m^{-2}.

As well as comparing surface energies from this work, a further reference to evaluate the accuracy of the computational technique is to measure the percentage relaxation of the uppermost aluminium atom, Al1, calculated by equation 5.2.

$$Relaxation = \frac{\left(D_{final} - D_{initial}\right)}{D_{initial}} \times 100 \qquad \text{Equation 5.2}$$

Where D_{final} is the Al1-O1 layer separation in the minimised structure and $D_{initial}$ is the equivalent separation in the bulk termination structure. The subsequent energy minimisation procedure in all cases discussed in section 1.2.1 finds the optimised output with this aluminium atom relaxed considerably towards the first oxygen layer as illustrated in figure 1.18. Depending on the method of calculation, this relaxation value can be between approximately 50 % to nearly 100 %. In the latter case, a relaxation of 100 % indicates that the aluminium atom forms a single layer with oxygen.

Table 5.8 shows the percentage relaxations and promotions of the first five interlayer separations for both the top and bottom surfaces when calculated with the ultrasoft pseudopotential, in which the average values are almost identical, an indication that the geometry optimisation is correctly converged.

The coarse and medium basis sets gave the O1-Al2 relaxation as negative, in contrast to the other results for the {0001} surface. This lead to a distortion of the average relaxation, when only the fine and precise basis sets are averaged we find +2.00 % for the O1-Al2 on one surface and +1.55 % for the other.

The ultrasoft pseudopotential precise basis set simulations show good agreement for the interlayer relaxations, for the top and bottom surfaces with values all within 1 %. As this combination was used for further calculations on adsorption modes, the precision of the results outlined in table 5.8 were compared to previous quantum mechanical

simulations described in section 1.2.3 and experimental studies discussed in section 1.2.2 on the {0001} surface of α-alumina.

	Relaxation (%)				
Surface one	coarse	medium	fine	precise	average
Al1-O1	-86.22	-86.25	-87.16	-85.12	-86.19
O1-Al2	-0.052	-0.25	+1.72	+2.27	+0.92
Al2-Al3	-45.65	-44.94	-47.02	-47.06	-46.17
Al3-O2	+19.35	+19.11	+20.45	+20.01	+19.73
O2-Al4	+3.96	+3.75	+4.28	+4.76	+4.19
Surface two					
Al1-O1	-87.44	-87.47	-86.98	-84.55	-86.61
O1-Al2	+0.41	+0.21	+1.25	+1.86	+0.93
Al2-Al3	-45.22	-44.51	-46.44	-46.06	-45.46
Al3-O2	+19.86	+19.62	+20.19	+19.55	+19.81
O2-Al4	+4.80	+4.59	+4.63	+4.81	+4.72

Table 5.8. Percentage relaxations for the two distinct {0001} surfaces of a α-alumina crystal calculated using the coarse, medium, fine and precise basis sets with the ultrasoft pseudopotential.

The relaxations shown in table 5.8 are in good agreement to previous density functional theory work in which reported values range between -72.5 % and -86 % for the Al1-O1 relaxation. The results presented here are at the top end of this scale at just less than -85 %, in agreement with the work carried out by de Felice and Northrup,[8] and the value of -86 % calculated by Manassidis *et al*,[9] Verdozzi *et al* [10] and Wang *et al*.[11] The average value for the marginal separation of the O1-Al2 layers is +2.1 %, this is 1 % lower than the majority of the density functional theory calculations outlined in section 1.2.3. Al2-Al3 layer merging value of -46.6 % is again comparable to the existing literature, although the values are more disparate further away from the surface layer as the range is from -42 % to -54 %, so the average for the top and bottom Al2-Al3 relaxation is in the middle of this scope of values. This trend is repeated when the Al3-O2 relaxation of +19.8 % is considered, which falls in the span of existing values which are between +18 % and +25 %.

The results outlined above indicate that the CASTEP program, using the combination of ultrasoft pseudopotentials and precise basis sets gives results for the {0001} surface of an α-alumina crystal consistent with existing theoretical results. However, when the results presented here are brought together with the existing theoretical results [12, 13, 14, 15, 16, 17, 18, 19, 20] and these set against the previous experimental [21] relaxations for the Al1-O1, O1-Al2, Al2-Al3 and Al4-O2 relaxations in table 5.9 and 5.10 respectively, the quantum mechanical results overestimate the Al1-O1 relaxation.

Layer	Experimental [21]	This work
Al1-O1	-51 %	-84.8 %
O1-Al2	+16 %	+2.1 %
Al2-Al3	-29 %	-46.6 %
Al3-O2	+20 %	+19.8 %

Table 5.9. Comparison of CASTEP relaxations for the {0001} α-alumina surface from this work, calculated using the ultrasoft pseudopotential and precise basis set, compared to the x-ray crystallographic experimental data.[21]

Layer	Ab initio results average [12-20]	This work
Al1-O1	-80.8 %	-84.8 %
O1-Al2	+2.4 %	+2.1 %
Al2-Al3	-38.4 %	-46.6 %
Al3-O2	+19.2 %	+19.8 %

Table 5.10. Comparison of CASTEP relaxations for the {0001} α-alumina surface calculated using the ultrasoft pseudopotential and precise basis set, compared to the average of previous ab initio relaxations shown in section 1.2.3. [12-20]

5.2.2 Electronic properties of the {0001} α-alumina surface.

The density of states plot for the α-alumina {0001} surface illustrated in figure 5.4 was calculated using the ultrasoft pseudopotential and precise basis set. The unit cell dimensions used in the calculation of the {0001} surface were a and b = 4.692 Å. This was doubled in the a and b direction to provide a four-fold surface area for subsequent

adsorptions of molecules. The vacuum gap was 13 Å, giving a c-direction repeat distance of 25.979 Å, allowing adsorbate molecules to effectively only interact with one surface.
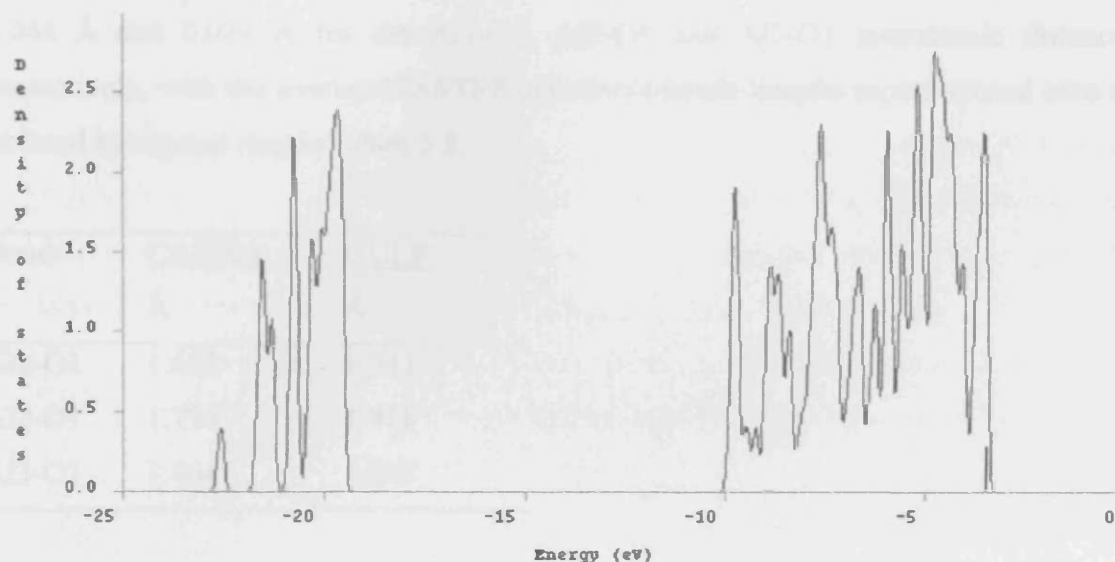
Figure 5.4. Density of states plot for the {0001} surface of α-alumina using the ultrasoft pseudopotential and precise basis set. LVBm = -22.58 eV, LVBM = -19.57 eV, UVBm = -9.87 eV and UVBM = -3.49 eV.

The density of states plot in figure 5.4 shows the lower valence band extending from -22.58 eV to -19.57 eV. The band gap of *ca.* 10 eV extends from -19.57 eV to -9.87 eV, with an upper valence band width of roughly 6 eV. Compared to the bulk crystal from which this surface is constructed, the lower valence band was reduced by about 6 eV, whereas the upper valence band maximum, UVBM, stays at *ca.* -3 eV, the upper valence band minimum, UVBm, undergoes a movement from -3.75 eV to -9.87 eV.

Figure 5.4 agrees reasonably well with the total density of states plot in figure 1.9 calculated by the local density approximation as the lower valence band falls in the region -16 eV to -19 eV and the upper valence band from 0 eV to -7.3 eV, a band gap of 8.7 eV, in close agreement with the CASTEP determined value.

In chapter four a hexagonal ring of the α-alumina {0001} surface, containing three surface oxygen O1 layer atoms, and three aluminium atoms, one from each of the terminating Al1 layer, the shallow subsurface Al2 layer and the deep subsurface Al3

layer was used in the analysis of surface structure. Table 5.11 details the interatomic bond lengths for this ring optimised with CASTEP compared to the equivalent GULP minimised bond distances as detailed in chapter four. Table 5.11 shows the three bond lengths generated by CASTEP are shorter than those found by GULP, by 0.089 Å, 0.044 Å and 0.029 Å for the Al1-O1, Al2-O1 and Al3-O1 interatomic distances respectively, with the average CASTEP calculated bonds lengths superimposed onto an isolated hexagonal ring in figure 5.5.

Bond	CASTEP	GULP
	Å	Å
Al1-O1	1.652	1.741
Al2-O1	1.774	1.818
Al3-O1	1.864	1.893

Table 5.11. Average lengths for the three distinct aluminium to oxygen bonds in one surface hexagonal ring calculated by CASTEP, compared to the equivalent GULP values originally shown in table 4.4.
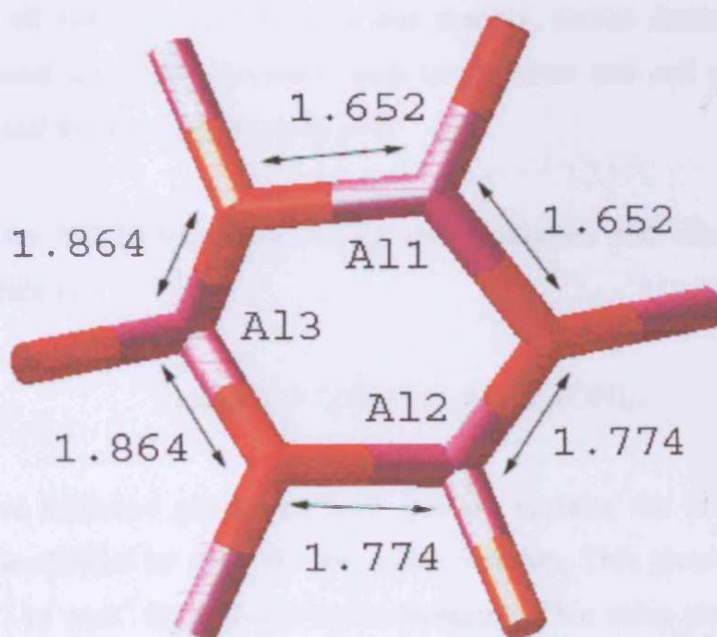

Figure 5.5. The average Al1-O1, Al2-O1 and Al3-O1 bond lengths shown for the CASTEP minimised hexagonal ring from the {0001} surface. All bond lengths are Angstroms, and each oxygen shown is from the O1 layer.

5.3 Hydroxylated {0001} α-alumina surface.

5.3.1 Structure of the hydroxylated {0001} α-alumina surface.

Water may adsorb on the α-alumina {0001} surface via either dissociative chemisorption or as a molecularly physisorbed species. The chemisorption yields a surface terminated by hydroxyl groups. As outlined in section 4.3, the initial hydroxylated surface was constructed by removing the terminating aluminium atoms on each surface to leave an oxygen terminated slab. One hydrogen atom was then placed 1 Å above each unsaturated oxygen atom, three of which are formed by Al^{3+} removal. This process retains stoichiometry, a zero charge in the unit cell and zero dipole across the cell. Equation 5.3 defines the chemisorption for any number of water molecules.

$$Al_{2x}O_{3y} + nH_2O \rightarrow Al_{2x}O_{3y+n}H_{2n} \qquad \text{Equation 5.3}$$
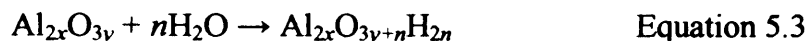
Both surfaces of the crystal are hydroxylated, with a sufficient vacuum gap to avoid any interaction between the surfaces in adjacent periodic crystals by using a c vector of 25.979 Å. For all reactions calculated in this manner, certain fundamental conditions must be consistent across the equation, such as the same unit cell parameters, kinetic energy cut-off and the k-point sampling grid.

The equation for full hydroxylation using the simulation slab discussed for the Al terminated surface is:

$$\tfrac{2}{3}Al_{24}O_{36} + 12H_2O \rightarrow Al_{16}O_{12}(OH)_{24} \qquad \text{Equation 5.4}$$
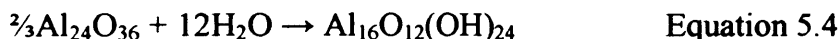
This has twelve hydroxyl groups on each {0001} surface, the calculated energy of reaction, ΔE_r, is -1184.4 kJ mol^{-1} for the entire reaction. This gives the hydroxylation energy as -98.7 kJ mol^{-1} for a single water molecule. This value compares favourably with existing experimental energies of hydroxylation, for example, Della Gatta et al [22] found the energy for molecular adsorption to be -75 kJ mol^{-1}, and Hendriksen et al [23] calculated the low coverage hydroxylation energy to be -109 kJ mol^{-1} against the high coverage value of -57 kJ mol^{-1}; the equivalent to this fully hydroxylated slab.

For the hydroxylated surface, the surface energy was first estimated by taking account of the total energy of an isolated water molecule:[24]

$$\gamma_s = \frac{E_{hydroxylated} - (E_{bulk} + nE_{water})}{2A}$$ Equation 5.5

Where $E_{hydroxylated}$ is the total energy of the hydroxylated surface, E_{bulk} is the total energy of the stoichiometric bulk optimised structure, nE_{water} is the total energy of the number of water molecules to balance equation 5.3 and A is the surface area. The surface energy for the product in equation 5.5 is -0.294 J m^{-2}. This is an unrealistic value as this indicates that the hydroxylated slab is thermodynamically preferred to the bulk crystal and will form spontaneously without any energy. However, equation 5.5 does not take into consideration the energy change defined above which is needed to hydroxylate the slab with the number of water molecules, nE_{water}. Equation 5.6 shows the inclusion of this term, which is described by the thermodynamic cycle in figure 5.6. The γ_s value for the clean surface is generated by $E_{hydroxide}$ and E_{bulk} as in equation 5.1

$$\gamma_s = \frac{E_{hydroxide} - (E_{bulk} + nE_{water} + \Delta E_r)}{2A}$$ Equation 5.6

This gives the surface energy, γ_s, as 1.00 J m^{-2}; a credible value when compared to the surface energies shown in table 5.9, as it is known the hydroxylated slab does not form spontaneously from the bulk crystal.
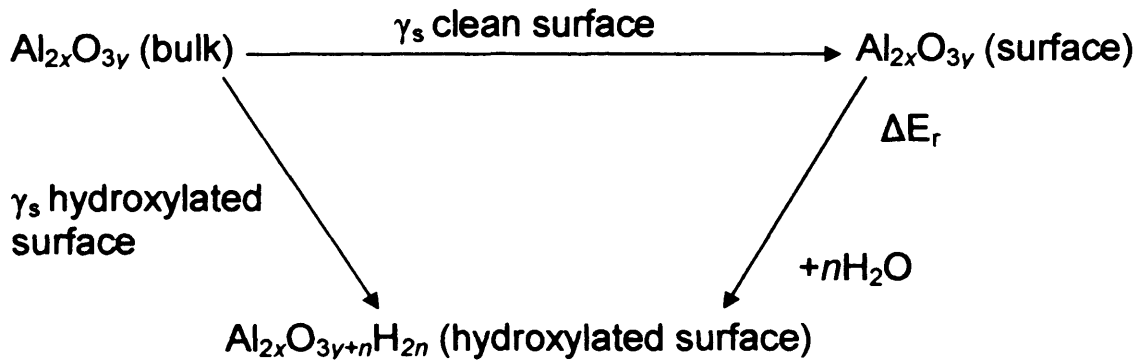

Figure 5.6. Thermodynamic cycle accounting for the inclusion of the ΔE_r and E_{water} terms to find the surface energy (γ_s) value for the hydroxylated {0001} α-alumina surface.

The layer separation relaxations of the hydroxylated surfaces were compared to the aluminium terminated clean surface. Table 5.12 shows the addition of hydroxyl groups to both {0001} surfaces in the slab does not substantially alter the sub-surface and bulk structure as the relaxations follow the positive or negative values presented in table 5.8. This gives the O1-Al2 average relaxation as +2.95 %, Al2-Al3 as -29.05 % and Al3-O2 as +9.15 %.

The first three layers are within approximately 1 % of the theoretical values determined by Bankhead using the localised basis set approach in the DSolid program shown in table 1.10.[20] The three layers for the other hydroxylated surface show good correlation with the first surface. The DFT-GGA work of Parker et al[25] shows the equivalent O1-Al2, Al2-Al3 and Al3-O2 relaxations to be +6.0 %, -39.1 % and +11.9 % respectively, comparing well to these results shown in table 5.12.

Layer	Clean relaxation	Hydroxylated relaxation
O1-Al2	+2.07 %	+2.95 %
Al2-Al3	-46.56 %	-29.05 %
Al3-O2	+19.78	+9.15 %

Table 5.12. Percentage relaxations for the clean and hydroxylated {0001} α-alumina surface, calculated using the ultrasoft pseudopotential and precise basis set combination.

Taking the method of analysing the interatomic bond distances in table 4.4, figure 5.7 illustrates the optimised hexagonal-based surface structure containing aluminium atoms from Al2 and Al3 layers, the terminating O1 layer oxygen atoms and the hydroxyl group hydrogen atoms.
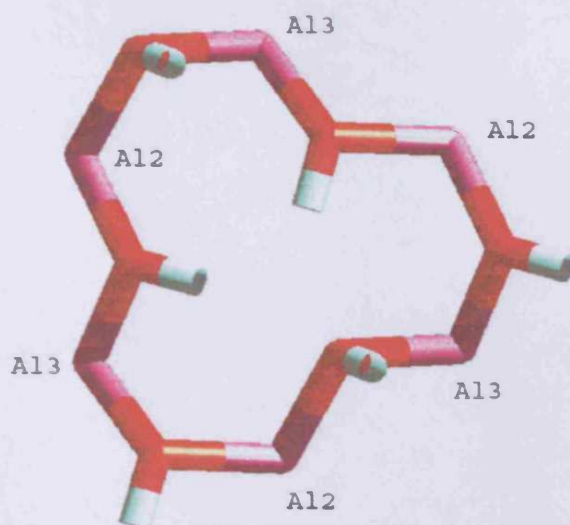
Figure 5.7. CASTEP calculated surface structure equivalent to that illustrated in figure 4.7 (a). This should be visualised as three hexagonal Al_3O_3 subunits joined together, with the central aluminium from the All layer removed. All oxygen atoms are from the O1 layer.

Compared to table 5.11 for the clean {0001} surface, the hydroxylated CASTEP determined bond lengths do not follow the trend of being marginally shorter than for the equivalent GULP minimised slab, as can be seen in table 5.13. Here, the average Al2-O1 bond is 0.012 Å longer than found with GULP, whereas the average Al3-O1 bond is 0.01 Å shorter, with the O1-H bond being 0.055 Å shorter. However, once again, there is good agreement at this local level between the two methods.

Bond	GULP value [Å]	CASTEP value [Å]
Al2-O1	1.768	1.780
Al3-O1	1.916	1.906
O1-H	1.027	0.972

Table 5.13. Comparison of the bond lengths, Al2-O1, Al3-O1 and O1-H in the terminating surface layer of the hydroxylated {0001} α-alumina surface, calculated using GULP and CASTEP.

193

5.3.2   Electronic structure of hydroxylated {0001} α-alumina surfaces.

The density of states plot for the relaxed hydroxylated {0001} surface of α-alumina is shown in figure 5.8. The lower valence band extends from -22.75 eV to -19.43 eV, the same range as for the clean surface, although the hydroxylated structure has more peaks present within this range and the large peak at the lower valence band maximum (LVBM) shown in figure 5.4 is not present, being replaced with three smaller peaks. This signifies the orbitals involving oxygen $2s$ character have fewer equivalent bonding directions than in the clean surface slab, possibly due to bonding with hydrogen, which occurs at different energies therefore spreading the peak. At the upper valence band minimum, the bonding oxygen $2s$ character is split from one high density peak in the clean surface density of states to three low density peaks.

There is a high density of states at the UVBM, indicating the bands are relatively flat consistent with the presence of a high density of oxygen $2p$ non-bonding atomic orbitals. The UVBm has moved downwards by 1 eV from its position in the clean surface density of states plot, resulting in a smaller LVB to UVB band gap of 8 eV.

Figure 5.9 illustrates the density of states plot for the isolated water molecule in the same periodic box compared to the clean surface and the hydroxylated surface to determine the effect that the oxygen-hydrogen bonds in both water and have on the density of states plot for the hydroxylated surface. The peaks occur at -24.92 eV, -12.88 eV, -9.05 eV and -7.13 eV. There are some similar energy peaks in the density of states plots for water and the hydroxylated surface, showing that oxygen-hydrogen bonds give rise to approximately similar energy peaks, although the shifts seen indicate that the Al-OH bonds occur at lower energies than the H-OH, as, for example the water peak at -24.92 eV in figure 5.9 disappears in the hydroxylated surface density of states plot in figure 5.8.

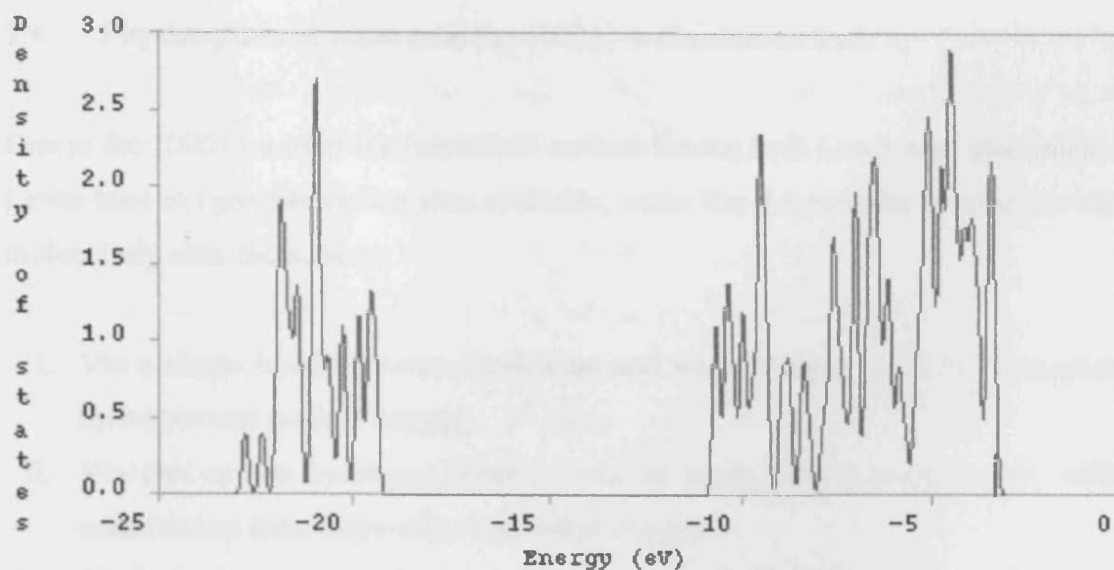*Figure 5.8. Total density of states plot for the hydroxylated {0001} surface of α-alumina, showing both the lower and upper valence bands. LVBm = -22.75 eV, LVBM = -19.43 eV, UVBm = -10.72 eV and UVBM = -3.33 eV*
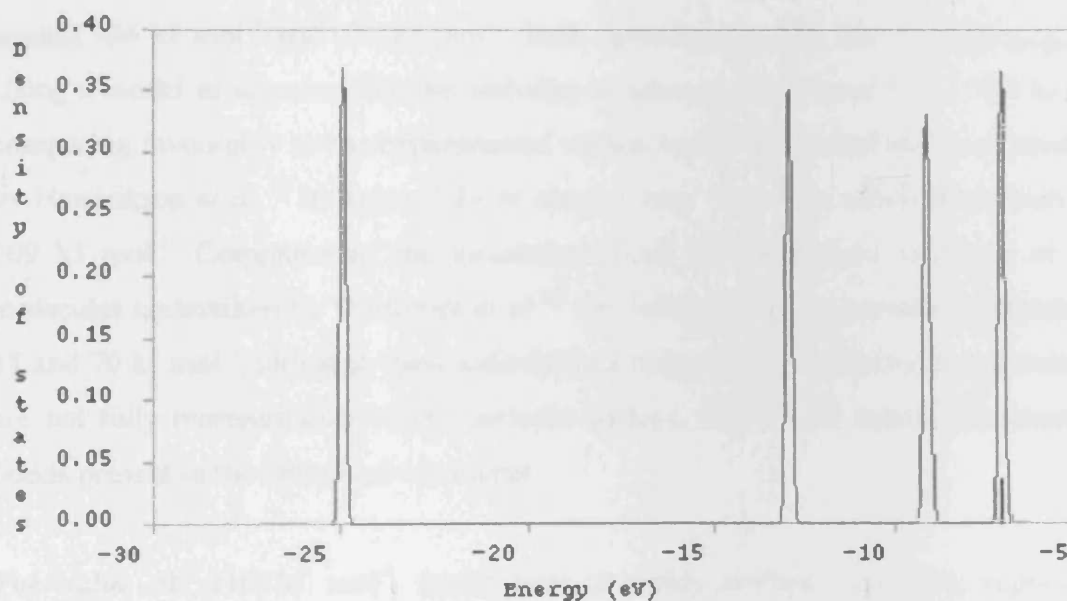

Figure 5.9. Total density of states for an isolated water molecule using the same method of calculation as for the hydroxylated surface. Peaks at -24.92 eV, -12.88 eV, -9.05 eV and -7.13 eV.

5.4   Physisorption of water onto the {0001} α-alumina surface.

Due to the {0001} α-alumina minimised surface having both Lewis acid aluminium and Lewis base oxygen adsorption sites available, water has three modes in which to adsorb molecularly onto the surface:

I.   Via a single bond between aluminium and water oxygen, with no interaction of hydrogen and surface oxygen.

II. Via one or two hydrogen bonds to one or more surface oxygen sites, with no contribution from aluminium and water oxygen.

III. Via both aluminium and water oxygen and one or two hydrogen to surface oxygen bonds. This is the adsorption mode most likely to lead to a transition state to dissociative adsorption.

Three models in scheme [II] initially with two hydrogen to surface oxygen interactions found enthalpies of adsorption of: -21 kJ mol^{-1} resulting in two $O_{surface}$-H_{water} bonds, against -34 kJ mol^{-1} and -21 kJ mol^{-1}, both optimised to find one $O_{surface}$-H_{water} bond. Using a model in scheme [III], the enthalpy of adsorption is found to be -116 kJ mol^{-1}, comparing favourably to the experimental values found for the enthalpies of adsorption by Hendriksen et al [23] in figure 1.23 in chapter one, where the initial adsorption was -109 kJ mol^{-1}. Compared to the theoretical work on the surface coverage of water molecules undertaken by Wittbrodt et al [26] this value is less by between approximately 15 and 70 kJ mol^{-1}, although these calculations took place on clusters of α-alumina that are not fully representative of the periodic surface. Table 5.18 details the interatomic bonds present in the optimised structures.

The value of -116 kJ mol^{-1} found here provides evidence that the experimental adsorption of water is favoured through the aluminium to water oxygen bond initially when there is no competition for adsorption sites, however, when the coverage increases, it could be found that the favourable method of adsorption is via hydrogen to available basic oxygen sites, as experimentally the heat of adsorption at high coverages falls to -57 kJ mol^{-1}, approaching the values calculated for scheme [II] above.

The density of states plot for the physisorption of water equalling -116 kJ mol^{-1} and proceeding via scheme [I] above is shown in figure 5.10. This shows the lower valence band extends for *ca.* 4 eV from -22.5 eV to -18.5 eV, a band gap of 7.9 eV to -9 eV. The upper valence band stretches from -9 eV to -2.5 eV, giving this a bandwidth of 8.1 eV. As the peak at -10.6 eV does not occur in the hydroxylated surface shown in figure 5.8, this low intensity peak is representative of molecular water, as figure 5.9 shows the isolated water total density of states, with a peak at -12.9 eV. The molecular adsorption of water causes this peak to shift towards the upper valence band; this region is associated with oxygen *2p* orbitals, and therefore it is assumed that these orbitals are responsible for the physisorption of water, interacting with aluminium surface orbitals and water hydrogen orbitals. The UVBm is a single intense peak from oxygen *2p* orbitals, upon dissociation of water, this peak combines with the isolated water peak at -10.6 eV to form the intermediate intensity bands stretching over approximately 2 eV at the UVBm.
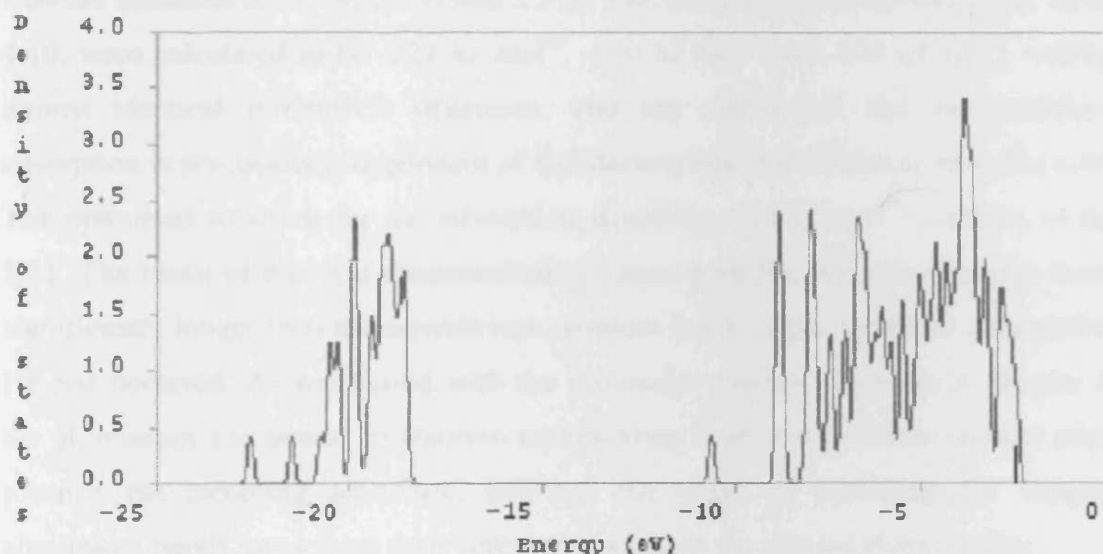
Figure 5.10. Total density of states for the molecular adsorption of water to the {0001} α-alumina surface using the CASTEP program. Peaks at -22.77 eV, -21.62 eV and -10.88 eV. LVBm = -21.3o eV, LVBM = -17.04, UVBm = -8.75 eV and UVBM = -2.81 eV.

The band structure for the physisorbed water will have the upper valence band maxima and minima relatively flat, although not densely populated, as this is the integral of the area under the UVBM and UVBm peaks at -2.5 eV and -9.0 eV in figure 5.10. The most densely populated bands will be at *ca.* -3.5 eV to -5.0 eV; this is the widest band with

the largest area. The band structure in the lower valence band will be flat across the Brillouin zone at the maxima, whilst the two small peaks at the minima will cause an uneven band structure, in the same arrangement as the fully hydroxylated density of states as shown in figure 5.8.

5.5 Reaction of hydrogen fluoride on the {0001} α-alumina surface.

5.5.1 Chemisorption of hydrogen fluoride.

Three models using the optimised {0001} α-alumina surface were considered for adsorption of hydrogen fluoride. The starting geometry was found by locating the molecule with the fluorine atom directly over a Lewis acid aluminium site with the hydrogen atom close to a neighbouring oxygen site in order to try to impose a 1-2 type adsorption. After optimisation, this type of adsorption was found to be favourable leading to dissociation of the HF molecule for three starting points with aluminium-fluorine distances of 1.5 Å, 2.0 Å and 2.5 Å. The energies of adsorption, using equation 4.10, were calculated to be -221 kJ mol^{-1}, -220 kJ mol^{-1} and -229 kJ mol^{-1}, leading to almost identical minimised structures, and the conclusion that the enthalpy of adsorption is practically independent of the starting adsorbate distance from the surface. The optimised structure for the adsorption equalling -221 kJ mol^{-1} is shown in figure 5.11. The result of this is a chemisorbed structure with the hydrogen fluorine distance significantly longer than the equilibrium covalent bond length, therefore dissociation of HF has occurred. As was found with the molecular mechanics results in chapter four, the aluminium site bound to fluorine moves away from the previous relaxed position towards the incoming adsorbate, this has the effect of stretching the oxygen to aluminium bonds away from their reference values in the relaxed clean surface.

As can be seen from figure 5.11, the Al1-O1 bond length increases from the clean surface value of 1.652 Å to 1.841 Å when both sites are involved in the chemisorption process. The Al1-O1 bond length is 1.898 Å when only the aluminium atom in the bond is involved in chemisorption. For the Al3-O1 bond length, an increase is again observed, due to the promotion of the oxygen site towards the hydrogen in the same manner as aluminium towards fluorine. This bond length is 1.971 Å against the clean

surface value of 1.864 Å; also illustrated in figure 5.11 is an Al3-O1 bond length of 1.878 Å this is not involved in HF adsorption, suggesting that the chemisorption of HF causes a minor intermediate range restructuring of the {0001} surface. This is reinforced by another Al1-O1 bond length shown to be 1.644 Å, shorter than the clean surface equivalent.
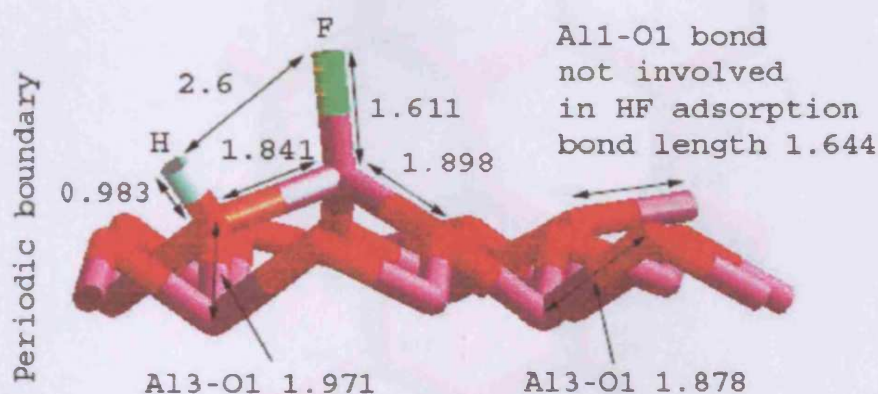
Figure 5.11. The optimised positions for 1-2 chemisorption of HF onto the {0001} α-alumina surface, where for clarity only the Al1, O1, Al2 and Al3 surface layers are shown. All bond lengths are in Angstrom units.

The other two adsorption calculations found aluminium to fluorine and hydrogen to oxygen distances virtually identical to the values shown in figure 5.11, meaning the same structure has been identified from three separate start points. The interatomic distances of the chemisorbed hydrogen fluoride molecule may be analysed in the same way as the previous {0001} α-alumina surface slabs: by removing all of the slab except the top four Al1, O1 Al2 and Al3 layers and in this case, the chemisorbed HF molecule. Figure 5.12 illustrates the plan view of this surface. The bond lengths for Al1-O1 are 1.694 Å and 1.698 Å, whilst the Al1-O1* bond length is 1.841 Å. The bond lengths can be further analysed fully in table 5.14.

Table 5.14 shows that there is a significant deviation from the aluminium terminated {0001} α-alumina surface structure even for bonds not directly involved in the chemisorption process. When the atoms are not involved in this process, the presence of

199

hydrogen fluoride does not cause any substantial rupturing of the surface hexagonal structures, for example, the average Al1-O1 bond is 0.044 Å longer when HF is present on the surface, but when both of these atoms are involved in the chemisorption, the Al1-O1* bond is 0.189 Å longer than the aluminium terminated surface. This is also the case for the Al2-O1/ Al2-O1* and Al3-O1/Al3-O1* bonds for when the HF is on the surface and when the O1* is the adsorption site for hydrogen.
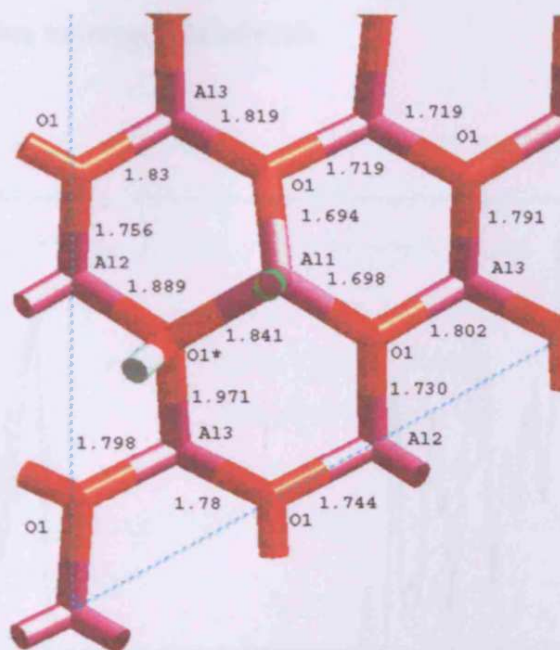
Figure 5.12. Plan view of the {0001} α-alumina surface hexagonal ring systems with the hydrogen fluoride molecule adsorbed in a 1-2 format. All distances are shown in Angstroms.

Bond	Al terminated surface	Chemisorbed HF surface
	Å	Å
Al1-O1	1.652	1.696
Al1-O1*	-	1.841
Al2-O1	1.774	1.734
Al2-O1*	-	1.889
Al3-O1	1.864	1.803
Al3-O1*	-	1.971

*Table 5.14. Full analysis of the interatomic bond lengths for the {0001} surface slab of α-alumina, where the * suffix indicates that the O1 site is responsible for the chemisorption of hydrogen.*

The density of states plot for the chemisorbed HF model illustrated in figures 5.11 and 5.12 is shown in figure 5.13. This compares well to the {0001} α-alumina surface density of states plot shown in figure 5.4 for the distribution of the upper and lower valence bands. In figure 5.13, there are three additional low intensity and width peaks at *ca.* -11 in the region expected for oxygen *2p* orbitals, and two peaks at *ca.* -23.5 eV and *ca.* -24.5 eV from the electronegative fluorine atom. The intense peak at *ca.* -21.5 eV in the hydroxylated structure density of states plot in figure 5.8 is also repeated in figure 5.10 and is likely to be due to oxygen 2s orbitals.
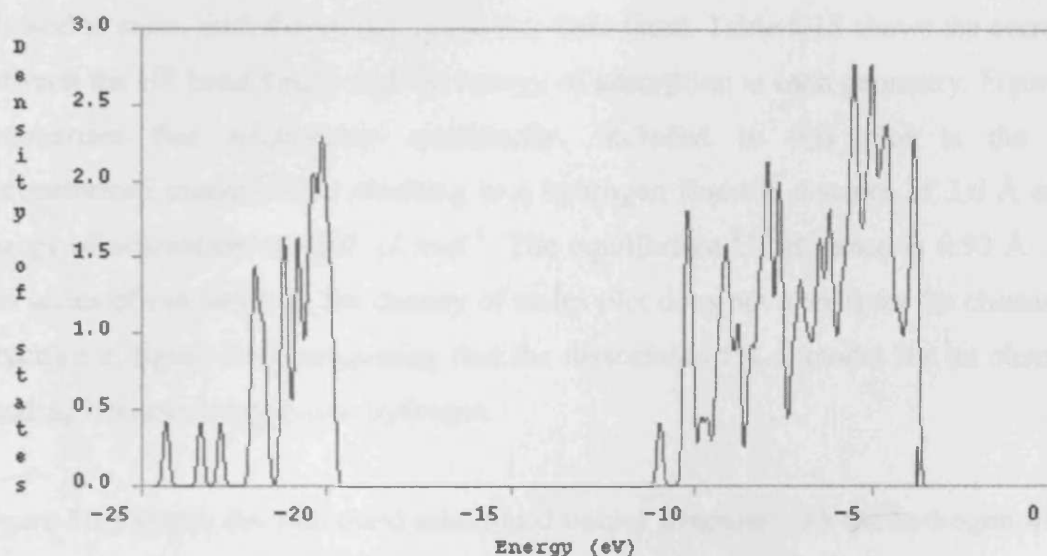
Figure 5.13. Density of states plot for adsorbed HF on the {0001} α-alumina surface, showing the lower valence bands at -24.5 eV to -20 eV and the upper valence band at -11 eV to -3.5 eV. Peaks at -24.31 eV, -23.35 eV, -22.82 eV and -10.93 eV. LVBm = -21.85 eV, LVBM = -19.8 eV, UVBm = -10.23 eV and UVBM = -3.73 eV.

The average energy of chemisorption value of -223 kJ mol⁻¹ is considerably lower than the *DSolid* density functional theory results by Bankhead *et al*,[27] discussed in section 1.3.6, in which the energy of adsorption is -132 kJ mol⁻¹ from a gas phase HF molecule in the presence of a dichloromethane molecule also in the gas phase.

5.5.2 Physisorption of hydrogen fluoride.

On the minimised structure shown in figure 5.12, further calculations were carried out to find a molecularly physisorbed hydrogen fluoride structure, with no dissociation to chemisorption. For such a simulation, the interatomic hydrogen to fluorine distances were constrained from 2.4 Å to 1.4 Å and these atomic coordinates held fixed in these positions across the optimisation procedure. As is seen in figure 5.11, the hydrogen to fluorine distance is 2.6 Å for chemisorption of HF.

With the constrained HF coordinates, the Al1, O1, Al2 and Al3 layer atoms were allowed to relax, with the other layer atoms held fixed. Table 5.15 shows the correlation between the HF bond length and the energy of adsorption at each geometry. Figure 5.14 summarises this relationship graphically. Included in this plot is the initial unconstrained minimisation resulting in a hydrogen fluoride distance of 2.6 Å and the energy of adsorption of -221 kJ mol^{-1}. The equilibrium HF distance is 0.93 Å. Along this series of calculations, the density of states plot does not alter from the chemisorbed structure in figure 5.13, suggesting that the dissociated 1.4 Å model has an element of bonding between oxygen and hydrogen.

Figure 5.15 shows the annotated minimised output structure with the hydrogen fluorine distance constrained at 1.4 Å. The same bond lengths shown in figure 5.11 for the chemisorption energy of -221 kJ mol^{-1} are shown in figure 5.15 for the HF constrained at 1.4 Å. The aluminium adsorption site distance to the fluorine atom is 1.705 Å, compared to 1.611 Å in the chemisorption model. This aluminium site is elevated towards the fluorine, the Al1-O1 bond length (where O1 is not involved in adsorption) is not increased significantly– the 1.671 Å value for physisorption is closer to the clean surface value of 1.652 Å. This is mirrored for the Al1-O1 bond where both Al1 and O1 are involved in adsorption, the distance being 1.782 Å, with the equivalent chemisorption distance of 1.841 Å. Here, O1 is also promoted similarly towards the adsorbate hydrogen atom. The surface oxygen (O1) distance to hydrogen is longer at 1.156 Å, compared to the corresponding chemisorbed value of 0.983 Å, indicating that the hydrogen-fluorine interaction has weakened the oxygen-hydrogen bond formed in the chemisorbed state.

Hydrogen to fluorine distance	Energy of adsorption
Å	kJ mol⁻¹
2.4	-224
2.2	-212
2.0	-190
1.8	-160
1.6	-119
1.4	-72

Table 5.15. Adsorption energy as a function of hydrogen – fluorine distance, with the physisorbed state at 1.4 Å to an entirely dissociated molecule at 2.4 Å.
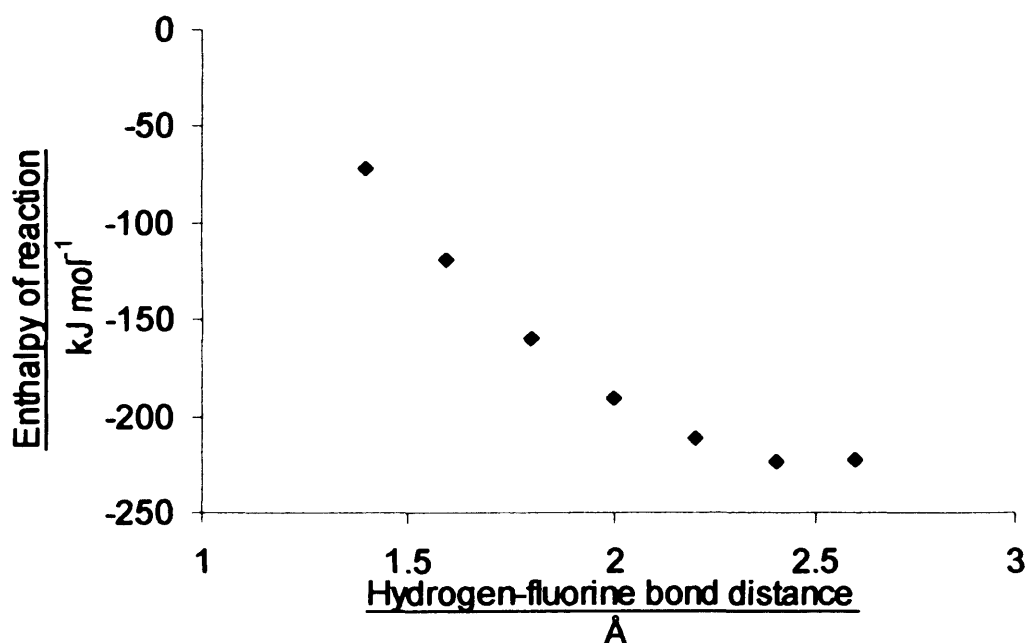
Figure 5.14. Graphical representation of the near-physisorbed to near-chemisorbed transition of HF energy of reaction as a function of bond length.

Due to the molecular coordinate constraint imposed upon HF for the optimised structure in figure 5.15, combined with the noticeable promotion of O1 away from the surface towards hydrogen, the Al3-O1 bond is stretched to 2.199 Å, an approximately 18 % increase upon the clean surface value. This shows the presence of molecular hydrogen fluoride causes a substantial restructuring of the immediate surface layer, which may be

consolidated by removing the constraints imposed to reach an energetically favourable configuration.
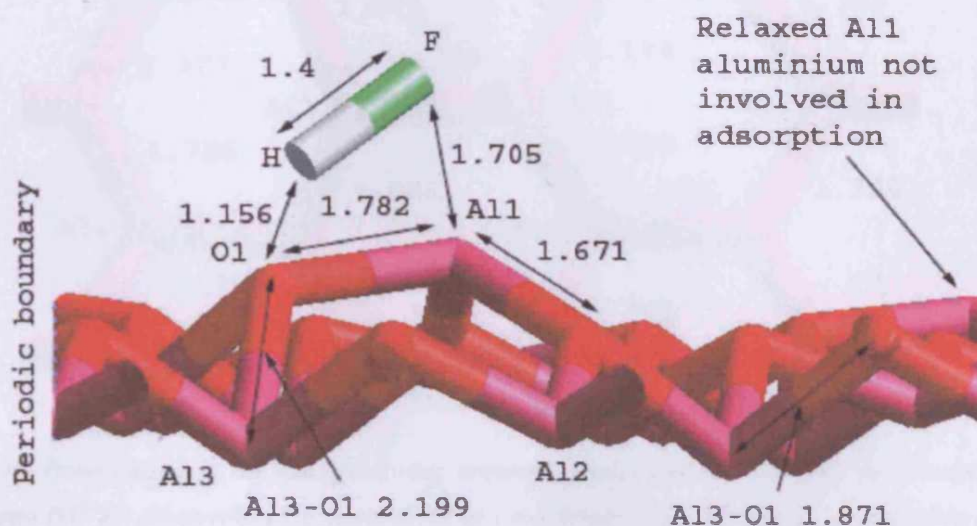
Figure 5.15. Optimised configuration of HF constrained at 1.4 Å, approaching a physisorbed state, showing the subsequent bond lengths in Angstroms. The energy of adsorption is -72 kJ mol⁻¹.

With the HF molecules constrained in this way giving a wide range of energies of adsorption, the effect on the local adsorption site environment is likely to be varied between the two extremes at -72 kJ mol-1 and at -224 kJ mol⁻¹. The hexagonal ring system is analysed for these two cases, in figure 5.16 for the adsorption yielding -72 kJ mol⁻¹ and in figure 5.17 for the adsorption at -224 kJ mol⁻¹.

As with the investigation into the bond lengths for the chemisorbed hydrogen fluoride molecule described previously, the bonds can be separated by whether they are directly involved or adjacent to an adsorption site, these can then be compared to the distances in the hexagonal ring systems that are not immediately involved in this adsorption and the aluminium terminated {0001} α-alumina surface notation. Table 5.16 summarises these bond lengths found for the two structures in figures 5.16 and 5.17.

Figure 5.16. Bond lengths in the hexagonal ring structures immediately surrounding the adsorption sites Al1 and O1* for physisorbed HF constrained at 1.4 Å bond length. The energy of adsorption is - 72 kJ mol⁻¹.

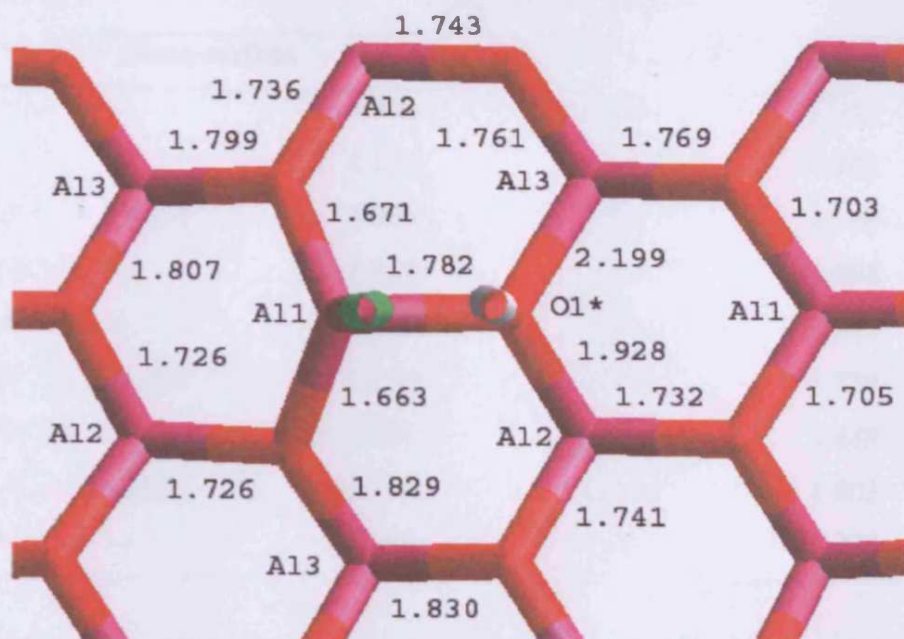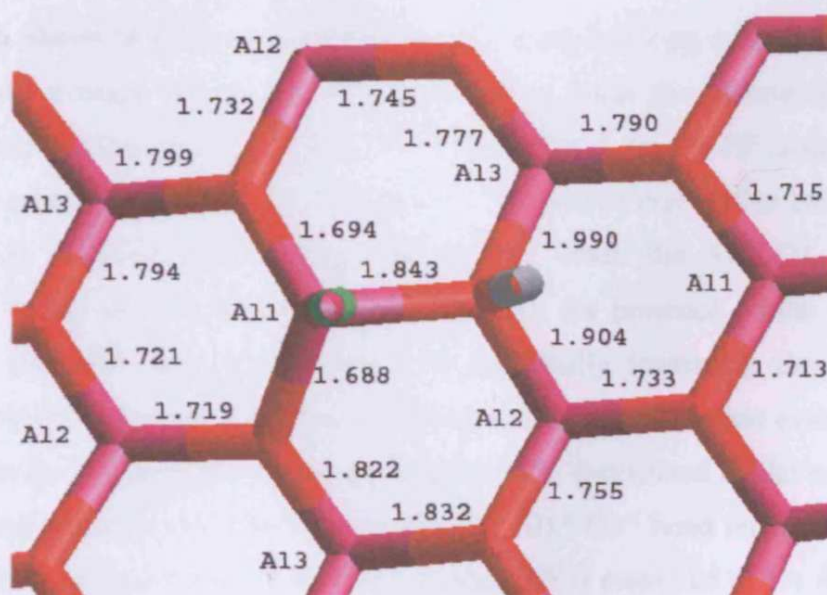*Figure 5.17. Bond lengths in the hexagonal ring structures immediately surrounding the adsorption sites Al1 and O1* for physisorbed HF constrained at 2.4 Å bond length. The energy of adsorption is - 224 kJ mol⁻¹. The oxygen site bound to the hydrogen is denoted O1*.*

	Interatomic distances			
	Clean surface	HF at 1.4 Å	HF at 2.4 Å	Chem. HF
Al1*-F	-	1.706	1.618	1.611
O1*-H	-	1.156	0.973	0.983
Al1-O1	1.652	1.704	1.714	1.696
Al1*-O1	-	1.667	1.691	1.898
Al1*-O1*	-	1.782	1.843	1.841
Al2-O1	1.774	1.734	1.734	1.734
Al2-O1*	-	1.928	1.904	1.889
Al3-O1	1.864	1.799	1.802	1.803
Al3-O1*	-	2.199	1.990	1.971

Table 5.16. Interatomic distances for the physisorbed HF structures where the energy of adsorption is -72 kJ mol⁻¹ where HF was constrained at 1.4 Å giving an energy of adsorption of -224 kJ mol⁻¹ with HF constrained at 2.4 Å. Al1* is the adsorption site for F and O1* is the adsorption site for H. The values for the clean aluminium terminated surface and the chemisorbed HF structure are included.

Table 5.16 shows there is an alteration in the hexagonal ring system, as the Al1-O1 bond length average across the surface increases from the aluminium terminating {0001} surface value of 1.652 Å to 1.704 Å and 1.714 Å for the HF constraint at 1.4 Å and 2.4 Å respectively; in figures 5.16 and 5.17 it is seen that neither atom of the Al1-O1 bond is involved in the adsorption of HF. When the Al1*-O1 distances are compared to the Al1-O1 distances, it is seen that the presence of the fluorine atom bound to the Al1* site has the effect of marginally increasing the bond lengths compared to the clean surface value in both cases of HF adsorption evaluated in table 5.16. When the HF molecule is approaching the fully dissociated model as found by the chemisorbed structure described previously, the Al1*-O1* bond lengthens from 1.652 Å in the clean surface structure, to 1.782 Å when HF is restricted to 1.4 Å and to 1.843 Å with the HF distance constrained at 2.4 Å compared to the Al1*-O1* distance for chemisorbed HF with no geometric limitations of 1.841 Å.

From table 5.16, it is seen that when HF is physisorbed with the constraints explained above, all of the average bond lengths increase from the aluminium terminated surface, the largest increase in bond length is when one of the atoms in the Al2-O1* and Al3-

O1* bonds is involved in adsorption. If neither of the atoms in these bonds is involved in adsorption (Al2-O1 and Al3-O1 in table 5.16) the bond length decreases when HF is introduced to the surface.

The aluminium Al1* adsorption site undergoes a movement away from the surface for both of these optimised structures, when the HF is constrained at 2.4 Å, the Al1* atom moves by 0.632 Å in the c direction away from its position in the minimised aluminium terminated slab. With the HF restricted to a bond length of 1.4 Å, the Al1* aluminium atom moves 0.549 Å in the c direction away from the optimised position. This shows that the Al1* atom is moving out of the surface as the HF bond is cleaved.

5.6   θ-Alumina.

5.6.1   Bulk structure determination of θ-alumina.

The θ-alumina structure is a transition polymorph precursor to the α-alumina phase in the thermal degradation of boehmite as described in chapter one and illustrated in figure 4.36. Within this study, the θ form of alumina is significant due to this crystal containing both octahedral and tetrahedral aluminium coordination sites, using density functional theory it is hoped to provide a quantitative difference between the two structures and offer conclusions as to the preferential adsorption aluminium Lewis acid site for molecules such as hydrogen fluoride and water, the latter leading ultimately to a hydroxylated surface.

Based on the accuracy of the ultrasoft pseudopotential and precise basis set employed within the bulk structure calculations of α-alumina, the decision was taken to concentrate purely on the ultrasoft pseudopotential initially using the three basis sets: medium, fine and precise to model the x-ray diffraction determined crystal structure. As with the α-alumina optimisations, the k-point sampling grid was retained at 2×2×2, with the kinetic energy cut-off for each minimisation altering according to the basis set. Table 5.17 shows the unit cell parameters compared to the experimental cell. For the α-alumina test case, the precise basis set was selected because of the close representation of the unit cell volume, for θ-alumina the precise function also has the lowest energy.

As for α-alumina, surface energy values were calculated with all three basis sets within the ultrasoft pseudopotential, from this an evaluation of which function to use for further calculations was taken. From the data presented in table 5.17, it was decided to adopt the precise basis set as the model for calculations based on θ-alumina. This also ensures that results are consistent with the α-alumina work.

| | A | b | c | Volume | Energy |
	Å	Å	Å	Å^3	kJ mol^{-1}
Experimental	11.795	2.91	5.621	187.371	
Medium	11.793	2.895	5.599	185.322	-5759.808
Fine	11.775	2.883	5.563	183.228	-5762.085
Precise	11.768	2.863	5.548	181.118	-5762.498

Table 5.17. Comparison of the medium, fine and precise basis sets calculated with the ultrasoft pseudopotential to the experimental unit cell parameters for the θ-alumina crystal.

Figure 5.18. Total density of states plot for the bulk structure of θ-alumina, calculated using the ultrasoft pseudopotential and precise basis set, illustrating the lower and upper valence bands. LVBm = -12.48 eV, LVBM = -10.04 eV, UVBm = -0.17 eV and UVBM = 6.27 eV.

Figure 5.18 illustrates the total density of states for the bulk crystal of θ-alumina, calculated using the ultrasoft and precise combination of pseudopotential and basis set. This gives the lower valence band from -12.5 eV to -10 eV, a band gap of 10 eV to the

upper valence band stretching from 0 eV to +6.5 eV. Figures 1.6 and 1.8b illustrate the density of states plots for θ-alumina, with the lower valence bands less than -15 eV, and the upper valence band maxima at equal to or less than 0 eV. Here, the upper valence band minimum is at 0 eV.

5.6.2 Surfaces of θ-alumina.

The ideal surfaces of θ-alumina in the overall context of this work contain both octahedral and tetrahedral aluminium sites accessible to small adsorbate molecules such as water and hydrogen fluoride. Using the Shiftcell program as outlined in chapter three to establish stoichiometric surfaces that exist with zero net dipole, energy minimisations of the low Miller index surfaces calculated using the ultrasoft pseudopotential and precise method revealed the surface energy (γ_s) values that are given in table 5.18.

From these surface energy values, even though the surface energies are in the ideal oxide range, only the {101} surface had a suitable termination along the above guidelines. This slab is illustrated in figure 5.19, showing the arrangement of the octahedral and tetrahedral aluminium sites, the {101} θ-alumina surface is considerably more complex than the aluminium terminated {0001} basal plane of α-alumina, although the surface energies fall into approximately the same range. The lack of a single terminating aluminium atom means the percentage relaxations are considered in a different way and are difficult to analyse due to the formal reordering of the terminating slab, with the minimised surface switching the tetrahedral aluminium sites from above the neighbouring oxygen sites to below this layer.

Figure 5.19. Minimised θ-alumina {101} surface, denoting both octahedral and tetrahedral aluminium Lewis acid sites, forming a mixed surface with bridging oxygen sites.
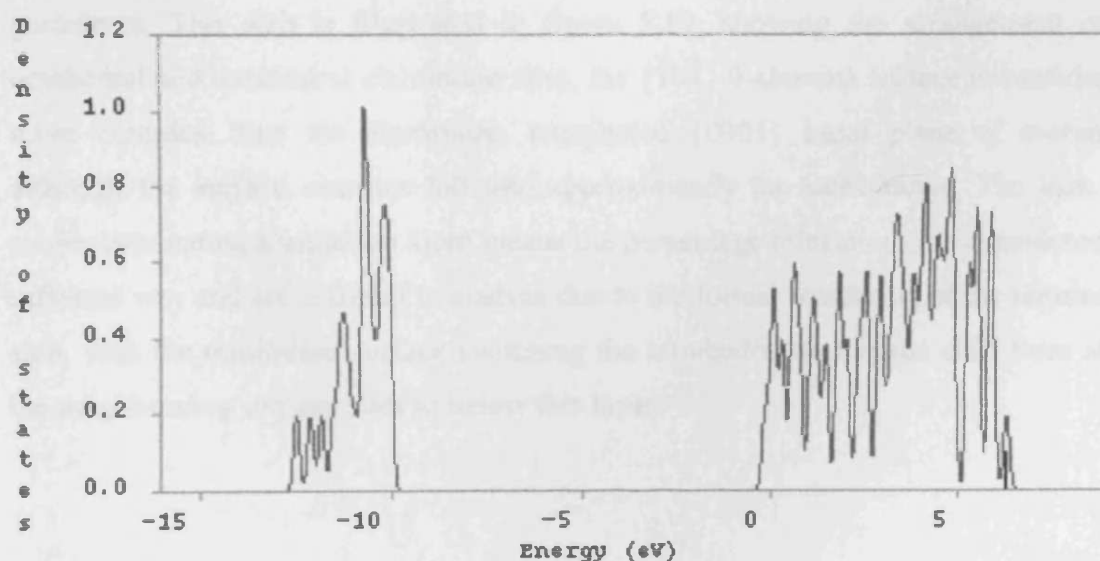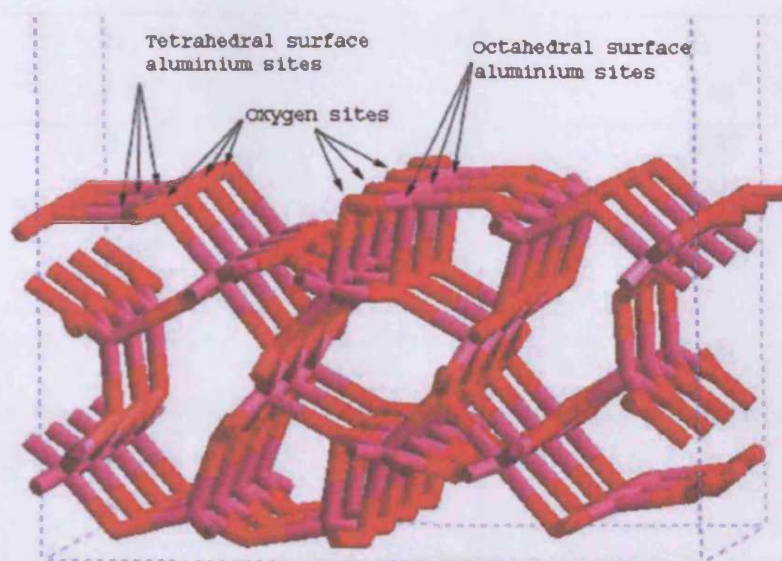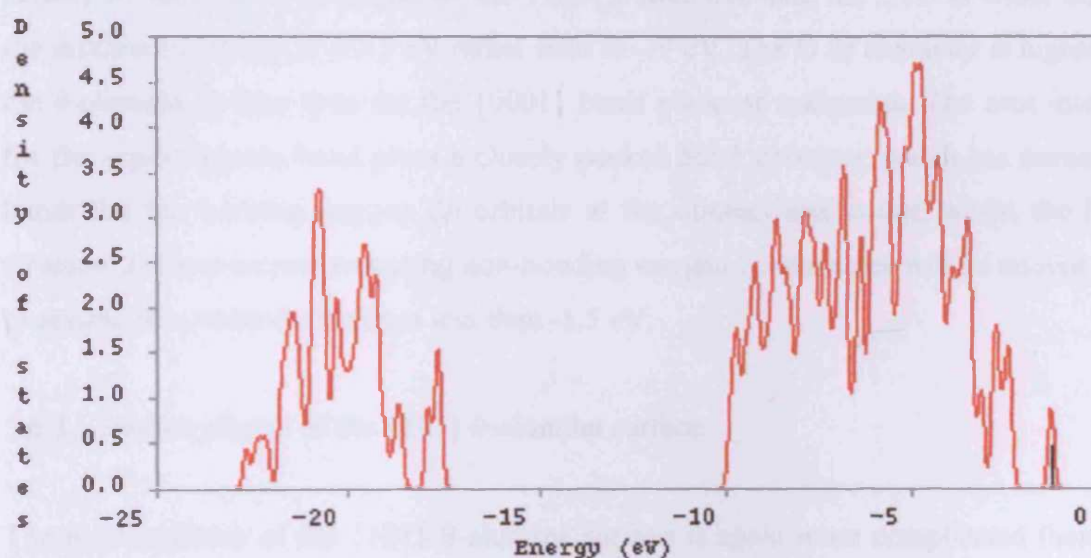

Figure 5.20. Total density of states plot for the {101} θ-alumina surface, calculated using the ultrasoft pseudopotential and precise basis set combination. LVBm = -22.65 eV, LVBM = -17.62 eV, UVBm = -9.92 eV and UVBM = -1.24 eV.

Surface	γ_s J m^{-2}	Surface	γ_s J m^{-2}
{001}	2.24	{101}	0.32
{010}	0.40	{110}	1.48
{011}	0.83	{111}	1.64
{100}	1.09		

Table 5.18. Surface energies for θ-alumina relaxed slabs, calculated using the ultrasoft pseudopotential and precise basis set combination.

The clean surface density of states plot, illustrates in figure 5.20, shows the lower valence band between -22.5 eV and -17.5 eV, with a 7.5 eV band gap to the upper valence band between -10 eV and -1.5 eV. This plot is similar to the {0001} α-alumina density of states plot, although for the {101} θ-alumina slab, the LVB is wider due to the minima occurring at -17.5 eV rather than at -19 eV. The O 2s character is higher for the θ-alumina surface than for the {0001} basal plane of α-alumina. The area integral for the upper valence band gives a closely packed band structure, which has numerous bands for the bonding oxygen 2p orbitals at the minima and is flat, whilst the band structure at the maxima, reflecting non-bonding oxygen 2p character will be uneven due to several low intensity peaks at less than -1.5 eV.

5.6.3   Hydroxylation of the {101} θ-alumina surface.

The hydroxylation of the {101} θ-alumina surface is again more complicated than the method used for the {0001} α-alumina slab, due to the presence of octahedral aluminium sites bound to more than three oxygen sites in the slab. This hydroxylation was carried out on a larger unit cell than figure 5.19 illustrates to include six tetrahedral aluminium sites, a doubling in the b direction. Hydroxylation is achieved by removing the four tetrahedral aluminium atoms and replacing them with twelve hydrogen atoms, placed 1 Å above the oxygen site in the vacuum gap in the same way as used for the {0001} α-alumina hydroxylation. Four octahedral aluminium surface sites were simultaneously removed, and again replaced by twelve hydrogen atoms. This process was repeated on the other surface of the slab. Figure 5.21 illustrates the plan view of the

smaller original slab termination, shown as a side projection in figure 5.19, with three tetrahedral and octahedral sites.

It can be appreciated from figure 5.21, that three oxygen sites are shared by two tetrahedral aluminium sites each. A removal of these three aluminium sites would mean that the addition of nine hydrogen atoms would be achieved by six attaching to an oxygen site, with an excess of three hydrogens. Consequently, three oxygen sites would have to contain two hydrogen atoms, this would not be an unrealistic situation, but would mean that direct comparisons to the previous hydroxylation of the {0001} α-alumina slab would be unfeasible. However, this situation may be resolved by removing only two of the tetrahedral aluminium sites, and adding six hydrogen atoms, with none sharing an oxygen site. The same argument is applied to octahedral sites. For the expanded cell used in the hydroxylated simulations, four of the six tetrahedral and octahedral sites are removed and the neighbouring oxygen atoms hydroxylated.

Figure 5.22 illustrates one minimised hydroxylated {101} θ-alumina slab, showing the remaining tetrahedral and octahedral aluminium sites with the oxygen atoms previously neighbouring the removed sites hydroxylated. As can be seen, this surface is not as simple as the fully hydroxylated {0001} α-alumina surface, due to the distribution of hydroxyl groups in distinct rows across the slab, leaving channels between rows of tetrahedral and octahedral hydroxyl environments.

The energy of hydroxylation may be determined using an adaptation of equation 5.3, this results in:

$$Al_{80}O_{120} + 24H_2O \rightarrow Al_{80}O_{96}(OH)_{48} \qquad \text{Equation 5.7}$$

The energy of hydroxylation for the entire process is -26.503 eV; -1.104 eV per water molecule. This equals -106.55 kJ mol^{-1} per water molecule, equating to approximately 8 kJ mol^{-1} per molecule more than the equivalent value for the full hydroxylation of the basal plane of α-alumina; -98.7 kJ mol^{-1}. The average oxygen to hydrogen bond lengths neighbouring the removed tetrahedral sites is 0.912 Å, whereas the average bond length

for the hydroxyl groups corresponding to octahedral sites is marginally longer at 0.955 Å.
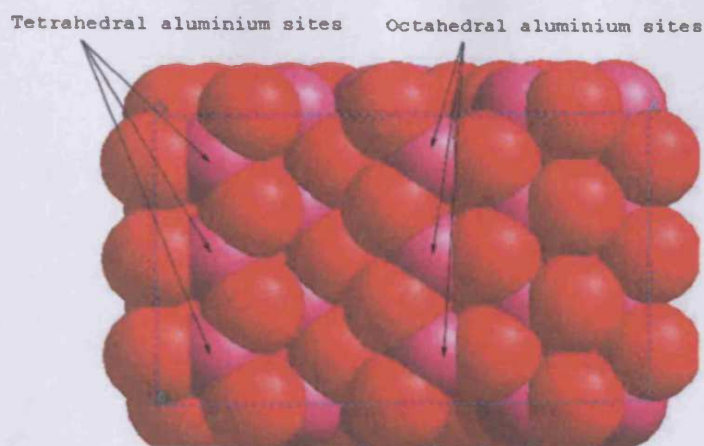
Figure 5.21. Plan view of the {101} θ-alumina surface, prior to surface aluminium site removal for subsequent replacement with hydrogen to give a hydroxylated slab.
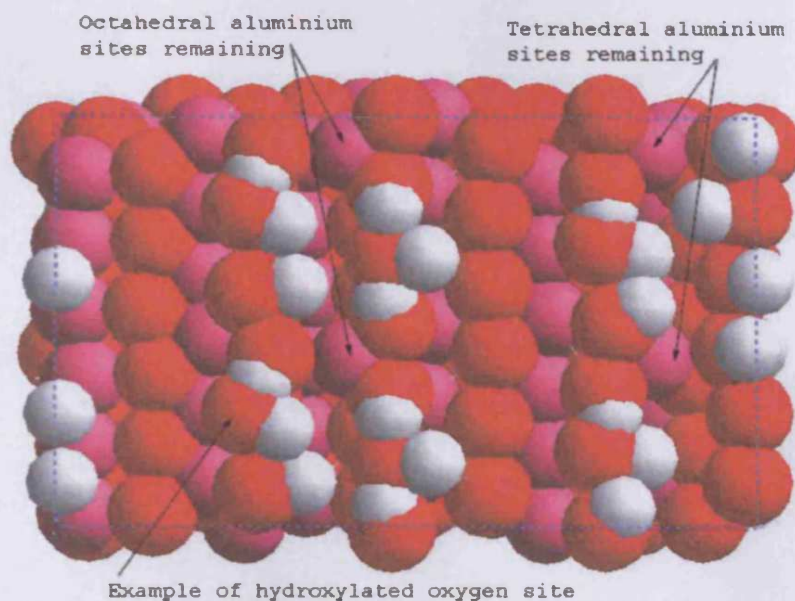
Figure 5.22. Example of one CASTEP minimised hydroxylated {101} surface of θ-alumina, showing one pattern of the removal of four tetrahedral and four octahedral aluminium sites, leaving two of each coordination, and the subsequent arrangement of hydroxyl groups with no oxygen site sharing. This unit cell is an expansion of fig. 5.19.

213

Figure 5.23. Total density of states for the hydroxylated {101} θ-alumina surface, calculated using the ultrasoft pseudopotential and precise basis set combination. LVBm = -22.73 eV, LVBM = -18.34 eV, UVBm = -11.12 eV and UVBM = -2.42 eV.

For the hydroxylated {101} surface, the total density of states is illustrated in figure 5.23, which gives a similar range for the upper and lower valence bands to the clean surface, although the differences lead to a reduction of the band gap by 1 eV to 6.5 eV, mi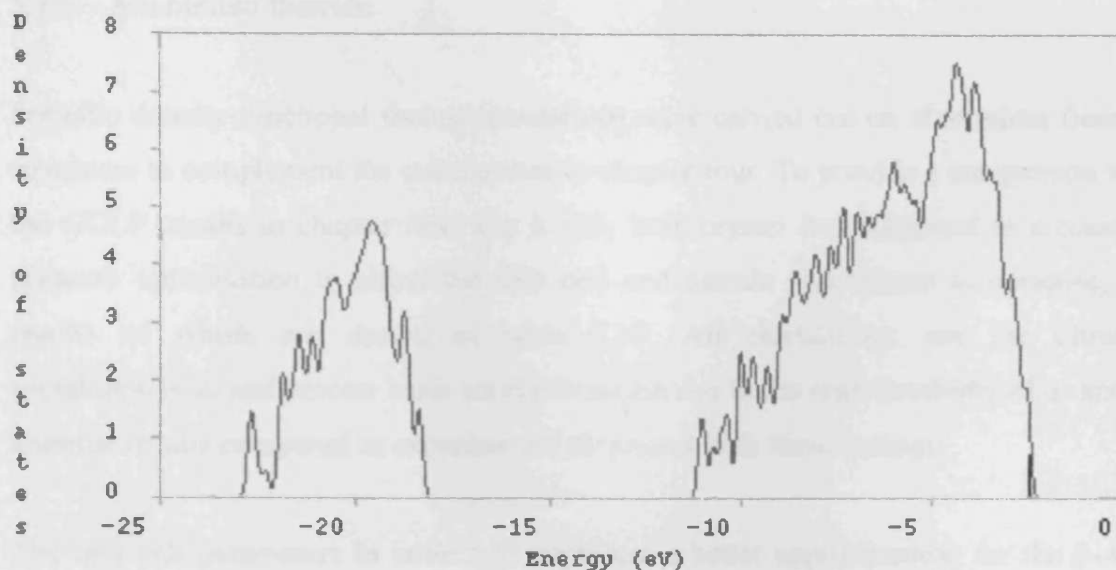rroring the situation found for the {0001} α-alumina surface. This is due to the presence of the electron density from the hydroxyl group, which shifts the UVBm to -11.5 eV, leading to the low intensity peaks at this minimum.

The surface energy of the hydroxylated {101} θ-alumina slab may be calculated using equation 5.6; this gives γ_s as 3.233 J m^{-2}. This compares to the clean {0001} α-alumina surface energy value of 1.53 J m^{-2} and the hydroxylated slab surface energy of 0.996 J m^{-2}.

The combination of this analysis and the energy of hydroxylation provides evidence that the presence of tetrahedral aluminium sites does affect the chemistry, electron density and band structure of θ-alumina surfaces, this conclusion being based on the {101} slab, containing both octahedral and tetrahedral Lewis acid aluminium sites. The simulations carried out for both the clean and hydroxylated surface of the {101} slab contain enough atoms in the unit cell to minimise size issues and surface effects across the slab.

5.7   Aluminium fluoride.

Periodic density functional theory simulations were carried out on aluminium fluoride structures to complement the calculations in chapter four. To provide a comparison with the GULP results in chapter four, the β-AlF$_3$ bulk crystal was subjected to a constant pressure optimisation to allow the unit cell and atomic coordinates to optimise, the results of which are shown in table 5.19. All calculations use the ultrasoft pseudopotential and precise basis set combination due to the reproducibility of α- and θ-alumina results compared to experimental structures with these settings.

The unit cell parameters in table 5.19 represent a better approximation for the β-AlF$_3$ system than the potentials approach in chapter four, due to the generated potentials overestimating the individual parameters and the cell volume, whereas the DFT approach in this chapter finds the parameters and volume to be smaller than the experimental crystal.[28]

Phase		a Å	b Å	c Å	Volume Å^3
β-AlF$_3$	Experimental [28]	6.931	12.002	7.134	593.448
	conp optimisation	6.885	11.945	7.111	584.778

Table 5.19. Unit cell parameters of the experimental β-AlF$_3$ bulk crystal,[28] with the minimised parameters after a constant pressure optimisation.

Constant volume optimisations preceded a Shiftcell analysis to find stable stoichiometric surfaces with no dipole across the slab. As with GULP, the β-AlF$_3$ {100} surface was found to be stable and stoichiometric. Table 5.20 gives the unrelaxed and relaxed surface energies for the β-AlF$_3$ {100} surface. The minimised β-AlF$_3$ {100} surface gives γ_s in the expected range for the precursor alumina surface slabs, this distribution of γ_s values between 1 and 5 J m^{-2} can be extended for this metal halide system, in accordance with de Leeuw's DFT work on the calcium fluoride {111} surface, where γ_s is 0.39 J m^{-2},[29] with an atomistically determined value of 0.52 J m^{-2}.[30]

Surface	Unrelaxed surface energy	Relaxed surface energy
	J m^{-2}	J m^{-2}
β {100}	2.868	1.520

Table 5.20. CASTEP unrelaxed and relaxed surface energies for the β-AlF₃ {100} surface calculated from single point and geometry optimisations respectively.

Figures 5.24a and 5.24b illustrate the side and plan views of the β-AlF$_3$ {100} surface. Compared to the aluminium and fluorine terminated surface minimised in GULP, it is seen that by selecting a fluorine terminated {100} slab configuration, whilst remaining stoichiometric, the surface energy values do not alter significantly between the DFT and atomistic methods. It is appreciable from figure 5.24b that the contribution from aluminium in this fluorine dominated surface is negligible, unlike the GULP surface. The average aluminium fluorine bond distance in the CASTEP crystal is 1.733 Å.

For the β-AlF$_3$ bulk crystal density of states, the lower valence band stretches from -23.3 eV to -21.8 eV, with the upper valence band extending from -8.4 eV to -1.9 eV. The {100} surface of this finds both bands of equal magnitude, but shifting towards higher energies; the lower valence band from -27.9 eV to -25.5 eV, and the upper valence band between -12.9 eV and -6.2 eV.
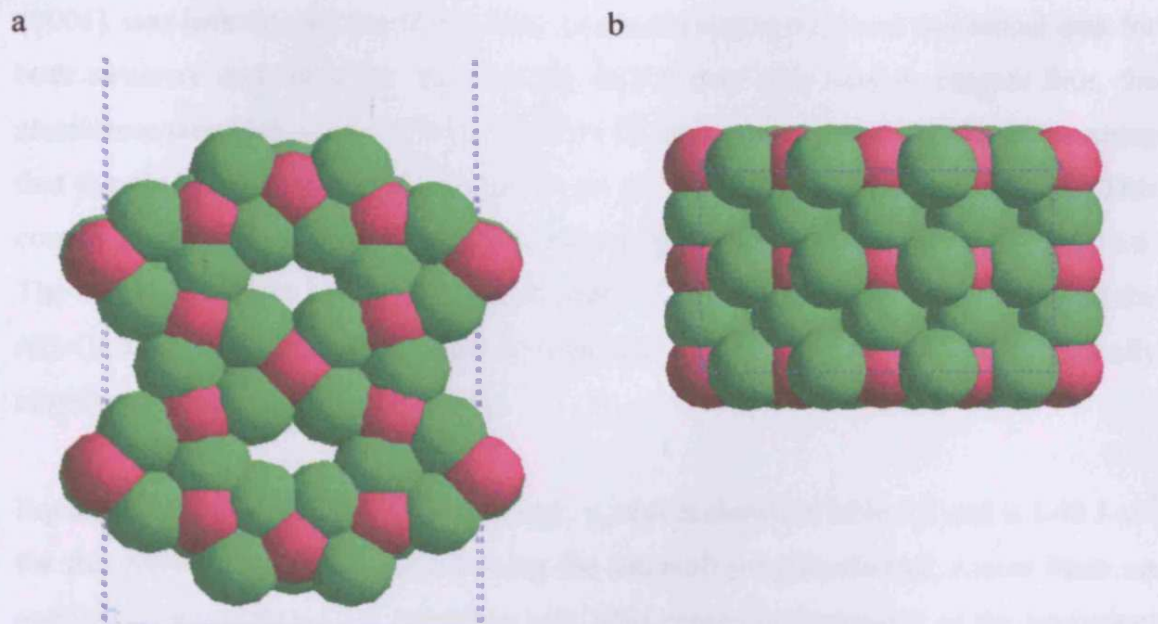
a   b

Figure 5.24. Side projection of the CASTEP minimised β-AlF₃ {100} surface (a) and (b) the plan view of this surface.

5.8   Summary of periodic density functional theory simulations.

The CASTEP results described in this chapter started with an evaluation to find the most appropriate combination of basis set and pseudopotential to model the bulk α-alumina crystal derived from experimental investigations. As with the GULP based simulations described in chapter four, the initial unit cell parameters are a = b = 4.759 Å and c = 12.991 Å. Figure 5.2 shows the unit cell volumes calculated with each basis set and pseudopotential combination, from this the lowest energy and volume combination of precise basis set and ultrasoft pseudopotential was selected. A Monkhurst-Pack k-point convergence grid of 2×2×2 was selected due to this reaching convergence with respect to total energy as figure 5.1 shows. The subsequent unit cell parameters of the constant pressure simulation with the variables as above were found to be a = b = 4.692 Å, c = 12.979 Å and the volume = 247.416 Å³.

From these parameters, a constant volume relaxation was undertaken to minimise the ionic positions whilst holding the unit cell parameters fixed. With this structure, Shiftcell was used to determine the stable surface configurations. The basal plane,

217

{0001} was investigated due to the wide range of experimental and theoretical data for both structure and reactions. As with the GULP data presented in chapter four, the aluminium terminated slab exhibited the Al1-O1 layer relaxing by -84.835 %, meaning that the final separation of these two layers is 15.165 % of the original value. This compares favourably to the density functional theory relaxations shown in table 1.6. The subsequent layer relaxations are O1-Al2 = 2.065 %, Al2-Al3 = -46.56 % and the Al3-O1 layer = 19.78 %. Again, these results fall into the expected magnitudes and ally closely with previous *ab initio* results.

Equation 1.3 calculates the surface energy, γ_s, this is shown in table 5.7 and is 1.43 J m^{-2} for the {0001} surface optimised using the ultrasoft pseudopotential, coarse basis set and 2×2×2 Monkhurst-Pack sampling grid. This compares favourably to the equivalent density functional theory literature values shown in table 1.6 of 1.76 J m^{-2}, 1.98 J m^{-2} and 1.76 J m^{-2}.

The hydroxylated basal plane of α-alumina was described in section 5.3, using the reaction of twelve water molecules to fully hydroxylate the slab, resulting in twelve hydroxyl groups on each of the two surfaces. As this simulation is carried out from first principles, the energy of hydroxylation can be calculated by using the total energies for the oxide slab, the hydroxylated slab and twelve water molecules. This is found to be -1184 kJ mol^{-1} for the full reaction, equalling -98.7 kJ mol^{-1} per water molecule. This links well with existing experimental data of -75 kJ mol^{-1} for physisorption and -109 kJ mol^{-1} and -57 kJ mol^{-1} for low and high coverages of water. An approach to calculating the surface energy using equation 5.6 including terms for the total energies of the hydroxide slab, bulk crystal and water molecules along with the energy of hydroxylation gave the γ_s value as 0.996 J m^{-2}. Again, this fits well with clean surface values. The total density of states for the hydroxylated slab is shown in figure 5.8, it was found that the oxygen 2s orbitals bond with hydrogen at different energies to that with aluminium in the oxide surface, spreading the peak at the lower valence band maximum.

The physisorption of water was described in section 5.4, giving energies of adsorption of -21 kJ mol^{-1} for two $O_{surface}$-H_{water} bonds, against -34 kJ mol^{-1} and -21 kJ mol^{-1} for a

single $O_{surface}$-H_{water} interaction. Where both $Al_{surface}$-O_{water} and $O_{surface}$-H_{water} interactions occur, the energy of adsorption was found to be -116 kJ mol^{-1}. This value is between 15 and 70 kJ mol^{-1} lower than literature cluster calculations for hydroxylation, as shown in table 1.8.[26] The density of states plot in figure 5.10 gave a peak at -10.6 eV, representative of molecularly adsorbed water, as this does not appear in the hydroxylated surface in figure 5.8.

Hydrogen fluoride dissociatively adsorbed onto the {0001} surface gave three energies of adsorption of -221, -220 and -229 kJ mol^{-1}. In the adsorbed state the aluminium adsorption site moves out of the surface plane toward the fluorine atom of the HF molecule. The total density of states plot for this structure is shown in figure 5.13, again finding an isolated peak at -10.93 eV, occurring from the oxygen to hydrogen interaction. Constrained optimisations attempted to find a physisorbed hydrogen fluoride molecule by gradually reducing the H-F separation to 1 Å. However, the systems with H-F at 1 Å and 1.2 Å did not reach convergence, whereas the six simulations in the range 1.4 Å to 2.4 Å shown in table 5.15 and figure 5.14 shows the preferred configuration of the hydrogen fluoride molecule is in a dissociated chemisorbed state.

As with molecular mechanical simulations shown in chapter four, simulations were also undertaken on θ-alumina surfaces, after a bulk optimisation using the same combination of basis set, pseudopotential and sampling grid as with α-alumina. All seven low Miller index surfaces were found to be electrostatically stable after a Shiftcell analysis, and thermodynamically stable after CASTEP minimisations to yield γ_s values of between 0.32 J m^{-2} and 2.24 J m^{-2} as shown in table 5.18. To provide a comparison with α-alumina surfaces containing only octahedral aluminium sites, the {101} θ-alumina surface with both octahedral and tetrahedral aluminium sites was hydroxylated as described in section 5.6.3. The energy of hydroxylation was found to be -106.55 kJ mol^{-1} for the reaction of twenty-four water molecules given in equation 5.7. The presence of tetrahedral aluminium can account for this difference to the -98.7 kJ mol^{-1} value for the hydroxylated {0001} α-alumina surface. The density of states for this hydroxylated surface is shown in figure 5.23, and provides a smoother profile than that found for the

hydroxylated {0001} α-alumina surface, although the upper and lower valence bands are across a similar range.

The density functional theory calculations found the bulk β-AlF₃ unit cell parameters to be close to the experimental values as given in table 5.19. The {100} β-AlF₃ was used as a comparison to judge the accuracy of the fitted potentials used in chapter four, giving a surface energy value of 1.52 J m⁻², in agreement with existing literature values for similar metal-fluoride surfaces and molecular mechanical AlF₃ surfaces shown in chapter four.

[1] B. Civalleri and N. M. Harrison, *Mol. Simulat.*, **28 (3)**, 213, (2002).

[2] P. P. Ewald, C. Hermann, *Strukturbericht*, vol. 1, 1913, p240.

[3] J. Lewis, D. Schwarzenbach and H. D. Flack, *Acta Crystallographica A* **38**, 733, (1982).

[4] R. W. G. Wyckoff, *Crystal Structures*, 2ⁿᵈ Edition. (Wiley, NY, 1964).

[5] A. Marmier and M. W. Finnis, *J. Phys.: Condensed Matter* **14**, 7797, (2002).

[6] S. Ciraci and I. P. Batra, *Physical Review B* **28**, 982 (1983).

[7] S. D. Mo and W. Y. Ching, *Phys. Rev. B*, **57 (24)** 15219 (1998).

[8] R. di Felice and J. E. Northrup, *Phys. Rev. B.* **60**, 16287, (1999).

[9] I. Manassidis, A. De Vita and M. Gillan, *Surf. Sci. Lett.*, **285**, L517, (1993).

[10] . Verdozzi, D. Jennings, P. Shultz and M. Sears, *Phys. Rev. Lett.*, **82**, 799, (1999).

[11] X.-G. Wang, A. Chaka and M. Scheffler, *Phys. Rev. Lett.*, **84**, 3650, (2000).

[12] I. Manassidis, A. De Vita and M. Gillan, *Surf. Sci. Lett.*, **285**, L517, (1993).

[13] C. Verdozzi, D. Jennings, P. Shultz and M. Sears, *Phys. Rev. Lett.*, **82**, 799, (1999).

[14] W. Mackrodt, R. Davey, R. Docherty and S. Black, *J. Cryst. Growth*, **80**, 441, (1987).

[15] V. E. Puchin, J. Gale, A. Shluger, E. Kotomin, J. Günster, M. Brause and V. Kempter, *Surf. Sci.*, **370**, 190, (1997).

[16] J. Gomes, I. Moreira, P. Reinhardt, A. Wander, B. Searle, N. Harrison and F. Illas. *Chemical Physics Letters*, **341**, 412, (2001).

[17] X.-G. Wang, A. Chaka and M. Scheffler, *Phys. Rev. Lett.*, **84**, 3650, (2000).

[18] R. di Felice and J. E. Northrup, *Phys. Rev. B.* **60**, 16287, (1999).

[19] I. G. Batirev, A. Alavi, M. Finnis and T. Deutsch, *Phys. Rev. Lett.*, **82**, 1510, (1999).

[20] M. Bankhead, *Ph.D. Thesis*, Liverpool University (2000).

[21] P. Guenard, G. Renaud, A. Barbier and M. Gautier-Soyer, *Surf. Rev. Lett.*, **5**, 321 (1998).

[22] G. Della Gatta, B. Fubini and L. Stradella, *J. Phys. Chem.*, **66**, 72, (1976).

[23] B. Hendriksen, D. Pearce and R. Rudham, *J. Catal.*, **24**, 82, (1972)

[24] N. H. de Leeuw and S. C. Parker, *J. Chem. Soc., Faraday Trans.*, **93(3)**, 467, (1997).

[25] S. C. Parker, S. Kerisit, A. Marmier, S. Grigoleit and G. W. Watson, *Farad. Discuss.*, **124**, 155, (2003).

[26] J. M. Wittbrodt, W. Hase and H. Schegel, *J. Phys. Chem. B*, **102** 6539, (1998).

[27] M. Bankhead, G. Watson, G. Hutchings, J. Scott and D. Willock, *Appl. Catal. A: Gen.* **200**, 263, (2000).

[28] J. A. A. Ketelaar, *Nature*, **128**, 303, (1931).

[29] N. H. de Leeuw, J. A. Purton, S. C. Parker, G. W. Watson and G. Kresse, *Surface Science*, **452**, 9, (2000).

[30] R. Bennewitz, M. Reichling and E. Matthias, *Surface Science*, **387**, 69, (1997).

Chapter 6

6 Conclusions.

This chapter will draw together the results and the conclusions found in this study and discussed in chapters four and five. A review of the molecular mechanics and density functional theory methods used to approach the simulation of α-alumina surfaces and the interaction of water and hydrogen fluoride with the {0001} basal plane to provide a quantitative investigation into the hydroxylation and fluorination of this surface. Using the information obtained it was hoped that the two approaches would give broadly similar results, for example the structure of the hydroxylated {0001} α-alumina surface is calculated faster using GULP, as with all simulations presented, if these prove to agree with CASTEP data then intensive work such as adsorptions can be predicted using GULP and confirmed using CASTEP calculations.

6.1 Discussion.

The main conclusions reached by this work will be discussed in the following order: The suitability of GULP and CASTEP to calculate the α-alumina bulk structure and the {0001} surface; the structure of the hydroxylated α-alumina {0001} surface and the modelling of water adsorption to achieve this; the adsorption of hydrogen fluoride to give both chemisorbed and physisorbed HF and the application to further alumina structures and aluminium fluoride.

6.1.1 The {0001} α-alumina surface.

The potentials used for the α- and θ-alumina structures are drawn from literature and the GULP website, a precise representation of the minimised bulk and surface structures was achieved. For example, the cell parameters obtained by GULP are in excellent agreement with experimental observations and compare well to the density functional theory approach taken in the CASTEP program. A summary of the lattice cell parameters for the two approaches is given in table 6.1 and compared against two experimental sets of lattice parameters.

Parameter	GULP	CASTEP	Experimental [1]	Experimental [2]
a [Å]	4.8178	4.692	4.7586	4.7602
b [Å]	4.8178	4.692	4.7586	4.7602
c [Å]	12.681	12.979	12.9897	12.9933
Volume [Å³]	254.903	247.416	254.737	254.977

Table 6.1. Comparison of the bulk structure parameters a, b and c along with the volume calculated using GULP and CASTEP (with the ultrasoft pseudopotential and precise basis set). Two experimentally determined lattice parameters are included for reference.

The CASTEP analysis of α-alumina began with a series of energy minimisations to determine the most suitable combination of pseudopotential and basis set cut-off energy. From these it was found that the ultrasoft pseudopotential and precise basis set offers the most suitable approach as the ultrasoft pseudopotentials have a low kinetic energy cut-off for the plane-wave basis set and provides reasonable agreement with the experimental cell parameters. All subsequent surface and reaction simulations were undertaken using this combination.

Following on from these minimised bulk structures, the Shiftcell program analysis determined surfaces that are electrostatically stable. For α-alumina, work concentrated on the basal {0001} plane. Table 6.2 summarises the surface energy values calculated in this work and compares these to the average value found for each method from the data presented in section 1.2.4, both results are higher than the respective average.

Method	Surface energy γ_s $J\ m^{-2}$
This work – GULP	2.23
This work – CASTEP	3.78
Atomistic forcefield	2.97,[3] 2.03,[4] 2.951,[5] 2.454,[5] 3.15,[6] 3.06.[6]
Ab initio	1.76,[7] 1.98,[8] 2.00,[9] 1.76.[10]
Experiment	2.6[11]

Table 6.2. Summary of minimised surface energy values for the two methods used in this work compared to the averages atomistic methods and ab initio density functional theory and Hartree-Fock methods shown in table 1.6.

Relaxation of the {0001} α-alumina surface results in movement of the Al1 layer towards the first oxygen O1 layer to produce a mixed aluminium and oxygen surface, experimentally this relaxation has been reported to be 51 %. Theoretical predictions range from 58 % to 98 % depending on the method employed. In this work the GULP calculated value was found to be 86.9 %, leading to both aluminium and oxygen remaining accessible on the surface. For the subsurface relaxations there is less difference between the literature values and the results presented in table 6.3.

Relaxation	This work – GULP	This work – CASTEP	DFT study [12]	Mol. mech. study [13]	Experimental [14]
Al1-O1	-86.9 %	-84.8 %	-86 %	-65 %	-51 %
O1-Al2	+8.0 %	+2.1 %	+3 %	-5 %	+16 %
Al2-Al3	-30.9 %	-46.6 %	-42 %	-32 %	-29 %
Al3-O2	+14.3 %	+19.8 %	+18 %	+14 %	+20 %

Table 6.3. Summary of interlayer relaxations calculated by GULP and CASTEP compared to the ab initio and molecular mechanic averages found from the data presented in section 1.2.3 and the XRD experimental data.

The data presented in tables 6.2 and 6.3 for the density functional theory results calculated using CASTEP and the atomistic potential method using the GULP code compare well to the previous theoretical literature presented in section 1.2.3 and the

three selected studies also presented in table 6.3. GULP offers an extremely quick and efficient method to produce values which are similar and correspond closely to the bulk of the previous *ab initio* relaxations in published literature.

Neither of the theoretical programs used in this work or any used in the published literature exactly reproduces experimental data, however, accurate models of the mixed aluminium and oxygen α-alumina {0001} surfaces are found using both GULP and CASTEP that can be used further with confidence.

6.1.2   Hydroxylated {0001} α-alumina surfaces.

To achieve hydroxylation experimentally, water is adsorbed onto the surface. Experimental heat of adsorption measurements show that at low coverage the energy of adsorption is -109 kJ mol^{-1} rising to the full coverage adsorption energy of -57 kJ mol^{-1}. Using the DFT theoretical methods outlined in section 5.7, water physisorbs onto the {0001} surface at -116 kJ mol^{-1} through an aluminium to water oxygen interaction. For adsorption via hydrogen and surface oxygen mode the energy of adsorption is between -20 and -33 kJ mol^{-1}, both yield a 1-2 physisorbed molecule. This means that the Al-OH$_2$ mode of adsorption gives good agreement with experimental results whilst the Al$_2$O-H$_2$O type of adsorption does not.

A chemisorbed process was also modelled resulting in the full hydroxylation of the {0001} surface; the energy of chemisorption per water molecule was calculated to be -99 kJ mol^{-1} in the reaction:

$$\tfrac{2}{3}Al_{24}O_{36} + 12H_2O \rightarrow Al_{16}O_{12}(OH)_{24} \qquad \text{Equation 6.1}$$
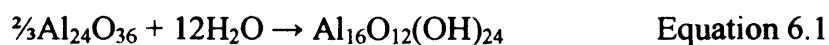
From the energies of chemisorption of water presented in table 1.9 for a variety of theory levels, of between -111.5 kJ mol^{-1} and -139.5 kJ mol^{-1}, this value of -99 kJ mol^{-1} compares favourably due to the larger dissociation values occurring on a smaller cluster of Al$_8$O$_{12}$, not a periodic cell of Al$_{16}$O$_{24}$ as in the earlier work. The surface coverage of the hydroxyl groups in the DFT method of calculation is 1.57 × 10^{15} OH cm^{-2}, compared to an LITD determined value of 0.32 × 10^{15} OH cm^{-2},[15] meaning that the

surface coverage of hydroxyls is higher in these theoretical simulations than in experimental data. For desorption experiments of water carried out at 210 K the surface coverage of hydroxyl groups was found to be 8.8×10^{15} OH cm^{-2}, giving energies of desorption of between *ca.* 50 and 160 kJ mol^{-1}, comparable to the energy of adsorption results presented here for the {0001} α-alumina surface.

Figures 6.1 and 6.2 illustrate the two energy level diagrams showing the relative profiles of the two physisorption modes outlined above with the ultimate chemisorbed water structure. This gives conflicting explanations for the stability of water physisorbed onto the {0001} surface of α-alumina, as in figure 6.1 the molecularly adsorbed water is more stable than the chemisorbed water by 17 kJ mol^{-1}, whereas in figure 6.2 the adsorbed water interacting via surface oxygen and water hydrogen can be considered a an intermediate to the dissociation and chemisorption of the water molecule. Compared to the experimental laser induced thermal desorption and temperature programmed desorption from *ca.* 195 K to *ca.* 600 K carried out by Nelson *et al*,[16] in which the energies of adsorption of a single water molecule were found to range from approximately -48 kJ mol^{-1} to -142 kJ mol^{-1}, the results shown in figures 6.1 and 6.2 appear consistent. The surface coverage of the single physisorbed water molecule in figures 6.1 and 6.2 is 5×10^{13} H$_2$O cm^{-2}, therefore giving a hydroxyl coverage of 2.5×10^{15} OH cm^{-2} upon dissociation of water.

Compared to the results found by Hendriksen *et al*,[17] the low coverage of 1×10^{14} water molecules per cm^2 gave the energy of hydroxylation to be 109 kJ mol^{-1} and at a high coverage of 1×10^{15} water molecules per cm^2 gave the energy of adsorption to be 57 kJ mol^{-1}. Therefore the low coverage physisorbed water adsorption energy value of -116 kJ mol^{-1} evaluates favourably with the experimental low coverage results as given in figure 1.23.
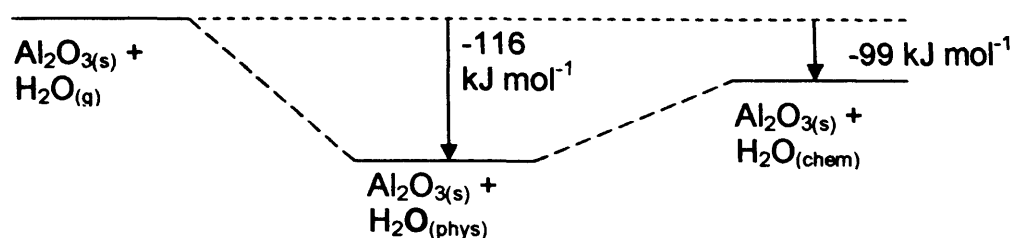
Figure 6.1. The energy profile for the initial physisorption of a gas phase water molecule via the aluminium to water oxygen (O) interaction, and the subsequent chemisorbed water giving the fully hydroxylated surface.
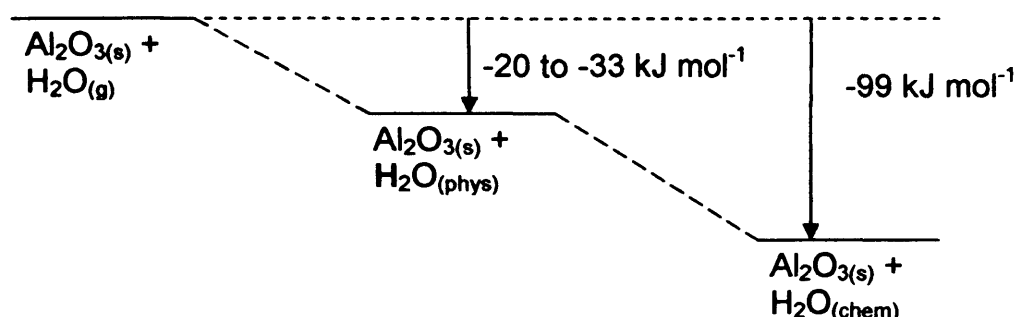

Figure 6.2. The energy profile for the three lower energy physisorptions occurring through the surface oxygen to hydrogen (H) interactions and the resultant chemisorbed structure. ΔH_{phys} = -20 kJ mol^{-1}, -21 kJ mol^{-1} and -34 kJ mol^{-1}.

Density functional theory calculations using CASTEP for the fully hydroxylated {0001} α-alumina surface take a long time compared to the molecular mechanical approach using GULP for the same structure. For example, to calculate the $Al_{16}O_{12}(OH)_{24}$ fully hydroxylated surface in GULP took 117.5 s, whereas the equivalent structure determined in CASTEP took 19 722 s. However, these two values must not be looked at in isolation due to the computing resources required to find the precursor {0001} stable surfaces and bulk structures as described in chapters four and five. For these reasons, only the fully hydroxylated {0001} α-alumina surface was calculated using CASTEP and an alternative approach was constructed using GULP and the thermodynamic cycle shown in figure 4.9 for the partial hydroxylation of this surface. This has been shown the estimate the hydroxylation energy based only on atomistic potential calculations at partial coverage.

Using the Born-Haber cycle shown in figure 4.9, a value for the correction factor, used to account for the difference in energies when extra potentials are introduced for the

hydroxylated surface to account for the interactions of hydroxyl oxygen and hydrogen, as given in table 3.5, was defined at 11.366 eV per water molecule adsorption. This compares to a previously determined value of -9.74 eV [18] and 4.365 eV. [19]

This value can then be inserted into equation 4.9, as a multiple of the number of water molecules considered in the reaction simulated to give ΔH_H, the energy of hydroxylation. Table 6.2 summarises the calculated range of values for ΔH_H.

Hydroxylation reaction	$\underline{\Delta H_H}$ $kJ\ mol^{-1}$
$Al_{64}O_{96} + 2H_2O \rightarrow Al_{64}O_{94}(OH)_4$	670
$Al_{64}O_{96} + 4H_2O \rightarrow Al_{64}O_{92}(OH)_8$	187
$Al_{64}O_{96} + 6H_2O \rightarrow Al_{64}O_{90}(OH)_{12}$	-20
$Al_{64}O_{96} + 8H_2O \rightarrow Al_{64}O_{88}(OH)_{16}$	-106
$Al_{64}O_{96} + 10H_2O \rightarrow Al_{64}O_{86}(OH)_{20}$	-176
$Al_{64}O_{96} + 12H_2O \rightarrow Al_{64}O_{84}(OH)_{24}$	-222

Table 6.2. The calculated range of values for ΔH_H, the energy of hydroxylation, found for each hydroxylation reaction by the cycle presented in figure 4.15 and using equation 4.9.

In these calculations, hydroxylation is brought about by the removal of the terminating aluminium atom from the Al1 layer to leave oxygens of the O1 layer exposed. To regain charge neutrality three hydrogen atoms for every aluminium atom removed are then added. Appropriate models for the hydroxylated surface have been found for both GULP and CASTEP, as illustrated in figure 4.8 for GULP and for the CASTEP surface in figure 6.3. The local geometry from the GULP results can be compared to the density functional theory produced CASTEP values for the bonding present in the hydroxylated α-alumina {0001} surface as in table 6.3. The GULP potentials used for the hydroxylated surface (shown in tables 3.6 and 3.9) reproduce the surface structure bond lengths found using CASTEP. To achieve full hydroxylation of the {0001} surface, the thermodynamic cycle method gave the energy of adsorption per water molecule as -222 kJ mol^{-1}, compared to the equivalent CASTEP determined value of -99 kJ mol^{-1}. The low coverage results of 670 kJ mol^{-1} and 187 kJ mol^{-1} for two and four hydroxyl groups per surface approach the low coverage water adsorption results found by Hendriksen et

al of 109 kJ mol⁻¹, with the most defective surface possibly accounting for the value of 670 kJ mol⁻¹, this effect is lessened with the addition of further water molecules to the system.
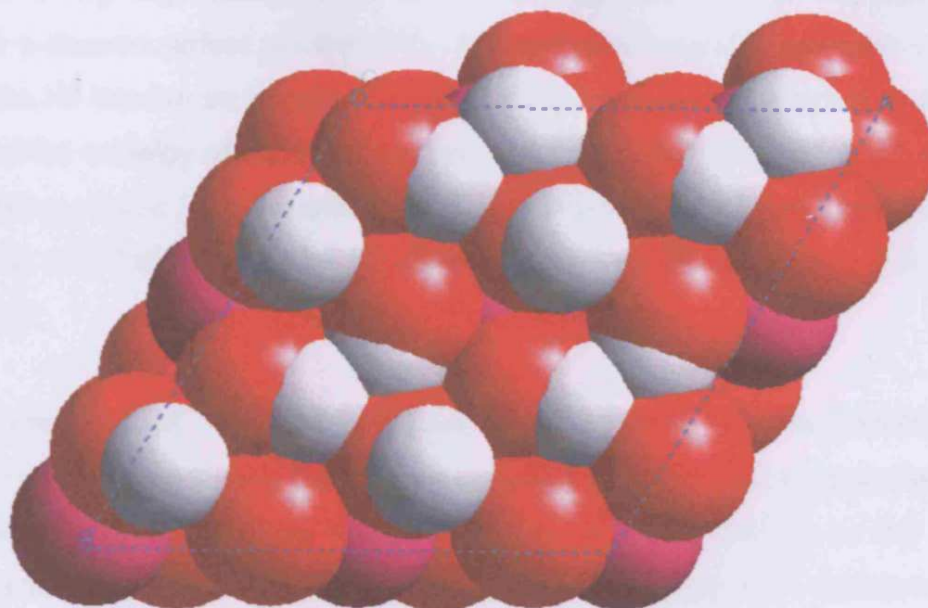

Figure 6.3. Plan view of the fully hydroxylated surface of {0001} α-alumina calculated using the CASTEP program. H-O·····H-O can be seen here.

Bond	CASTEP	GULP	Percentage difference
Al2-O1	1.780	1.768	0.007 %
Al3-O1	1.906	1.916	0.005 %
O1-H	0.972	1.027	0.57 %

Table 6.3. Comparison of the GULP and CASTEP calculated hydroxyl bond (O1-H) and the two bonds from these oxygen atoms to the aluminium atoms in the two layers of (Al2 and Al3) immediately beneath.

6.1.3 Physisorption and chemisorption of hydrogen fluoride.

Addition of hydrogen fluoride to the α-alumina {0001} surface is an important aim of the work presented in this thesis, this has been achieved using CASTEP to model the chemisorption of HF, and a series of constrained optimisations intended to obtain a physisorbed state for the HF molecule where F is directly positioned over an aluminium site. For three start points at 1.5 Å, 2.0 Å and 2.5 Å aluminium to fluorine distance the

229

average energy of chemisorption was found to be -223 kJ mol^{-1}, giving a value for the dissociation of the hydrogen to fluorine bond to yield 1-2 chemisorption structures, indicating that fluorination is thermodynamically preferred over hydroxylation. -223 kJ mol^{-1} is a very high adsorption energy value, suggesting that the fluorination of the {0001} α-alumina surface is irreversible. The method of imposing geometric constraints to fix the HF bond to six lengths from the 2.4 Å (nearest the chemisorbed length) to 1.4 Å found the enthalpy of chemisorption reduced from -224.1 kJ mol^{-1} to -71.9 kJ mol^{-1} as shown in figure 5.14. However, no purely physisorbed structure could be obtained from the CASTEP calculations as optimisations with HF less than 1.4 Å failed to converge.

Physisorption of HF was modelled using the GULP code, as with CASTEP, it was found the aluminium Lewis acid site moved away from the bulk structure towards the adsorbed fluorine atom along with a movement of surface oxygen to the incoming hydrogen. As no bond breaking or forming occurred during these calculations, there was no need to consider a thermodynamic cycle as with the progressive hydroxylation simulations, the enthalpy of physisorption could be determined using equation 6.2.

$$\Delta H_{adsorption} = E_{alumina+HF} - (E_{alumina} + E_{HF}) \qquad \text{Equation 6.2}$$

Where E$_{alumina+HF}$ is the lattice energy for the physisorbed structure and E$_{alumina}$ and E$_{HF}$ are the lattice energies for the periodic reactants. Both 1-2 and 1-4 modes of adsorption were found for the initial physisorption, where the 1-4 modes of adsorption were found to be higher in energy at -69.9 kJ mol^{-1}, compared to the 1-2 modes of -58.1 kJ mol^{-1}. The single Al-F interaction is also responsible for an adsorption, this average was found to be -51.3 kJ mol^{-1}. Gale [20] found the energy of adsorption for a hydrogen fluoride molecule adsorbing onto a surface allowed to geometrically relax to be -38.6 kJ mol^{-1}, approximately 30 kJ mol^{-1} less favourable than the 1-4 mode, 20 kJ mol^{-1} less favourable than the 1-2 mode and 13 kJ mol^{-1} less favourable than the Al-F method of adsorption found in this work.

When two HF molecules are modelled simultaneously onto the {0001} α-alumina surface, both the 1-2 and 1-4 modes of adsorption were found, the total energy of physisorption being -129.9 kJ mol^{-1}.

CASTEP is unable to provide an optimised structure for purely physisorbed HF, while GULP has been shown to offer HF molecularly adsorbed in three geometries: single bond Al-F, 1-2 and 1-4 modes, as defined in figure 4.19. The reverse of this is also true, that GULP is not a practical method to investigate chemisorbed HF whilst CASTEP finds the minimised structure without complications.

The energies of physisorption in GULP are lower than the energies of chemisorption in CASTEP, due to the presence of an energy term required to break the hydrogen-fluorine bond in the latter, whilst the CASTEP approximation of a 1-2 physisorbed HF molecule finds the energy of adsorption at -72 kJ mol^{-1}, this is close to the GULP 1-2 physisorbed value of -58.1 kJ mol^{-1}. These results enable a reaction profile to be constructed using the two codes, as shown in figure 6.4. The results fit well in comparison to the *ab initio* periodic CASTEP calculations and yield two reaction profiles which exhibit the thermodynamic behaviour expected when the scheme outlined in section 1.3.6 is taken into account for the physisorption of HF. The reaction profile for the constrained CASTEP HF adsorption calculations is shown in figure 5.14.

It would be expected that the 1-2 adsorbed mode would have to overcome a smaller barrier to the transition state and ultimately the chemisorbed structure as this structure is less thermodynamically stable and is geometrically hindered. The 1-4 mode is found to be a more stable lattice and is therefore requiring more energy to undergo a similar conversion.
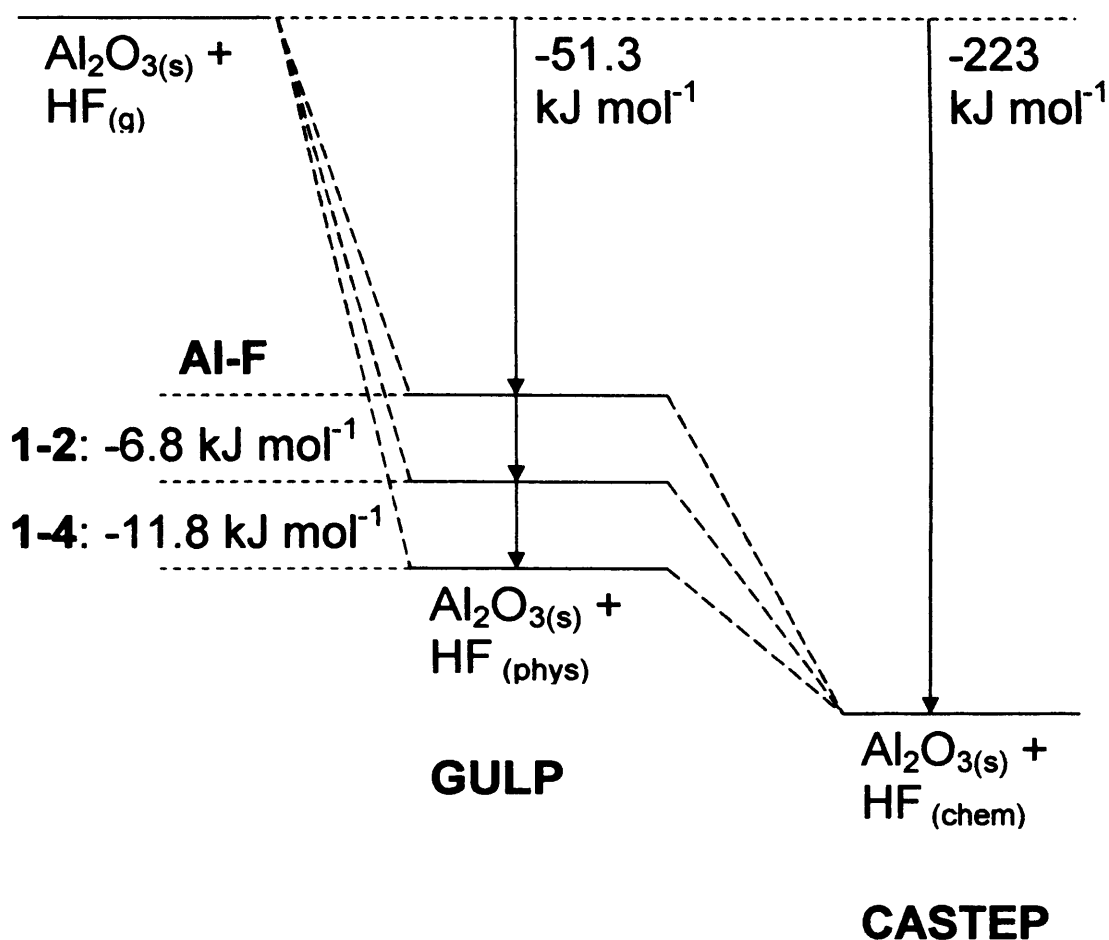
Figure 6.4. Reaction profile for the physisorption of HF using GULP, shown at -51.3 kJ mol⁻¹ for a single Al-F interaction, -58.1 kJ mol⁻¹ for a 1-2 mode of adsorption and -69.9 kJ mol⁻¹ for the 1-4 mode. Also shown is the closest approximation to physisorbed HF CASTEP calculated where the HF bond length is 1.4 Å and the energy of adsorption is -72 kJ mol⁻¹ leading to the full dissociation and chemisorption at -223 kJ mol⁻¹.

In experimental work undertaken by Jones,[21] the zinc promotion of γ-alumina catalysts was investigated with clean γ-alumina surfaces for the adsorption of HF. The γ-alumina surface does not undergo surface fluorination at under 150 °C, this surface shows activity to CCl_4 fluorination at higher temperatures than fluorinated Zn/γ-alumina surface. It was suggested an autocatalytic process was responsible for a sharp increase in activity where HF is removed from the Al^{3+} site in γ-alumina, allowing a chlorocarbon to adsorb and react with the HF. A vacancy was then created for another HF molecule, releasing another active site. The presence of zinc at 6.5 % (w/w) gave increased activity to both fluorination and dismutation of chlorocarbons and chlorofluorocarbons. In this scheme, chemisorbed hydrogen fluoride species exist on tetrahedral zinc sites and provides a source of fluorine for fluorination reactions. Three

modes of HF adsorption to the most active promotion of 6.5 % zinc on γ-alumina/fluorine centres were proposed, as shown in figure 6.5. The heats of adsorption for the three modes are -92 kJ mol^{-1} for type 1, -64 kJ mol^{-1} for type 2 and -48 kJ mol^{-1} for the type 3.
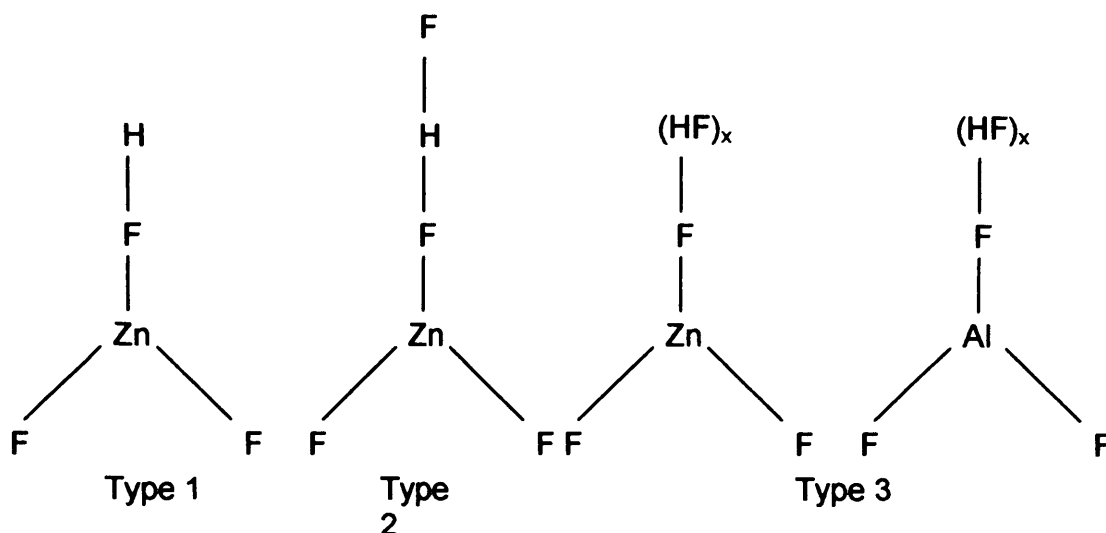

Figure 6.5. Three proposed adsorption environments for HF on 6.5% Zn/γ-alumina.[21]

The type 3 adsorption in figure 6.5 can be considered against the single aluminium-fluorine interaction on the {0001} α-alumina surface as shown in chapter four, where the energies of adsorption range from -50.6 kJ mol^{-1} to -52.5 kJ mol^{-1}.

6.1.4   θ-alumina and AlF₃.

The work on θ-alumina was undertaken to provide a comparison between the purely octahedral aluminium α-alumina system and the tetrahedral and octahedral structure found for θ-alumina. Previous work has not agreed on the ratio of the two co-ordinations, varying from approximately equal in a 1:1 ratio [22] [23] to almost entirely octahedral.[24] This work finds, for the bulk structure, that the ratio is 1:1 for both the CASTEP and GULP calculations. The CASTEP simulations found that the θ-alumina polymorph is 9.21 kJ mol^{-1} higher in energy per Al₂O₃ formula unit than the α-alumina corundum structure when the total energies of the two phases are considered. The analogous GULP calculations found the θ-alumina phase to be 209 kJ mol^{-1} higher per Al₂O₃ formula unit. These two values can be compared to the Hartree-Fock calculations

finding the θ-alumina phase to be 42 kJ mol-1 higher per Al_2O_3 unit,[25] both values in this work confirm that the corundum structure is energetically more stable, justifying why the α-alumina phase is the final stage in the thermal dehydration of both boehmite and bayerite precursors, as defined in figure 1.1. The surface calculations undertaken on the {101} plane found the ratio of tetrahedral to octahedral aluminium sites to be 5:3, a 60 % tetrahedral excess. The GULP calculations found this relaxed surface energy to be 0.59 J m^{-2}, reduced from 6.85 J m^{-2} for the unrelaxed single point surface energy; whereas CASTEP gave the relaxed surface energy at 0.32 J m^{-2}, a good agreement between the two codes. The hydroxylated form of the {101} surface was modelled using CASTEP by removing tetrahedral and octahedral terminating aluminium sites and subsequently adding hydrogen atoms to the remaining oxygen atoms, as a 100% removal of aluminium sites would result in an excess of hydrogens due to shared oxygen sites. The energy of hydroxylation for the reaction shown in equation 5.7 was found to be -107 kJ mol^{-1}, compared to the {0001} α-alumina hydroxylation value of - 99 kJ mol^{-1}.

Using an approach of calculating the surface energy for a hydroxylated surface, using the cycle outlined in figure 5.6 and defined in equation 5.6 gave the value of γ_s to be 3.23 J m^{-2}. This compares to the hydroxylated {0001} α-alumina surface energy of 1.00 J m^{-2}. This indicates that the presence of tetrahedral aluminium sites has an effect on the reaction of the {101} θ-alumina surface with water compared to the {0001} α-alumina surface.

The aluminium fluoride, AlF_3, structure was modelled to represent the fully fluorided form of alumina. The CASTEP code modelled the β-AlF_3 structure from first principles, finding the unit cell parameters close to the experimental values. The {100} surface was found to be stable with a relaxed surface energy of 1.52 J m^{-2}, lowered as expected from the single point calculation γ_s value of 2.87 J m^{-2}. An alternative approach was constructed in the GULP program, requiring a set of appropriate potentials to be fitted to the experimental bulk structure as described in chapter three. The Buckingham potential used for the aluminium-fluorine non-bonding interaction was $A = 1359.041$ eV and $\rho = 0.2725$ Å, acting to a maximum of 12 Å. These parameters were fitted over the

β-, κ- and θ-AlF$_3$ experimentally determined aluminium fluoride structures, and offer unit cell parameters in close agreement with the respective experimental lattices.

Surfaces constructed using the Shiftcell program found the {100} β-AlF$_3$ to be electrostatically stable in accordance with the criteria defined in chapter three. The unrelaxed surface energy was found to be 3.44 J m^{-2}, against the single point value of 2.09 J m^{-2}. This confirms that the Buckingham potential used for the simulation of the aluminium fluoride series offers a suitable alternative to the intensive periodic CASTEP for structural determination. The GULP simulations completed in 27.5 s, whereas the CASTEP calculations took 131 342 s. Two different terminations were selected to provide comparisons between the surface containing aluminium accessible to adsorbate molecules in the GULP calculations, whereas the surface termination used in the CASTEP calculations had no such available aluminium sites.

6.2 Future work.

The scope for future work includes simulations on α- and θ-alumina using both periodic *ab initio* and molecular mechanical methods for reaction mechanisms, as well as extensive investigations into the surfaces and reactions of the aluminium fluoride structure to represent the fully fluorided form of alumina.

Given sufficient and powerful enough computing resources, the possibility exists for analogous density functional theory calculations on partially hydroxylated {0001} α-alumina surfaces to relate to the GULP determined values shown in chapter four and table 6.2, and so remove the need for the E$_{correction}$ term.

The γ-alumina phase also contains both tetrahedral and octahedral aluminium environments and is the subject of a wider range of experimental and theoretical techniques, offering a greater number of comparisons to catalytic work.

The zinc promotion of γ-alumina has been shown to allow the adsorption of HF and to improve the fluorination activity of the catalyst. The subsequent nucelophilic S$_N$2 reaction with an adsorbed chlorofluorocarbon is shown in figure 6.6. This temperature

programmed desorption work can be extended for computational simulations into the effect of zinc doping on the {0001} α-alumina and the {100} β-AlF₃ surfaces; and the reactions that hydrogen fluoride may undergo on these surfaces.
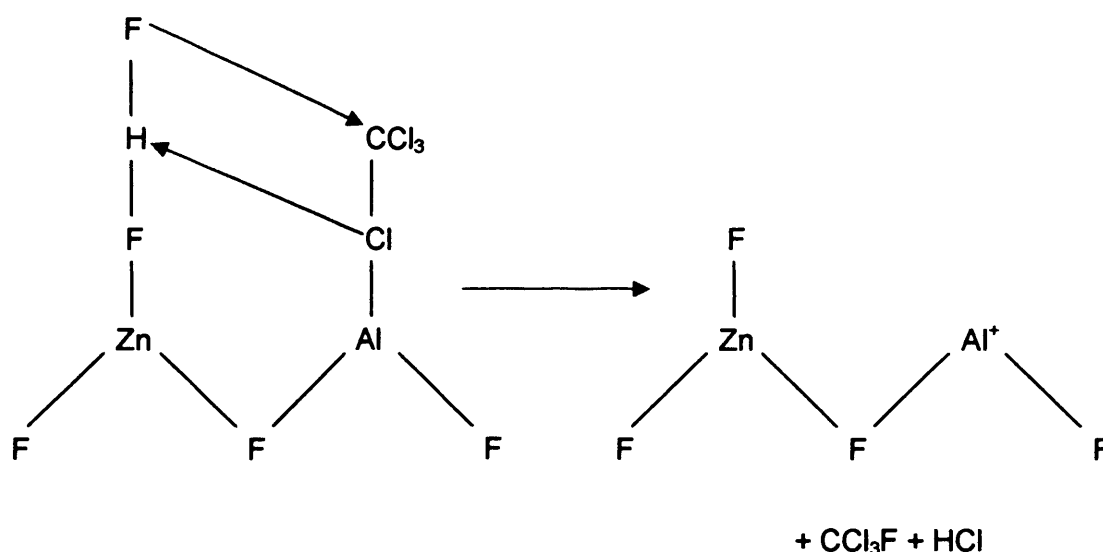

Figure 6.6. Proposed mechanism for the fluorination of CCl4 over Zn/γ-alumina exposed to HF.²¹

The work of Barclay *et al* ²⁶ showed that exposure of H¹⁸F to β-AlF₃ undergoes both exchange and retention. However, when the ¹⁸F labelled surface was exposed to CCl₂FCClF₂, no measurable inclusion of ¹⁸F was found in the chlorofluorocarbon, suitable simulations could be constructed using DFT methods to determine the reaction profile as investigated by Bankhead *et al*.²⁷

¹ P. P. Ewald and C. Hermann, *Strukturbericht* vol. 1, 1913-1926 p240.
² J. Lewis, D. Schwarzenbach and HD. Flack, *Acta Crystallographica A*, **38**, 733 (1982).
³ P. W. Tasker. 'Advances in Ceramics' in *Structure and Properties of MgO and Al₂O₃ Ceramics*, Vol. **10**, p276, (1984).
⁴ W. C. Mackrodt, *J. Chem. Soc., Faraday Trans.* **2**, **85**, 541, (1989).
⁵ A. Marmier and M. W. Finnis, *J. Phys.: Condensed Matter* **14**, 7797, (2002).
⁶ M. Baudin and K. Hermansson, *Surf. Sci.*, **474**, 107, (2001).
⁷ I. Manassidis and M. J. Gillan, *J. Amer. Chem. Soc.*, **77**, 335, (1994).
⁸ R. di Felice and J. E. Northrup, *Phys. Rev. B.* **60**, 16287, (1999).
⁹ W. C. Mackrodt, *Phil. Trans. R. Soc. London A.* **341**, 301, (1992).
¹⁰ I. Manassidis, A. De Vita and M. Gillan, *Surf. Sci. Lett.*, **285**, L517, (1993).
¹¹ J. M. McHale A. Auroux, A. Perrotta and A. Navrotsky, *Science*, **277**, 788, (1997).
¹² C. Verdozzi, D. Jennings, P. Shultz and M. Sears, *Phys. Rev. Lett.*, **82**, 799, (1999).
¹³ C. R. A. Catlow, R. James, W. Mackrodt and R. F. Stewart, *Phys. Rev. B*, **25**, 1006, (1982).
¹⁴ P. Guenard, G. Renaud, A. Barbier and M.Gautier-Soyer, *Surf. Rev. Lett.*, **5**, 321 (1998).
¹⁵ J. W. Elam, C. E. Nelson, M. Cameron, M. Tolbert and S. George, *J. Phys. Chem. B*, **102** 7008, (1998).
¹⁶ C. E. Nelson, J. W. Elam, M. A. Tolbert and S. M. George, *Applied Surface Science*, **171**, 21, (2001)
¹⁷ B. A. Hendriksen, D. Pearce and R. Rudham, *J. Catal.*, **24**, 82, (1972).
¹⁸ C. R. A. Catlow, *J. Phys. Chem.*, **38**, 1131, (1977).
¹⁹ M. A. Nygren, D. H. Gay and C. R. A. Catlow, *Surf. Sci.* **380**, 113 (1997).

[20] J. D. Gale, *Faraday Diss.* **106**, 219, (1997).

[21] M. J. Jones, Ph.D. thesis, Cardiff University 2004.

[22] G. Yamaguchi, I. Yasui and W. Chiu, *Bull. Chem. Soc. Japan*, **43**, 2487, (1970).

[23] C. Wolverton and K. Hass, *Physical Review B*, **63**, #024102, (2000).

[24] C. S. John, V. C. M. Alma and G. R. Hays, *Appl. Catal.*, **6**, 341-346, (1983).

[25] . P. Borosy, B. Silvi, M. Allavena and P. Nortier, *J. Phys. Chem.*, **98**, 13189, (1994).

[26] C. H. Barclay, H. Bozorgzadeh, E. Kenmitz, M. Nickkho-Amiry, D. Ross, T. Skapin, J. Thomson, G. Webb and J. Winfield, *J. Chem. Soc. Dalton Trans.*, 40, (2002).

[27] M. Bankhead, G. Watson, G. Hutchings, J. Scott and D. Willock, *Appl. Catal. A: Gen.*, **200**, 263, (2000).